Control of Naval Electric Drives

Final Report
ONR Grant N00014-95-1-0723

Alex M. Stanković, PI
astankov@cdsp.neu.edu
617.373.3007

Gilead Tadmor

Ismail Agirman
Z. Coric
V. Davidkovich
T. Sakharuk

April 22, 1999

Northeastern University
Department of Electrical and Computer Engineering
409 Dana Building
Boston, MA 02115

Contents

1 Background and Overview **1**

2 Introduction on Dissipativity–Based Control of PMSM **7**

2.1 Overview 7

2.2 PMSM Thesis Outline 11

3 Permanent Magnet Synchronous Motors **14**

3.1 Introduction 14

3.2 Brushless Motors Classification 14

3.3 Materials for PMSMs 16

3.4 Construction 16

3.5 Classification of PMSMs 17

3.5.1 Surface Mounted PMSMs 17

3.5.2 Interior PMSMs 19

3.6 Mathematical Model of PMSM 20

3.6.1 Electrical Dynamics 21

3.6.2 Mechanical Dynamics 24

3.6.3 Transformation of PMSM Model 26

3.7 Motor Comparison 32
3.8 Losses and Efficiency 33
3.9 Challenges in Control of PMSM 34

4 Passivity Based Control of PMSMs 36

4.1 Introduction 36
4.2 The PM Synchronous Motor 38
4.3 The Control Problem 39
4.4 The Primary Control 40
  4.4.1 The Desired Torque 40
  4.4.2 The Desired Currents 41
  4.4.3 The Primary Voltage Input 42
4.5 Incremental State Dynamics and Control 43
  4.5.1 Torque Estimation Errors And The Mechanical Incremental System 43
  4.5.2 The Electrical Incremental System and Incremental Control . 45
4.6 Eigenvalue Placement for Controller Parameter Calculation 47

5 Experimental Test-Bed 52

5.1 Control DSP 53
5.2 Drive DSP 56
  5.2.1 Drive DSP characteristics 57
  5.2.2 Rotor Position Sensors and Resolver-to-Digital Converter . . . 60
  5.2.3 Drive DSP operation 63
5.3 Power Inverter Stage 65

5.3.1 Generation of Sinusoidal Voltages by means of PWM 66

5.3.2 Deadtime and Pulse Deletion Specifications 67

5.4 Permanent Magnet Synchronous Motor 71

5.4.1 Identification of Motor Drive Parameters 71

6 Simulation and Experimental Results **78**

6.1 Sudden Change in Load Torque 80

6.2 Sudden Change in Reference Speed 87

6.3 Periodic Reference Speed 91

7 Passivity Based Sensorless Control of PMSM **93**

7.1 Introduction 93

7.2 $\alpha\beta$ and dq Models of PMSM 94

7.3 Observer Design 95

7.4 Observer Gain Selection 101

7.5 Simulations of the Passivity-Based State Observer 103

8 Conclusions and Future Research on PMSM **110**

9 Introduction to Switched Reluctance Motors **114**

9.1 SRM Model 116

9.2 SRM Control Algorithms 118

9.3 SRM Drive Inverter Topologies 122

10 Optimal Waveform Profiling **129**

10.1 Introduction 129

10.2 Low Ripple Control 131

10.3 Simulations with Uncertain Models 136

10.4 Experimental Results 140

10.5 Conclusions and Research Directions 145

11 Adaptive Closed loop Control 147

11.1 Introduction 147

11.2 Identification of the SRM 149

11.2.1 Modeling the flux current ralationship 152

11.2.2 Estimation of the J and B of the motor 154

11.3 Control Design 155

11.3.1 The Commutation Strategy 155

11.3.2 Closed loop and Adaptation law 157

11.4 Simulations and Experimental Results 160

11.5 Limitations of the adaptive algorithm 164

11.5.1 Limitations due to hysteretic current control 165

11.5.2 Limitations due to quality of speed measurement 166

11.5.3 Limitations due to the controller structure 168

11.6 Conclusions on SRM 169

12 Introduction on Modeling of PWM Systems 171

12.1 Background 171

12.2 General class of systems under consideration 175

13 Averaging Theory 179

14 Basic PWM Control of the DC Servo Motor **186**

14.1 Conventional Controller design 187

14.2 State space dynamical equations for the closed-loop system 189

14.3 Linearization of the PWM gain 193

15 Delay effects **195**

16 Discrete-time simulation **200**

17 Existence of a T-Periodic Steady State **206**

17.1 A Necessary Condition for Existence of a T-Periodic Steady State of the Approximate System 209

17.2 Further Necessary and Sufficient Conditions for Existence of a T-Periodic Stable Equilibrium (Based on the Approximate System) . . . 213

17.3 Examples 219

17.3.1 Current programmed DC-DC converter. 219

17.3.2 DC servo motor. 226

17.3.3 PWM with uniform sampling. 227

17.3.4 PWM with two sided sawtooth function 229

17.4 Conclusions 231

18 Effects of Low Switching Frequency on AC Drives **232**

18.1 Introduction 233

18.2 Model of an AC Drive 236

18.3 Voltage space vector PWM 238

18.3.1 Saturation issues 244

18.3.2 Switching pattern 246

18.3.3 An analytical expression for d-q voltages 247

18.4 Open-loop PWM gain 250

18.4.1 Estimation of the current ripple magnitude 254

18.5 Closed-loop PWM gain 262

18.6 Example 267

18.7 Conclusions 269

19 Conclusions on PWM Modeling **270**

19.1 Summary 270

19.2 Suggestions for future work 279

Bibliography **281**

A Selection of controller parameters **296**

B Stability of dissipative systems **304**

C Calculation of Speed Error Power **309**

D Parameters of the DC servo motor setup **313**

E The ripple function coefficients **314**

F Derivation of the piecewise affine map **315**

List of Figures

3.1 Mechanical construction of surface-mounted PMSMs: projecting type (left) and inset type (right). 18

3.2 Construction of interior PMSMs. 20

3.3 Vector diagram for two-phase transformation 27

3.4 Vector diagram for *dq* transformation 30

4.1 Block diagram of the passivity based closed loop system. 47

5.1 Overall drive system setup 53

5.2 Basic inverter scheme. 65

5.3 IGBT turn-off process: Q1 gate signal (upper) and phase A output voltage (lower). 68

5.4 Gate driver time delay. 69

5.5 PMSM phase current generated by means of PWM. 70

5.6 Performance characteristics of R43HENA: peak torque (upper line) and continuos torque (lower line) 73

5.7 Trace of motor phase backEMF. 74

5.8 Spindown test results. 77

6.1 Simulations of speed transients (left) and required actuation V_q (right) following the load torque step change. Three eigenvalues of $A_{2,2}$ are placed at -20 (solid line), -20 and -20±20$\jmath$ (dashed line), -20 and -20±40$\jmath$ (dash-dotted line.) 80

6.2 Speed transients (left) and required actuation V_q (right) following the load torque step change. Three eigenvalues of $A_{2,2}$ are placed at -20 (largest speed dip), -20 and -20±20$\jmath$, -20 and -20±40$\jmath$ (smallest speed dip.) Scaling: horizontal axis - 0.2 sec/division, vertical axis - 5 rad/sec/division (speed) and 8.45 volts/division (V_q). 81

6.3 Simulations of speed transients (left) and required actuation V_q (right) following the load torque step change. Three eigenvalues of $A_{2,2}$ are placed at -20 and -20±20$\jmath$ (solid line), -30 and -30±30$\jmath$ (dashed line), -40 and -40±40$\jmath$ (dash-dotted line.) 82

6.4 Speed transients (left) and required actuation V_q (right) following the load torque step change. Three eigenvalues of $A_{2,2}$ are placed at -20 and -20±20$\jmath$ (largest speed dip), -30 and -30±30$\jmath$, -40 and -40±40$\jmath$ (smallest speed dip.) Scaling: horizontal axis - 0.2 sec/division, vertical axis - 5 rad/sec/division (speed) and 8.45 volts/division (V_q). 83

6.5 Required actuation V_q (upper) and speed transients (lower) following the load torque step change. Three eigenvalues of $A_{2,2}$ are placed at -40 (left) and -80 (right). Scaling: horizontal axis - 0.2 sec/division, vertical axis - 5 rad/sec/division (speed) and 8.45 volts/division (V_q). 84

6.6 Required actuation V_q (upper) and speed transients (lower) following the load torque step change. Three eigenvalues of $A_{2,2}$ are placed at -120 (left) and -150 (right). Scaling: horizontal axis - 0.2 sec/division, vertical axis - 5 rad/sec/division (speed) and 8.45 volts/division (V_q). 84

6.7 Required actuation V_q (upper) and speed transients (lower) following the load torque step change. Three eigenvalues of $\acute{A}$ are placed at -40; one is placed at -140 (left) and -120 (right). Scaling: horizontal axis - 0.2 sec/division, vertical axis - 5 rad/sec/division (speed) and 8.45 volts/division (V_q). 86

6.8 Required actuation V_q (upper) and speed transients (lower) following the load torque step change. Three eigenvalues of $\acute{A}$ are placed at -40; one is placed at -110 (left) and -90 (right). Scaling: horizontal axis - 0.2 sec/division, vertical axis - 5 rad/sec/division (speed) and 8.45 volts/division (V_q). 86

6.9 Simulations of speed transients (left) and required actuation V_q (right) following the commanded speed step change. Three eigenvalues of $A_{2,2}$ are placed at -30 (solid line), -30 and -30$\pm$30$\jmath$ (dashed line), -30 and -30$\pm$60$\jmath$ (dash-dotted line.) 88

6.10 Speed transients (left) and required actuation V_q (right) following the commanded speed step change. Three eigenvalues of $A_{2,2}$ are placed at -30 (least oscillatory response), -30 and -30$\pm$30$\jmath$, -30 and -30$\pm$60$\jmath$ (most oscillatory response.) Scaling: horizontal axis - 0.02 sec/division, vertical axis - 5 rad/sec/division (speed) and 3.38 volts/division (V_q). 88

6.11 Simulations of speed transients (left) and required actuation V_q (right) following the commanded speed step change. Three eigenvalues of $A_{2,2}$ are placed at -20 and -20±20$\jmath$ (solid line), -40 and -40±40$\jmath$ (dashed line), -60 and -60±60$\jmath$ (dash-dotted line.) 90

6.12 Speed transients (left) and required actuation V_q (right) following the commanded speed step change. Three eigenvalues of $A_{2,2}$ are placed at -20 and -20±20$\jmath$ (least oscillatory response), -40 and -40±40$\jmath$, -60 and -60±60$\jmath$ (most oscillatory response.) Scaling: horizontal axis - 0.02 sec/division, vertical axis - 5 rad/sec/division (speed) and 3.38 volts/division (V_q). 90

6.13 Required actuation V_q (upper) and speed transients (lower) following the commanded speed step change, variation of λ. λ is chosen such that the forth eigenvalue is placed at ≈ -190 with no λ effect (left plot) and at -90 (right plot). Scaling: horizontal axis - 0.025 sec/division, vertical axis - 5 rad/sec/division (speed) and 8.45 volts/division (V_q). 91

6.14 Tracking of sinusoidally varying commanded speed: required actuation V_q (upper traces) and commanded and actual speeds (lower traces). Frequency of commanded speed is 20 Hz (left plot), and 40 Hz (right plot). Scaling: horizontal axis - 20 (left), and 5 (right) millisec/division, vertical axis - 5 rad/sec/division (speed) and 16.9 volts/division (V_q). 92

7.1 Location of the closed loop system eigenvalue with the smallest absolute value as a function of ρ and κ for various values of ν 103

7.2 Location of the closed loop system eigenvalue with the smallest absolute value as a function of ρ and ν for various values of κ 104

7.3 Estimation of motor speed (upper left), load torque (upper right), rotor position (lower left) and q component of the motor current (lower right) for $\nu = 10$ (slowest convergence), 15 and 20 (fastest convergence). . . 106

7.4 Estimation of motor speed (left) and load torque (right), for $\kappa = 15$ (slowest convergence), 10 and 5 (fastest convergence) 107

7.5 Estimation of motor speed (left) and load torque (right), for $\rho = 50$ (slowest convergence), 100 and 150 (fastest convergence) 107

7.6 Use of passivity-based observer in control loop. Speed transients (left) and required actuation V_q (right) following sudden load torque change. ρ=50 (solid line slowest response), ρ=100 (dashed line), ρ=200 (dash-dotted line - fastest response.) 108

7.7 Use of passivity-based observer in control loop. Speed transients (left) and required actuation V_q (right) following step change in commanded speed. 108

9.1 Voltage controlled drive. 119

9.2 The LMB1008 Controller. 120

9.3 Current-fed Controller. 121

9.4 The bridge converter. 123

9.5 The split capacitor converter. 124

9.6 The Miller converter. 125

9.7 The C-dump converter. 125

9.8 The sood converter. 127

10.1 Illustration of arc notation. 132

10.2 Optimized current (top trace) and the corresponding voltage (bottom trace) for the experimental SRM for $\tau_o = 0.8$ Nm, ω=300 rpm, and r_{phase}=1Ω. 134

10.3 Flux function $\lambda_l(\theta, i_l)$ for the experimental SRM used in this chapter. 136

10.4 Optimal constant current waveform (dashed) and optimal current waveform (solid); left figure. Corresponding torque deviations assuming accurate model; right figure. 137

10.5 True (solid) and perturbed (dashed) inductance for two neighboring phases. 139

10.6 Torque deviations for the proposed controller (solid) and traditional controller (dashed), assuming inaccurate model and unequal phases. 140

10.7 Measured steady-state waveforms for the conventional policy: top trace - actual currents for two opposite phases; middle trace - torque variations (amplitude is 32 % of the mean); bottom trace - reference current waveforms for the same two phases. 142

10.8 Measured steady-state waveforms for the proposed switching policy: top trace - actual currents for two opposite phases; middle trace - torque variations (amplitude is 16 % of the mean); bottom trace - reference current waveforms for the same two phases. 143

10.9 Measured normalized magnitude spectrum of the torque ripple, top figure: traditional control policy, bottom two figures: optimized control policy with both hard and soft chopping inverter operation. 144

11.1 Magnetic hysteresis curve 150
11.2 A fit for measured flux for different θ 152
11.3 Torque function for different current levels 152
11.4 Current waveforms for different models 157
11.5 Corresponding torques for Figure 4 157
11.6 Torque produced by the motor with harmonic adaptation 161
11.7 The estimated harmonic coefficients 161
11.8 Estimate of dc component when harmonic adaptation is eliminated . 162
11.9 Torque generated under only dc adaptation 162
11.10 Experimental results: torque-ripple spectrum without harmonic adaptation 163
11.11 Experimental results: torque-ripple spectrum with harmonic adaptation 163
11.12 Hysteretic approximation with high supply voltage 166
11.13 Torque ripple spectrum with better hysteretic approximation 167

12.1 Block diagram of a PWM actuated system. 174
12.2 PWM input a) and output b) voltages. 176

13.1 Averaged trajectory and ripple function. 182

14.1 DC servo motor block diagram. 187
14.2 Magnitude of the current ripple, A 192

14.3 Comparison of the ideal and effective averaged PWM gain 193

14.4 Linearization of the PWM gain around three points 194

15.1 PWM input a) and output b) voltages. 196

15.2 Absolute deviations ($\tau - m(\mathbf{z})/V_d$ in %) of the averaged normalized PWM gain from ideal as a function of $m(\mathbf{z})/V_d$ for different time delays. 197

15.3 The PWM sawtooth (triangles) and PWM input (200μs per division horizontally) 199

16.1 Different types of intersection $\frac{m(\mathbf{x}(t/T))}{V_d}$ (solid line) and tri$(t,1)$ (dashed line) for DC motor, $\frac{V_d}{M} = 0.421$. 203

16.2 PWM input voltage and a sawtooth in the presence of a delay. 204

17.1 Stability regions on (α,β) plane: (a) $t_s/T < \beta/(\beta-\alpha) < 1$, (b) $1 > t_s/T > \beta/(\beta-\alpha)$, (c) uniform sampling. 209

17.2 Different types of intersections for the time interval $T < t \leq 2T$ . . . 210

17.3 A current -programmed buck converter. 219

17.4 Geometries of inductor current in steady state. 221

17.5 Geometries of inductor current in steady state. 224

17.6 $3T$-periodic stable equilibrium. The PWM input voltage and sawtooth - (a). The evolution of the state vector (τ_k, m_k) - (b). 227

17.7 Aperiodic behavior. The PWM input voltage and sawtooth - (a). The evolution of the state vector (τ_k, m_k) - (b). 228

17.8 Two sided PWM input and output voltages. 230

18.1 AC servo motor block diagram. 235

18.2 Inverter for three-phase AC motor. 240

18.3 Explanation of the definition of reference input voltage vectors. In this example $N = \frac{T}{T_0} = 12$ and $t_s = 0$. 241

18.4 Voltage vectors created by the switching states of the inverter. 242

18.5 3-Phase output voltage of the PWM, $t \in [0, T/6]$, $N = T/T_0$. 249

18.6 Typical voltages and corresponding currents waveform patterns for one basic inverter cycle T_0. Magnitude of the current ripple is defined differently for each pattern $\Delta i_{3,2} = (i_3 - i_2)/2$ and $\Delta i_{4,1} = (i_4 - i_1)/2$. 256

18.7 Magnitude of d-current ripple normalized by V_{DC} as a function of R^* and θ_0 ($N = 24$, $n = 1$, $M/V_{DC} = 0.195$), theoretical (-) obtained by formula $\max[|\Delta i^d_{4,1}|, |\Delta i^d_{3,2}|]$ and experimental obtained by simulation of the nonlinear closed-loop system (+). 258

18.8 Magnitude of q-current ripple normalized by V_{DC} as a function of R^* and θ_0 ($N = 24$, $n = 1$, $M/V_{DC} = 0.195$), theoretical (-) obtained by formula $\max[|\Delta i^q_{4,1}|, |\Delta i^q_{3,2}|]$ and experimental obtained by simulation of the nonlinear closed-loop system (+). 262

18.9 PWM 3-phase line voltages. 268

18.10Output of the PWM in d-q coordinates, actual (thin lines) and approximated (bold lines). 269

C.1 The actual dependence of angle on computational cycle time 309

Chapter 1

Background and Overview

This document is a final technical report for the ONR grant N00014-95-0723. The work on the project was completed in the period 6/95–12/98 (with extensions). The senior personnel included A.M. Stankovic (P.I.) and Prof. G. Tadmor, both of Northeastern University. Four graduate students were supported in part by the grant: Z. Coric (MS in 1996), V. Davidkovich (PhD, 1998), T. Sakharuk (PhD, 1998), and I. Agirman (PhD, 1999).

Main technical problems addressed in the project included:

- Nonlinear control of permanent magnet synchronous motors – PMSM (PhD thesis of V. Davidkovich),
- Control-oriented modeling of pulse width modulated (PWM) systems (PhD thesis of T. Sakharuk),
- Nonlinear control of switched reluctance motors – SRM (MS thesis of Z. Coric and PhD thesis of I. Agirman).

The results contained in this report were presented in a number of journal and conference papers (with acknowledgment to ONR in all cases):

- V. Davidkovich, A.M. Stanković, G. Tadmor, "Dissipativity Approach to Speed Servo Control of Permanent Magnet Synchronous Motors", submitted to *IEEE Transactions on Control System Technology*.
- I. Agirman, A.M. Stanković, G. Tadmor, H. Lev-Ari, "Adaptive Torque Ripple Minimization in Switched Reluctance Motors" submitted to *IEEE Transactions on Industrial Electronics*.
- T. Sakharuk, A.M. Stanković, G. Tadmor, "Effects of Finite Switching Frequency on Space Vector Modulated AC Drives", submitted to *IEEE Transactions on Circuits and Systems-I: Fundamental Theory and Applications*.
- T. Sakharuk, B. Lehman, A.M. Stanković, G. Tadmor, "Effects of Finite Switching Frequency and Delays on PWM Controlled Systems", to appear in *IEEE Transactions on Circuits and Systems-I: Fundamental Theory and Applications*.
- A.M. Stanković, G. Tadmor, Z. Ćorić, I. Agirman, "On Torque Ripple Reduction in Current-Fed Switched Reluctance Motors", *IEEE Transactions on Industrial Electronics*, 46(1), Feb. 1999, pp. 177-183.
- I. Agirman, A.M. Stanković, G. Tadmor, "Adaptive Torque Ripple Minimization in Switched Reluctance Motors Using Observer-based Back-stepping", accepted for the *Power Electronics Specialists Conference*, June 1999.

- I. Agirman, A.M. Stanković, G. Tadmor, "Adaptive Torque Ripple Minimization in Switched Reluctance Motors", *IEEE Conference on Decision and Control*, Dec. 1998, pp. 983-989.

- T.A. Sakharuk, A.M. Stanković, G. Tadmor, "Effects of Low Switching Frequency on Synchronous AC Drives", *IEEE Conference on Decision and Control*, Dec. 1998, pp. 4664-4669.

- I. Agirman, A.M. Stanković, G. Tadmor, "Adaptive Torque Ripple Minimization in Switched Reluctance Motors with Low Complexity Models", *Naval Symposium on Electric Machines*, Oct. 1998, pp. 247-253.

- T.A. Sakharuk, A.M. Stanković, G. Tadmor, "Effects of Low Switching Frequency on Permanent Magnet AC Drives", *Naval Symposium on Electric Machines*, Oct. 1998, pp. 265-272.

- O.Y. Bas, A.M. Stanković, G. Tadmor, "Passivity–Based Sensorless Control of Smooth–Rotor Permanent Magnet Synchronous Motors", *IEEE Conference on Decision and Control*, San Diego, Dec. 1997, pp. 239-244.

- V. Davidkovich, A.M. Stanković, G. Tadmor, "Analysis and Experiments with Dissipativity–Based Control of Permanent Magnet Synchronous Motors", *IEEE Industry Applications Society Annual Meeting*, New Orleans, Oct. 1997, pp. 451-458.

- T. A. Sakharuk, B. Lehman, A.M. Stanković, G. Tadmor, "Effects of Finite Switching Frequency and Computational Delay on Pulse Width Modulation Controlled Servo Drives", *IEEE Industry Applications Society Annual Meeting*, New Orleans, Oct. 1997, pp. 699-707.

- O.Y. Bas, V. Davidkovich, A.M. Stanković, G. Tadmor, "A Dissipativity–Based Approach to Adaptive Control of Permanent Magnet Synchronous Motors", *IEEE Conference on Control Applications*, Hartford, Oct. 1997, pp. 238-243.

- O.Y. Bas, V. Davidkovich, A.M. Stanković, G. Tadmor, "Globally Stable Adaptive Control of Permanent Magnet Synchronous Motors", *Naval Symposium on Electric Machines*, Newport, July 1997, pp. 119–126.

- A. Barnett, V. Davidkovich, A.M. Stanković, G. Tadmor, "A Versatile Test–Bed for Evaluation of Controllers for Permanent Magnet AC Drives", *Naval Symposium on Electric Machines*, Newport, July 1997, pp. 259–265.

- V. Davidkovich, A.M. Stanković, G. Tadmor, "Dissipativity-Based Control of Permanent Magnet Synchronous Motors with Guaranteed Convergence Rates", *IEEE International Symposium on Industrial Electronics*, Guimaraes, Portugal, July 1997, pp. 95–100.

- V. Davidkovich, A.M. Stanković, G. Tadmor, "Global Controllers for Permanent Magnet Synchronous Motors", *Energy, Power and Motion Control Congress*, Israel, May 1997, pp. 1–6.

- T. Sakharuk, A.M. Stanković, G. Tadmor, S. Dussy, "An Examination of Servo DC Motor Controller Structure Using Robust Synthesis", *Energy, Power and Motion Control Congress*, Israel, May 1997, pp. 94–99.
- A.M. Stanković, G. Tadmor, Z. Ćorić, "Low Torque Ripple Control of Current-Fed Switched Reluctance Motors", *IEEE Industry Applications Society Annual Meeting*, Oct. 1996, Vol. 1, pp. 84-91.

The project was instrumental in the development of research infrastructure for electric drives at the Northeastern University, as a new versatile test bed for PMSM and SRM was developed. This laboratory facility is presently undergoing further development under NSF and ONR support.

This document is a compilation of two PhD theses (Davidkovich and Sakharuk) and thesis draft manuscript (I. Agirman). Thus, it consists of three self-contained parts ordered as follows:

- Control of PMSM,
- Control of SRM,
- Modeling of PWM systems.

While the work on this project greatly benefited from the technical discussions and expertise developed within the ONR power electronics building block (PEBB) program, all views expressed here are those of the authors.

We thankfully acknowledge guidance and support provided by the technical project managers LCDR Cliff Whitcomb and Terry Ericsen who repeatedly demonstrated their understanding of idiosyncrasies of university research. We are proud to have been associated with the PEBB program, and we hope that our project will help further the long range objectives of that unique research endeavor.

Chapter 2

Introduction on Dissipativity–Based Control of PMSM

2.1 Overview

Electrical motors are widely used in industry in order to convert electrical energy to mechanical work. The permanent magnet synchronous motor (PMSM) represents one of these electromechanical devices. PM machines fall into a generalized classification known as “doubly-excited” machines, which have two sources of excitation – usually known as the armature and the field. In PM machines, the excitation or field winding is replaced by a permanent magnet and no external source of electrical energy is required. Recent advances in the manufacturing of rare earth magnets with a higher energy density and coercivity have opened up new possibilities for large-scale applications of PMSMs.

The PMSM is considered as one of the most promising candidates for future variable frequency drives [93], often achieving higher efficiency than comparable induction and other machines. One of the chief merits of PM machines as compared to non-permanent magnet machines is the possibility to be designed in many non-standard sizes and shapes, that especially fits demanding applications in automotive and aerospace industries [74]. Permanent magnet synchronous motors form a natural partner with power electronic circuits and devices and are easily controllable by digital logic systems which are becoming the main mode of PMSM control [25, 29].

The automatic control of an electric motor is required in order to achieve its desirable performance. In many practical cases the motor performance can be characterized by its response to sudden changes in the applied load torque and to changes in the reference speed. The transition from one operating point to another is usually required to be fast and smooth, and at the same time, refrain from excessive power consumption. These requirements, being applied to any dynamical system, are contradictory enough . The PMSM, particularly, makes this task even more complicated. The specific challenges in the control of PMSM are caused by several factors:

- nonlinear structure of the motor equations;
- electrical and mechanical subsystem time constants usually differ by order of magnitude;
- only the electrical subsystem is directly available for actuation;

These non-typical constraints inherent in PMSM require nonstandard control approach. Existing control schemes (such as the nested loop PI regulator with cancellation of nonlinearities in the current loop) can provide satisfactory performance only by widening the bandwidth of the current loop and thus, typically require excessive power during transients. This is only possible in the cases when overall system efficiency is of secondary concern. Therefore, the development of fundamentally different PMSM control algorithm is of equal importance both from theoretical and from practical perspectives.

The design of the controller in this thesis falls into the classification of energy shaping designs. A recent review of motion control schemes for PMSM and a description of nonlinear control methods can be found in [99]. More accurately, this design uses energy dissipation and energy exchange between various physical states as the main design tool. This allows for deeper insight into more fundamental properties of the physical system “PMSM – closed loop controller”.

The presented controller design is different from the known approaches ([80, 81, 103]) in the way the algorithm was developed and controller outputs are constructed. Much greater attention is paid to the lossless exchanges between electrical and mechanical incremental states since these exchanges are instrumental in shifting incremental energy from the mechanical component, where direct actuation is not available, to the electrical component, where that incremental energy can be dissipated. This eliminates the need that the bandwidth in current response be much wider than that of the speed loop which means that higher performance (measured, for example, by speed response) is achievable with fixed actuation resources, better noise rejection and lower requirements to the sampling frequency of the digital implementation.

The research presented in this thesis has several objectives.

First, a theoretical design of a nonlinear controller using energy dissipation as a main design tool was considered. The control objective is the tracking of infrequent step changes, as well as of continuous changes in the reference speed and in the load torque.

Second, a practical (simulations and experiments) verification of the proposed control scheme was required. The main purpose of the experimentation was to test the developed control algorithm, applied to an actual PMSM and drive hardware, where non-idealities and deviations of mathematical abstractions from the physical device properties explicate themselves.

Taken together, the fulfilment of these two goals amounts to a well-developed and practically reliable passivity based control scheme for PMSM. In addition to that, the designed passivity based control algorithm has been extended to a case when no shaft position information is available and position and speed estimation is necessary. The position sensorless control algorithm for PMSM has been designed and investigated via numerical simulations.

2.2 PMSM Thesis Outline

This thesis consists of six chapters, introduction and conclusion. Chapter 3 presents the classification of the PMSM, concisely describes magnet materials, compares PMSM to other classes of AC motors used in servo drive applications. The derivation of a space phasor mathematical model of the PMSM is reviewed. The connection between the physical abc frame and the mathematically constructed dq frame is shown and a direct and quadrature axis model of a PMSM is naturally derived through the transformation from stationary to rotating reference frame. The assumptions and simplifications in the analysis of PMSM are also specified.

Chapter 4 develops a passivity-based control algorithm for the PMSM. The available measurements in that algorithm are stator currents and rotor position. The controller output is direct and quadrature voltages. A detailed, step-by-step design of the primary and incremental controls is presented. The primary controller determines the desired torque level based on torque estimation. This becomes a basis for the desired currents (optimized to minimize ohmic losses in the motor) and for desired primary voltage outputs. The incremental controller guarantees stability of the system and shapes the transients. The selections of the controller gains (various options and numerical algorithms) are specifically addressed in this chapter.

Chapter 5 concentrates on the practical implementation of the control algorithm in software and hardware. The separation of tasks performed by the control DSP board and the drive DSP board is considered and their functions are determined.

Since the successful implementation of the developed control scheme heavily relies on the accurate realization of sinusoidal phase voltages by means of a power inverter, its operation and ways to improve it are discussed. Finally, the possible sources for motor nonidealities such as torque ripple due to nonsinusoidal back emf are described. The electrical and mechanical parameters of the used PMSM are measured and tabulated.

Chapter 6 completes the second objective of this thesis, namely, it provides experimental verification of the developed passivity based control algorithm. Simulation and experimental results for sudden changes in motor load and reference speed are presented and compared. They illustrate various options on the selection of the controller design parameters. The significant improvement of the motor response due to "widening" of the energy exchange channel between the electrical and the mechanical motor states is corroborated by experimental plots. The satisfactory tracking of the periodic reference speed is also shown.

Chapter 7 addresses the design of the passivity based position sensorless control scheme for PMSM. A full state observer is designed based on passivity principles. The selection of observer gains is considered. The operation of the passivity based state observer in open loop and closed loop applications is illustrated by extensive numerical simulations. As seen from the simulation results, this observer provides reliable tracking of step changes in unknown load torque and in reference speed.

Chapter 8 summarizes the results and shows possible directions of future improvements and evolution of this thesis.

The appendices supplement the results presented in previous chapters. Appendices A and B provide rigorous proofs of the stability of dissipative systems. Appendix **??** represents modified Assembly code for the drive DSP controller.

Chapter 3

Permanent Magnet Synchronous Motors

3.1 Introduction

Permanent magnet synchronous motors (PMSMs) are an attractive solution for servo drives in the kW-range [73, 74]. They are being used in a wide range of applications, from general purpose line-start pump or fan drives to high performance machine tools, servos, robotics, aerospace generators and actuators, and electric vehicles.

3.2 Brushless Motors Classification

The brushless DC motor is essentially configured as a permanent magnet rotating past a set of current-carrying conductors. In this respect it is equivalent to an inverted DC commutator motor, in that the magnet rotates while the conductors remain stationary. In both cases, the current in the conductors must reverse polarity every time a magnet pole passes by, in order to ensure that the torque is unidirectional.

In the DC commutator motor, the polarity reversal is performed by the commutator and brushes. Since the commutator is fixed to the rotor, the switching instants are automatically synchronized with the alternating polarity of the magnetic field through which the conductors are passing. In the brushless DC motor, the polarity reversal is performed by power transistors which must be switched in synchronism with the rotor position. The process of commutation is similar in the two machines, and the resulting performance equations and speed/torque characteristics are almost identical.

When the phase currents in the brushless DC motor are of this type, i.e. DC current which switches polarity in synchronism with the passage of alternate N and S magnet poles, the motor is said to operate with squarewave excitation. The back-EMF in this case is usually arranged to be trapezoidal, and the terms squarewave and trapezoidal are used interchangeably to refer to the motor and its controller.

There is however, another mode of operation, in which the phase currents are sinewaves. The back-EMF in this case should ideally be sinusoidal. Physically the motor and its controller look similar to the squarewave motor and drive, but there is an important difference. The sinewave motor operates with a rotating ampere-conductor distribution, similar to the rotating magnetic field in the induction motor or the AC synchronous machine. This type of brushless motor is a pure synchronous AC motor, with fixed excitation from the permanent magnets. It is more similar to the wound-rotor synchronous machine than to the DC commutator motor, and for this reason it is often called a brushless AC motor. Many brushless permanent-magnet motors from Japan and Europe are referred to as AC servo motors rather than brushless DC machines.

3.3 Materials for PMSMs

The desirable properties of the materials used for the construction of permanent magnets in PMSMs are:

- High flux density.
- High coercivity.

Certain "rare earth" magnetic materials best satisfy these requirements. Samarium-Cobalt, with high flux density (up to 1T) and very large coercive force (up to 7000 A/cm), is one of the materials used.

At present, Neodymium-Iron-Boron magnets are more commonly used, especially due to their low cost. Further the magnets made of these materials require less space for the same flux and, with proper design, there is less danger of accidental demagnetization through short circuit.

3.4 Construction

One of the primary requirements for servo applications is smooth torque operation. Therefore cogging due to slotting must be minimized. The reduction of cogging torque can be achieved in a number of ways, such as skewing the magnets on the rotor with respect to the rotor axis, skewing the stator, coordinating the number of stator slots, slot opening, and magnet dimensions.

The magnets can be fixed to the rotor in different ways as described below.

3.5 Classification of PMSMs

The PMSM consists of a three phase stator similar to that of an induction motor and a rotor with permanent magnets. The rotor is provided with a squirel cage if the machine is to be line started. Most of the PMSM drives are fed from inverters and a cage is not necessary in the rotor. The motor characteristics depend on the type of magnets used and the way they are located on the rotor. The magnets are either mounted on the surface of the rotor or buried in the interior of the rotor. Accordingly PMSMs are classified as:

1. Surface-mounted PMSMs.
2. Buried or interior PMSMs.

3.5.1 Surface Mounted PMSMs

There are two variations in the surface mounted PMSMs:

- Projecting type – in which the magnets project from the surface of the rotor.
- Inset type – in which the magnets are inset into the rotor providing a smooth rotor surface.

Figure 3.1 schematically shows both types.

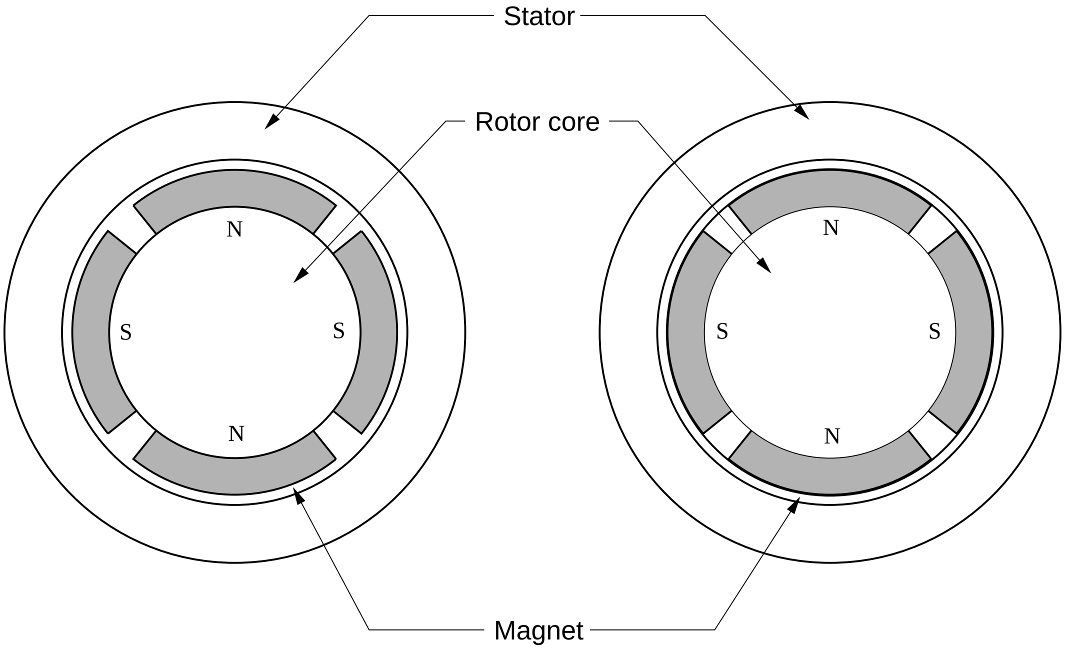

Figure 3.1: Mechanical construction of surface-mounted PMSMs: projecting type (left) and inset type (right).

Mounting the magnets on the surface of the motor is the simplest and cost effective method for constructing a PMSM. Epoxy glue is used to affix the magnets to the rotor surface in the projecting and inset surface mounted PMSMs. Therefore, these constructions are less robust compared to interior magnet type rotor and are not suited for high speed applications.

As the relative permeability of the magnet is approximately equal to that of air, the projecting surface mounted motor has almost uniform airgap. This results in equal direct and quadrature axis inductances. The motor torque is therefore derived from the magnet flux only, and there is no reluctance torque as might have been expected from the salient magnet construction. The projecting magnets present a large airgap in the magnetic circuit, so that inductance in the machine is small. The lower value of inductance gives rise to a smaller stator time constant. Also the surface mounted designs tend to yield smaller rotor diameter with lower inertia. This fact enables the machine to exhibit good dynamic performance. Such drives are suitable for high performance machine tool feed drives and industrial robots.

The inset PMSMs have magnets that span less than a pole pitch, mounted into the rotor surface with an iron rotor tooth filling the space between the magnets as shown in Figure 3.1, right. This design makes the machine mechanically more robust; the inductance is much larger compared with the projecting surface mounted PMSMs. The quadrature inductance is larger than the direct axis inductance, owing to the magnet being equivalent to an airgap in the direct axis. This saliency gives rise to a significant reluctance torque which adds to the magnetic torque.

3.5.2 Interior PMSMs

The alternative to mounting magnets on the surface of the rotor is to embed them in the interior of the rotor as shown in Figure 3.2. Interior magnet designs offer the advantage of mechanical robustness and a smaller airgap. The reluctance torque obtained is much higher than that in the inset magnet motors. The major disadvantage of interior PMSMs is more complicated rotor design and manufacturing.

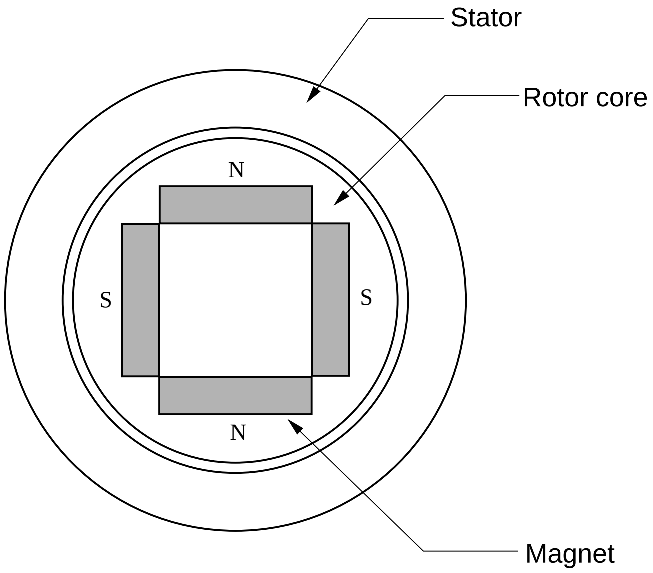

Figure 3.2: Construction of interior PMSMs.

3.6 Mathematical Model of PMSM

For the purpose of understanding and designing control algorithms for PMSM drives, it is necessary to know the dynamic model of the machine subjected to control. The machine models which are necessary to design a controller are very different from those used for designing the machine [40, 39]. Machine designers must have tolerance levels which are less than one percent, while control designs are only rough approximations, where even ten percent error can be considered acceptable. This is because every control scheme must absorb the changes of the plant parameters, due to changes in temperature, supply non-linearity, etc. The effects of the load are only approximately considered.

The following provides a brief overview of PMSM model derivations. The model describes the combined and coupled electrical and mechanical dynamics of PMSM.

3.6.1 Electrical Dynamics

In general, a rotational electrical machine consists of two solid parts referred to as stator and rotor. Each part may have stationary electrical conductors forming windings. The windings are usually referred to as phases. The curents carried by the windings generate magnetic flux that is guided by the magnetic circuit to link windings. Assuming linear magnetics, the flux in each winding

$$\Psi_m(t) = \sum_{n=1}^{N} L_{m,n}(\theta(t)) i_n(t) \tag{3.1}$$

where Ψ_m is the flux linked by winding m, i_n is the current carried by winding n, $L_{m,n}$ is the mutual inductance from winding n to m, N is the total number of windings, and θ is the rotational position of the rotor with respect to the stator.

A voltage applied to the terminals of a winding drives a time variation of the flux linked by that winding and a current through the resistance of that winding. Expressing voltages, currents and fluxes in vector format one can write (based on Faraday's and Ohm's laws)

$$\mathbf{v}(t) = \mathbf{R_p}\mathbf{i}(t) + \frac{d}{dt}\mathbf{\Psi}(t) \tag{3.2}$$

where $\mathbf{v}(t) = [v_1(t), v_2(t), ..., v_N(t)]^T$, $\mathbf{i}(t) = [i_1(t), i_2(t), ..., i_N(t)]^T$, and $\mathbf{\Psi}(t) = [\Psi_1(t), \Psi_2(t), ..., \Psi_N(t)]^T$. The matrix of phase resistances $\mathbf{R_p} = diag\{R_1, R_2, ..., R_N\}$. The flux vector can be written compactly as

$$\mathbf{\Psi}(t) = \mathbf{L_p}(\theta(t))\mathbf{i}(t) \tag{3.3}$$

where $\mathbf{L_p}(\theta(t))$ is a matrix of self and mutual inductances.

It is possible to show that the two matrices $\mathbf{R_p}$ and $\mathbf{L_p}$ defined above are invertible, symmetric and positive definite [37]. These properties will be used in further derivations.

Now we will concentrate on a more specific type of the electrical machine, namely, on a three-phase single-salient permanent magnet synchronous motor used in the controller design. The non-salient case is then obtained as a simplification of the more general, salient rotor case. We will also assume that all phase windings are identical and have spatial separation of $2\pi/3$ electrical radians.

Although (3.2) does not have terms representing permanent magnets, it is possible to think of each magnet as being demagnetized and excited by an imaginary winding carrying a known current. The imaginary rotor winding can be treated in the same manner as the real winding. The inductance matrix is then

$$\mathbf{L_p}(\theta(t)) = \begin{bmatrix} L_{aa} & L_{ab} & L_{ac} & L_{ar} \\ L_{ba} & L_{bb} & L_{bc} & L_{br} \\ L_{ca} & L_{cb} & L_{cc} & L_{cr} \\ L_{ra} & L_{rb} & L_{rc} & L_{rr} \end{bmatrix} \tag{3.4}$$

and the resistance matrix

$$\mathbf{R_p} = \begin{bmatrix} R_s & 0 & 0 & 0 \\ 0 & R_s & 0 & 0 \\ 0 & 0 & R_s & 0 \\ 0 & 0 & 0 & R_r \end{bmatrix} \tag{3.5}$$

where R_s is the stator phase resistance and R_r is the equivalent of the rotor magnet imaginary resistance.

Since the current in the imaginary winding is predetermined, the voltage equation for the imaginary winding can be omitted resulting in a simpler representation of PMSM's system of equations

$$\mathbf{v}(t) = \mathbf{R}\mathbf{i}(t) + \frac{d}{dt}\mathbf{\Psi}(t) \tag{3.6}$$

where $\mathbf{v}(t) = [v_a(t), v_b(t), v_c(t)]^T$ is the vector of stator phase voltages, $\mathbf{i}(t) = [i_a(t), i_b(t), i_c(t)]^T$ is the vector of stator phase currents, $\mathbf{\Psi}(t) = [\Psi_a(t), \Psi_b(t), \Psi_c(t)]^T$ is the vector of total fluxes linking stator phases, $\mathbf{R} = diag\{R_s, R_s, R_s\}$ is the matrix of stator phase resistances. The expression for the flux also simplifies to

$$\mathbf{\Psi}(t) = \mathbf{L}(\theta(t))\mathbf{i}(t) + \mathbf{\Psi_r}(t) \tag{3.7}$$

where $\mathbf{L}(\theta(t)) = \begin{bmatrix} L_{aa} & L_{ab} & L_{ac} \\ L_{ba} & L_{bb} & L_{bc} \\ L_{ca} & L_{cb} & L_{cc} \end{bmatrix}$ is a 3-by-3 matrix of stator self and mutual inductances, $\mathbf{\Psi_r}(t) = [L_{ar}(\theta(t))I, L_{br}(\theta(t))I, L_{cr}(\theta(t))I]^T$ is the vector of fluxes produced by the rotor field and I is the constant magnetizing current in the fictitious rotor winding.

For a symmetrical machine we can represent the inductance matrix as a function of mechanical angle between stator and rotor as follows [69]

$\mathbf{L}(\theta) =$

$$\begin{bmatrix} L_{s0} + L_{s2}\cos(2P\theta) & -L_{ss}+L_{s2}\cos(2P\theta-2\pi/3) & -L_{ss}+L_{s2}\cos(2P\theta+2\pi/3) \\ -L_{ss}+L_{s2}\cos(2P\theta-2\pi/3) & L_{s0}+L_{s2}\cos(2P\theta+2\pi/3) & -L_{ss} + L_{s2}\cos(2P\theta) \\ -L_{ss}+L_{s2}\cos(2P\theta+2\pi/3) & -L_{ss} + L_{s2}\cos(2P\theta) & L_{s0}+L_{s2}\cos(2P\theta-2\pi/3) \end{bmatrix} \tag{3.8}$$

where L_{s0} is the average self inductance of each stator phase, L_{s2} is the positive coefficient of stator-phase self and mutual inductance which arises from rotor saliency, L_{ss} is the positive average mutual inductance between stator phases, P is the number of rotor pole pairs. The rotor field flux is

$$\mathbf{\Psi_r} = MI \begin{bmatrix} \cos(P\theta) \\ \cos(P\theta - 2\pi/3) \\ \cos(P\theta + 2\pi/3) \end{bmatrix} \tag{3.9}$$

where the parameter MI represents the strength of the permanent magnet flux that is linked by the stator phases.

3.6.2 Mechanical Dynamics

The torque produced by the electrical machine can be determined by studying energy conservation. Electrical energy input to the machine through its winding terminals is either converted to thermal energy through dissipation in its windings, stored in its magnetic field, or converted to mechanical energy and output through its rotor shaft.

The power input electrically through the terminals of winding n is

$$i_n(t)v_n(t) = i_n(t)\frac{d}{dt}\Psi_n(t) + R_n i_n^2(t) \tag{3.10}$$

The second term on the right is the power dissipated thermally in winding n. The first term on the right is the contribution from winding n to the combined rate of increase in stored magnetic energy and to the power converted and output mechanically through the rotor shaft. One can therefore write

$$\sum_{n=1}^{N} i_n(t)\frac{d}{dt}\Psi_n(t) = \frac{d}{dt}W_M(t) + T_M(t)\omega(t) \tag{3.11}$$

where W_M is the total magnetic energy stored in the electrical machine, $\omega(t) = \frac{d}{dt}\theta(t)$, and T_M is the electromagnetic torque produced by the machine. We can rewrite (3.11) as

$$dW_M = \mathbf{i}^T d\mathbf{\Psi} - T_M d\theta \tag{3.12}$$

Using the chain rule for differentiation, one obtains

$$\mathbf{i}^T(\mathbf{\Psi}, \theta) = \left.\frac{\partial W_M(\mathbf{\Psi}, \theta)}{\partial \mathbf{\Psi}}\right|_{\theta = const} \tag{3.13}$$

$$T_M(\mathbf{\Psi}, \theta) = -\left.\frac{\partial W_M(\mathbf{\Psi}, \theta)}{\partial \theta}\right|_{\mathbf{\Psi} = const} \tag{3.14}$$

Finding $W_M(t)$ and using (3.3) leads to the following expression for the electromagnetic torque:

$$T_M(t) = \frac{1}{2}\mathbf{i}^T(t)\frac{d\mathbf{L}_\mathbf{P}(\theta(t))}{d\theta}\mathbf{i}(t) \tag{3.15}$$

Mechanically, T_M opposes the load torque acting on the rotor of the electrical machine. The difference between the two torques accelerates the rotor according to

$$H\frac{d\omega(t))}{dt} = T_M(t) - T_L - B\omega(t) \tag{3.16}$$

where H is the combined rotational inertia of the rotor and the mechanical load connected to it, T_L is the constant component of the load torque, B is the viscous friction coefficient. Together, (3.15) and (3.16) describe the mechanical dynamics of the electrical machine. These dynamics are coupled to the electrical dynamics through the dependence of T_M on Ψ and $\mathbf{i}$.

Based on the above representation of the $\mathbf{L_p}$ for the PMSM, (3.15) can be expanded to

$$T_M(t) = \frac{1}{2}\mathbf{i}^T(t)\frac{d\mathbf{L}(\theta(t))}{d\theta}\mathbf{i}(t) + \mathbf{i}^T(t)\frac{d\mathbf{\Psi_r}(\theta(t))}{d\theta} + T_{cog}(\theta(t)) \tag{3.17}$$

where the last term T_{cog} represents cogging torque due to the interaction between rotor magnets and stator slots. It is considered to be small compared to the other terms in (3.17) and therefore neglected in this thesis.

3.6.3 Transformation of PMSM Model

The above equations apply to a three-phase model of PMSM. As stated earlier, an N-phase electrical machine is also possible resulting in more complex mathematical representation. When any number of sinusoidally-wound phases is excited on one side of the air gap, the result is equivalent to the excitation of a single sinusoidally-wound phase with the appropriate spatial orientation and excitation. Such an equivalent phase has two degrees of freedom which can also be obtained from two phases having variable excitation but different fixed orientation. Therefore, N-phase sinusoidally-wound electrical machine can be modeled by two phases with fixed orientation and variable excitation. This reduces the order of the model.

The 3-to-2 transformation, also known as $\alpha\beta 0$ transformation, is given by the unitary matrix

$$\mathbf{S} = \sqrt{\frac{2}{3}}\begin{bmatrix} \cos(0) & \cos(2\pi/3) & \cos(-2\pi/3) \\ \sin(0) & \sin(2\pi/3) & \sin(-2\pi/3) \\ \frac{1}{\sqrt{2}} & \frac{1}{\sqrt{2}} & \frac{1}{\sqrt{2}} \end{bmatrix} \tag{3.18}$$

The transformed vector is then obtained as

$$\mathbf{X}_{\alpha\beta 0} = \mathbf{S}\mathbf{X}_{abc} \tag{3.19}$$

where $\mathbf{X}$ denotes the voltage, current, or flux. The important consequence of the unitarity of $\mathbf{S}$ is that it is a power-invariant transformation. Therefore, the power input into an electrical machine is in the same units for both the original and transformed sets of electrical variables. Figure 3.3 graphically represents the transformation operation.

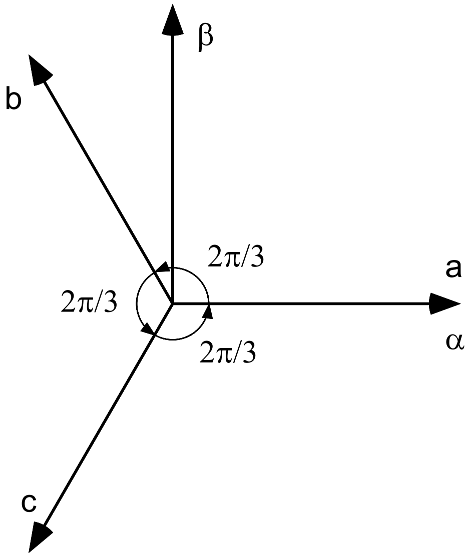

Figure 3.3: Vector diagram for two-phase transformation

The application of the transformation S to the flux vector, the current vector and the electromagnetic torque gives the model of PMSM in $\alpha\beta0$ frame:

$$\begin{aligned}\Psi_{\alpha\beta0} &= \begin{bmatrix} L_{s0}+L_{ss}+\frac{3}{2}L_{s2}\cos(2P\theta) & \frac{3}{2}L_{s2}\sin(2P\theta) & 0 \\ \frac{3}{2}L_{s2}\sin(2P\theta) & L_{s0}+L_{ss}-\frac{3}{2}L_{s2}\cos(2P\theta) & 0 \\ 0 & 0 & L_{s0}-2L_{ss} \end{bmatrix} i_{\alpha\beta0} \\ &\quad +\sqrt{\tfrac{3}{2}}MI\begin{bmatrix}\cos(P\theta)\\ \sin(P\theta)\\ 0\end{bmatrix}\end{aligned} \tag{3.20}$$

$$\mathbf{v}_{\alpha\beta\mathbf{0}}(t) = \mathbf{R}\mathbf{i}_{\alpha\beta\mathbf{0}}(t) + \frac{d}{dt}\mathbf{\Psi}_{\alpha\beta\mathbf{0}}(t) \tag{3.21}$$

$$\begin{aligned}\tfrac{d}{dt}\omega &= -\tfrac{3PL_{s2}}{2H}\mathbf{i}^{T}_{\alpha\beta0}\begin{bmatrix}\sin(2P\theta) & -\cos(2P\theta) & 0\\ -\cos(2P\theta) & -\sin(2P\theta) & 0\\ 0 & 0 & 0\end{bmatrix}\mathbf{i}_{\alpha\beta0} \\ &\quad -\sqrt{\tfrac{3}{2}}\tfrac{PMI}{H}\begin{bmatrix}\sin(P\theta) & -\cos(P\theta) & 0\end{bmatrix}\mathbf{i}_{\alpha\beta0}-\tfrac{B}{H}\omega-\tfrac{T_L}{H}\end{aligned} \tag{3.22}$$

$$\frac{d}{dt}\theta = \omega \tag{3.23}$$

Equations (3.20) and (3.21) show that the zero-sequence flux and current are decoupled from the other two fluxes and currents. In addition to that, the zero-sequence current produces no torque (3.22), but does contribute to losses inside the machine. For this reason, zero phase is best left unexcited, in which case it may be discarded from the model. This is the rationale behind the two-phase transformation. Thus, the PMSM can be described as

$$\begin{aligned}\Psi_{\alpha\beta} &= \begin{bmatrix} L_{s0}+L_{ss}+\frac{3}{2}L_{s2}\cos(2P\theta) & \frac{3}{2}L_{s2}\sin(2P\theta) \\ \frac{3}{2}L_{s2}\sin(2P\theta) & L_{s0}+L_{ss}-\frac{3}{2}L_{s2}\cos(2P\theta)\end{bmatrix} i_{\alpha\beta} \\ &+\sqrt{\tfrac{3}{2}}MI\begin{bmatrix}\cos(P\theta)\\ \sin(P\theta)\end{bmatrix}\end{aligned} \tag{3.24}$$

$$\mathbf{v}_{\alpha\beta}(t) = \mathbf{R}\mathbf{i}_{\alpha\beta}(t) + \frac{d}{dt}\mathbf{\Psi}_{\alpha\beta}(t) \tag{3.25}$$

$$\begin{aligned}\tfrac{d}{dt}\omega &= -\tfrac{3PL_{s2}}{2H}\mathbf{i}_{\alpha\beta}^{T}\begin{bmatrix}\sin(2P\theta) & -\cos(2P\theta)\\ -\cos(2P\theta) & -\sin(2P\theta)\end{bmatrix}\mathbf{i}_{\alpha\beta} \\ &-\sqrt{\tfrac{3}{2}}\tfrac{PMI}{H}\begin{bmatrix}\sin(P\theta) & -\cos(P\theta)\end{bmatrix}\mathbf{i}_{\alpha\beta} - \tfrac{B}{H}\omega - \tfrac{T_L}{H}\end{aligned} \tag{3.26}$$

$$\frac{d}{dt}\theta = \omega \tag{3.27}$$

where $\mathbf{\Psi}_{\alpha\beta}$, $\mathbf{v}_{\alpha\beta}$, and $\mathbf{i}_{\alpha\beta}$ are the vectors in the $\alpha\beta$ frame.

The trigonometric dependencies in (3.24)-(3.27) make the PMSM model quite inconvenient to use. Further simplification can be achived by expressing the equations in the rotor reference frame. This transformation between stationary and rotating reference frames is known as dq, or Blondel-Park, transformation [11, 77]. In general, the dq transformation is applicable to any two-phase sinusoidally-wound electrical machine. It expresses the electrical dynamics of the stator and rotor over a common reference frame. The graphical representation of the $\alpha\beta$-to-dq transformation is shown in Figure 3.4.

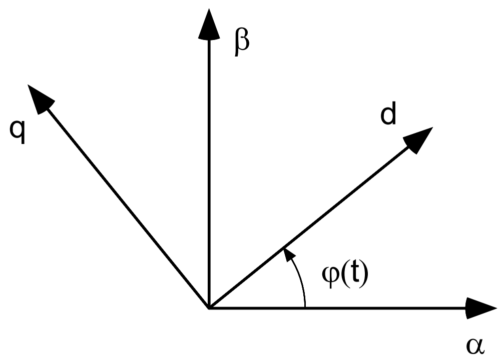

Figure 3.4: Vector diagram for dq transformation

The transformation is then defined as

$$\mathcal{T} = \begin{bmatrix} \cos(P\varphi) & \sin(P\varphi) \\ -\sin(P\varphi) & \cos(P\varphi) \end{bmatrix} \tag{3.28}$$

The matrix $\mathcal{T}$ is unitary and, therefore, is power invariant. The vector relationship is then

$$\mathbf{X}_{dq} = \mathcal{T}\mathbf{X}_{\alpha\beta} \tag{3.29}$$

The dq transformation matrix can be expressed in a much simpler form:

$$\mathcal{T} = \begin{bmatrix} \cos(P\varphi) & \sin(P\varphi) \\ -\sin(P\varphi) & \cos(P\varphi) \end{bmatrix} = I - \varphi J + \frac{\varphi^2}{2!}J^2 - \frac{\varphi^3}{3!}J^3 + \cdots - \cdots \equiv e^{-\varphi J} \tag{3.30}$$

where $J = \begin{bmatrix} 0 & -1 \\ 1 & 0 \end{bmatrix}$ and I is the 2×2 identity matrix. It is easy to show that the matrix exponential in (3.30) satisfies the relations

$$\left[e^{\varphi J}\right]^{-1} = \left[e^{\varphi J}\right]^{T} = e^{-\varphi J} \tag{3.31}$$

and

$$\frac{d}{d\varphi}e^{\varphi J} = Je^{\varphi J} = e^{\varphi J} \tag{3.32}$$

For the sinusoidally-wound electrical machine the direct (d) axis is aligned with the rotor of the machine, and the quadrature (q) axis is leading it by 90 degrees. The angle between $\alpha\beta$ and dq frames $\varphi(t)$ is set equal to the rotor angle $\theta(t)$. Then, combining (3.24) and (3.25), we can write the system of PMSM equations in dq coordinates:

$$\begin{aligned} \tfrac{d}{dt} i_{dq} \quad = \quad & -\left(\begin{bmatrix} \frac{R_s}{L_d} & 0 \\ 0 & \frac{R_s}{L_q} \end{bmatrix} + JP\omega \begin{bmatrix} \frac{L_d}{L_q} & 0 \\ 0 & \frac{L_q}{L_d} \end{bmatrix} \right) i_{dq} - \sqrt{\tfrac{3}{2}} MI\, P\omega \begin{bmatrix} 0 \\ \frac{1}{L_q} \end{bmatrix} \\ & + \begin{bmatrix} \frac{1}{L_d} & 0 \\ 0 & \frac{1}{L_q} \end{bmatrix} v_{dq} \end{aligned} \tag{3.33}$$

$$\frac{d}{dt}\omega = i_{dq}^T \sqrt{\frac{3}{2}} \frac{MI\, P}{H} \begin{bmatrix} 0 \\ 1 \end{bmatrix} + \frac{3L_{s2}P}{2H} i_{dq}^T \begin{bmatrix} 0 & 1 \\ 1 & 0 \end{bmatrix} i_{dq} - \frac{B\omega}{H} - \frac{T_L}{H} \tag{3.34}$$

$$\frac{d}{dt}\theta = \omega \tag{3.35}$$

where $i_{dq} = \begin{bmatrix} i_d & i_q \end{bmatrix}^T$, $v_{dq} = \begin{bmatrix} v_d & v_q \end{bmatrix}^T$, $L_d = L_{s0} + L_{ss} + \frac{3}{2}L_{s2}$, and $L_q = L_{s0} + L_{ss} - \frac{3}{2}L_{s2}$. As one can see, the equations of the motor dynamics are no longer position dependent which is the major benefit of application of the dq transformation.

The equations (3.33) and (3.34) represent an intermediate result of dq-model derivations and can be brought into more convenient format. We use the following change of notations: $MI_{dq} \doteq \sqrt{\frac{3}{2}}MI$ and $\omega_{el} \doteq P\omega$. We will further omit the subscripts "s" for R_s, "dq" for MI, "el" for ω assuming that the necessary scaling factors are used appropriately. Thus, the model of PMSM in dq coordinates can be represented as

$$\begin{aligned}
L_d \frac{di_d}{dt} &= -Ri_d + \omega L_q i_q + v_d \\
L_q \frac{di_q}{dt} &= -Ri_q - \omega L_d i_d - \omega MI + v_q \\
H \frac{d\omega}{dt} &= MIi_q + (L_d - L_q) i_d i_q - B\omega - T_L \\
\frac{d\theta}{dt} &= \omega
\end{aligned} \tag{3.36}$$

where the inertia H, the viscous friction B and the load torque T_L are all normalized by the number of pole pairs P.

The equations (3.36) describe a general model of PMSM in rotating reference frame. The non-salient rotor model can be easily obtained by setting $L_{s2} = 0$ in (3.8) or, equivalently, by setting $L_d = L_q$ in (3.36).

3.7 Motor Comparison

As the stator is considered the same for the induction motor (IM), PMSM and reluctance synchronous motor (RSM), they can be compared the following way [14]:

- Torque capability.
- Losses-to-torque ratio.
- Speed of torque transients.

The peak torque in PMSM is limited to avoid the demagnetization of permanent magnets and in general smaller than the peak torque of the IM and RSM for the same stator and stator flux linkage [14, 64].

For a given I_q (and given I_d for the IM and RSM), about the same torque can be obtained with all three rotors; the lowest winding losses occur in the PMSM case and the highest in the IM. It should be mentioned, that field weakening operation of PMSM would have increased its winding losses significantly.

The torque transient speed is very important for fast torque, speed, or position response in modern drives. At low speeds I_d is kept constant (nonzero for the IM and RSM and zero for PMSM) in order to provide fast I_q (and thus torque) response. The torque response is in general (with $I_d = constant$) fastest at low speeds for the IM and slowest for the PMSM. However, as the voltage ceiling is sufficiently high and the motion induced voltage remains small, the differences are not very significant. For the PMSM the flux produced by the magnets is always there. This is a "built-in" advantage of the PMSM.

At high speeds and full available voltage, the torque transients for a constant rotor flux for the IM and with $I_d = 0$ for the PMSM, designed for a maximum torque, are identical (with the stator resistance neglected.)

3.8 Losses and Efficiency

Synchronous PM motors are potentially much more efficient than induction machines. There is no equivalent of the loss in the rotor bars of the induction motors. Also, the stray losses which result mainly from magnetic interaction of the closely adjacent stator and rotor teeth in the induction motor are effectively elliminated by the large iron-to-iron gap of the PM motor. With NdFeB magnets, the resistivity is such that losses due to tooth ripple variations in the air-gap flux density produce little loss in the magnet material for most designs. This loss may however become significant for motors operated at very high frequencies and speeds.

The PM motor can be operated at unity power factor while the induction motor will always have a lagging power factor, typically in the range 0.8–0.9 for four-pole motors and lower for greater number of poles. For the same power rating, the ratio of the stator currents of the two motors will be this power factor. Thus the ratio of the stator winding losses for the PM and induction motors will be the induction motor power factor squared. If the ratings of the two motors are the same, the total losses in the PM motor will typically be about 50–60% of those of the induction motor. Predicted values of PM motor efficiency are about 95–97% for a ratings of 10–100 kW [15, 72].

3.9 Challenges in Control of PMSM

Being conveniently suited for various servo applications due to flexible electromechanical design PMSMs at the same time represent an uneasy task for achieving accurate and fast control performance. First, the structure of the differential equations describing PMSM is nonlinear. This fact essentially disallows to use "classical" control analysis and design methods requiring for advanced nonlinear control techniques.

Second, according to [27, 94, 92], the electrical and mechanical time constants associated with the motor typically vary by an order of magnitude. Traditional approach in this case would be to neglect the shortest of them and to concentrate on the design for the slower (i.e., mechanical) subsystem. Such a design does not allow to shape transients in the electrical part of the motor thus resulting in the "improved" but not the best performance.

Finally, and typically for a broad class of electromechanical systems, only electrical subsystem is directly available for actuation. As a consequence, one would (traditionally) need to use a much faster actuation for the electrical states (currents) in order to achieve a desirable response in the mechanical states (torque, speed.) The available actuation resources (power supply voltage, current and rates of their change) and safety limits for the instantaneous electrical coordinates in the PMSM become a serious issue in this case.

Chapter 4

Passivity Based Control of PMSMs

4.1 Introduction

The control objective considered here is the tracking of infrequent step changes, as well as continuous changes in the load torque and in the reference speed. The suggested design utilizes large-signal electro–mechanical models, and guarantees global exponential stability of the desired operation setpoint in the closed loop. The compensator requires position and current measurements, while the load torque is estimated.

The methodology suggested here follows a two step design procedure: the primary control selects a desired mode of operation (here it includes the option of minimization of resistive losses in steady state); the secondary, incremental control, assures robust stability. Our methodology builds on some recent developments that are largely associated with the so–called "passivity-based" approach [41] to the control of electric drives, whereby stability is assured via the dissipation of a naturally available and physically motivated quadratic “incremental energy”.

Traditional passivity-based design consists of three distinct stages [80, 103]: 1) the primary design phase is concerned solely with steady state; 2) the main part of the incremental control design is the enhancement – where possible – of the dissipative component of an allied incremental system (governing tracking errors); 3) finally, a certain state dependent matrix is perturbed by use of feedback, to guarantee a skew symmetric structure, meaning that effects of non-dissipative components of the incremental state equation are neutralized.

The controller design presented, further changes this partition: first, a transient component, added to the “primary” control, holds a significant responsibility for accelerating the decay of speed transients; second, a much greater attention is paid to the shaping the said skew symmetric matrix. The lossless incremental state dynamics that this matrix governs forms conduits for indirect actuation of states that cannot be directly actuated (e.g., speed), and for indirect observation of non-accessible quantities (e.g., the load torque.) Incrementally lossless exchanges are instrumental in shifting incremental energy from the mechanical component, where direct actuation is not available, to the electrical component, where that incremental energy can be dissipated. Therefore, shaping lossless dynamics is equally significant to the design as is the direct manipulation of dissipative components. The resulting design allows an assignment of transient decay rates for *all* state variables, restricted only by capabilities of the available power supplies.

One consequence of the suggested design is the elimination of the need for the substantial difference between the electrical and the mechanical time constants that is typical in standard operation of small and medium-size electric motors. In practice, closed loop bandwidth in the electrical subsystem is restricted by available power supply, DSP capabilities and by other typical design considerations, such as noise attenuation, avoidance of unmodeled higher frequency phenomena, etc. Elimination of the need that the bandwidth in current response be much wider than that of the speed loop means that higher performance (measured, for example, by speed response) is achievable with fixed actuation resources, better noise rejection and lower requirements to the sampling frequency of the digital implementation.

4.2 The PM Synchronous Motor

For convenience, we restate a standard PMSM model in the d-q coordinates

$$\begin{array}{rcl} L_d \frac{d}{dt} i_d & = & \omega L_q i_q - R i_d + v_d \\ L_q \frac{d}{dt} i_q & = & -\omega L_d i_d - R i_q - \omega M I + v_q \\ H \frac{d}{dt} \omega & = & (MI + \Delta L i_d) i_q - B\omega - T_L \end{array} \qquad (4.1)$$

where i_d and i_q, v_d and v_q are the d and q axis currents and applied voltages; ω is the motor speed in radians per second; L_d and L_q are the total d and q axis inductances, $\Delta L = L_d - L_q$; MI is the flux due to permanent magnets; finally, H is the moment of inertia, B is the friction coefficient and T_L is the load torque, both normalized by the number of pole pairs.

Basic Notations

The transpose of a matrix or a vector is denoted by the superscript "T". The Euclidean norm of a real vector $\eta = [\eta_1, \dots, \eta_n]^T$ is denoted by $\|\eta\|_E = \sqrt{\sum_{i=1}^{n} \eta_i^2}$. The $L_2[a,b]$ norm of a signal x will be denoted as $\|x\|_{L_2[a,b]} = \sqrt{\int_a^b \|x(t)\|_E^2 dt}$. The norm of a real matrix M, denoted simply as "$\|M\|$", is its maximal singular value; i.e., $\|M\|^2$ is the maximal eigenvalue of $M^T M$.

4.3 The Control Problem

The control objective considered here is the tracking of a reference speed trajectory, denoted ω_d, subject to an unknown load torque trajectory, T_L. Both trajectories are assumed to be smooth. Infrequent step changes are viewed as changes in initial conditions and performance will be addressed as a stability issue. When slow, persistent changes in the load take place, the time derivative of the load torque will be viewed as an unknown disturbance. It will be assumed that the derivatives $\dot{\omega}_d$ and $\ddot{\omega}_d$ are part of the reference input; we will comment also on the more commonly considered situation where only the value of ω_d is included in the reference command. One straightforward option, when ω_d is slowly varying, is to substitute zero instead of the true small values of $\dot{\omega}_d$ and of $\ddot{\omega}_d$. That will result with error terms, proportional to the true values, appearing as inhomogeneous terms – or "disturbances" – in the system's dynamic equations.

4.4 The Primary Control

The first step in the selection of the primary component of the control input is the selection of the desired value of the produced motor torque, denoted with $T_{M,d}$. Currents that can produce that torque will be selected in a second step and finally, the applied voltage that would result with such currents will determine the actual value of the primary control.

4.4.1 The Desired Torque

The desired *steady state* motor torque balances friction and the load torque at the desired speed: $T_{M,\infty} = H\dot{\omega}_d + B\omega_d + T_L$. Since load torque measurements are not available, a dynamic estimate (denoted $\widehat{T}_L$), will have to be used in our control derivation. The dynamic load torque estimate that we use here is of the form

$$\frac{d}{dt}\widehat{T}_L = -\tau^2 H(\omega - \omega_d) \tag{4.2}$$

This type of dynamic observers have been previously used in [76] and will be justified later, along with guidelines for the selection of the design parameter τ.

If a transient term, negatively proportional to the deviation from that desired value, say $-\mu(\omega - \omega_d)$, were added to the produced torque, the convergence of speed to its desired value would be accelerated. That term would act, in effect, as "friction in the increment". Such a scheme cannot be implemented directly in our algorithm, due to a technicality: as will be seen shortly, the selection of the primary voltage component requires differentiation of $T_{M,d}$; if the suggested term were added, this would have required acceleration measurement, which is impractical. Instead, we will use a filtered version of the speed tracking error, denoted e_5. (This notation will be consistent with other notation that will be introduced later.) The dynamics of e_5 will be governed by a first order system of the following form

$$\frac{d}{dt}e_5 = -\zeta e_5 - \sigma H(\omega - \omega_d) \tag{4.3}$$

In these terms, the desired value of the produced motor torque is set to

$$T_{M,d}(t) = H\dot{\omega}_d + B\omega_d + \widehat{T}_L + \sigma e_5 \tag{4.4}$$

Invoking (4.2) and (4.3), the derivative of the desired produced torque trajectory is

$$\dot{T}_{M,d}(t) = H\ddot{\omega}_d + B\dot{\omega}_d - (\tau^2 + \sigma^2)H(\omega - \omega_d) - \zeta\sigma e_5 \tag{4.5}$$

4.4.2 The Desired Currents

The desired current levels, denoted with $i_{d,d}$ and $i_{q,d}$, should be chosen as required to produce the desired motor torque. Given an available degree of freedom, it is natural to add an objective such as "maximal torque per Amp" [74], with the purpose of minimizing resistive losses. With this added objective, the desired currents, $(i_{d,d}, i_{q,d})$, will form the solution of the optimization problem

$$\min\left\{i_d^2 + i_q^2 \ : \ (MI + \Delta L i_d)i_q = T_{M,d}\right\} \tag{4.6}$$

This optimization problem is solved in terms of the following implicit equations, characterizing the optimal currents

$$i_{q,d} = \frac{T_{M,d}}{MI + \Delta L i_{d,d}}, \qquad i_{d,d} = \frac{T_{M,d}^2 \Delta L}{(MI + \Delta L i_{d,d})^3} \tag{4.7}$$

When the PMSM has a "non-salient rotor", implying $\Delta L = 0$, these formulas reduce to the much simpler

$$i_{q,d} = \frac{T_{M,d}}{MI}, \qquad i_{d,d} = 0 \tag{4.8}$$

This simplification translates to lower computational requirements in implementing the controller. The use of (4.8), instead of (4.7), may therefore be a worthwhile tradeoff even when $\Delta L \neq 0$ is small, which is typical of many PMSMs.

Based on (4.7) (or (4.8)), (4.4) and (4.5), derivatives of the desired currents can be characterized in terms of the desired currents, the measured speed, the reference speed and of the trajectory e_5. Explicitly,

$$\begin{aligned} \frac{d}{dt} i_{q,d} &= \frac{(MI + \Delta L i_{d,d})\dot{T}_{M,d} - \Delta L T_{M,d} \frac{d}{dt} i_{d,d}}{(MI + \Delta L i_{d,d})^2} \\ \frac{d}{dt} i_{d,d} &= \frac{2\Delta L (MI + \Delta L i_{d,d}) T_{M,d} \dot{T}_{M,d}}{(MI + \Delta L i_{d,d})^4 + 3\Delta L^2 T_{M,d}^2} \end{aligned} \tag{4.9}$$

which, in the "non-salient rotor" case, reduces to

$$\frac{d}{dt} i_{q,d} = \frac{\dot{T}_{M,d}}{MI}, \qquad \frac{d}{dt} i_{d,d} = 0 \tag{4.10}$$

4.4.3 The Primary Voltage Input

The primary ("desired") voltage input, v_d, is obtained by requiring that the dynamic equations of the electric component of (4.1) be satisfied with the desired currents and at the actual speed:

$$\begin{aligned} v_{d,d} &= L_d \frac{d}{dt} i_{d,d} + R i_{d,d} - \omega L_q i_{q,d} \\ v_{q,d} &= L_q \frac{d}{dt} i_{q,d} + R i_{q,d} + \omega (L_d i_{d,d} + MI) \end{aligned} \tag{4.11}$$

4.5 Incremental State Dynamics and Control

Having defined the primary control inputs, we assure that the closed loop system be stable. In addition to that we use the elements of the incremental state matrix to improve the transient convergence rate. In what follows we will denote the incremental states, representing momentary deviations from desired values, by $e_1 = L_d(i_d - i_{d,d})$, $e_2 = L_q(i_q - i_{q,d})$ and $e_3 = H(\omega - \omega_d)$. A variable $e_4 = \frac{1}{\tau}(\widehat{T}_L - T_L)$ will represent the torque estimation error; e_5 is defined by (4.3).

4.5.1 Torque Estimation Errors And The Mechanical Incremental System

By direct computation

$$\frac{d}{dt} \begin{bmatrix} e_3 \\ e_4 \\ e_5 \end{bmatrix} = A_{2,1} \begin{bmatrix} e_1 \\ e_2 \end{bmatrix} + A_{2,2} \begin{bmatrix} e_3 \\ e_4 \\ e_5 \end{bmatrix} + B_2 \frac{d}{dt} T_L \tag{4.12}$$

where

$$\begin{aligned} A_{2,1} &= \begin{bmatrix} \eta^T \\ 0 \\ 0 \end{bmatrix}, \qquad \eta = \Delta L \begin{bmatrix} \frac{i_q}{L_d} \\ \frac{i_{d,d}}{L_q} \end{bmatrix} + MI \begin{bmatrix} 0 \\ \frac{1}{L_q} \end{bmatrix}, \\ A_{2,2} &= \begin{bmatrix} -\frac{B}{H} & \tau & \sigma \\ -\tau & 0 & 0 \\ -\sigma & 0 & -\zeta \end{bmatrix}, \qquad B_2 = -\tfrac{1}{\tau} \begin{bmatrix} 0 \\ 1 \\ 0 \end{bmatrix} \end{aligned} \tag{4.13}$$

The matrix $A_{2,2}$ governs the homogeneous component of (4.12). It is the sum of a negative semidefinite and a skew-symmetric matrix. As explained in Appendix B, this form guarantees that solutions of the homogeneous equation $\dot{z} = A_{2,2}z$ have the property that the "energy" storage function $0.5\|z\|_E^2$ decays monotonically along trajectories. In particular, this matrix structure implies stability. The goal of shaping $A_{2,2}$ explains the structure of the dynamic torque estimate and the added dynamics of e_5: "incremental energy", represented, by $0.5\|[e_3, e_4, e_5]^T\|_E^2$, can be shifted through lossless channels from both the speed tracking error and the load estimation error to the dynamic variable e_5, and dissipated there. Both the rate of lossless dynamics and of dissipation are determined by selection of the design parameters later. In fact, it is easily observed that having set a desired exponential decay rate, say $-\rho$ ($<< -\frac{B}{H}$), the design parameters ζ, σ and τ can be selected to place all the three eigenvalues of $A_{2,2}$ at $-\rho$, or (e.g., for a faster rise time) place a single real eigenvalue at $-\rho$ and a pair of complex conjugate eigenvalues at $-\rho \pm \jmath\xi$, with a designated ξ.

The cost of adding imaginary components to two of the eigenvalues is widening the bandwidth of the second order subsystem that these two eigenvalues form, as will be demonstrated by simulations and experimental results in Chapter 6. For simplicity, we will assume in the ensuing discussion that parameters are assigned to place three distinct eigenvalues for $A_{2,2}$, in which case the exponential matrix $exp(A_{2,2}t)$ decays with a bound proportional to $exp(-\rho t)$. (In the case of repeated eigenvalues, bounds proportional to $t \cdot exp(-\rho t)$ or $t^2 \cdot exp(-\rho t)$ have to be used.)

4.5.2 The Electrical Incremental System and Incremental Control

The following equations govern the open loop dynamics of the electrical incremental states:

$$\frac{d}{dt}\begin{bmatrix} e_1 \\ e_2 \end{bmatrix} = \begin{bmatrix} -\frac{R}{L_d} & \omega \\ -\omega & -\frac{R}{L_q} \end{bmatrix} \begin{bmatrix} e_1 \\ e_2 \end{bmatrix} + \begin{bmatrix} v_{d,e} \\ v_{q,e} \end{bmatrix} \tag{4.14}$$

where $v_{d,e}$ and $v_{q,e}$ are the incremental input voltages. Differentiating the candidate Lyapunov function $V = 0.5(e_1^2 + e_2^2)$ along trajectories of (4.14), it is noted that the incremental electric subsystem is (uniformly exponentially) stable even when zero incremental voltage inputs are used, as $\dot{V} = -R\left(\frac{1}{L_d}e_1^2 + \frac{1}{L_q}e_2^2\right)$. The rate of convergence can be increased – limited only by the available power supply and bandwidth considerations – by incremental control selection. One option is a selection of the form:

$$\begin{bmatrix} v_{d,e} \\ v_{q,e} \end{bmatrix} = \begin{bmatrix} -\rho + \frac{R}{L_d} & \gamma - \omega \\ \omega - \gamma & -\rho + \frac{R}{L_q} \end{bmatrix} \begin{bmatrix} e_1 \\ e_2 \end{bmatrix} - \lambda^2 \eta e_3 \tag{4.15}$$

where $-\rho$ is set here to be equal to the desired closed loop exponential decay rate and where γ and λ are design parameters.

As can be easily seen, one effect of (4.15) is that the homogeneous component of the closed loop incremental electric system is a second order linear time invariant (LTI) system with eigenvalues at $-\rho \pm \jmath\gamma$. This readily explains the effects of the selection of the design parameters ρ and γ. At this point we note that most often the desired mechanical time constant is longer than the open loop electric time constant of the motor, in which case there is no need to accelerate current response. Then one may use a set of zero diagonal entries in (4.15).

Introducing a non zero selection of the design parameter λ, we create an additional energy exchange channel between the electrical and the mechanical incremental systems, and thus an additional mechanism for shaping incremental transients. A non zero selection of λ can help us create a faster mechanical response by shifting incremental energy from the relatively slow mechanical subsystem to the naturally faster electrical subsystem. However, if λ is too large it can also cause oscillatory behavior. We should remark here that the eigenvalue placement of $A_{2,2}$ can be replaced, when $\lambda \neq 0$ is used, with asymptotic eigenvalue placement of the combined mechanical and electrical incremental system. The validity of such eigenvalue assignment will be global in the case of a non–salient motor, where the combined 5×5 incremental system is LTI.

Figure 4.1 clarifies interconnections and links between various parts of the developed PMSM passivity based closed loop system.

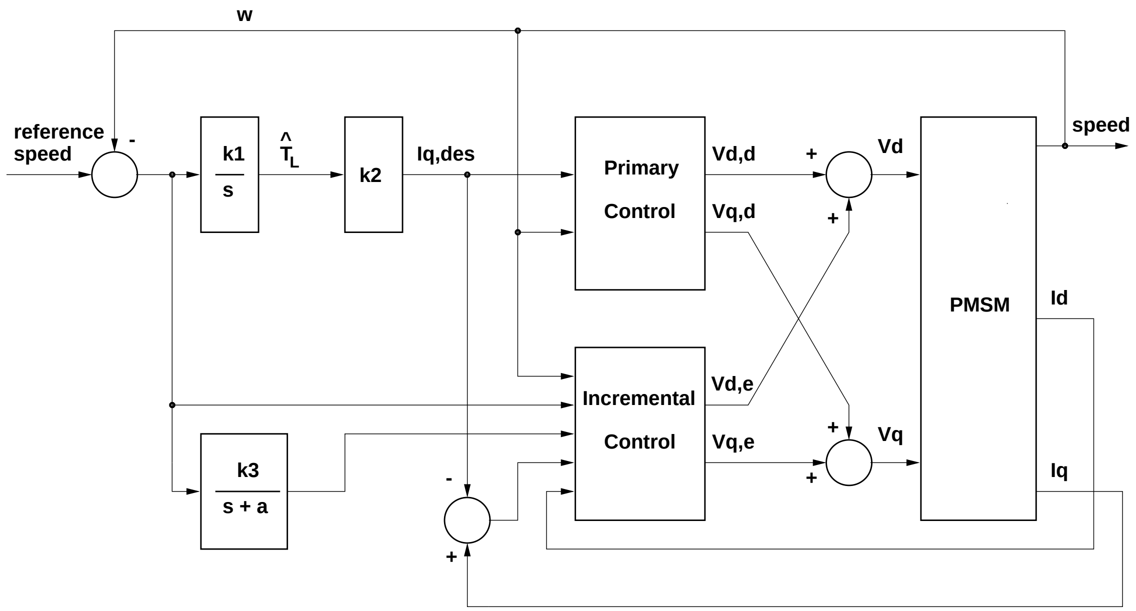
w
reference speed
-
k1
s
^
T_L
k2
Iq,des
Primary Control
Vd,d
Vq,d
+
+
Vd
speed
PMSM
Id
Incremental Control
Vd,e
Vq,e
+
+
Vq
Iq
k3
s + a
-
+

Figure 4.1: Block diagram of the passivity based closed loop system.

4.6 Eigenvalue Placement for Controller Parameter Calculation

After having described the theoretical foundation for the proposed passivity based controller design, we show the rules and recomendations for the selection of the controller parameters τ, σ, ζ, and λ. We assume here and use further for verification a non-salient PMSM structure. For convenience of reading we rewrite the closed loop state equation for the incremental system:

$$\frac{d}{dt}\begin{bmatrix} e_1 \\ e_2 \\ e_3 \\ e_4 \\ e_5 \end{bmatrix} = \begin{bmatrix} -\rho & \gamma & 0 & 0 & 0 \\ -\gamma & -\rho & -\lambda^2 \frac{MI}{L} & 0 & 0 \\ 0 & \frac{MI}{L} & -\frac{B}{H} & \tau & \sigma \\ 0 & 0 & -\tau & 0 & 0 \\ 0 & 0 & -\sigma & 0 & -\zeta \end{bmatrix} \begin{bmatrix} e_1 \\ e_2 \\ e_3 \\ e_4 \\ e_5 \end{bmatrix} \tag{4.16}$$

Choosing zero values for γ we effectively decouple electrical states e_1 and e_2 from each other. In this case one of the eigenvalues of A is placed at $-\rho$ governing the transients in i_d only. This allows for analysis of the lower 4-by-4 block of the state matrix A separately (this block is denoted by $\acute{A}$.)

The mechanism for the design of the control gains is based on the placement of system eigenvalues in predetermined locations. First, we analyze all possible choices for the eigenvalue locations of

$$\acute{A} = \begin{bmatrix} -\rho & -\lambda^2 \frac{MI}{L} & 0 & 0 \\ \frac{MI}{L} & -\frac{B}{H} & \tau & \sigma \\ 0 & -\tau & 0 & 0 \\ 0 & -\sigma & 0 & -\zeta \end{bmatrix} \tag{4.17}$$

The possibilities for the location of eigenvalues of $\acute{A}$ include four real eigenvalues (say, r_1, r_2, r_3, r_4), two real and one complex pair of eigenvalues (denote them r_1, r_2, $r_3 \pm \jmath q$) or two pairs of complex eigenvalues ($r_1 \pm \jmath q_1$, $r_2 \pm \jmath q_2$.) The case of multiple poles is naturally included in one of these choices. Considering the characteristic polynomial for a given case of eigenvalues placement (real, mixed , or complex)

$$P(s) := s^4 + a_3 s^3 + a_2 s^2 + a_1 s + a_0 \tag{4.18}$$

one can equate corresponding coefficients of (4.18) to those of $\det(sI - \acute{A})$

$$P(s) = \det(sI - \acute{A}) \tag{4.19}$$

to solve for the unknown controller gains τ, σ, ζ, and λ.

The determination of $a_0, ..., a_3$ is fairly simple and the result is given here for the case of real eigenvalues only:

$$\begin{aligned} a_3 &= -r_1 - r_2 - r_3 - r_4 \\ a_2 &= r_1 r_2 + r_3 r_4 + (r_1 + r_2)(r_3 + r_4) \\ a_1 &= -r_1 r_2 (r_3 + r_4) - r_3 r_4 (r_1 + r_2) \\ a_0 &= r_1 r_2 r_3 r_4 \end{aligned} \tag{4.20}$$

Obviously, one should select negative real parts for the roots of the characteristic polynomial (4.18).

The general solution is of the form

$$\begin{aligned} \zeta &= a_3 - \frac{B}{H} - \rho \\ \tau &= \sqrt{\frac{a_0}{\zeta\rho}} \\ \sigma &= \sqrt{\frac{\Delta_\sigma}{\Delta}} \\ \lambda &= \sqrt{\frac{\Delta_\lambda}{\Delta}} \end{aligned} \tag{4.21}$$

where

$$\begin{aligned} \Delta &= (\zeta - \rho)\left(\tfrac{MI}{L}\right)^2 \\ \Delta_\sigma &= (\zeta k_1 - k_2)\left(\tfrac{MI}{L}\right)^2 \\ \Delta_\lambda &= k_2 - \rho k_1, \\ \\ k_1 &= a_2 - \zeta\tfrac{B}{H} - \tau^2 - \rho(\tfrac{B}{H} + \zeta) \\ k_2 &= a_1 - \zeta\tau^2 - \rho(\zeta\tfrac{B}{H} + \tau^2) \end{aligned} \tag{4.22}$$

There are several options for placing eigenvalues of $\acute{A}$. One of them (and not the best in terms of performance) is to leave one of the eigenvalues exactly at $-\rho$. This results in $\lambda = 0$ and still allows us to use (4.21) to determine the remaining parameters. In this case we effectively manipulate only the parameters of the mechanical subsystem. The electrical time constants remain unchanged and the "bandwidth" of the electrical states directly affects incremental voltages. This potentially means that shifting mechanical subsystem eigenvalues to the left may increase the speed of response to disturbance changes but would result in "noisier" voltage command due to a larger mechanical subsystem bandwidth and due to a speed noise directly affecting the voltage actuation signal. The practical choice for the location of the remaining three eigenvalues is determined by the desired speed of transient response (i.e., duration of transients in mechanical states), additional requirements to overshoot in the response, and physical limitations on the supplied power. Two natural options are to place all three eigenvalues in one place on the negative real axis or to have one real eigenvalue and one pair of complex eigenvalues. In the latter case one can manipulate the imaginary component using it as a tool to reach a compromise result in terms of overshoot and speed of response requirements.

A second option in the eigenvalues placement is to have a fixed value of ρ, say, $\rho = \frac{R}{L}$, and vary the value of λ to change the location of $\acute{A}$ eigenvalues. In this case we provide an additional channel for lossless energy exchange between e_2 and e_3, e_4, e_5. Potentially this can allow for achieving the same dynamic response characteristics *without* opening the bandwidth of the electrical subsystem. One can try to place all four eigenvalues of $\acute{A}$ in one location on the negative real axis which would be the best compromise solution that balances dynamic qualities of the controller and requirements to the existing physical actuator (power supply.) There is one practical limitation in this case. The value of ζ representing the cut-off frequency of the filter on speed error must be positive for stability considerations. This establishes a lower bound on the value of a_3 and, therefore, a lower bound on a sum (taken with an opposite sign) of all four real parts of roots in (4.18.) One possible and proposed strategy would be to keep three eigenvalues of $\acute{A}$ at one predetermined location creating tripple pole of the characteristic polynomial and move the fourth one towards them starting at $-\rho = -\frac{R}{L}$.

Various design options for the selection of controller gains are considered and the results of their utilization are analyzed in Chapter 6.

Chapter 5

Experimental Test-Bed

The purpose of this chapter is to provide operational description of the experimental laboratory setup used for development, implementation and real-time evaluation of different drive control algorithms for PMSMs. The availability of high-power digital signal processors has allowed the implementation of increasingly complex drive algorithms and control functions in digital hardware.

The block diagram in Figure 5.1 shows the overall drive system. Control algorithms are implemented using two DSP subsystems, one dedicated to the development and implementation of control algorithms (based on a Texas Instruments' TMS320C31 DSP) and the other to the implementation of standard drive functions such as analog data acquisition and PWM (based on an Analog Devices' ADSP-2101 DSP). Separation of the control system in this manner provides for two significant advantages: 1) software processing time for the control DSP sub-system is minimized, providing the fastest possible cycle time and highest controller bandwidth, and 2) all other hardware in the system will perform the same functions regardless of control algorithms implemented, and can be treated as a fixed subsystem. This will allow a comparison of the relative merits of various control algorithms, as the hardware and software for routine drive system functions will be common [9].

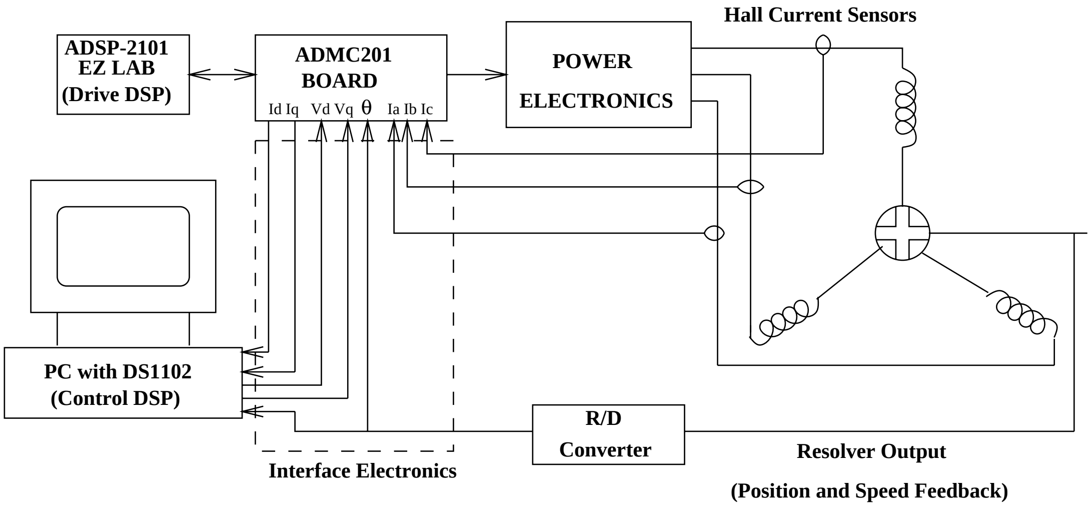
Hall Current Sensors
ADSP-2101 EZ LAB (Drive DSP)
ADMC201 BOARD
Id Iq Vd Vq θ Ia Ib Ic
POWER ELECTRONICS
PC with DS1102 (Control DSP)
R/D Converter
Interface Electronics
Resolver Output
(Position and Speed Feedback)

Figure 5.1: Overall drive system setup

5.1 Control DSP

The primary reason for the implementation of two DSP systems for the drive control functions is to allow for a processor dedicated solely to control algorithm development and implementation via Simulink block diagrams. Due to the reduced number of functions the processor is required to implement, the time required to complete one full cycle of the given control algorithm will be considerably less than in a single DSP approach. This yields a higher compensator bandwidth, or allows for implementation of more complex, time consuming algorithms.

The control DSP functions are implemented in a DS1102 DSP board made by dSPACE Inc. The main processor is a TMS320C31 40 MHz 32 bit floating point DSP (made by Texas Instruments). The board also has 4 analog to digital converters (ADCs), four digital to analog converters(DACs), two 24 bit incremental encoder blocks, a PWM block, and 16 digital input/output lines (the digital I/O capability has not been utilized by this system). Each of these blocks, and their inputs or outputs, can be accessed by including the appropriate symbol in a given Simulink model.

The dSPACE DSP board provides the development environment based on Matlab for analysis, design, optimization, and off-line data processing. It uses Simulink for block diagram-based off-line simulation, Real-Time Workshop for generating C code from the block diagram, Real-Time Interface (RTI) for making this code run on single-processor (or, possibly, multiprocessor) target DSP systems, and a set of software tools to interact with the experiment, both directly as a user or automated through Matlab. The Real-Time Workshop is a code generation extension provided by Mathworks, Inc. Along with the producing C code directly from the block diagram, it allows the user to introduce his/her own code into the block diagram by special blocks. That C code is used in off-line simulation, and will become a part of the real-time code.

Since the Real-Time Workshop does not target DSP specifically, dSPACE has added this functionality via its Real-Time Interface by adding blocks for I/O, and by completely integrating all other steps required to make use of the C code and other information coming out of the Real-Time Workshop. The major services are:

- generating the makefile for compiling;
- providing the real-time frame source code including timer-interrupt driven execution, start, stop and pause functions, execution time profile, and overload check;
- providing hooks for expansions and modifications by user;
- deriving names of all Simulink variables and parameters for easy accessability by Trace and Cockpit, including the mapping of the whole block hierarchy for navigating in big programs;
- connecting the block diagram with the running application on the DSP for parameter changes.

The control system is "built" as if a standard Simulink simulation were to be performed. Once the model is completed, it is converted to equivalent C code using Matlab's Real Time Workshop. The cycle time, or step size, must also be entered by the user. This sets the maximum execution time (providing that DSP capabilities are not exceeded) for the control algorithm. The final step is to compile the generated C code into TMS320 assembly code, and download the program into the DSP memory.

The compensator gains or constants can be adjusted during real-time operation, allowing for interactive tuning without regenerating the code or downloading the program anew. Current and position feedback are available via the on-board ADCs and incremental encoder inputs. Scaling and filtering can be done, if necessary, using gain blocks or other Simulink capabilities such as the transfer function block or the built in filter blocks.

One practical limitation arising with the use of dSPACE DSP board is the controller bandwidth. Practically, the controller bandwidth in digital implementation needs to be at least by order of magnitude smaller than the available bandwidth of the DSP calculation cycle. Although being a common problem for any digital control implementation ([97, 29]), this constraint becomes more important in the case when dSPACE board is used. It would be fair to state that the utilization of dSPACE gains universality by sacrificing the performance. The minimum possible calculation time of the implemented passivity-based control scheme has been brought down to 0.5 ms resulting in a bandwidth of 2 kHz.

5.2 Drive DSP

It was desired to free the control processor from having to perform the non-control-related drive functions, such as Park transformations and pulse width modulation. For this reason, a second DSP system was implemented. The drive DSP subsystem is built around an Analog Devices ADSP-2101, an ADMC201 motion coprocessor, and an AD2S83 resolver to digital converter. The primary functions for this system are as follows:

- Analog data acquisition (phase B and C current inputs, V_d and V_q inputs from the control DSP system).
- Forward and reverse Park transformation, including shaft position measurement from the resolver to digital converter circuit.
- Pulse width modulation calculation and duty cycle implementation.

5.2.1 Drive DSP characteristics

The Analog Devices' ADSP-2101 is a 20 MHz 16 bit fixed point DSP. It features:

- 25 MIPS, 40 ns maximum instruction rate;
- separate on-chip buses for program and data memory;
- program memory stores both instructions and data (three-bus performance);
- dual data address generators with modulo and bit-reverse addressing;
- efficient program sequencing with zero-overhead looping;
- automatic booting of on-chip program memory from byte-wide external memory;
- double-buffered serial ports with companding hardware, automatic data buffering, and multichannel operation.

Summarizing, ADSP-2101 is a single-chip microprocessor/microcomputer optimized for digital signal processing and other high speed numeric processing applications.

Every instruction can execute in a single cycle. In one cycle the ADSP-21xx can perform all of the following operations:

- generate the next program address;
- fetch the next instruction;
- perform one or two data moves;
- update one or two data address pointers;
- perform a computation;
- receive or transmit data via serial port.

The more detailed description of the ADSP-2101 characteristics and assembly language instructions set can be found in [1, 2].

In addition to the ADSP-2101 the motion coprocessor ADMC201 has been used. It provides the functionality that is required to implement a digital control system. In a typical application, the DSP or micro-controller performs the control algorithms (position, speed, torque and flux loops) and the ADMC200 provides the necessary motor control functions: analog current data acquisition, vector transformation, and PWM drive signals. ADMC201 features:

- Analog input block: 11-bit resolution analog-to-digital converter, 7 single-ended analog inputs, 3.2 μs conversion time per channel, PWM synchronized sampling capability;

- 12-bit PWM timer block: three-phase center-based PWM, 1.5 kHz - 25 kHz PWM switching frequency range, programmable deadtime and pulse deletion, external PWM shutdown;
- Vector transformation block: 12-bit forward and reverse Park and Clarke transformations, 2.9 μs transformation time;
- Programmable digital I/O port: 6-bit configurable digital I/O, change of state interrupt support;
- DSP and microcontroller interface: 12-bit memory-mapped registers;
- 6.25 to 25 MHz operating clock range.

The vector transformation block of ADMC201 performs both Park and Clarke coordinate transformations to control a three-phase motor (Permanent Magnet Synchronous Motor or Induction Motor) via independent control of the decoupled rotor torque and flux currents. The Park and Clarke transformations combine to convert three-phase stator current signals into two orthogonal rotor referenced current signals I_d and I_q. These signals are used by the processor's motor torque control algorithm to calculate the required direct V_d and quadrature V_q voltage components for the motor. The forward Park and Clarke transformations are used to convert the V_d and V_q voltage signals in the rotor reference frame to three phase voltage signals V_a, V_b and V_c in the stator reference frame. These are then scaled by the processor and written to the

ADMC200's PWM registers in order to drive the inverter. More detailed description of ADMC201 operation and its connection with the main processor is given in [4].

5.2.2 Rotor Position Sensors and Resolver-to-Digital Converter

The power transistors in the inverter must receive conduction commands from a system of logic which is synchronized with the rotor position. The necessary synchronizing signals are usually derived from a shaft position transducer, and three types are commonly used: the resolver, the optical encoder and the Hall-effect transducer.

The resolver provides very fine resolution in the shaft position signal. Its output is a two-phase (sine/cosine) signal at the carrier frequency, modulated sinusoidally by the rotation of the rotor past the stator. The demodulated output can be transformed into a pulse train by resolver-to-digital converter, which is usually a single integrated circuit. Typically, 1000 – 4000 pulses per revolution can be obtained [38]. The resolver is an absolute position transducer because it provides a signal at any position and any speed, including zero speed. The direction of rotation can be determined from the relative phasing between the two channels (phases), and analog or digital signals are also readily available. The resolver is used when rpm or tachometer information or a precise shaft-positioning signal is needed. It has the advantage of ruggedness and can be used at high speeds. The resolver rotor mounts on a shaft extension of the brushless DC motor at the non-drive end, without couplings.

Like the resolver, the optical encoder is used when more information is needed than just commutation pulses. It consists of a set of pairs of phototransistors and light sources, used in conjunction with a glass or metal encoder disc. The pattern of slits on the disc defines the frequency and waveform of the pulse trains which are produced by the phototransistors. Usually, commercial incremental encoders have two tracks which are in quadrature (i.e., with a phase shift of one-quarter of a slit-pitch). An index pulse (one slit per revolution) is also provided as a simple absolute position reference. More complex encoder disks have special patterns (e.g., Gray Scales) which can be used to provide absolute position information with very fine resolution and high accuracy. Typically, resolution of the encoder used in motor drives is 1000 lines/revolution.

Optical encoders produce pulses directly which makes them very attractive for interfacing to digital commutation circuitry. However, they have some practical limitations. The encoder cannot operate at such high temperatures as the resolver, and it does not provide the necessary mechanical ruggedness.

In addition to these two types of position sensors, the Hall-effect sensor is used for generating commutation pulses. A Hall switch is a semiconductor switch that opens or closes when placed in a magnetic field higher than a certain level. It is based on the Hall effect, which is the generation of an EMF proportional to flux-density when semiconductor is carrying current. The EMF, the flux-density, and the current (usually a few mA) must be supplied by an external source. For a three-phase brushless motor, three Hall switches are arranged spaced at 60^0 or 120^0 electrical, and mounted on the stator frame. Either a separate trigger magnet with the correct pole spacing is mounted on the shaft in close proximity to the Hall switches, or the Hall switches can be mounted close enough to the rotor magnets, where they are energized by leakage flux at the appropriate rotor position.

According to the requirements to the experimental setup and due to a used motor model a resolver position sensing approach has been implemented. The conversion from the resolver signal to the digital data representing absolute position has been done by means of a resolver-to-digital converter AD2S83.

The AD2S83 is a monolithic 10-, 12-, 14- or 16-bit tracking resolver-to-digital converter contained in a 44-pin PLCC package. It combines the advantages of CMOS logic and bipolar high accuracy linear circuits on the same chip. The converter allows users to select their own resolution and dynamic performance with external components. This allows the users great flexibility in defining the converter that best suits their system requirements. The resolution can be selected at 10, 12, 14 or 16 bits.

The AD2S83 converts resolver format input signals into a parallel natural binary digital word using a ratiometric tracking conversion method. This ensures high noise immunity and tolerance of long leads allowing the converter to be located remote from the resolver. The position output from the converter is presented via 3-state output pins which can be configured for operations with 8- or 16-bit bus. BYTE SELECT, ENABLE and INHIBIT pins ensure easy data transfer to 8- and 16-bit data bus, and outputs are provided to allow for cycle or pitch counting in external counters.

A precise analog signal (0.1% linearity in the frequency range 0 – 3600 rpm) proportional to velocity is also available and can replace a tachogenerator.

In the built experimental setup the carrier frequency is set to 5 kHz and the resolution used is 14 bits that provides 487.5 rpm/V dc speed output. In addition to the parallel 14-bit digital position output, an artificial incremental encoder signals have been created and fed to the dSPACE board that uses them in incremental encoder block.

5.2.3 Drive DSP operation

The ADSP-2101 is implemented using Analog Devices' EZ-LAB DSP design system. The motion coprocessor and required software and support circuitry are implemented in an evaluation board, the details of which are described in [3]. The basic functions of the software and hardware in the ADMC201 board were modified to meet the requirements of the drive sub-system. The primary modification was to allow for position input from an AD2S83 resolver to digital converter circuit. The software performs the following sequence of operations:

1. Read in analog inputs (phase B and C currents, V_d and V_q control outputs).
2. Perform a reverse Park's transformation on the phase currents. Write results to the DACs for input to the control DSP.
3. Perform a forward Park's transformation using the V_d and V_q control inputs.

4. Use the results of the forward transformation to calculate PWM duty cycles, and implement them using the PWM registers.

Communication between the two DSP subsystems is done using analog signals. The outputs of the control DSP system are the inputs to the drive DSP system, and vice versa.

The output of any vector control algorithm to be implemented in this system will be the direct and quadrature axis voltages. These are calculated by the Matlab-based control algorithm and written to the DS1102's DACs. These signals are then scaled and read into the ADMC201, where they are used in the forward Park transformation and eventually implemented by the PWM section.

The inputs to the control DSP system are the instantaneous shaft speed and the direct and quadrature axis currents. The shaft speed is calculated using the DS1102 encoder input block. The direct and quadrature axis currents are calculated by the ADMC201, based on the instantaneous phase currents. These are written to the drive DSP system's DACs, scaled, and read into the DS1102 through its ADCs.

Communication between the sub systems in this manner eliminates handshaking constraints and allows the two systems to operate asynchronously. The 16 digital I/O lines on the DS1102 are updated once every control cycle, thus the 4 signals described above would have to be transmitted sequentially, with updates for a given control signal occurring every 4 control cycles. The communication method implemented allows for simultaneous transmission and receipt of the required signals.

5.3 Power Inverter Stage

The purpose of the power inverter stage is to convert a power supply DC voltage into the three-phase AC system of voltages. The phase shift between phase voltages is to be equal to 120 electrical degrees, and the frequency is to be determined by the synchronous speed of the motor. Figure 5.2 shows the basic inverter system.

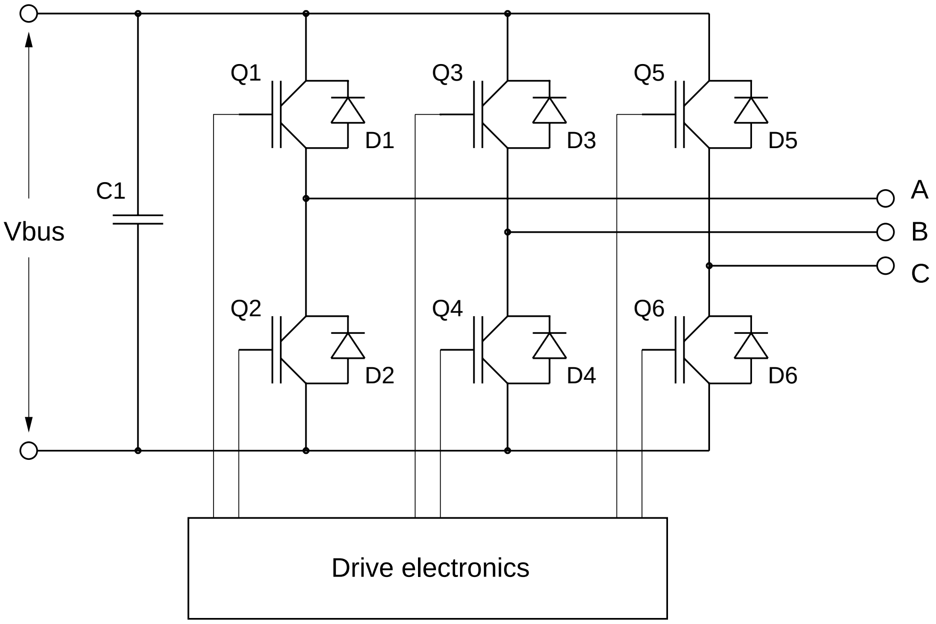

Figure 5.2: Basic inverter scheme.

Current flows out of a given inverter leg and into the motor phase when a potential difference exists between one inverter leg and either one or both of the other legs. This condition occurs if the upper switch in a given leg (say, Q1) and the lower switches in the other two phases (say, Q4 and Q6) are turned on. Current will not flow if the inverter outputs are all at the same potential. This will occur when all upper switches are on, all lower switches are on, all switches are off, or each device is operated at 50% duty cycle, with the upper and lower drive signals in a given switch leg being the compliment of each other. This last mode of operation is used by ADMC201. In this mode of operation, when each switch is operated at 50% duty cycle, the average voltage at each inverter leg output is equal to half the bus voltage. Since all phase outputs are at the same potential, no current flows through the motor winding.

5.3.1 Generation of Sinusoidal Voltages by means of PWM

The system of sinusoidal voltages with a phase shift of 120 electrical degrees between phases should be applied to the motor in order to create a rotating electromagnetic field which varies sinusoidally in space and time. This could be done by means of PWM of the power inverter control voltages. It should be assumed that the PWM carrier frequency is much higher than the main harmonic of the waveform to be generated. Practically, the PWM frequency to main harmonic frequency ratio of 100 – 500 is desirable. The upper limitation for PWM carrier frequency is that the thermal losses are directly proportional to the number of on-off transitions per unit time, i.e. to PWM frequency.

One of the ways to create a sinusoidal voltage is to use a complimentary PWM. In this case the duty ratio of each switch varies sinusoidally around the 50 % point. Then, with respect to this 50 % point a duty ratio greater than 50 % will create a positive net voltage and that less than 50 % will create a negative net voltage. In ideal case, if the duty ratio of the upper IGBT is d %, then the lower IGBT has a complimentary duty ratio of 100 % - d. The result of this operation is the application of sinusoidal voltages to the motor phase windings, with sinusoidal current flow. Since the phase shift between different phases' duty cycles is 120 electrical degrees, the resultant phase shift between different phase voltages is also 120 electrical degrees.

5.3.2 Deadtime and Pulse Deletion Specifications

Ideally, the commutation of the upper and lower switches in the same leg should be done simultaneously. Practically, the power switches are not ideal and require some time to turn on and off. This time also varies as a function of commutated current. For the used IGBT 6-pack module the specified turn-off time varies from 150 ns to 350 ns for the current of 0.1 – 15 Amps. Laboratory tests have been performed in order to determine the turn-off time constants more accurately for the phase current limited from practical considerations. The results of this experiment are presented in Figure 5.3.

It can be seen from the oscilloscope traces that the IGBT turn-off time with the drain current of 4.5 A does not exceed 220 ns. This number gives the lower margin for the deadtime specifications. The lower value of the deadtime will cause the inverter shoot-through fault and irrecoverable inverter damage. Since the drive electronics also contributes to the deadtime value, it is important to estimate these numbers. Several tests have been performed to determine the value of time delay introduced by the gate driver circuitry itself. Figure 5.4 gives some numerical specifications for this parameter.

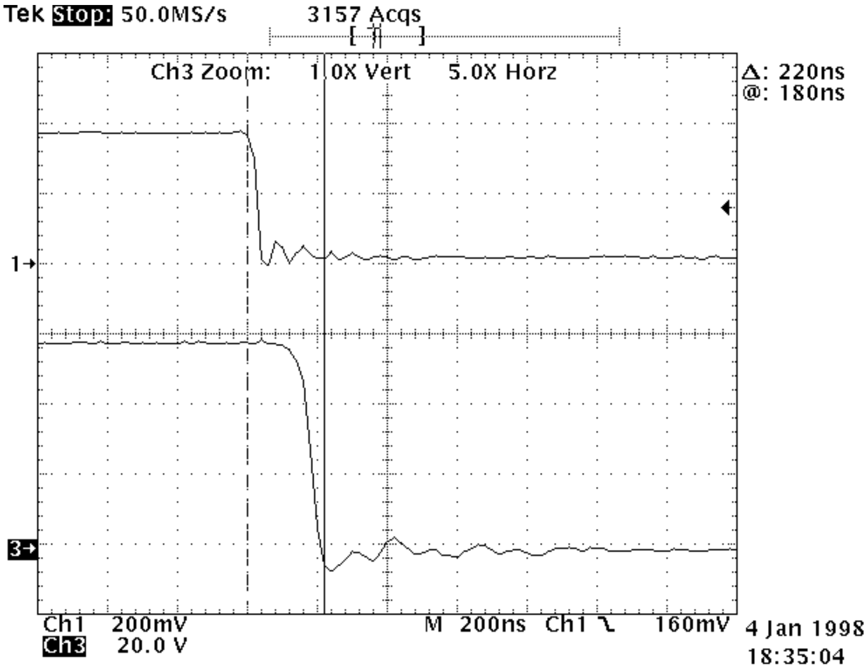

Figure 5.3: IGBT turn-off process: Q1 gate signal (upper) and phase A output voltage (lower).

The upper two traces (scope channels 1 and 2) show the input voltages to the gate drivers for the upper and lower IGBT in the same leg with a time separation of approximately 1.116 μs. The lower two traces show the output voltages of the gate drivers with a delay of approximately 1.268 μs. This adds up approximately 150 ns of extra deadtime delay, basically due to the "slower" low-to-high transition in the gate driver.

Another issue, present in practical inverter drives, is a pulse deletion problem. Due to the nonlinear (sinusoidal) waveform generation some of the PWM pulses results in the duty ratio values of no greater than 0.5% – 1% . Since the "contribution"

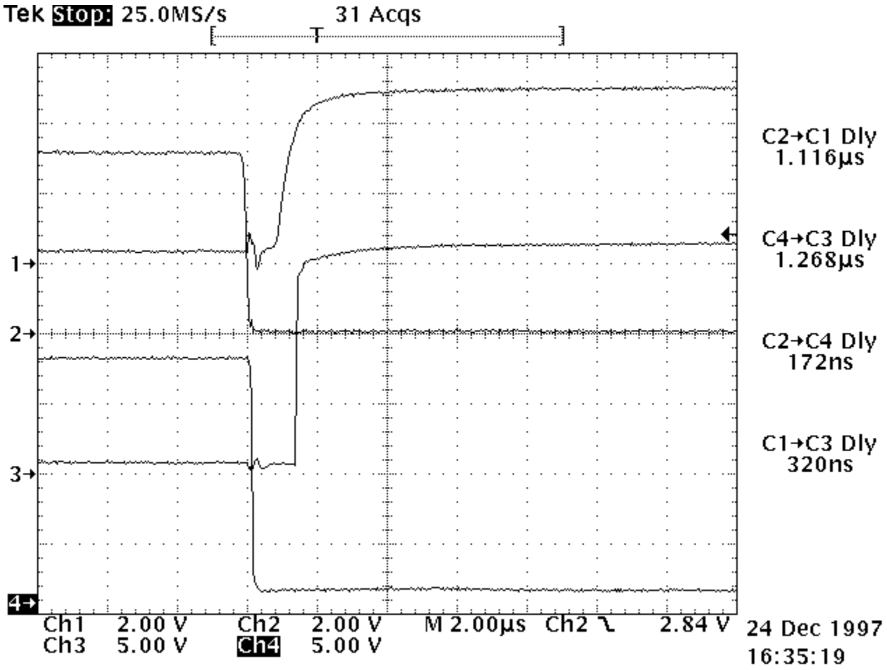

Figure 5.4: Gate driver time delay.

of such short pulses to the average value of the output voltage is negligible, they could be simply deleted. As a result, there is no turn-on – turn-off transition of the power switch at this particular moment and power losses are lowered per period of the generated waveform. This power losses minimization becomes important if power switches work on the edge of their performance, i.e., drain current and commutated voltage are close to their rated values. In the particular case of the used laboratory setup the IGBTs' currents are about one third of their nominal value and, therefore, the generated sinusoidal voltage precision should be preferred over power losses minimization.

Practically, in the used laboratory setup the pulse deletion time has been set to

1000 ns, and that of the deadtime has been set to 400 ns. This choice guarantees proper inverter performance and satisfies all safety consideration. The resulted phase current is shown in Figure 5.5.

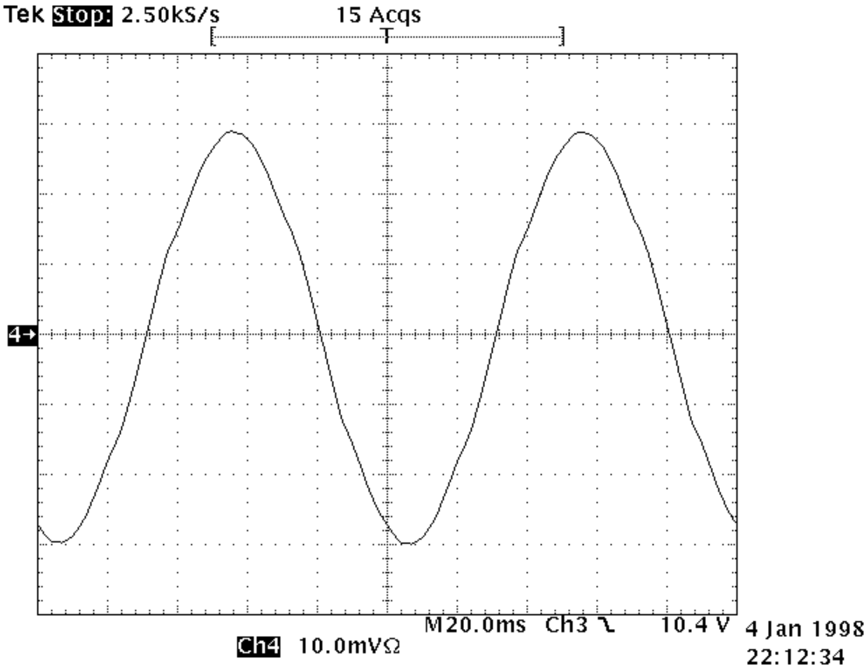

Figure 5.5: PMSM phase current generated by means of PWM.

As one can see, the resultant current waveform has no visible "bumps" and no visible distortion around zero-crossing points. Additional improvement in the quality of the current waveform would have required for increase in PWM switching frequency and would not be practically possible.

5.4 Permanent Magnet Synchronous Motor

The choice of the particular PMSM was stipulated by the following technical considerations:

- input power available from laboratory power sources;
- reliable operation in the speed range of hundreds rpms;
- primary speed feedback availability through the resover mounted on the rotor shaft;
- ease of mechanical mounting from the rotor face plate.

The PMSM model number R43HENA manufactured by Motion Technology Division of Pacific Scientific was chosen for the laboratory test purposes.

5.4.1 Identification of Motor Drive Parameters

The manufacturer provided the following motor parameters and winding data:

Parameter	Symbol	Units	Data
Continuous Stall Torque	T_{cs}	lb-in	33
Peak Torque	T_{pk}	lb-in	135
Inertia	J_m	lb-in-sec^2	0.0018
Static friction (max.)	T_f	lb-in	0.26
Viscous damping coefficient	K_{dv}	lb-in/Krpm	0.10
Torque constant (line-line)	K_t peak	lb-in/A	5.4
Voltage constant (line-line)	K_e peak	V/Krpm	64
Continuous stall current	I_{cs}	A	6.9
Current at peak torque	I_{pk}	A	53
Resistance (line-line)	R_c cold	Ohms	2.5
Resistance (line-line)	R_c hot	Ohms	3.7
Inductance (line-line)	L	mH	13.3

In addition to this data, the motor performance curves (motor torque versus speed) were available for continuos and intermittent modes of operation. The performance characteristics of R43HENA are shown in Figure 5.6.

Since the test results would benefit from more accurate knowledge of the drive system parameters, additional measurements and unit conversions to SI unit system have been performed. The necessity of the winding data recalculation was based on the fact that the above mentioned motor parameters were given for the R43H model in general but not for the specific unit used in experiments. The manufacturer tolerance usually falls in the range of 10% - 20% whereas some control experiments would require much better accuracy.

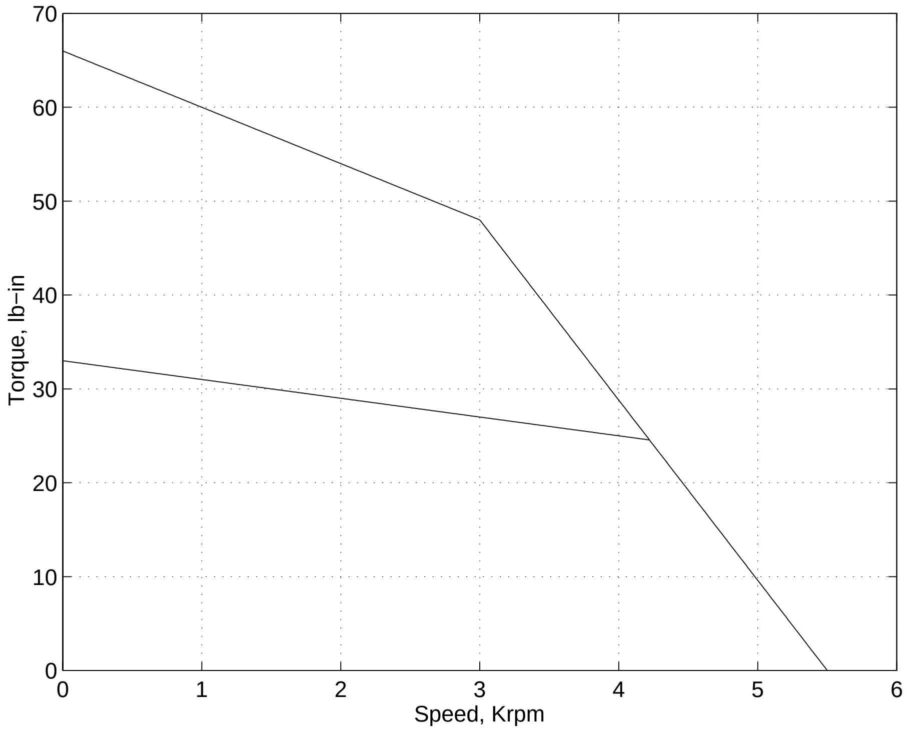

Figure 5.6: Performance characteristics of R43HENA: peak torque (upper line) and continuos torque (lower line)

A number of straightforward tests was performed to obtain line-line resistance and inductance. As far as inductance is concerned we took advantage of the nonsalient structure of the motor rotor and assumed inductance independent of rotor angular position. The line-line inductance average value was 18.2 mH, which is approximately 37% larger than manufacturer's data. The line-line resistance was 2.5 Ohms when cold.

In order to determine the value of the voltage constant (also called back EMF constant) the back-spinning motor test was used. The PMSM was disconnected from the inverter and mechanically coupled with another motor. When back driven by another motor, the PMSM operates as a generator and produces EMF which is equivalent to motor back EMF under normal conditions of operation. The value of the back EMF magnitude can be mapped versus speed of rotation which immediately provides the value of the back EMF constant. When converted to SI units and transformed to the *dq* coordinate frame the value of the back EMF constant appeared to be 0.3983 V/(rad/sec). The calculated value is 0.4313 V/(rad/sec) which deviates from the experimental one by approximately 8%. Figure 5.7 shows the oscilloscope trace of the back EMF shape. The additional square wave trace in the scope picture is a most significant bit of the resolver-to-digital converter output used for resolver alignment.

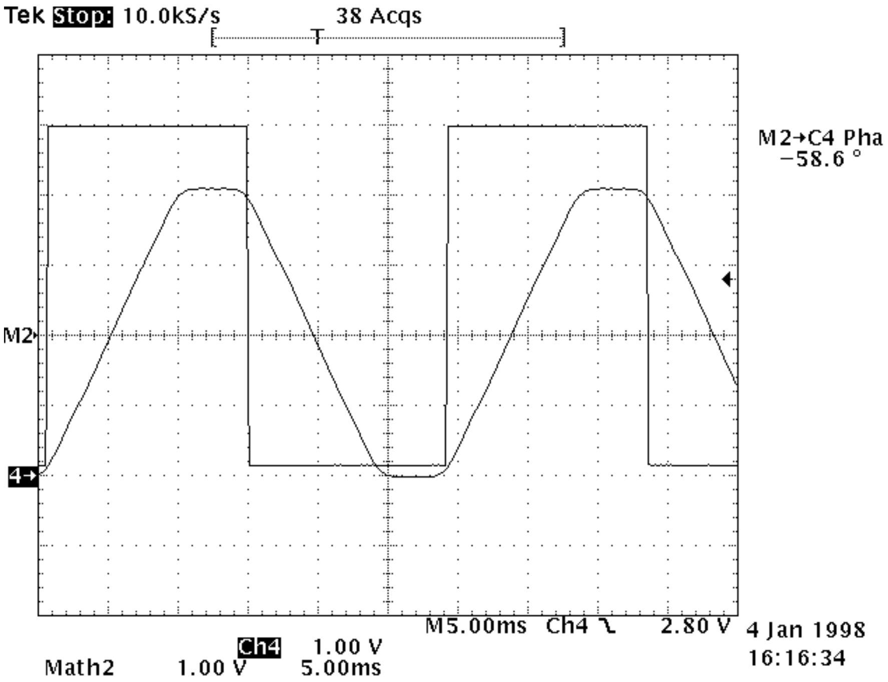

Figure 5.7: Trace of motor phase backEMF.

As seen from the plot, the back EMF shape is clearly trapezoidal. The reason for this can be both non-sinusoidal distribution of the stator windings and the geometry of the rotor magnets and the stator slots and pole shoes. The period of the back EMF is 360 electrical degrees. Knowing that the PMSM used in our experimental setup has two pole pairs, this will result in the deviation of the gap flux from sinusoidal with a frequency twice as high as the frequency of rotation. The motor thus will produce a cogging torque which magnitude will depend on the magnitude of this deviation. The frequency of the main harmonic of the cogging torque component will be equal to the doubled frequency of the main harmonic in the air gap flux. This becomes apparent considering that the air gap flux squared enters the equation for the cogging torque [39]. The effect of the cogging torque is expected to be seen in the experimental speed traces. The frequency of the main harmonic in motor speed variation will be the same as the frequency of the main harmonic in the cogging torque.

Since the overall drive system consists of PMSM, Hysteretic Dynamometer and Torquemeter, additional calculations of the drive inertia and viscous damping coefficient have been done. It is necessary to mention the fact that usually the manufacturer's inertia data is quite accurate since it is measured the following way. The rotor itself is suspended on the string (similar to a guitar string) which is considered to be weightless. The rotor is spun a given number of revolutions in one direction and then the same number of revolutions in the opposite direction. The inertia is then calculated as

$$J_m = \left(\frac{T_m}{T_{known}}\right)^2 J_{known} \tag{5.1}$$

where: J_{known} - inertia of the known cylinder; T_{known} - time it takes for such a cylinder to make a given number of revolutions; T_m - time it takes for the unknown rotor to make the same number of revolutions. The effect of rotor – stator interaction due to magnets is then eliminated. The inertia data for the motor, torquemeter and load cell are taken as correct. Unfortunately, the viscous damping coefficient was not given in the technical specifications for other components of the drive system and had to be determined. To do that, a set of spindown tests has been performed and the speed data has been approximated by exponential function. The spindown curve for speed is shown in Figure 5.8.

The curve fit with one exponential function resulted in time constant of 0.467 sec. Then the overal drive system viscous damping coefficient is equal to the ratio of overall drive inertia to mechanical time constant. The table below summarizes the manufacturer's data on mechanical parameters of all drive system components and totals the values for the system.

Parameter	Units	PMSM R43HENA	Torquemeter MCRT	Load Cell HD-705
Inertia	kg·m^2	0.0002	0.00025	0.00149
Viscous Damping	N·m·sec	0.00011		
Total Inertia	kg·m^2	0.002		
Total Viscous Damping	N·m·sec	0.0043		

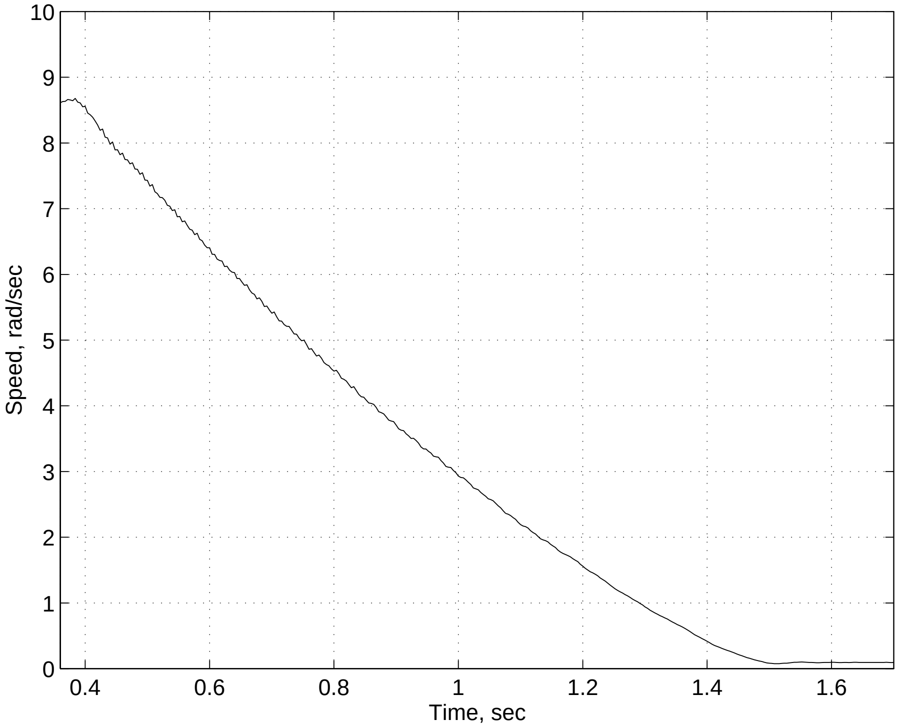

Figure 5.8: Spindown test results.

Chapter 6

Simulation and Experimental Results

The passivity based control algorithm presented has been verified through extensive simulations and laboratory experiments. The simulation results have been obtained using Matlab and Simulink numerical simulation software packages. The closed loop model consisting of PMSM (for generality, a “salient rotor” system of equations has been used) and passivity based controller has been created. Several numerical integration methods have been tried, including fixed-step Euler method and variable-step modified Rosenbrock method. All of them proved to satisfactory solve the system of simulated nonlinear equations within the tolerance requirements.

The experimental results have been collected using the experimental setup described in Chapter 5. The purpose of gathering experimental data was to

1. Obtain real-life proof of correctness of the designed control scheme.
2. Verify gain selection algorithm using eigenvalues placement technique.

3. Find practical limitations on achieving the ultimate system performance.

The simulation and experimental tests have been done on the sets of identical conditions, i.e., the same parameters have been used in mathematical modeling and experimental tests. This allows us to conveniently compare the results in each case to conclude on the closeness of these two test approaches, and to consider causes for their possible mismatch.

Three sets of tests, common to motor control practice, have been performed. First, we consider sudden changes in load torque in the wide range of loads. Second, we estimate the system's performance when speed command changes stepwise. Finally, a tracking of the sinusoidally changing speed command is investigated. The combination of all these results provides a solid ground for further analysis of the proposed passivity based control approach.

As to the selection of the incremental controller gains, the design parameter "γ" was set to zero throughout. This means that the d component of the electrical system was decoupled from the active q component, as is common in traditional, PI vector control of PMSM. The rest of gains were selected exactly according to (4.21). Due to structural imperfections of the motor, mainly to non-sinusoidal shape of the back EMF, the unmodeled torque ripple would be considerably amplified if we move eigenvalues of $A_{1,1}$ significantly further to the left than the "natural" ratio of $-\frac{R}{L}$. A considerably more aggressive selection of the incremental voltage input, v_e, results in practical performance deterioration due to ripple amplification. The effects of the time constant that we use in the incremental electrical subsystem are mostly offset by the fact that incremental currents are typically very small (several orders of magnitude smaller than the actual current levels.) This was the reason for selecting $-\rho = -\frac{R}{L} \approx -190$ in the simulations and experiments presented here.

Both simulations and experimental results will be represented by two plots: the speed response, and the "q" component of the applied voltage. (Recall that since here $\Delta L = 0$, the torque production is due to the "q" component of the stator current only.)

6.1 Sudden Change in Load Torque

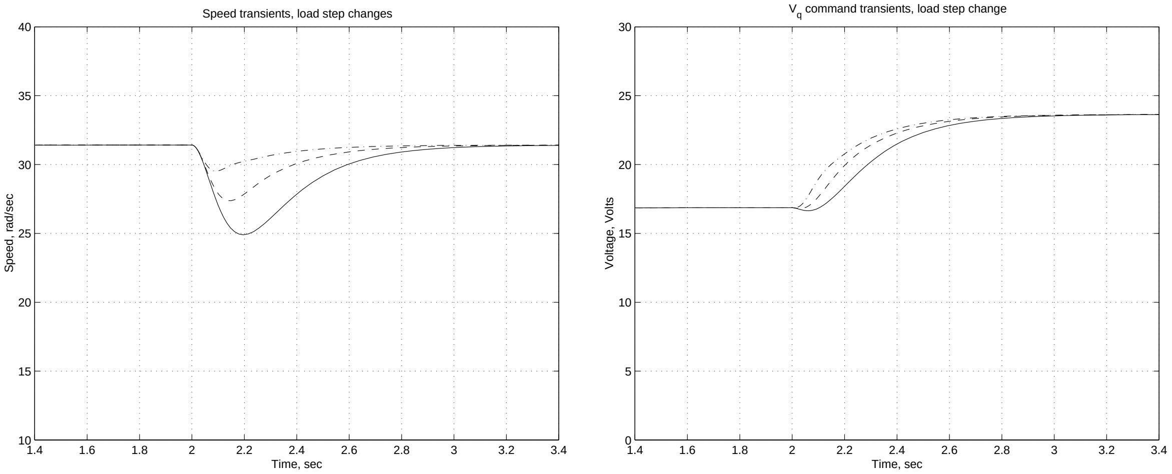

Figure 6.1: Simulations of speed transients (left) and required actuation V_q (right) following the load torque step change. Three eigenvalues of $A_{2,2}$ are placed at -20 (solid line), -20 and -20$\pm 20\jmath$ (dashed line), -20 and -20$\pm 40\jmath$ (dash-dotted line.)

The first sequence of simulations and experiments represents the response of the system to the sudden change in the load torque. The commanded speed is the constant

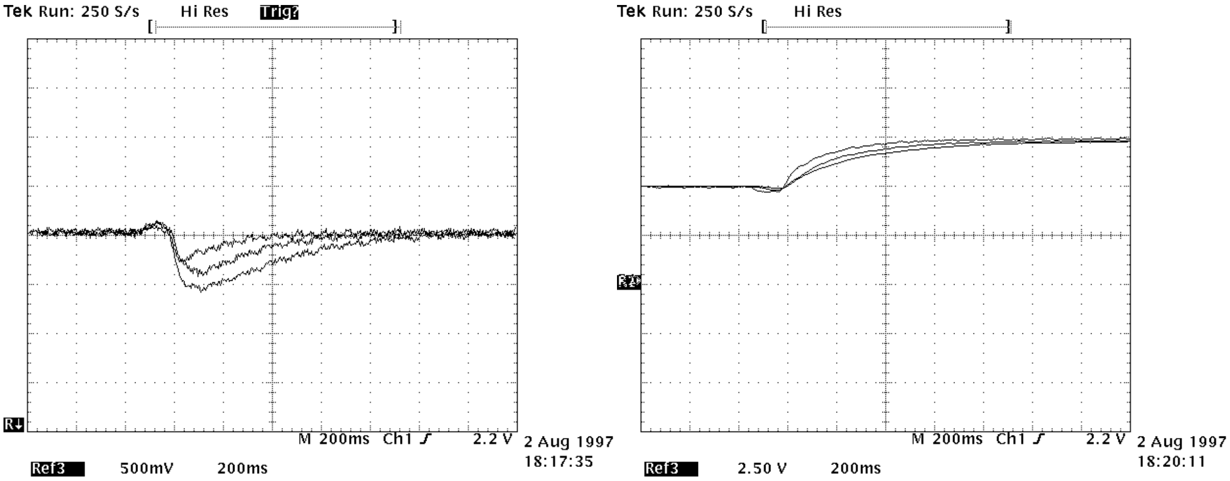

Figure 6.2: Speed transients (left) and required actuation V_q (right) following the load torque step change. Three eigenvalues of $A_{2,2}$ are placed at -20 (largest speed dip), -20 and -20±20$\jmath$, -20 and -20±40$\jmath$ (smallest speed dip.) Scaling: horizontal axis - 0.2 sec/division, vertical axis - 5 rad/sec/division (speed) and 8.45 volts/division (V_q).

$\omega_d = 31.4$ rad/sec (300 rpm). The step change in load torque has been set to 25% to 100% of its rated value. Several combinations of design parameters are tested. In the first set of tests, within this sequence, we set $\lambda = 0$ and consider several selections of eigenvalues for the block "$A_{2,2}$".

In Figures 6.1 and 6.2 we represent the results of three experiments. In the first the three eigenvalues are all placed at -20. Without changing the associated time constant, in the second and the third experiments imaginary components of $\pm 20\jmath$ and $\pm 40\jmath$ are added to two of the three eigenvalues, resulting in an increasingly faster speed response provided that the commanded voltage derivative is within the rate limitation of the power supply.

The next set of three experiments, depicted in Figures 6.3 and 6.4, presents the effects of shortening the time constant of $A_{2,2}$ on further shortening response and settling time, while concurrently showing an increased ripple due to widening the controller bandwidth. Here eigenvalue selections for $A_{2,2}$ are -20 and $-20 \pm 20\jmath$ (slowest response), -30 and $-30 \pm 30\jmath$ and -40 and $-40 \pm 40\jmath$ (fastest response.) This selection of control parameters is analogous to the "classical" 45° pole placement option [79]. In all these experiments the required applied voltage is very moderate; in particular, voltage transients are very smooth without spikes and overshoot.

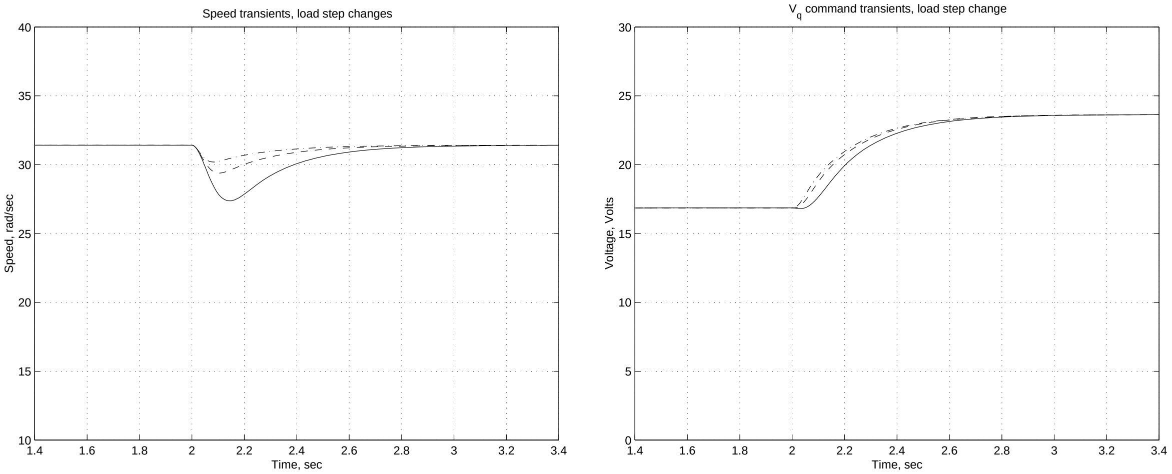

Figure 6.3: Simulations of speed transients (left) and required actuation V_q (right) following the load torque step change. Three eigenvalues of $A_{2,2}$ are placed at -20 and $-20\pm20\jmath$ (solid line), -30 and $-30\pm30\jmath$ (dashed line), -40 and $-40\pm40\jmath$ (dash-dotted line.)

As seen from the plots, simulation results are quite close to the experimental ones in terms of dynamic performance (speed dip and settling time parameters). The difference in the V_q voltage levels is caused by the specific ways of dq-to-abc conversion done in hardware. The simulation plots will therefore be omitted in the following analysis of the passivity based control performance of PMSM subject to sudden changes in the level of load torque.

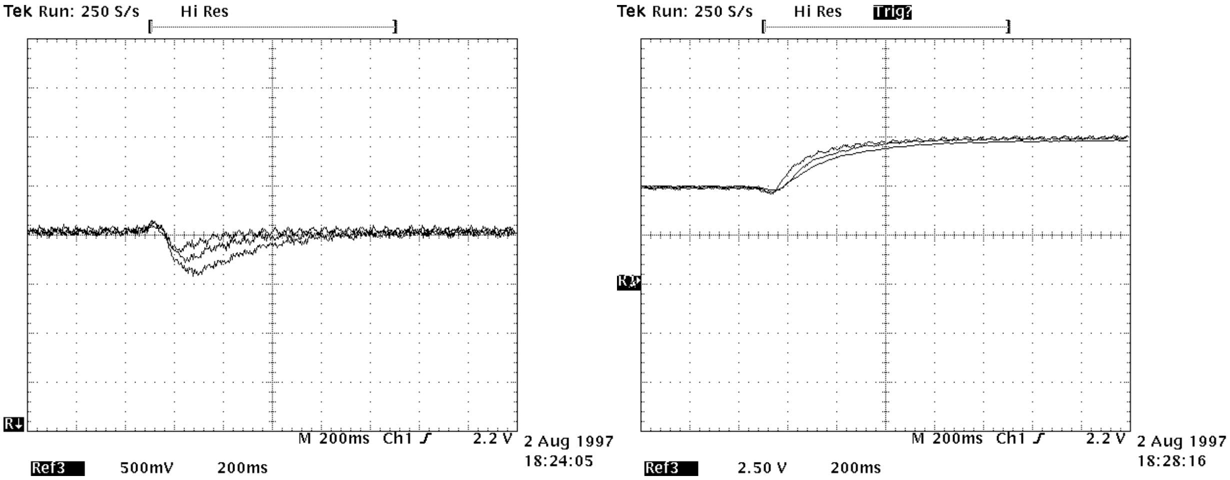

Figure 6.4: Speed transients (left) and required actuation V_q (right) following the load torque step change. Three eigenvalues of $A_{2,2}$ are placed at -20 and -20±20$\jmath$ (largest speed dip), -30 and -30±30$\jmath$, -40 and -40±40$\jmath$ (smallest speed dip.) Scaling: horizontal axis - 0.2 sec/division, vertical axis - 5 rad/sec/division (speed) and 8.45 volts/division (V_q).

The next set of experiments has been conducted with the goal of exploring the best achievable controller performance in the existing (and limited) conditions of the laboratory setup. The purpose was to show the fastest response to the sudden change in the load disturbance and simultaneously examine the shape of the commanded q axis voltage. The range of the load change was, as before, 25% to 100% of the rated motor torque value.

First, the λ parameter has been set to zero. This resulted in the electrical subsystem eigenvalues placed in the location $-\frac{R}{L}$. The "mechanical" eigenvalues were set at one location on the real axis assuring non-oscillatory response to the changes in disturbance. Several examples are shown in Figures 6.5 and 6.6.

As one can immediately see from the experimental plots, shifting the eigenvalues of

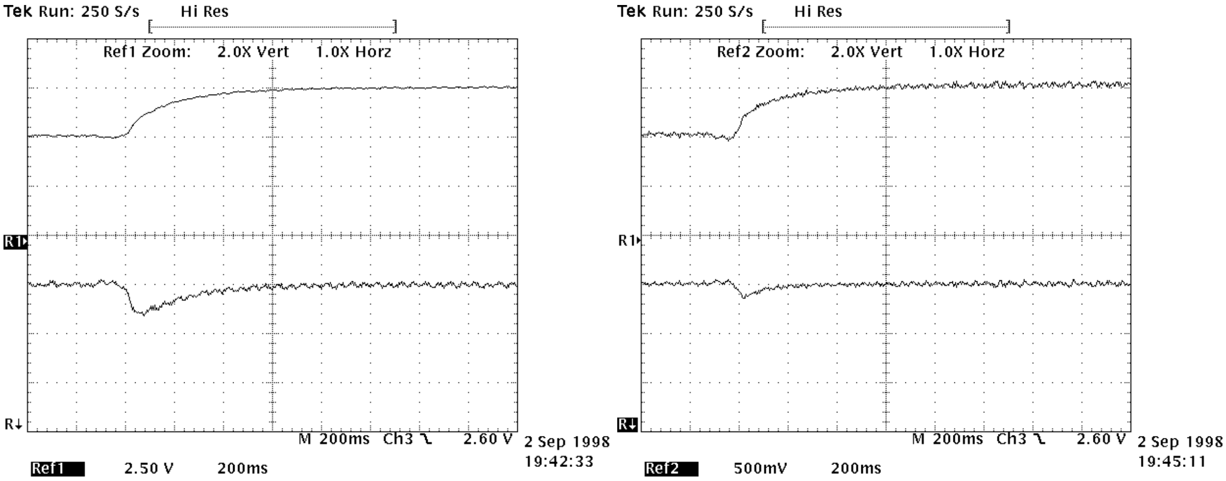

Figure 6.5: Required actuation V_q (upper) and speed transients (lower) following the load torque step change. Three eigenvalues of $A_{2,2}$ are placed at -40 (left) and -80 (right). Scaling: horizontal axis - 0.2 sec/division, vertical axis - 5 rad/sec/division (speed) and 8.45 volts/division (V_q).

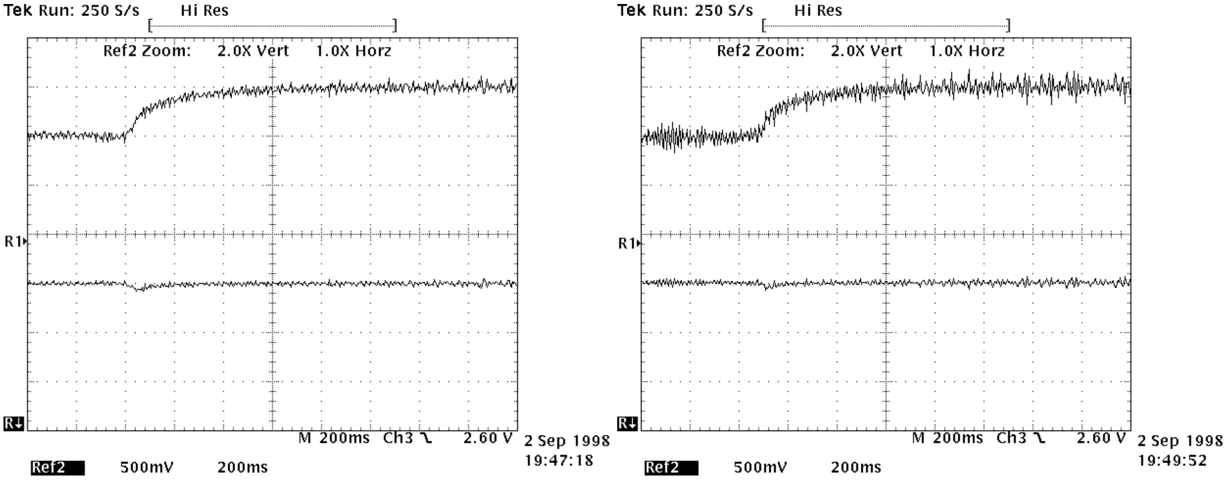

Figure 6.6: Required actuation V_q (upper) and speed transients (lower) following the load torque step change. Three eigenvalues of $A_{2,2}$ are placed at -120 (left) and -150 (right). Scaling: horizontal axis - 0.2 sec/division, vertical axis - 5 rad/sec/division (speed) and 8.45 volts/division (V_q).

$A_{2,2}$ towards negative infinity makes the controller response to the disturbance faster.

The speed dip in the last oscilloscope set of traces is hardly noticable. Theoretically, there is no limitations on how far away from zero one can place mechanical subsystem eigenvalues and based on their location calculate the gains τ, σ, and ζ of the controller. Practically, there is a serious restriction on the position of the eigenvalues of $A_{2,2}$: moving them towards $-\infty$ increases the value of ζ and, consequently, opens the bandwidth of the filter on the speed error. As a result, noise in speed measurements along with the speed variation due to motor imperfections enters the commanded voltage channel and becomes heavily amplified. The power supply required needs to have an output voltage slew rate significantly higher than the derivative of the commanded voltage which is not always possible to implement. Another practical limitation for obtaining very fast transient response is that the motor phase current should not exceed specifications based on the safe motor operation.

As an alternative to the simple "pushing" mechanical subsystem eigenvalues towards $-\infty$ we propose another approach in the design of passivity based controller gains. The idea is to facilitate the energy transfer between electrical (e_2) and mechanical (e_3, e_4, e_5) incremental states. The manipulation of the design parameter λ becomes a tool for providing this bidirectional energy exchange. Obviously, simple change in the value of λ does not place four eigenvalues of $\acute{A}$ as desired. One should use (4.21) to determine the controller gains based on the eigenvalues placement.

The results of such experiments are presented in Figures 6.7 and 6.8. The only case considered here is with all real eigenvalues, although other options with imaginary components of the selected eigenvalues locations are also possible. The value of ρ has

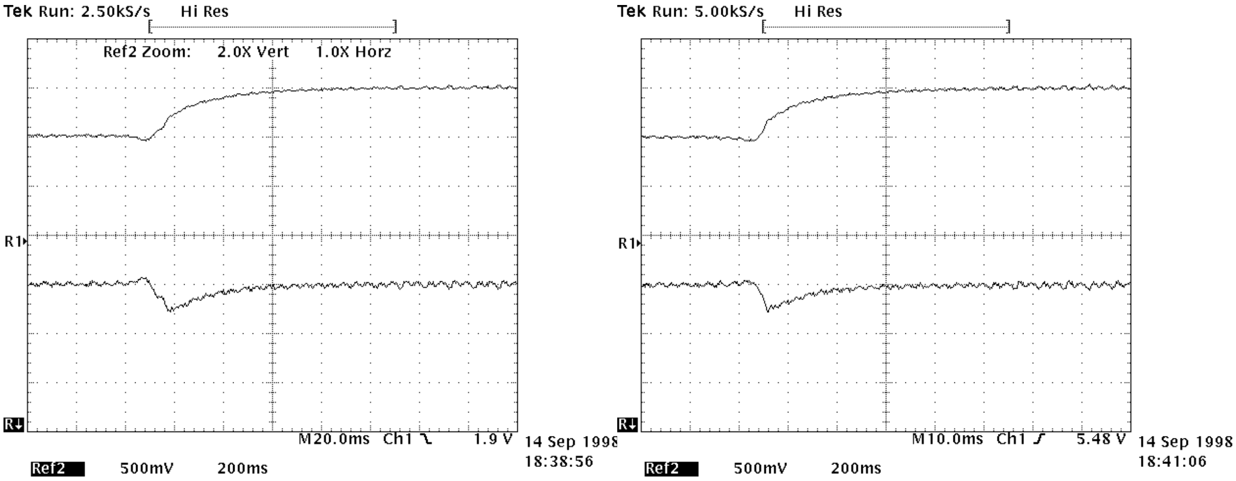

Figure 6.7: Required actuation V_q (upper) and speed transients (lower) following the load torque step change. Three eigenvalues of $\acute{A}$ are placed at -40; one is placed at -140 (left) and -120 (right). Scaling: horizontal axis - 0.2 sec/division, vertical axis - 5 rad/sec/division (speed) and 8.45 volts/division (V_q).

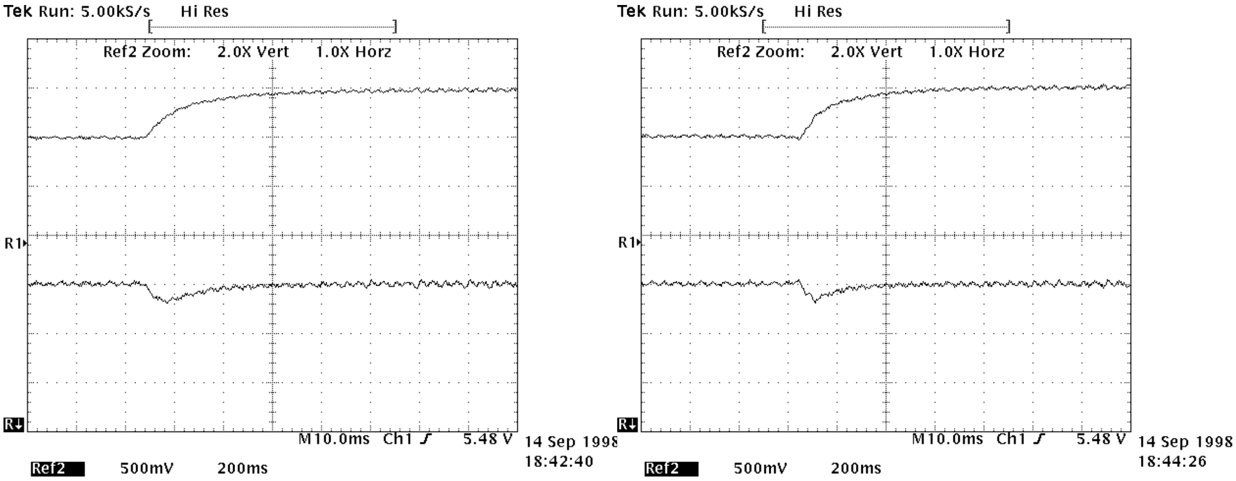

Figure 6.8: Required actuation V_q (upper) and speed transients (lower) following the load torque step change. Three eigenvalues of $\acute{A}$ are placed at -40; one is placed at -110 (left) and -90 (right). Scaling: horizontal axis - 0.2 sec/division, vertical axis - 5 rad/sec/division (speed) and 8.45 volts/division (V_q).

been chosen at $\frac{R}{L}$. Three out of four eigenvalues of $\acute{A}$ are placed at -40. The remaining fourth eigenvalue has been sequentially moved closer to those three eigenvalues away from its location at $-\rho$ for $\lambda = 0$. The experimental results are shown for the fourth eigenvalue's location at -140, -120, -110, and -90. This required the increase in the value of λ from 0 to ≈1.57. At the same time the value of ζ went down from ≈118 to ≈20. The smoothness of the speed response is improved. The required voltage command is not sensitive to the input noise in the speed error signal. Comparing to the analogous case with $\lambda = 0$ (Figure 6.5, left), note that the speed dip has been reduced by approximately 70%, while the settling time has shortened in less than half. By introducing the energy exchange channel described above, we effectively reduce the bandwidth of the electrical subsystem and improve the dynamic response of the system at the same time. This phenomenon can be contrasted with the common practice in standard nested loop control design, where the electrical loop needs to have a bandwidth by order of magnitude larger than the mechanical loop.

6.2 Sudden Change in Reference Speed

A second sequence of experiments concerns the response to a step change in the commanded speed, from $\omega_d = 15.7$ rad/sec (150 rpm) to $\omega_d = 25.1$ rad/sec (240 rpm). A constant load torque is maintained at 2.26 N·m (or 60% of the rated torque.)

The three sets of experiments essentially parallel those of the first sequence. In the first set, depicted in Figures 6.9 and 6.10, $\lambda = 0$ and eigenvalues of $A_{2,2}$ are placed all at -30 (slowest response), one at -30 and two at $-30 \pm 30\jmath$ (middle) and finally, one at -30 and two at $-30 \pm 60\jmath$ (fastest, and the most oscillatory, response). The

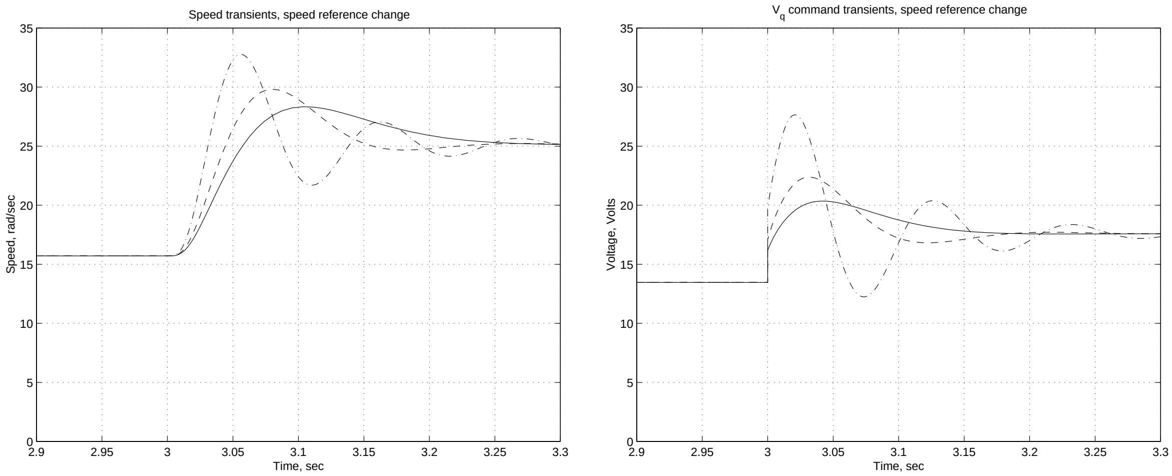

Figure 6.9: Simulations of speed transients (left) and required actuation V_q (right) following the commanded speed step change. Three eigenvalues of $A_{2,2}$ are placed at -30 (solid line), -30 and -30±30$\jmath$ (dashed line), -30 and -30±60$\jmath$ (dash-dotted line.)

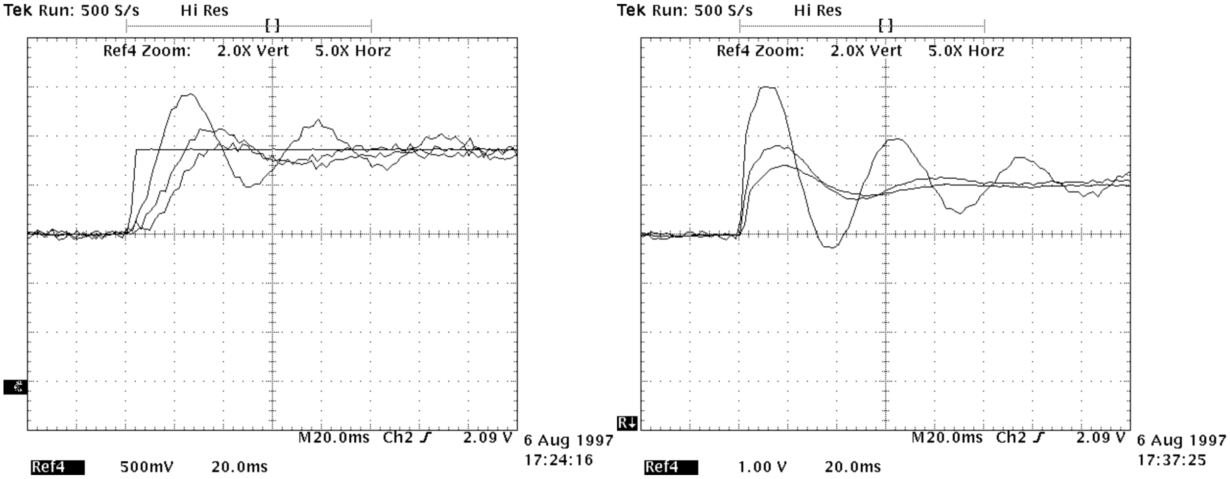

Figure 6.10: Speed transients (left) and required actuation V_q (right) following the commanded speed step change. Three eigenvalues of $A_{2,2}$ are placed at -30 (least oscillatory response), -30 and -30±30$\jmath$, -30 and -30±60$\jmath$ (most oscillatory response.) Scaling: horizontal axis - 0.02 sec/division, vertical axis - 5 rad/sec/division (speed) and 3.38 volts/division (V_q).

simulations results and oscilloscope traces demonstrate the effects of increasing the imaginary part – and the associated bandwidth – on faster but more oscillatory response and required voltages. It is seen that the traditional 45° pole placement results in an effective compromise. One important remark regarding the difference between the numerical simulations and experimental plots is that the latter show more oscillatory response. This can be explained completely by several features of the experimental setup. First, the sampling frequency was limited due to the existing digital implementation through the dSPACE DSP board and set to 2 kHz. Second, the only available numerical integration algorithm at this sampling rate was the fixed step Euler method which lacks accuracy, especially at low sampling rates.

The following three experiments, shown in Figures 6.11 and 6.12, demonstrate the effect of shortening the time constant of $A_{2,2}$. Again $\lambda = 0$ and the three selections are of eigenvalues at -20 and $-20 \pm 20\jmath$ (slowest response), -40 and $-40 \pm 40\jmath$ (middle) and -60 and $-60 \pm 60\jmath$ (fastest response). We observe the tradeoff of faster response vs. overshoot and increased voltage demand. The faster time constant requires significantly more oscillatory control voltages that is typically not acceptable.

The last set of experiments in this sequence concerns the effects of the design parameter λ. First, we consider the closed-loop response when the selection of controller parameters places three eigenvalues of $\acute{A}$ at -40 and the fourth one at ≈ -190 so that $\lambda = 0$. The experimental results are presented in Figure 6.13, left. Then we recalculate the controller gains to place the fourth eigenvalue at -90 keeping the rest of them at the same location (-40). This results in increase of λ from 0 to ≈ 1.57 (Figure 6.13, right).

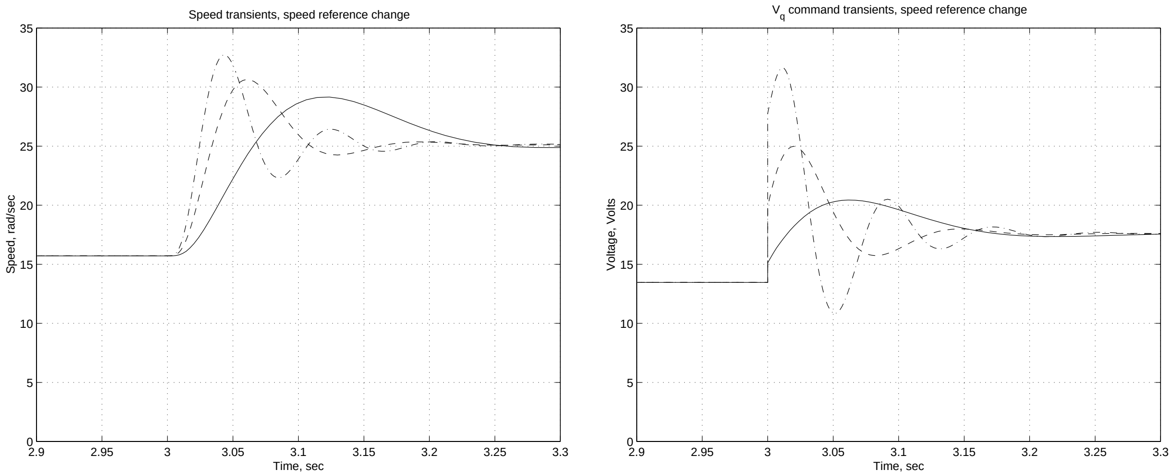

Figure 6.11: Simulations of speed transients (left) and required actuation V_q (right) following the commanded speed step change. Three eigenvalues of $A_{2,2}$ are placed at -20 and -20±20$\jmath$ (solid line), -40 and -40±40$\jmath$ (dashed line), -60 and -60±60$\jmath$ (dash-dotted line.)

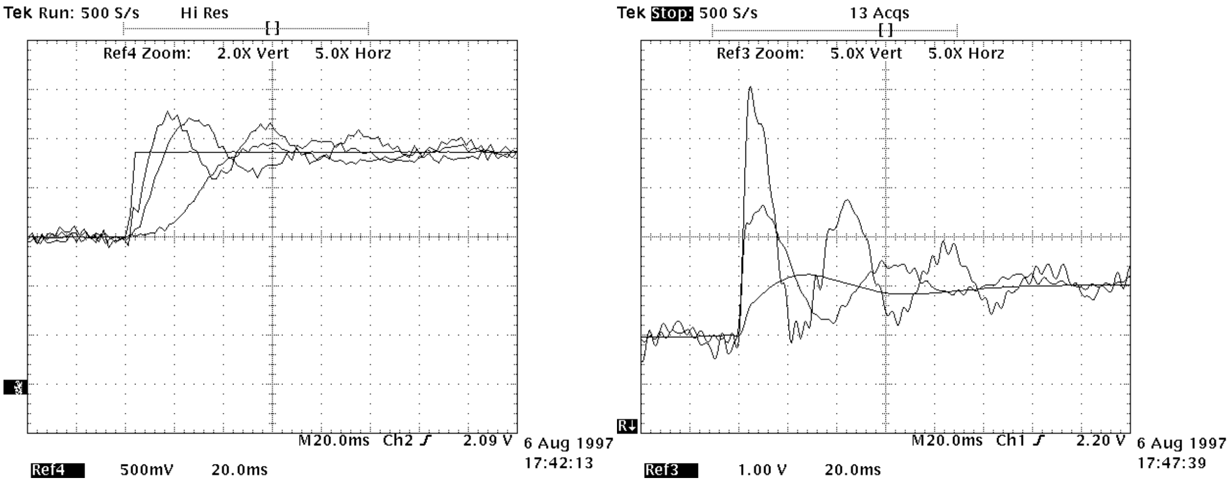

Figure 6.12: Speed transients (left) and required actuation V_q (right) following the commanded speed step change. Three eigenvalues of $A_{2,2}$ are placed at -20 and -20±20$\jmath$ (least oscillatory response), -40 and -40±40$\jmath$, -60 and -60±60$\jmath$ (most oscillatory response.) Scaling: horizontal axis - 0.02 sec/division, vertical axis - 5 rad/sec/division (speed) and 3.38 volts/division (V_q).

Again we see the significant improvement in response time when we manipulate λ; both the rise time and the settling time became half shorter, while the value of the

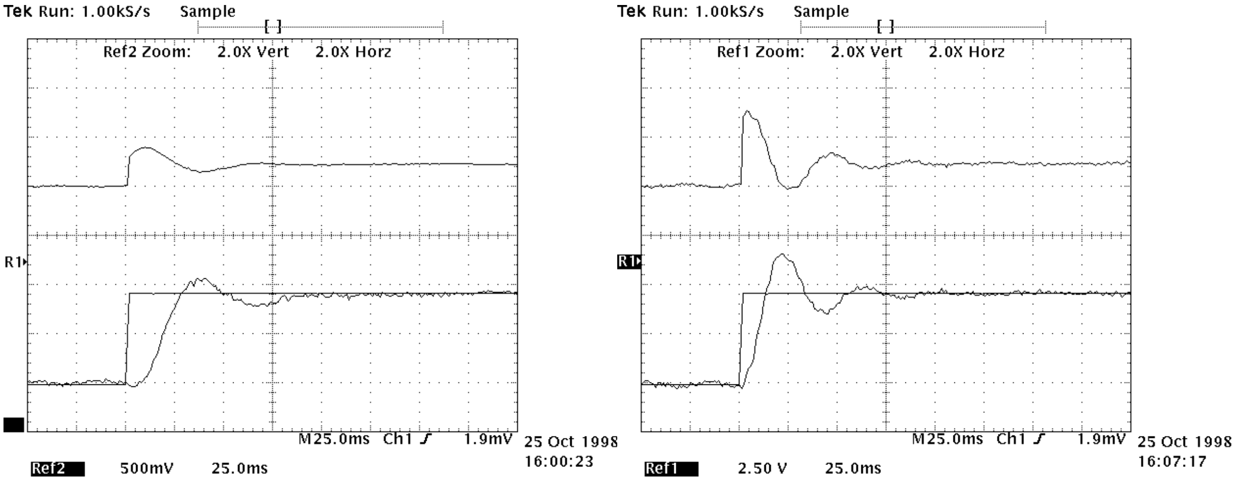

Figure 6.13: Required actuation V_q (upper) and speed transients (lower) following the commanded speed step change, variation of λ. λ is chosen such that the forth eigenvalue is placed at ≈ -190 with no λ effect (left plot) and at -90 (right plot). Scaling: horizontal axis - 0.025 sec/division, vertical axis - 5 rad/sec/division (speed) and 8.45 volts/division (V_q).

speed overshoot is still acceptable.

6.3 Periodic Reference Speed

The third set of experiments (Figure 6.14) demonstrates tracking of a sinusoidal reference input. The commanded speed oscillates sinusoidally between 15.7 rad/sec (150 rpm) and 25.1 rad/sec (240 rpm), with frequencies of 20 Hz and 40 Hz, represented in the left and right oscilloscope traces, respectively. In these experiments we use information on both ω_d and its first two derivatives in a reference command, as discussed earlier. The simulations show the perfect tracking of sinusoidal speed command for (theoretically) any frequency of the commanded speed. Practical limitation is the maximum slew rate of the commanded voltage, and the maximum transient value of the phase current. The latter becomes more important at higher frequencies of the reference speed. Both experiments show that the high performance operation of the standard PMSM can be achieved with the proposed passivity-based controller scheme. The delay in speed response in experimental results is about 1.7 ms which is due to the digital implementation of the control algorithm, and to the drift of motor parameters during operation. As expected, when the derivatives $\dot{\omega}_d$ and $\ddot{\omega}_d$ are assumed to be unknown and are replaced by zero in (4.4) and (4.5), the result (not shown) is a more delayed response; that delay is proportional to the frequency of the commanded speed reference.

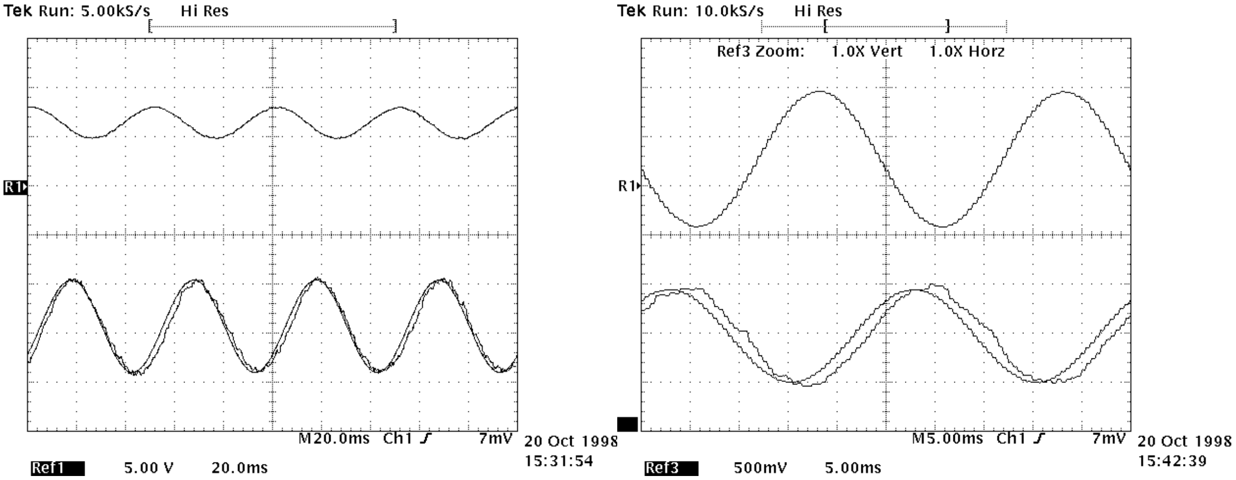

Figure 6.14: Tracking of sinusoidally varying commanded speed: required actuation V_q (upper traces) and commanded and actual speeds (lower traces). Frequency of commanded speed is 20 Hz (left plot), and 40 Hz (right plot). Scaling: horizontal axis - 20 (left), and 5 (right) millisec/division, vertical axis - 5 rad/sec/division (speed) and 16.9 volts/division (V_q).

Chapter 7

Passivity Based Sensorless Control of PMSM

7.1 Introduction

As was mentioned earlier, one of the possible extensions of the passivity based approach in the control of PMSM will be a position sensorless operation of the motor drive. The majority of currently used motor drive schemes utilizes some sort of position measurements. As was described earlier, this approach would require to use additional electromechanical devices that increase an overall system cost and reduce its robustness. The alternative in this case would be to create an estimate of the motor position in real time and to use this estimate in the control scheme. The measurements of the motor currents and phase voltages become the input parameters for the position and speed estimator.

Some known techniques include Kalman filtering, state observers, direct calculations and others [107, 83, 90, 68]. The solution analyzied in this chapter is based on the passivity arguments in the state observer design with the purpose of minimizing a quadratic incremental energy function of the total electrical and mechanical error. Developments are focused on the non-salient rotor case, where $\Delta L = L_d - L_q = 0$.

7.2 $\alpha\beta$ and dq Models of PMSM

The following is the stationary $(\alpha\beta)$ frame counterpart of the dq model (4.1)

$$\begin{aligned} \tfrac{d}{dt} i_{\alpha\beta} &= -\tfrac{R}{L} i_{\alpha\beta} - \tfrac{MI}{L}\omega e^{J\theta} \begin{bmatrix} 0 \\ 1 \end{bmatrix} + \tfrac{1}{L} v_{\alpha\beta} \\ \tfrac{d}{dt}\omega &= \tfrac{MI}{H} [0 \quad 1]\, e^{-J\theta} i_{\alpha\beta} - \tfrac{B}{H}\omega - \tfrac{1}{H}\tau_L \\ \tfrac{d}{dt}\theta &= \omega \end{aligned} \tag{7.1}$$

where: $i_{\alpha\beta}$ and $v_{\alpha\beta}$ are currents and voltages in $\alpha\beta$ frame, respectively; θ is the angular position in electrical degrees; $J = \begin{bmatrix} 0 & -1 \\ 1 & 0 \end{bmatrix}$. We also assume a symmetrical machine with equal resistances R and inductances L in all phases. As before, back-emf constant is defined as MI and the mechanical subsystem parameters are ω for speed, H for inertia, B for viscous friction coefficient and τ_L for load torque.

This model is related to (4.1) by Blondel-Park transformation

$$i_{d-q} = e^{-J\theta} i_{\alpha\beta}, \qquad v_{d-q} = e^{-J\theta} v_{\alpha\beta} \tag{7.2}$$

and the $d-q$ frame representation of the PMSM:

$$\begin{aligned}
\tfrac{d}{dt}i_d &= -\tfrac{R}{L}i_d + \omega i_q + \tfrac{1}{L}v_d \\
\tfrac{d}{dt}i_q &= -\tfrac{R}{L}i_q - \omega i_d - \tfrac{MI}{L}\omega + \tfrac{1}{L}v_q \\
\tfrac{d}{dt}\omega &= \tfrac{MI}{H}i_q - \tfrac{B}{H}\omega - \tfrac{1}{H}\tau_L \\
\tfrac{d}{dt}\theta &= \omega
\end{aligned} \tag{7.3}$$

While design will be based on the dq model (4.1), it is observed that actual current measurements are available only in the stationary frame. Thus, instead of actual dq measurements we will use the approximate values

$$\breve{i}_{d-q} = e^{-J\hat{\theta}} i_{\alpha\beta}, \quad \breve{v}_{d-q} = e^{-J\hat{\theta}} v_{\alpha\beta} \tag{7.4}$$

where $\hat{\theta}$ is an estimated angular position.

7.3 Observer Design

We denote the estimated states by a hat. Based on (4.1) and (7.4), we introduce an observer structure of the form

$$\begin{aligned}
\tfrac{d}{dt}\hat{i}_d &= -\tfrac{R}{L}\hat{i}_d + \hat{\omega}\hat{i}_q + \tfrac{1}{L}\breve{v}_d - f_d \\
\tfrac{d}{dt}\hat{i}_q &= -\tfrac{R}{L}\hat{i}_q - \hat{\omega}\hat{i}_d - \tfrac{MI}{L}\hat{\omega} + \tfrac{1}{L}\breve{v}_q - f_q \\
\tfrac{d}{dt}\hat{\omega} &= \tfrac{MI}{H}\hat{i}_q - \tfrac{B}{H}\hat{\omega} - \tfrac{1}{H}\hat{\tau}_L - f_\omega \\
\tfrac{d}{dt}\hat{\theta} &= \hat{\omega} - f_\theta \\
\tfrac{d}{dt}\hat{\tau}_L &= -f_\tau
\end{aligned} \tag{7.5}$$

where the correction vector $F = [f_d \;\; f_q \;\; f_\omega \;\; f_\theta \;\; f_\tau]^T$ has yet to be determined.

The incremental currents are defined as

$$\begin{aligned} \Delta i_d &= \breve{i}_d - \hat{i}_d \\ \Delta i_q &= \breve{i}_q - \hat{i}_q \end{aligned} \tag{7.6}$$

The rest of the incremental states are defined as the difference between the actual and estimated states. We denote them by Δ.

Ignoring higher order terms, the matrix exponential can be approximated by two linear components of the Taylor series expansion:

$$e^{J\theta} = e^{J(\hat{\theta}+\Delta\theta)} \approx e^{J\hat{\theta}}(I + J\Delta\theta) \tag{7.7}$$

where $\Delta\theta = \theta - \hat{\theta}$ and where I is the 2-by-2 identity matrix. Using (7.4) $e^{J\hat{\theta}}\breve{i}_{d-q} = i_{\alpha\beta}$ and $\dot{i}_{\alpha\beta} = e^{J\hat{\theta}}J\dot{\hat{\theta}}\breve{i}_{d-q} + e^{J\hat{\theta}}\dot{\breve{i}}_{d-q}$. Using (7.1) and (7.4) the trajectory of $\dot{\breve{i}}_{d-q}$ satisfies

$$\dot{\breve{i}}_{d-q} = -\frac{R}{L}\breve{i}_{d-q} - \frac{MI}{L}\omega\begin{bmatrix}0\\1\end{bmatrix} - \frac{MI}{L}\omega J\Delta\theta\begin{bmatrix}0\\1\end{bmatrix} + \frac{1}{L}e^{-J\hat{\theta}}v_{\alpha\beta} - J\breve{i}_{d-q}\hat{\omega} + J\breve{i}_{d-q}f_\theta \tag{7.8}$$

The dynamics of incremental states of the electrical subsystem is thus governed by

$$\begin{aligned} \Delta\dot{i}_d &= -\tfrac{R}{L}\Delta i_d + \tfrac{MI}{L}\omega\Delta\theta + \hat{\omega}\Delta i_q + f_d' \\ \Delta\dot{i}_q &= -\tfrac{R}{L}\Delta i_q - \tfrac{MI}{L}\Delta\omega - \hat{\omega}\Delta i_d + f_q' \end{aligned} \tag{7.9}$$

where

$$\begin{aligned} f_d' &= -\breve{i}_q f_\theta + f_d \\ f_q' &= \breve{i}_d f_\theta + f_q \end{aligned} \tag{7.10}$$

The incremental states of the mechanical subsystem satisfy the differential equations

$$\begin{aligned}
\Delta\dot{\omega} &= \tfrac{MI}{H}\Delta i_q + \tfrac{MI}{H}(i_q - \check{i}_q) - \tfrac{B}{H}\Delta\omega - \tfrac{1}{H}\Delta\tau_L + f_\omega \\
\Delta\dot{\theta} &= \Delta\omega + f_\theta \\
\Delta\dot{\tau}_L &= f_\tau
\end{aligned} \tag{7.11}$$

Using (7.7), the expression for $\Delta\dot{\omega}$ can be approximated as

$$\Delta\dot{\omega} = \frac{MI}{H}\Delta i_q - \frac{MI}{H}\check{i}_d\Delta\theta - \frac{B}{H}\Delta\omega - \frac{1}{H}\Delta\tau_L + f_\omega \tag{7.12}$$

It will be convenient to use the notion of the "total" load torque

$$T_L = B\omega + \tau_L \tag{7.13}$$

and its estimated version

$$\hat{T}_L = B\hat{\omega} + \hat{\tau}_L \tag{7.14}$$

In these terms the motor speed satisfies

$$\frac{d}{dt}\omega = \frac{MI}{H}i_q - \frac{1}{H}T_L \tag{7.15}$$

and, when τ_L is slowly varying, the derivatives of T_L and $\hat{T}_L$ are

$$\begin{aligned}
\tfrac{d}{dt}T_L &= B\tfrac{d}{dt}\omega + \tfrac{d}{dt}\tau_L \approx \tfrac{B\,MI}{H}i_q - \tfrac{B}{H}T_L \\
\tfrac{d}{dt}\hat{T}_L &= B\tfrac{d}{dt}\hat{\omega} + \tfrac{d}{dt}\hat{\tau}_L = \tfrac{B\,MI}{H}\hat{i}_q - B\tfrac{B}{H}\hat{\omega} - \tfrac{B}{H}\hat{\tau}_L - Bf_\omega - f_\tau
\end{aligned} \tag{7.16}$$

Here we neglect the derivatives of the static torque τ_L and $\hat{\tau}_L$.

The incremental states $\Delta\dot{\omega}$ and $\Delta\dot{T}_L$

$$\begin{aligned}
\Delta\dot{\omega} &= \tfrac{MI}{H}\Delta i_q - \tfrac{MI}{H}\check{i}_d\Delta\theta - \tfrac{1}{H}\Delta T_L + f_\omega \\
\Delta\dot{T}_L &= \tfrac{B\,MI}{H}\Delta i_q - \tfrac{B\,MI}{H}\check{i}_d\Delta\theta - \tfrac{B}{H}\Delta T_L + f_T
\end{aligned} \tag{7.17}$$

where

$$f_T = Bf_\omega + f_\tau \tag{7.18}$$

Using f_T notation we can rewrite (7.16) as

$$\frac{d}{dt}\hat{T}_L = \frac{B\,MI}{H}\hat{i}_q - \frac{B}{H}\hat{T}_L - f_T \tag{7.19}$$

The overal closed loop incremental system representation is

$$\Delta\dot{x} = \mathbf{A}\Delta x + \mathbf{F} \tag{7.20}$$

where: $\Delta x = [\Delta i_d \;\; \Delta i_q \;\; \Delta\omega \;\; \Delta\theta \;\; \Delta T_L]^T$ and $\mathbf{F} = \left[f'_d \;\; f'_q \;\; f_\omega \;\; f_\theta \;\; f_T\right]^T$. We will further neglect terms proportional to $\breve{i}_d\Delta\theta$ in (7.17) since the direct axis current component does not enter the dynamics of actual speed, and, therefore, the impact of its approximate value will be considered as a small perturbation. Then,

$$\mathbf{A} = \begin{bmatrix} -\frac{R}{L} & \hat{\omega} & 0 & \frac{\omega\,MI}{L} & 0 \\ -\hat{\omega} & -\frac{R}{L} & -\frac{MI}{L} & 0 & 0 \\ 0 & \frac{MI}{H} & 0 & 0 & -\frac{1}{H} \\ 0 & 0 & 1 & 0 & 0 \\ 0 & \frac{B\,MI}{H} & 0 & 0 & -\frac{B}{H} \end{bmatrix} \tag{7.21}$$

In order to determine the vector $\mathbf{F}$ we introduce the change of basis $\mathbf{T}$ such that the resultant incremental closed loop system matrix $\mathbf{A}_{cl}$ has negative diagonal elements governing energy dissipation process and off-diagonal elements creating a skew symmetric structure to facilitate energy transfer between states. It is important to mention that since we have a direct access to incremental currents only, the lower

3-by-3 block of the $\mathbf{A}_{cl}$ must be "shaped" to the desirable form by means of the transformation matrix only. In addition to that, we would like to keep the same incremental electrical states (Δi_d and Δi_q) so that we can easily manipulate the elements of the lower left block of $\mathbf{A}$.

One possible change of basis satisfying our requirements is given as:

$$\mathbf{T} = \begin{bmatrix} 1 & 0 & 0 & 0 & 0 \\ 0 & 1 & 0 & 0 & 0 \\ -\kappa & \kappa\hat{\omega} & 1 & 1 & 0 \\ \kappa & \kappa\hat{\omega} & 1 & -1 & 0 \\ 0 & \nu & 0 & 0 & -2\frac{L}{\nu MIH} \end{bmatrix} \tag{7.22}$$

Here κ and ν are the design parameters that need to be determined. Having selected a change of basis $\mathbf{T}$, we define a new state vector ξ as $\mathbf{T}\,[\Delta i_d \;\; \Delta i_q \;\; \Delta\omega \;\; \Delta\theta \;\; \Delta T_L]^T$. The new state satisfies

$$\dot{\xi} = \mathbf{A}_{new}\xi + \zeta \tag{7.23}$$

where $\mathbf{A}_{new} = (\mathbf{TA} + \dot{\mathbf{T}})\mathbf{T^{-1}}$ and the new correction term is $\zeta = \mathbf{TF}$. The correction terms ζ is calculated to make the off-diagonal elements of $\mathbf{A}_{cl}$ skew symmetric, i.e., $\mathbf{A}_{cl}(i,j) = -\mathbf{A}_{cl}(j,i),\;\; i \neq j,\;\; \overline{(i \geq 3) \oplus (j \geq 3)}$. This forcing term will be of the form

$$\zeta = [\mathbf{Q}_{5\times 2} \quad \mathbf{0}_{5\times 3}]\,\xi \tag{7.24}$$

where $\mathbf{Q}$ is given below. The closed loop system is then

$$\dot{\xi} = (\mathbf{A}_{new} + [\mathbf{Q}_{5\times 2} \quad \mathbf{0}_{5\times 3}])\,\xi \tag{7.25}$$

The actual correction then will be obtained as

$$\mathbf{F} = \mathbf{T}^{-1} \left[\mathbf{Q}_{5\times 2} \quad \mathbf{0}_{5\times 3} \right] \mathbf{T}\, \Delta x \tag{7.26}$$

Based on (7.22), the matrix $\mathbf{A}_{new} = [\mathbf{A}_{new1}, \quad \mathbf{A}_{new2}]$ is built of the following two blocks

$$\begin{aligned}
\mathbf{A}_{new_1} &= \begin{bmatrix}
-\frac{R}{L} + \frac{\kappa\,\hat{\omega}\ MI}{L} & \hat{\omega} \\
-\hat{\omega} & -\frac{R}{L} + \frac{\kappa\,\hat{\omega}\ MI}{L} \\
\frac{\kappa\,R}{L} - \kappa\,\hat{\omega}^2 - \frac{\kappa^2\hat{\omega}\ MI}{L} & \frac{\kappa^2\hat{\omega}^2\,MI}{L} + \left(-2\,\kappa - \frac{\kappa\,R}{L}\right)\hat{\omega} - \frac{1}{2}\,\frac{\nu^2\,MI}{L} + \frac{MI}{H} + \kappa\,\dot{\hat{\omega}} \\
-\frac{\kappa\,R}{L} - \kappa\,\hat{\omega}^2 + \frac{\kappa^2\hat{\omega}\ MI}{L} & \frac{\kappa^2\hat{\omega}^2\,MI}{L} + \left(2\,\kappa - \frac{\kappa\,R}{L}\right)\hat{\omega} - \frac{1}{2}\,\frac{\nu^2\,MI}{L} + \frac{MI}{H} + \kappa\,\dot{\hat{\omega}} \\
-\nu\,\hat{\omega} & -\frac{\nu\,R}{L} - 2\,\frac{LB}{H^2\,\nu} + \frac{\nu\ MI\kappa\,\hat{\omega}}{L} + \frac{\nu\,B}{H}
\end{bmatrix} \\
\mathbf{A}_{new_2} &= \begin{bmatrix}
\frac{1}{2}\,\frac{\hat{\omega}\ MI}{L} & -\frac{1}{2}\,\frac{\hat{\omega}\ MI}{L} & 0 \\
-\frac{1}{2}\,\frac{MI}{L} & -\frac{1}{2}\,\frac{MI}{L} & 0 \\
\frac{1}{2} - \frac{\kappa\,\hat{\omega}\ MI}{L} & \frac{1}{2} & \frac{1}{2}\,\frac{\nu\ MI}{L} \\
-\frac{1}{2} & -\frac{1}{2} - \frac{\kappa\,\hat{\omega}\ MI}{L} & \frac{1}{2}\,\frac{\nu\ MI}{L} \\
-\frac{1}{2}\,\frac{\nu\ MI}{L} & -\frac{1}{2}\,\frac{\nu\ MI}{L} & -\frac{B}{H}
\end{bmatrix}
\end{aligned} \tag{7.27}$$

The correction matrix $\mathbf{Q}$ is selected as

$$\mathbf{Q} = \begin{bmatrix}
\frac{R}{L} - \frac{\kappa\,\hat{\omega}\ MI}{L} - \rho & -\hat{\omega} \\
\hat{\omega} & \frac{R}{L} - \frac{\kappa\,\hat{\omega}\ MI}{L} - \rho \\
-\frac{\kappa\,R}{L} + \kappa\,\hat{\omega}^2 + \frac{\kappa^2\hat{\omega}\ MI}{L} - \frac{1}{2}\,\frac{\hat{\omega}\ MI}{L} & -\frac{\kappa^2\hat{\omega}^2\,MI}{L} - \left(-2\,\kappa - \frac{\kappa\,R}{L}\right)\hat{\omega} + \frac{1}{2}\,\frac{\nu^2\,MI}{L} - \frac{MI}{H} - \kappa\,\dot{\hat{\omega}} + \frac{1}{2}\,\frac{MI}{L} \\
\frac{\kappa\,R}{L} + \kappa\,\hat{\omega}^2 - \frac{\kappa^2\hat{\omega}\ MI}{L} + \frac{1}{2}\,\frac{\hat{\omega}\ MI}{L} & -\frac{\kappa^2\hat{\omega}^2\,MI}{L} - \left(2\,\kappa - \frac{\kappa\,R}{L}\right)\hat{\omega} + \frac{1}{2}\,\frac{\nu^2\,MI}{L} - \frac{MI}{H} - \kappa\,\dot{\hat{\omega}} + \frac{1}{2}\,\frac{MI}{L} \\
\nu\,\hat{\omega} & \frac{\nu\,R}{L} + 2\,\frac{LB}{H^2\,\nu} - \frac{\nu\ MI\kappa\,\hat{\omega}}{L} - \frac{\nu\,B}{H}
\end{bmatrix} \tag{7.28}$$

In these terms, the closed loop state matrix is of the "negative diagonal + skew symmetric" form:

$$\mathbf{A}_{cl} = \begin{bmatrix} -\rho & 0 & \frac{1}{2}\frac{\hat{\omega}\,MI}{L} & -\frac{1}{2}\frac{\hat{\omega}\,MI}{L} & 0 \\ 0 & -\rho & -\frac{1}{2}\frac{MI}{L} & -\frac{1}{2}\frac{MI}{L} & 0 \\ -\frac{1}{2}\frac{\hat{\omega}\,MI}{L} & \frac{1}{2}\frac{MI}{L} & \frac{1}{2}-\frac{\kappa\,\hat{\omega}\,MI}{L} & \frac{1}{2} & \frac{1}{2}\frac{\nu\,MI}{L} \\ \frac{1}{2}\frac{\hat{\omega}\,MI}{L} & \frac{1}{2}\frac{MI}{L} & -\frac{1}{2} & -\frac{1}{2}-\frac{\kappa\,\hat{\omega}\,MI}{L} & \frac{1}{2}\frac{\nu\,MI}{L} \\ 0 & 0 & -\frac{1}{2}\frac{\nu\,MI}{L} & -\frac{1}{2}\frac{\nu\,MI}{L} & -\frac{B}{H} \end{bmatrix} \tag{7.29}$$

Finally, the actual correction vector $\mathbf{F}$ is obtained from (7.26)

$$\mathbf{F} = \begin{bmatrix} \frac{R}{L}-\frac{\kappa\,\hat{\omega}\,MI}{L}-\rho & -\hat{\omega} & 0 & 0 & 0 \\ \hat{\omega} & \frac{R}{L}-\frac{\kappa\,\hat{\omega}\,MI}{L}-\rho & 0 & 0 & 0 \\ 0 & \kappa\,\hat{\omega}\,\rho+\frac{1}{2}\frac{\nu^2\,MI}{L}-\frac{MI}{H}-\kappa\,\dot{\hat{\omega}}+\frac{1}{2}\frac{MI}{L} & 0 & 0 & 0 \\ -\kappa\,\rho-\frac{1}{2}\frac{\hat{\omega}\,MI}{L} & \kappa\,\hat{\omega} & 0 & 0 & 0 \\ 0 & -\frac{1}{2}\frac{\nu^2\,MI\,H\rho}{L}-\frac{B\,MI}{H}+\frac{1}{2}\frac{\nu^2\,MI\,B}{L} & 0 & 0 & 0 \end{bmatrix} \Delta x \tag{7.30}$$

The inclusion of $\dot{\hat{\omega}}$ in $\mathbf{F}$ creates an algebraic loop in a real time implementation. This loop can be resolved resulting in the following dynamical representation of $\hat{\omega}$:

$$\frac{d}{dt}\hat{\omega} = \left(\frac{MI}{H}\hat{i}_q - \frac{1}{H}\hat{T}_L - f_\omega\right)\frac{1}{1-\kappa\Delta i_q} \tag{7.31}$$

where we assume $f_\omega = \left(\kappa\omega\rho + \frac{1}{2}\frac{\nu^2 MI}{L} - \frac{MI}{H} + \frac{1}{2}\frac{MI}{L}\right)\Delta i_q$.

7.4 Observer Gain Selection

The choice of parameters κ, ν and ρ in (7.30) becomes complicated for nonlinear time-varying system. Some better insight can be obtained based on the eigenvalues analysis of the closed loop system matrix (7.29). As a simplification accepted further the value of $\hat{\omega}$ is considered slowly varying and equal to 10π rad/sec. This value is taken in subsiquent simulations as well. As a measure of the observer dynamic performance we choose the value of the eigenvalue with the smallest absolute value. All gains are chosen such that the closed loop matrix is stable. The other method of analysis, namely root locus, would result in a more complicated graphical representation of eigenvalues locations.

Since we have a set of three unknown parameters we would need to have a four-dimensional coordinate system to simultaneously picture changes in the eigenvalues position. Some trials utilizing three dimensions of geometrical coordinates plus the fourth dimension being the color of the point on the plot have been performed. As it turned out this way did not give any clear idea of what the set of possible values of κ, ν and ρ should be. As an alternative we represent here several set of plots when one of the parameters is "frozen" and the other two vary in a given range. Figures 7.1 and 7.2 represent the location of the closed loop system eigenvalue with a smallest magnitude for variation of ρ, ν and κ.

As one can observe, the increase in the values of ρ and ν as well as the decrease in the values of κ moves the smallest magnitude eigenvalue towards $-\infty$ while keeping it real. Some undesirable effects have been observed for sufficiently small positive values of κ in which case the eigenvalue with the smallest real part started to be complex.

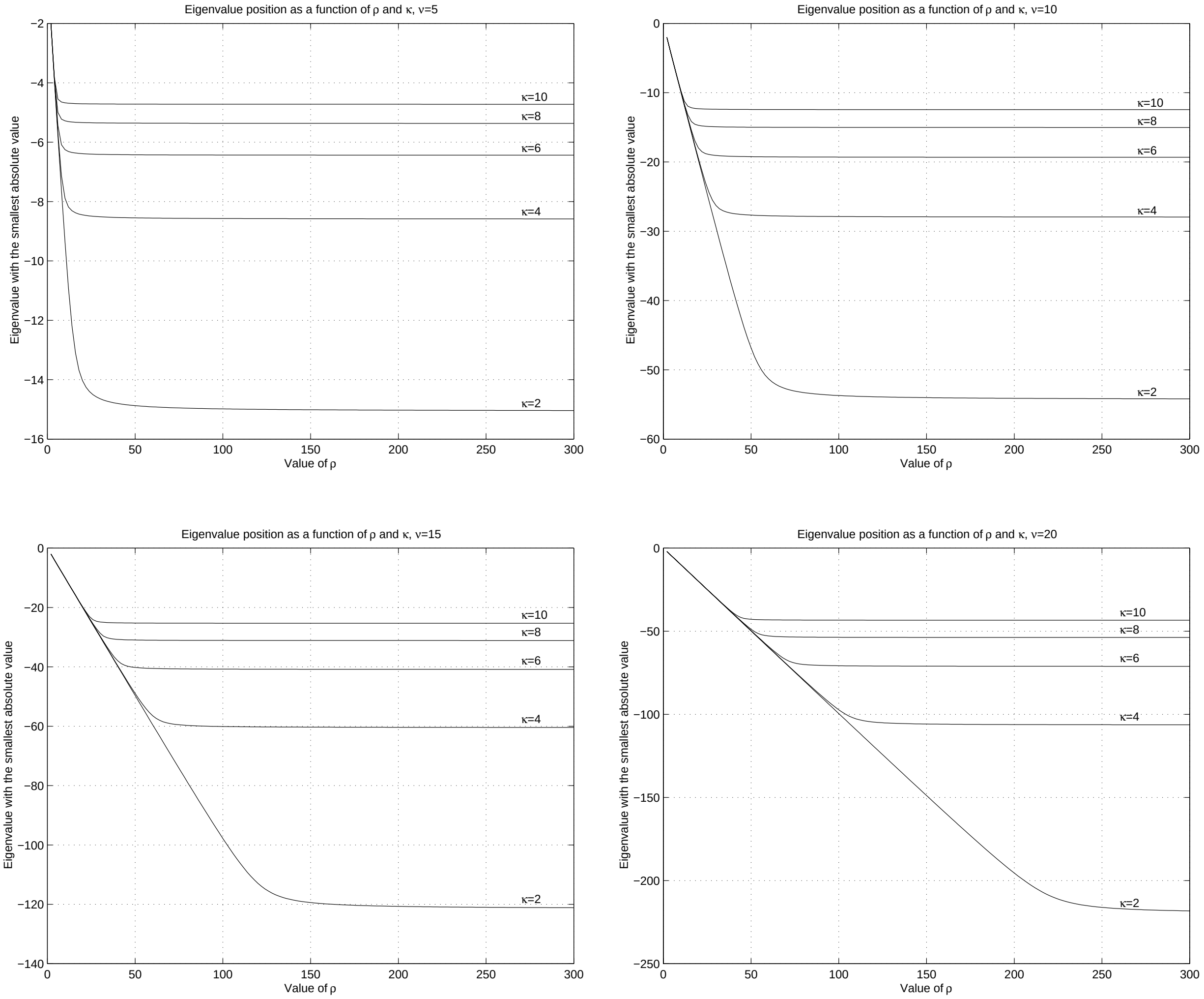

Figure 7.1: Location of the closed loop system eigenvalue with the smallest absolute value as a function of ρ and κ for various values of ν

7.5 Simulations of the Passivity-Based State Observer

The behavior and performance of the state observer presented above have been verified via numerical simulations. As a numerical simulation tool, the Simulink package of Matlab was extensively used. The intention was to model the estimator operation

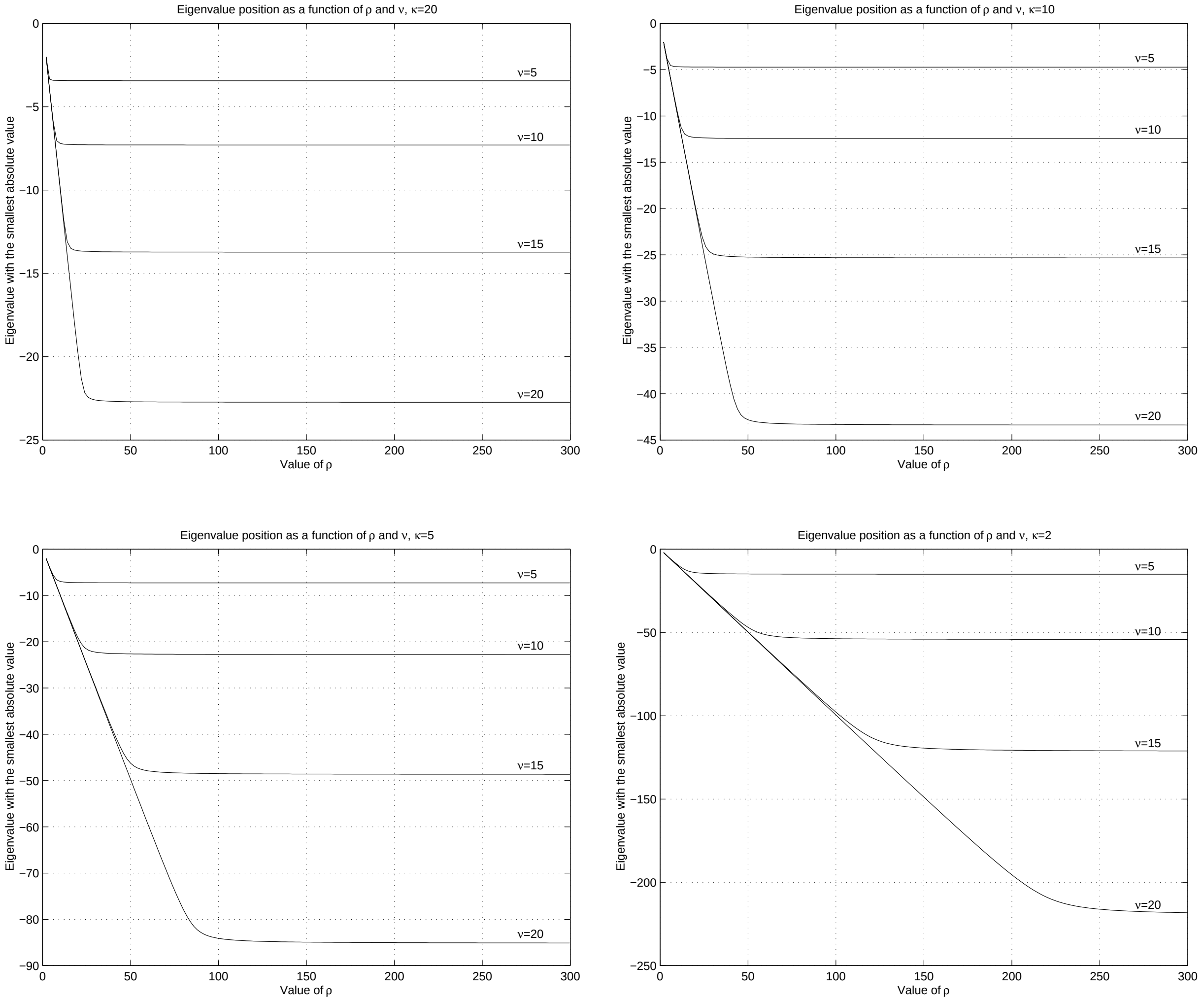

Figure 7.2: Location of the closed loop system eigenvalue with the smallest absolute value as a function of ρ and ν for various values of κ

for different selections of the gains in (7.30) and to compare changes in the speed of estimation and the convergence of the estimated states to their actual values when κ, ν and ρ change according to Figures 7.1 and 7.2.

The estimator was simulated together with the model of the non-salient PMSM although no actual motor data was available for the estimator calculations. The only assumption here was that the motor position at zero time was also zero degrees. This assumption seems to be practical since it can be implemented if only one of the motor phases is being excited to move the PMSM's rotor to the predetermined position. It is important to mention, that in this case we can use the state estimator even in the start-up operation which is a serious problem in some other sensorless schemes.

The following three sets of figures show the estimator operation when motor is fed by constant V_d and V_q voltages. Figures show the start-up estimation of states and the estimation of states when the step change in the load torque occurs. The load torque (which is not known to the estimator) changes from 25 % to 100 % of the motor rated value. In other words, the presented simulations correspond to the actual servo drive operating conditions. Figure 7.3 shows the actual (solid line) and the estimated (dashed lines) states of the motor when the value of ν varies. The values of ρ and κ are set to 50 and 10, respectively.

Figures 7.4 and 7.5 represent the actual and estimated states of the system for variation of κ and ρ. The values of ρ and ν in Figure 7.4 and the values of κ and ν in Figure 7.5 are set to 50 and 10, and to 5 and 10, respectively. Since it was quite difficult to distinguish between the actual and estimated position and actual and estimated currents plots I decided to omit them here.

In addition to simulations of the open loop motor drive with the passivity based state observer, the simulations of the closed loop system have been performed. The

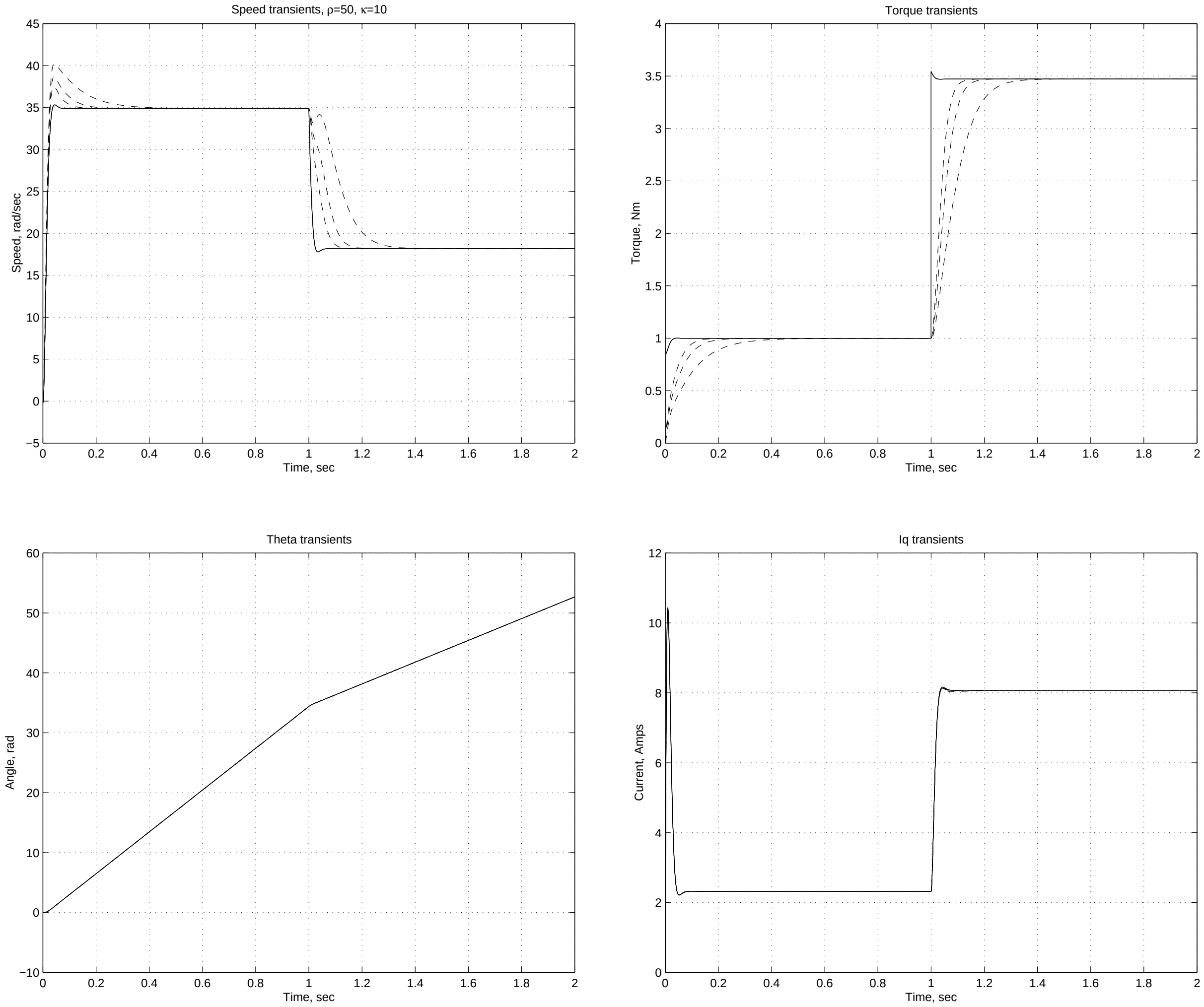

Figure 7.3: Estimation of motor speed (upper left), load torque (upper right), rotor position (lower left) and q component of the motor current (lower right) for $\nu = 10$ (slowest convergence), 15 and 20 (fastest convergence).

simple proportional-integral (PI) controller has been used in this experiment. The input to the controller was the difference between the reference speed and the estimated (not measured) speed. The controller output was connected as V_q voltage component to the motor model. The rationale here was not to use a sophisticated control algorithm (the used control scheme and the choice of the gains in the PI regulator are

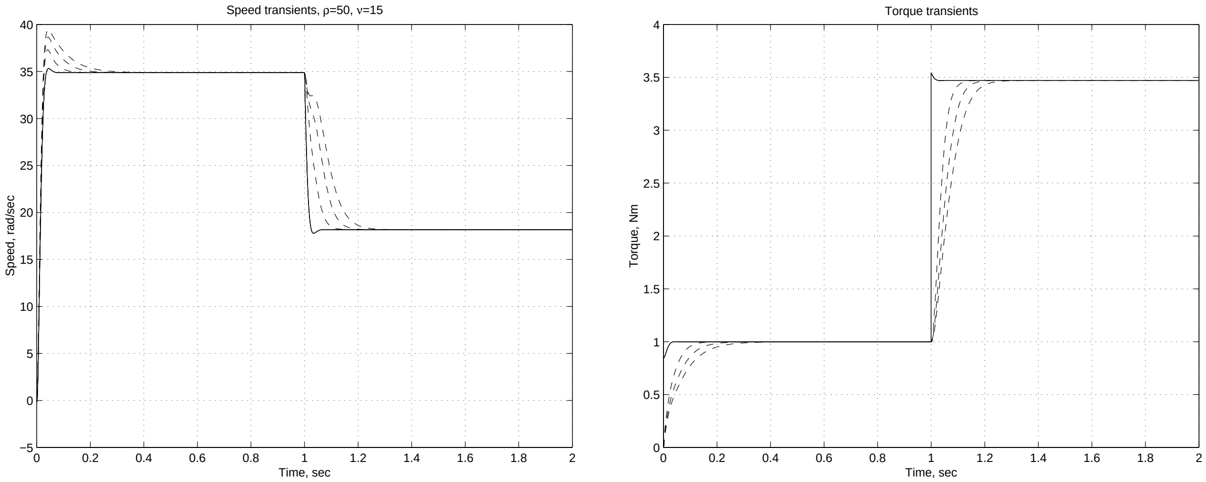

Figure 7.4: Estimation of motor speed (left) and load torque (right), for $\kappa = 15$ (slowest convergence), 10 and 5 (fastest convergence)

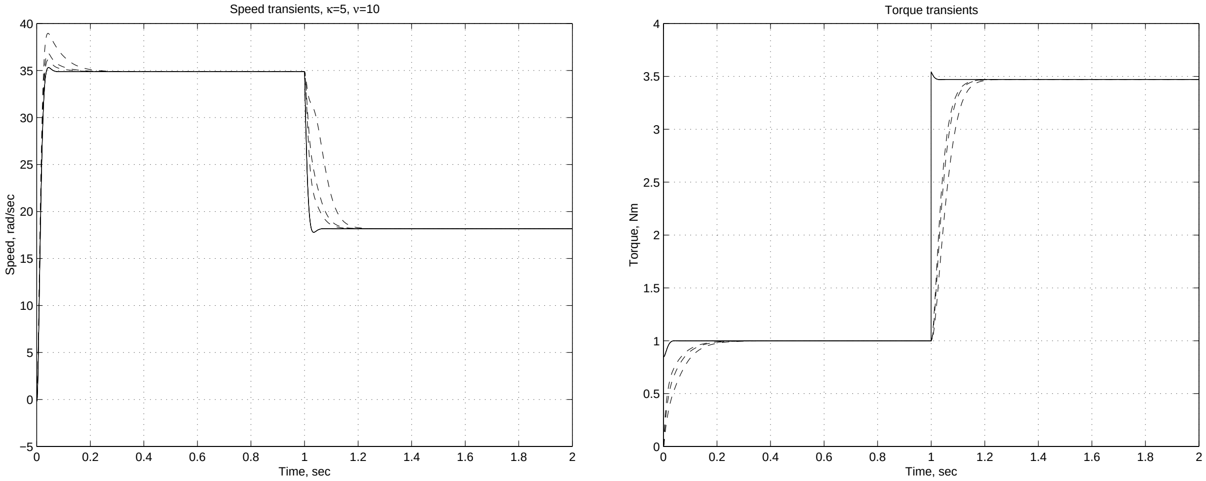

Figure 7.5: Estimation of motor speed (left) and load torque (right), for $\rho = 50$ (slowest convergence), 100 and 150 (fastest convergence)

quite intuitive) but rather to test the usability of the estimated state (speed) in the closed loop system operation.

Two typical tests have been performed. The first one was a sudden change in

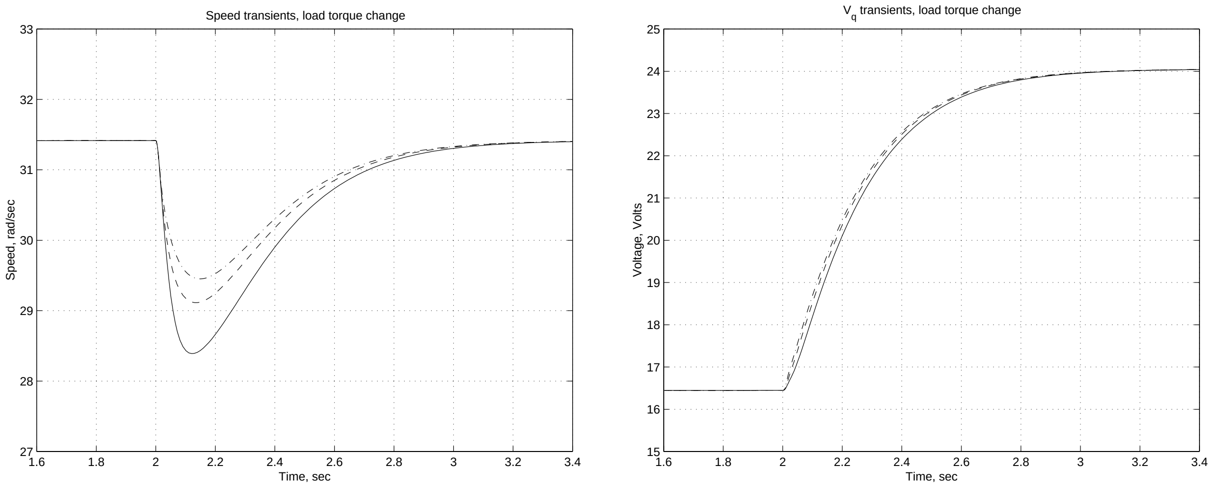

Figure 7.6: Use of passivity-based observer in control loop. Speed transients (left) and required actuation V_q (right) following sudden load torque change. ρ=50 (solid line slowest response), ρ=100 (dashed line), ρ=200 (dash-dotted line - fastest response.)

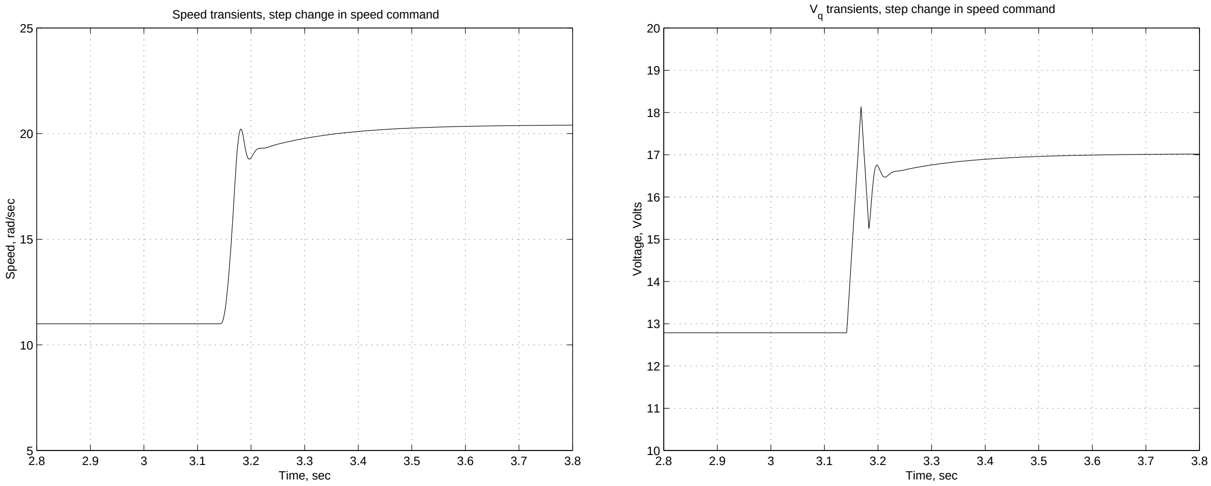

Figure 7.7: Use of passivity-based observer in control loop. Speed transients (left) and required actuation V_q (right) following step change in commanded speed.

the load torque, as before, from 25 % to 100 % of the rated value. The commanded speed was set to 10π rad/sec. The estimator gains were selected as follows: κ=5,

ν=15 and ρ was set to 50, 100 and 200 (three different selections.) The results of the simulation are presented in Figure 7.6. The selection of higher gains in ρ moves the smallest magnitude eigenvalue towards negative infinity thus allowing for faster state estimation (load torque, in particular) and, consequently, faster convergence.

The second test applied to the system was a stepwise change in the commanded speed. The range of change was from 5π to 8π rad/sec while the load torque was kept constant at the value of 80% of the nominal value. The use of the estimated speed in this case also resulted in satisfactory performance presented in Figure 7.7. The choice of the estimator gains was at 5 for κ, 15 for ν and 50 for ρ. Interesting enough that changes in these gains did not affect the performance significantly (it was not seen on the plot, at least) and therefore not shown. The reason for that is that the choice of the proportional and integral gains of the controller dominates over the speed of the motor speed estimation. Another important remark here is that the voltage command was limited using the slew rate limiter (at 200 V/sec, which would be a very low number for a real system.) The affect of this limitation is clearly seen in the V_q plot in Figure 7.7.

Chapter 8

Conclusions and Future Research on PMSM

This thesis has developed and successfully tested a passivity based control of permanent magnet synchronous motors for servo applications. A nonlinear structure of PMSM's differential equation requires innovative approach to design a control algorithm.

The design that relies on energy shaping criteria has been proposed. The major contribution of this design is in the use of transient torque shaping and in the direct manipulation of the dynamics of incremental energy terms. The voltage output consists of two components: a primary controller output that assures a required steady state setpoint and minimizes ohmic losses in the motor, and a secondary controller output that shapes the transients in the incremental states. The design of the incremental controller gains is based on the orderly procedure of the closed loop eigenvalues placement. This reduces the need for a lengthy trial-and-error tuning process so common for a traditional nested loop PI regulator design. All possible options for eigenvalues assignment have been considered and corresponding equations for controller gains calculation have been derived.

The validity of the developed control algorithm has been tested via numerical simulations and laboratory experiments. The experimental results are very close to the simulated ones. Two possible options in the eigenvalues placements were used. The first option was to vary energy dissipation rates in mechanical states without utilization of the lossless energy exchange channels between electrical and mechanical states. This option proved to be useful, especially in the case when the hardware setup has high noise immunity and high slew rate power supply. Then the system's experimental response to the sudden changes in the load torque and sudden changes in the reference speed can be made "arbitrarily" fast.

Another, and conceptually new, option of the controller gains selections was to incorporate lossless energy exchanges between electrical and mechanical incremental states. In this case the excessive energy can be freely transfered to/from electrical states to allow for faster transient response. Thus, dynamics of the motor currents become dependent on motor's mechanical states and vice versa. This mechanism of motor performance improvement seems to be quite useful in practice since it does not require for wider bandwidth of the current loop in order to achieve faster mechanical transients. Therefore, a better performance is possible in noisier environment with moderate actuation resources. The experimental results fully agree with this idea.

Since the practical implementation of the proposed control algorithm relies on the quality of the generated sinusoidal voltage waveforms, several improvements to the existing laboratory setup have been proposed and built in hardware. It was shown that for the current ratings of the built power inverter board the values of the deadtime and pulse deletion parameters could be reduced. This resulted in significant improvements of the phase current waveforms and further reduction in torque ripple.

The passivity based design approach has been successfully extended to a position sensorless control of a sinusoidally fed PMSM. A full state observer has been developed. Its operation has been verified via numerical simulations both in open loop and in closed loop applications. It has been shown that the start-up operation of the proposed sensorless control scheme is possible providing that the initial angle of the rotor is known. The latter is completely realizable by, for example, short term excitation of a PMSM's single phase. The closed loop operation of the passivity based state observer is possible (and its dynamic performance is satisfactory) even in the case when saturation and slew rate limits are imposed on the quality of the power supply voltage. Although having been succesfully verified in simulations, the sensorless control failed to be tested experimentally due to imperfections of the existing laboratory setup: high noise and spikes in measured currents made it virtually impossible for the observer to correctly estimate mechanical states.

The recommendations for future work are as follows.

The implementation of the advanced control algorithms, such as sensorless control, relies on the quality of the available measurements. Therefore, the noise immunity of the experimental setup needs to be improved. This applies, first of all, to the measurements of the motor phase currents. The partial re-design of the existing drive DSP interface board should be considered, and the issues of electromagnetic interference should be addressed. In addition to this, some measures need to be taken to improve the symmetry of the generated phase voltages by means of PWM. This will eliminate time skewing of the signals applied to the IGBT's of the power inverter stage.

One further change, associated with the experimental stand, is to improve the accuracy of the hysteresis load cell. This will result in much better repeatability of the experiments with the sudden changes in the load torque.

The research in passivity based control of PMSM can be naturally extended to the adaptive control. The adaptation to various changes in electrical (resistance, inductance) and mechanical (inertia, viscous damping) parameters is necessary in the course of the motor operation due to the variation of motor and load parameters. The utilization of the passivity principles can provide a feasible solution to this problem.

Chapter 9

Introduction to Switched Reluctance Motors

Advantages of Switched Reluctance Motor (SRM) drives include a simple structure (hence low cost), the ability to operate in harsh environments (such as at high temperatures) and under partial hardware failures, and a wide speed range. Industrial acceptance of SRM drives is presently limited by crude, almost model-independent control patterns that are easy to implement, but do not achieve the desirable smooth operation. The fact that SRMs are driven into magnetic saturation in energy efficient use causes their main disadvantages: inherent non-linearities that present a modeling challenge and a substantial torque ripple. The advent of power electronics and fast digital hardware, along with improved nonlinear and adaptive control methods, enables a re-evaluation of these issues.

In this report we will propose several such control strategies that build upon each other. First, phase current profiling is investigated for finding optimal –in the sense that the peak phase voltage is minimized– reference currents that generate constant torque. The calculation of optimal reference currents are based on complete machine model. It is suggested that those current waveforms can be parameterized for different reference torque levels to be used in closed loop operation. Experimental results show that this approach is promising but limited due to some inevitable implementation and modeling issues. Second, the design and implementation of an adaptive torque ripple minimization algorithm is presented. The algorithm assumes the use of a sub-optimal but easily computable phase current profiles for a given torque reference. Then the resulting torque ripple incurred due to simplification is modeled as an unknown load and is expanded in to a Fourier series. In the closed loop (that performs a speed servo task) a dynamic commanded torque profile is generated based on dynamic estimation of the unknown external load and the harmonic components of the torque ripple. Experimental results show that this approach can eliminate sub-harmonics in the produced torque and can attenuate the main torque ripple harmonic more than 20dB. An analysis is provided to show that this approach is limited by the resolution of the inverter, and by the quality of the speed measurements. The organization of this part of the report is as follows: This chapter presents standard models of SRM under various assumptions ; the next chapter describes phase current profiling for low ripple control; The final chapter on SRMs presents an adaptive torque ripple minimization algorithm using a simplified phase current profile (torque sharing current waveform);

9.1 SRM Model

SRM dynamics are governed by the following time domain equations [65]

$$\begin{aligned}\frac{d\lambda}{dt} &= -Ri + v \\ \frac{d\theta}{dt} &= \omega \\ J\,\frac{d\omega}{dt} &= \tau_M(\theta, i) - B\omega - \tau_L \qquad (9.1)\end{aligned}$$

where $i, \lambda \in \mathbb{R}_+^n$ and $v \in \mathbb{R}^n$ are the respective phase current, flux linkage and voltage vectors and n is the number of stator phases; θ and ω are the angular position and velocity; J, R and B are the moment of inertia, the electrical resistance in each phase and the friction coefficient, respectively; τ_M is the motor torque and T_L the load torque.

A key component here is the function $\lambda(\theta, i)$, relating flux linkage to current and angular displacement. The function is periodic in θ, and monotonically increasing in i. It can be expressed as $\lambda(\theta, i) = L(\theta, i)\ i$, in terms of the inductance function L. Models assuming linear magnetics ignore the current dependence of L (thus $L = L(\theta)$), while in more realistic, non-linear magnetics models $L(\theta, i)$ is monotonically decreasing in i (due to saturation).

The expression for the torque produced by a single phase k in case of magnetically independent phases can be evaluated from the coenergy as:

$$\tau_{M_k}(\theta, i) = \frac{\partial}{\partial\theta}\left[\int_0^i \lambda_k(\theta, i')di' \,|_{i=\mathtt{const}}\right] \qquad (9.2)$$

summing over all phases k for the total torque. This expression is simplified to

$\tau_{M_k}(\theta, i) = \frac{1}{2} i^T \frac{dL(\theta)}{d\theta} i$ in the linear magnetics context. Using the relations of current and flux, the equation (9.1) can easily be transformed to a differential equation in the state $(i^T, \theta, \omega)^T$, or $(\lambda^T, \theta, \omega)^T$.

In analysis of many electric machines it is advantageous to seek a (Blondel–Park type) coordinate transformation in which the flux and speed equations do not depend on θ. However, it was shown in [60] that in general such transformation does not exist for an SRM even in case of linear magnetics. It is thus natural to base control design directly on (9.1), and to allow control strategies to explicitly depend on (measured or estimated) θ.

The control inputs in (9.1) are voltages; an alternative is to assume current actuation, whereby only the last two equations in (9.1), corresponding to the mechanical subsystem, are of interest; such drives are denoted as “current–fed”. In practice, commanded currents in the latter setting are usually produced with voltage input, employing a form of current tracking hysteretic control. The current actuation assumption is justified by the fact that, in small and medium size drives, the dynamics of the electrical subsystem is much faster than the mechanical subsystem. (This approach can be theoretically formalized using an argument based on singular perturbations [52]). Throughout this work “current–fed” SRMs are used to validate the control approaches proposed.

9.2 SRM Control Algorithms

From section 9.1 it is apparent that there exist two kinds of control algorithms. One is the voltage-fed control as suggested by the motor dynamical equations, while the other is current-fed control. In current-fed control the electrical sub-system is assumed to be much faster than the mechanical sub-system. In both cases the phase turn-on and turn-off angles play a key role in providing positive torque at higher speeds. At low speeds since the motor back-EMF is low, the turn-on and turn-off angles could be set such that $\frac{dL(\theta,i)}{d\theta}$ is positive. Since at the very beginning of a positive torque producing phase the torque produced is small the turn off angle could even be retarded further for efficient torque production.

The voltage-fed control strategy implements a pulse width modulated (PWM) voltage regulation. For low performance control applications this strategy is generally preferred. Figure 9.1 shows a general diagram of a voltage controlled SRM drive. In a speed servo task the closed loop compansator that acts on the speed error calculates the voltage reference for the PWM control which in turn generates the duty ratio. Although a voltage controlled drive does not use current feedback for high performance control, it needs current sensing for protection against over-current conditions. A successful application of the voltage-fed control strategy is the LMB1008 IC produced by National Semiconductor shown on Fig. 9.2. The speed error amplifier produces a pulse train whose duty cycle is proportional to the speed error, and this is used to switch the inverter power devices at a fixed frequency [65]. For commutation

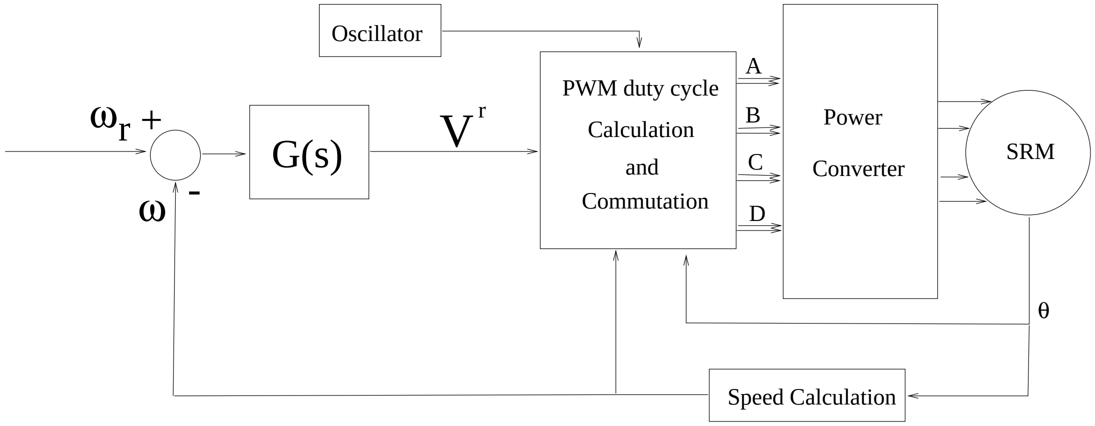
Oscillator
ω_r +
ω -
G(s)
V^r
PWM duty cycle Calculation and Commutation
A
B
C
D
Power Converter
SRM
θ
Speed Calculation

Figure 9.1: Voltage controlled drive.

the position information should be provided from the shaft. Clearly this control algorithm is not model based. The basic premise is that the torque generated (hence the speed) by the motor increases as the electrical power supplied to the motor increases and vice versa.

In current-fed applications the closed loop speed tracking task is implemented as a torque regulator. In this case the outer loop provides a torque reference which in turn is converted to reference phase currents via the inverse of the torque function $\tau_M(\theta, i)$. Then the reference currents are supplied to the inverter controller units to be impressed into the motor phases. For this reason it is necessary to have current sensors for current-fed machines. A general block diagram of a current-fed drive is shown on Fig. 9.3 The implementation of the reference currents in to motor phases is generally implemented via a hysteretic current tracking controller. This strategy

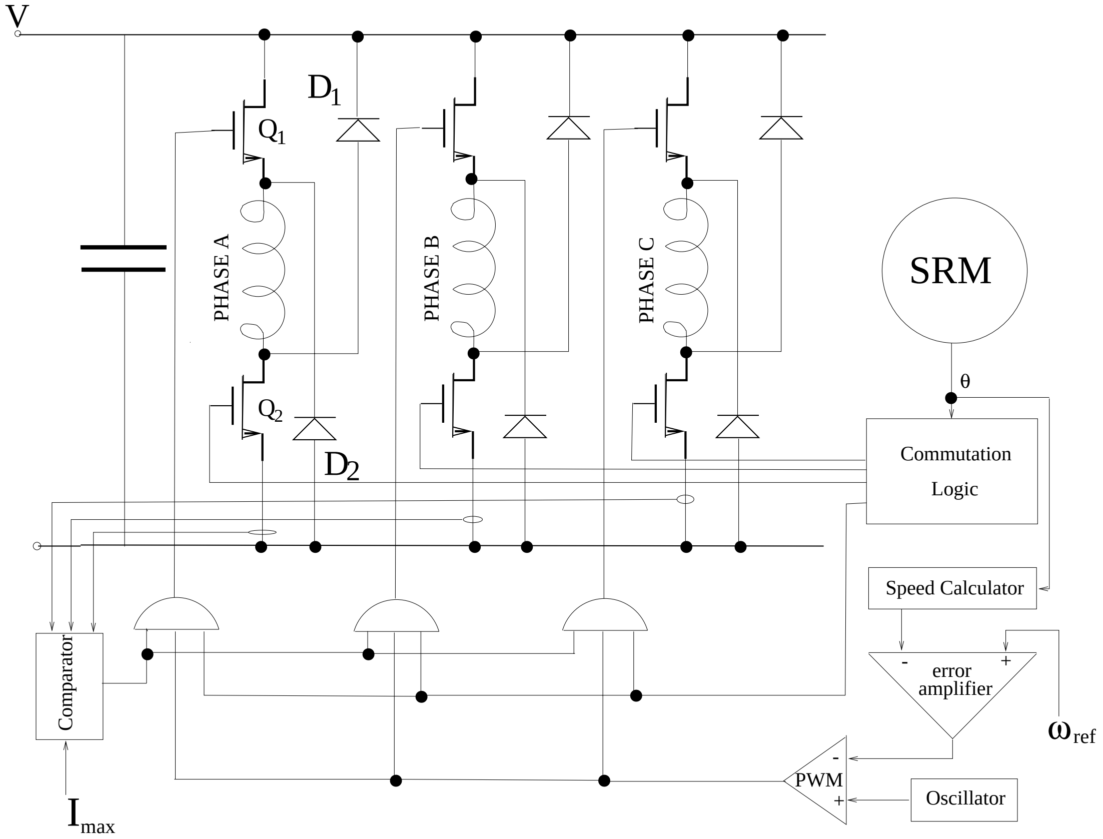
V
D1
Q1
PHASE A
PHASE B
PHASE C
Q2
D2
SRM
θ
Commutation
Logic
Speed Calculator
-
+
error
amplifier
ω_ref
Comparator
PWM
-
+
Oscillator
I_max

Figure 9.2: The LMB1008 Controller.

will be discussed further in the later chapters.

It is necessary, especially at higher speeds, to have some control on phase turn–on and turn–off angles (θ_{on} and θ_{off}) for both voltage-fed and current-fed machines. A simple phase angle control algorithm is provided in [17] assumes at the very initial stages of phase turn on, the voltage drop across on the resistor is negligible and the back-EMF is small. In this way a simple formula is provided for the amount of angle advance in θ_{on} and θ_{off}; however this approach is limited to a specific operating point. To ensure satisfactory angle advance at every operating point, a closed loop

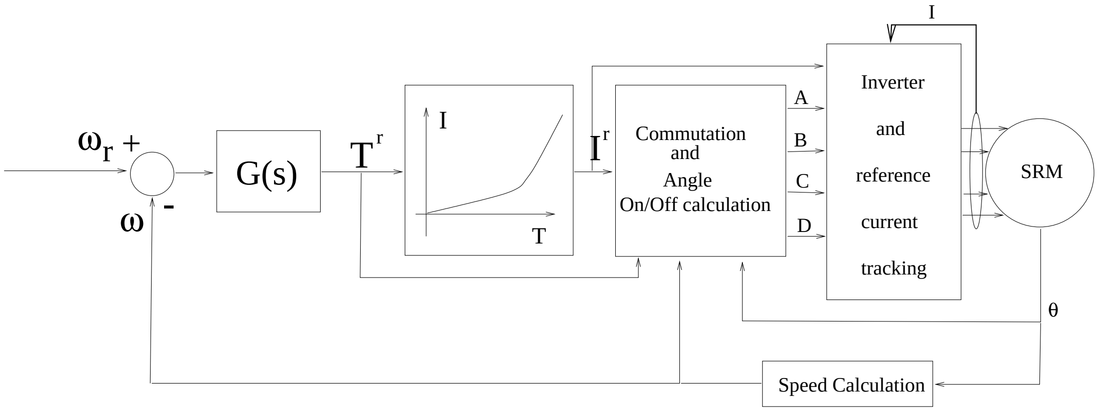
ωr +
ω
-
G(s)
Tr
I
T
Ir
Commutation and Angle On/Off calculation
A
B
C
D
I
Inverter and reference current tracking
SRM
θ
Speed Calculation

Figure 9.3: Current-fed Controller.

algorithm build upon this is provided in [61] to calculate the correct angle advance. This advance angle regulator measures the phase angle at which the phase current first reaches its reference value I_{ref} (called θ_{ov}). The phase advance angle is then updated to cancel the error between the measured and desired θ_{ov} via some kind of PI regulator. Another angle advance algorithm is proposed in [5] that corrects the initial choice of θ_{on} by acting on the speed error and the instantaneous torque when the generated torque is negative. Simply when the average torque is negative the angle is advanced. The portion of the algorithm that acts on the speed error is a non-windup PI type controller.

9.3 SRM Drive Inverter Topologies

In this section we will summarize some of the popular inverter topologies used in SRM drives. The unidirectional nature of current flow and the electrical isolation between phases in the SRM allow a variety of inverter topologies. Because of the cost of high power switches, a large effort has been made to reduce the number of power devices. Although the low cost of such circuits with reduced number of switches is desirable they somewhat limit the performance and flexibility of the SRM drive. In this section we are going to classify the switches according to their VA (volt-ampere) ratings as a measure of the actual silicon area in the converter, and as a correlate of the cost of the converter. Another important factor is the number of floating drivers needed to switch the high side devices. Although the number of components are also important, the main focus for a laboratory set-up would be the control flexibility. Reliability becomes an important issue in actual implementations.

Although there are many possibilities of inverter configurations, here only five of the popular are addressed. 1) the *bridge converter* , 2) the *Miller circuit* , 3) the *C-dump circuit* , 4) the *split-capacitor circuit*, and 5) the *sood inverter*. The *bifilar circuit* [65] has a special inverter because of its bifilar wound phases which is not considered in this thesis.

Bridge Converter: Figure 9.4 shows the topology of the bridge circuit. It uses two switches per phase to energize the motor phase and with two diodes to return the stored magnetic energy in to the supply. This topology gives the advantage of complete and independent control of each motor phase at any instant of time. This topology enables a complete utilization of the maximum torque capability of the motor. As a side comment note that this topology also allows operation of the inverter in position sensorless control that we do not consider here. The bridge circuit also places the minimal stress on each power device. This circuit allows both hard chopping and soft chopping inverter operation [26] that will be described later in this thesis. The major drawback of this circuit is that there is need for two switches per phase. Moreover, the upper transistors need to have floating supply to be controlled. This adds complexity to the circuit and in increases the number of components. The operation of this circuit will be described later as a component of the experimental set up used in this research.

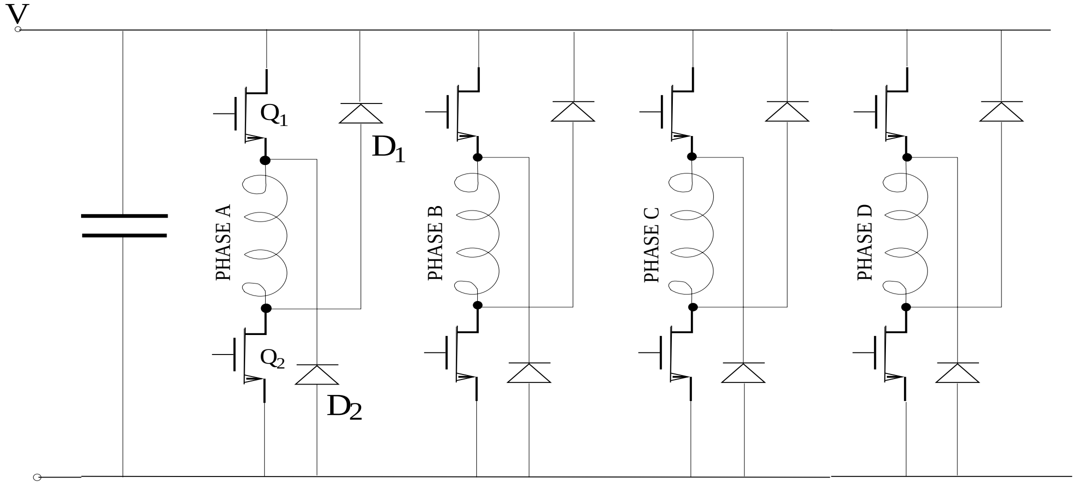

Figure 9.4: The bridge converter.

Split-Capacitor Converter: Figure 9.5 shows the split capacitor topology that has one switch per phase as an advantage. However it also suffers from a number

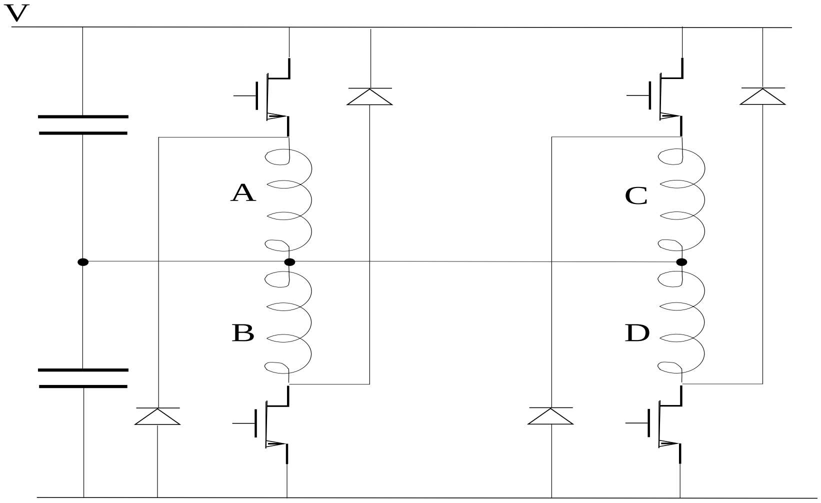

Figure 9.5: The split capacitor converter.

of disadvantages: for example, it needs an even number of motor phases, and the phases should have balanced currents to avoid charging or discharging of the capacitor midpoint. This topology needs capacitors that have good ripple ratings (the capacitor midpoint is connected to all motor phases). The operation of this converter is as follows: when a phase is to be energized, the switch in series to it has to be opened. This applies V/2 volts across the phase. To de-energize a phase the switch in series with the phase is turned off and the current free wheels across the associated diode with -V/2 volts across the phase; however, the voltage stress across the switch is V at the turn off.

Miller Converter: The Miller converter is developed by [65] is shown on Fig. 9.6. It uses N+1 switches to drive N phase machine. To energize a phase the common switch and the switch associated with the phase is turned on. Meanwhile, if the upper switch is turned off and the lower is kept on, the phase current free wheels across the diode. To de-energize the phase both switches should turn off applying (-V) across the phase. A clear disadvantage is that this circuit does not allow independent control over all phases, and especially it does not allow torque sharing. Moreover, the stress over the upper transistor is high because it conducts for all phases. Hence the silicon area should be increased for a longer life time.

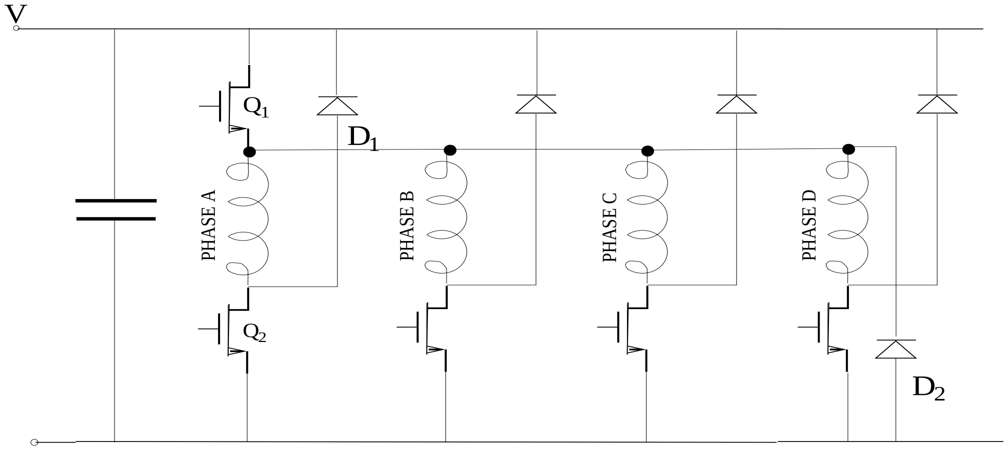
V
Q1
D1
PHASE A
PHASE B
PHASE C
PHASE D
Q2
D2

Figure 9.6: The Miller converter.

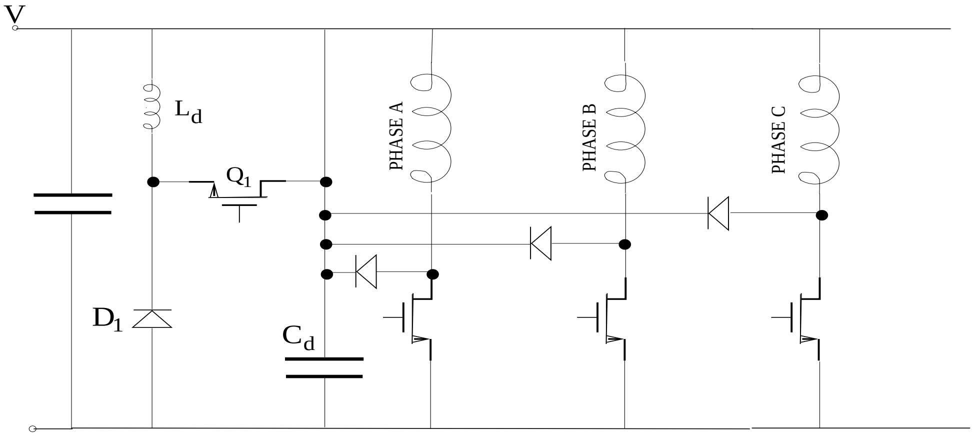
V
Ld
Q1
PHASE A
PHASE B
PHASE C
D1
Cd

Figure 9.7: The C-dump converter.

C-Dump Converter: The C-dump converter shown on Fig. 9.7 employs one switch per phase, and uses the extra components: a switch, a capacitor, and a reactor. Those extra components are used to return the motor's stored magnetic energy into the DC supply. In this circuit the capacitor is charged to a value higher than the supply voltage. Therefore, the capacitor has to be able to handle a large ripple. The operation of the inverter is as follows: to energize a phase, the switch in series with the phase is turned on to build up the current; to de-energize the phase, the switch is turned off which in turn charges the capacitor to a value greater than V. The reactor and the additional switch is then used to return the energy back to the supply.

This circuit has the advantages of needing one floating supply to control the additional switch, and the fewer number of switches. Since the voltage across the capacitor exceeds the supply voltage, the VA rating of this topology is comparable to the bridge converter [10]. Its advantage over Miller circuit is that it can operate with phase conduction overlap. The capacitor and the reactor add to the complexity of the converter and cause additional loses.

The Sood Converter:

This circuit is presented in Fig. 9.8, and is the last converter that we consider. The sood circuit is one of the most recent and it is believed that it needs a minimal number of components. The main characteristics of this circuit are: 1) the elimination of a dc link inductance (when compared to C-dump topology), 2) a capacitor, and 3) the direct transfer of capacitor energy to the motor windings. Although the topology

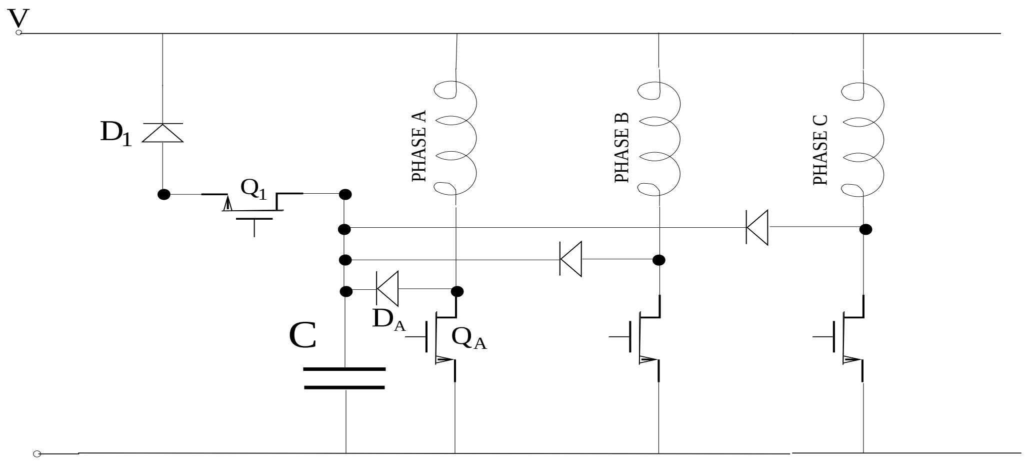

Figure 9.8: The sood converter.

of the sood inverter is similar to the C-dump circuit, its operation is fundamentally different as it involves four states: 1) Magnetization from unfiltered ac line– Q_A is on and the phase is charged with the ac line; 2) Magnetization from capacitor–both Q_1 and Q_A are on and a capacitor voltage larger than ac line charges the phase winding; 3) Demagnetization through freewheeling–Q_1 and D_A conduct, shorting the winding; 4) Demagnetization by charging the capacitor–both Q_1 and Q_A are off and the energy is returned back to the line through D_A and C.

Clearly this topology offers higher degree of freedom for control due to the increased number of states, but at the same time it complicates the inverter controller circuit. One significant disadvantage is that it has the highest voltage rating among the circuits considered here[105].

In [105] these five topologies are compared in terms of their VA ratings. It turns out that the bridge converter provides the best VA rating and the C-dump inverter has VA rating that is close to that of the bridge inverter. The converter that we used through out this research is the bridge converter that provides greater control flexibility and ease of implementing current-fed control algorithms.

Chapter 10

Optimal Waveform Profiling

10.1 Introduction

Current profiling for torque ripple minimization has been pursued previously; the unique feature of the approach described here is the complete parameterization of current waveforms yielding (nominally) torque ripple–free operation, serving as a basis for waveform optimization. Several optimization criteria can be used, with the general goal of minimizing power supply requirements and reducing sensitivity to model inaccuracies. In this chapter the design based on one such criterion – peak input voltage minimization – is illustrated in both simulations and hardware experiments, demonstrating the robustness of its performance advantage over conventional designs. This work builds on previous developments in [50], where bounded-input bounded-output stability is discussed as well.

Control strategies for ripple–free SRM operation have been studied extensively, and only a sample of approaches of immediate relevance to this work is listed here.

Reference [48] reports a feedback linearizing velocity controller; it uses a single phase at a time and thus requires very high flux variations, often leading to voltage saturation and to high sensitivity to inevitable model uncertainties. Difficulties in practical implementations of feedback linearization based control are documented in [84]. An interesting cascade control structure is proposed in [31], but it was derived for a motor with a very high number of rotor poles (150), resulting in a simple torque-flux relationship that does not hold in every SRM (such as the one used in the experiments of this work). Reference [24] presents methods for computing simple reference currents for a current tracking feedback control to minimize torque ripple, while [47] proposes a solution to the same problem that utilizes contour functions. In [106], nominal currents which result in constant torque are computed for reduced peaks and slopes under the constraint that at "critical" rotor positions each of the active phases contributes half of the total torque while excited with the same current. Reference [19] considers adjustments in firing angles for an SRM with nonlinear magnetics, and presents simulations for an "8/6" SRM (this choice of current shapes and the influence of motor geometry is discussed later). Although [30] claims zero torque ripple, it requires a very special (and ideal) motor construction, and does not address current actuator limitations. In [89] the goal motivated by energy efficiency is to minimize the peak phase current while requiring linear torque change in the angular range where two phases overlap. Several papers have addressed adaptive control ideas for SRM drives: [6] presents adaptive feedback linearization for SRM with linear magnetics;

[22] describes a "back-stepping" control design for an SRM with linear magnetics; [16] presents a model reference adaptive controller based on B-spline functions; [7] addresses adaptive control under fault conditions.

The control design procedure presented in this chapter uses the SRM model presented in section 9.1. The experimental setup described in this chapter uses a current fed SRM, and a hysteretic tracking of the commanded current. The analysis and control design approach that are presented here are based on non–linear magnetics, and it is assumed that $L(\theta, i)$ is (approximately) known. Fig. 10.3 shows the flux dependence on the phase current for various positions for the SRM used in the experiments presented in this chapter.

10.2 Low Ripple Control

The first step in the control design procedure is to derive a complete and computationally efficient parameterization of all n-tuples of currents that achieve a fixed torque τ^o. In this section motor operation is considered in the region below the "base speed", where voltage actuators can produce the required control inputs (phase currents in laboratory experiments reported in section V). Thus, inputs that will avoid actuator saturation will be investigated. In other words, by optimizing the current waveform used, the "base speed" is maximally extended for given actuator (voltage) limitations.

For conceptual simplicity, SRMs are considered where at most two phases can contribute positive torque at any given time. Many popular designs satisfy this condition, including the four-phase stator and six pole rotor "8/6" SRM used in the experiments. For the same reason, it is assumed that phases are magnetically decoupled (i.e. $L(\theta, i)$ is diagonal). This condition is, again, often satisfied to a large degree, and, in particular, it approximately holds for the SRM of this work. An extension of the design suggested here to a general setting where either or both assumptions are removed can be carried out at the price of straightforward, but notationally unpleasant computations.

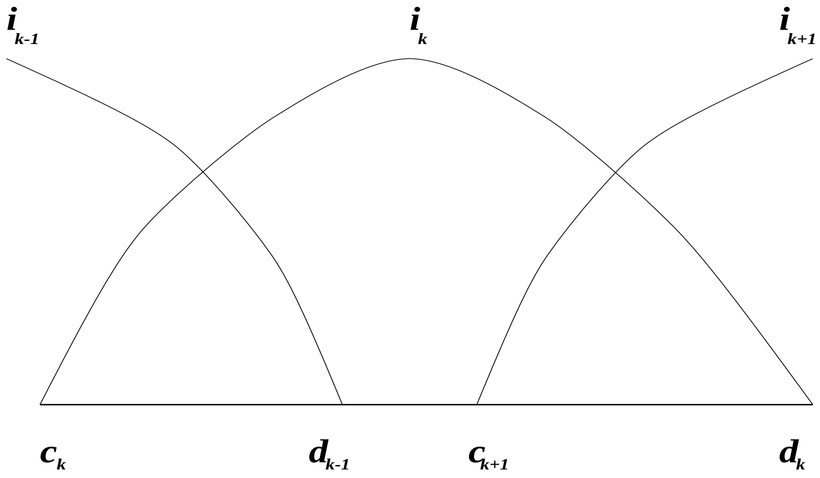

Figure 10.1: Illustration of arc notation.

The torque developed by an SRM is independent of the polarity of stator currents, but it depends on θ, as its sign equals the sign of $\partial L/\partial\theta$. To maintain constant torque efficiently, nominal current trajectories should contribute only positive components to τ_M. Hence, phase currents will be kept at zero over the half–period arc where the phase inductance is decreasing. The arc corresponding to positive $\partial L/\partial\theta$, where a nonzero k-th phase current i_k will be produced, is denoted by $\Theta_k = [c_k, d_k]$. As shown in Fig. 10.1, there is an overlap between Θ_k and the arcs Θ_{k-1} and Θ_{k+1}, for the preceding and following phases (denoted with $k-1$ and $k+1$, respectively). For the rotor positions $\theta \in (d_{k-1}, c_{k+1})$, the only nonzero phase current is i_k, and the value of i_k that is needed to produce a desired torque $\tau_M = \tau^o$ is uniquely determined by equation (9.2). From the fact that phase currents are periodic and form constant angular shifts in relation to each other, it suffices to consider $i_k(\theta)$ for half of the region $[c_k, d_k]$ to determine i_k for the remaining part of Θ_k . The desired torque production thus allows one degree of freedom, subject to the constraints that $i_{k-1}(d_{k-1}) = 0$ and $i_k(c_k) = 0$ have already been determined . This degree of freedom will be used in optimizing the selected current waveform. For 8/6 SRMs the points d_{k-1} and c_{k+1} coincide. Currents are periodic with the spatial angle of 60 degrees, where in the second half of these 60 degrees the current is kept zero to avoid negative (breaking) torque. To make current waveform optimization tractable, the original set of time-domain candidate waveforms will be approximated by a finite dimensional parameter set. In experiments the parameterization was based on specifying the current i_k in $N_p = 9$ points over the spatial domain of 30°; i_k was then evaluated over $N_c = 12N_p$

points using cubic splines, and i_{k-1} was determined to ensure that the two phases jointly generate the torque τ^o. The choice of angles above is such that the current is expected to change little between two points, so that it can be well approximated with splines, justifying the term "complete" . The choice of N_p and N_c requires a tradeoff between the computational time and the capability to capture the current variation.

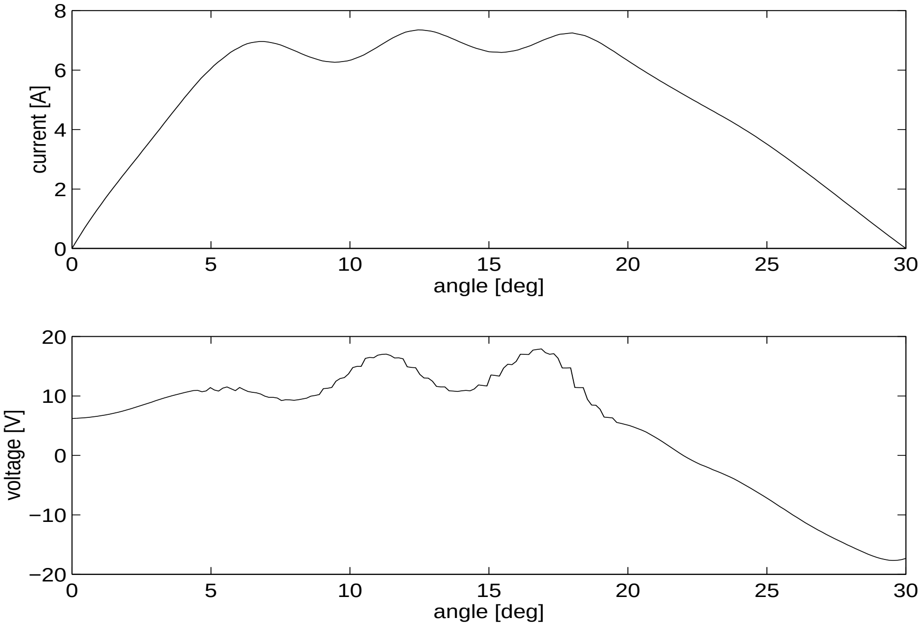

Figure 10.2: Optimized current (top trace) and the corresponding voltage (bottom trace) for the experimental SRM for $\tau_o = 0.8$ Nm, ω=300 rpm, and r_{phase}=1Ω.

Previous studies of control policies for ripple-free operation of SRM (e.g. [106, 20]) have repeatedly come to the conclusion that the required input voltages tend to be "spiky". This phenomenon is due to the nonlinear relationship between phase voltages and phase currents, whereby even relatively smooth current waveforms may require very high input voltages. Another source of control difficulties is in the fixed magnitude (V_{dc}) of the dc voltage in (hysteretically) switched power inverters. Setting a high value for V_{dc}, to accommodate a rapidly varying waveform, will result in increased average switching frequency over time intervals where a moderate continuous voltage is needed. This leads to increased switching losses and poor efficiency. Voltage magnitude is therefore the main factor constraining control capability, and a useful criterion for the selection of a current waveform is the minimization of the highest voltage required to produce the constant torque τ^o. This criterion relates also to yet another source of control limitations, which is the proportionality between the bandwidth of speed regulation and the difference between V_{dc} and the voltage required at a given time. The optimized current and voltage waveforms that minimize the required voltage magnitude are shown in Fig. 10.2. Both the optimized current and the traditional current are sketched in Fig. 10.3. Observe that the proposed policy and the traditional policy are similar in terms of energy efficiency (as the areas under the current curves are comparable). It can be seen from the figure that the peaks of the optimized current are around the denser regions of flux-current-angle plot, as expected from (9.2).

The parameterization of the current set can be used for efficient computations with optimization criteria other than voltage minimization, which could prove beneficial in other applications. Some examples are: (a) In high-speed operation (i.e., above the "base-speed") it is of interest to maximize the achievable ripple–free torque subject to actuator constraints; (b) Maximization of efficiency at low speed operation; (c) Torque ripple minimization with one or more faulted phases (where the parameterization has to be modified to accommodate the broken symmetry between phases); and (d) The minimization of ripple in radial forces which are primarily responsible for acoustic noise of SRM through the "ovalization" of the stator [21].

10.3 Simulations with Uncertain Models

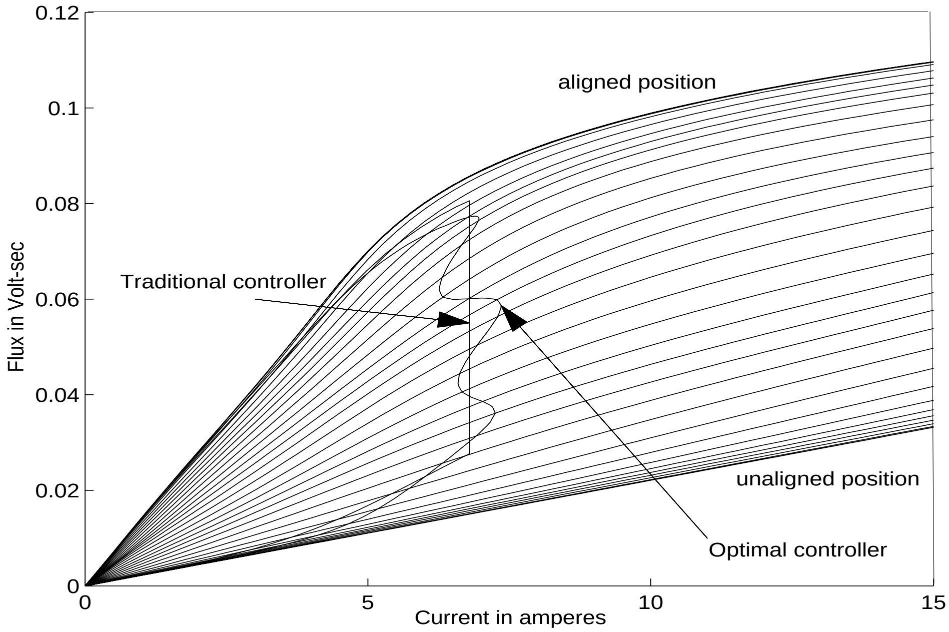

Figure 10.3: Flux function $\lambda_l(\theta, i_l)$ for the experimental SRM used in this chapter.

The simulation and experimental data were obtained with an “8/6” SRM whose inductance characteristics are shown in Fig. 10.3.

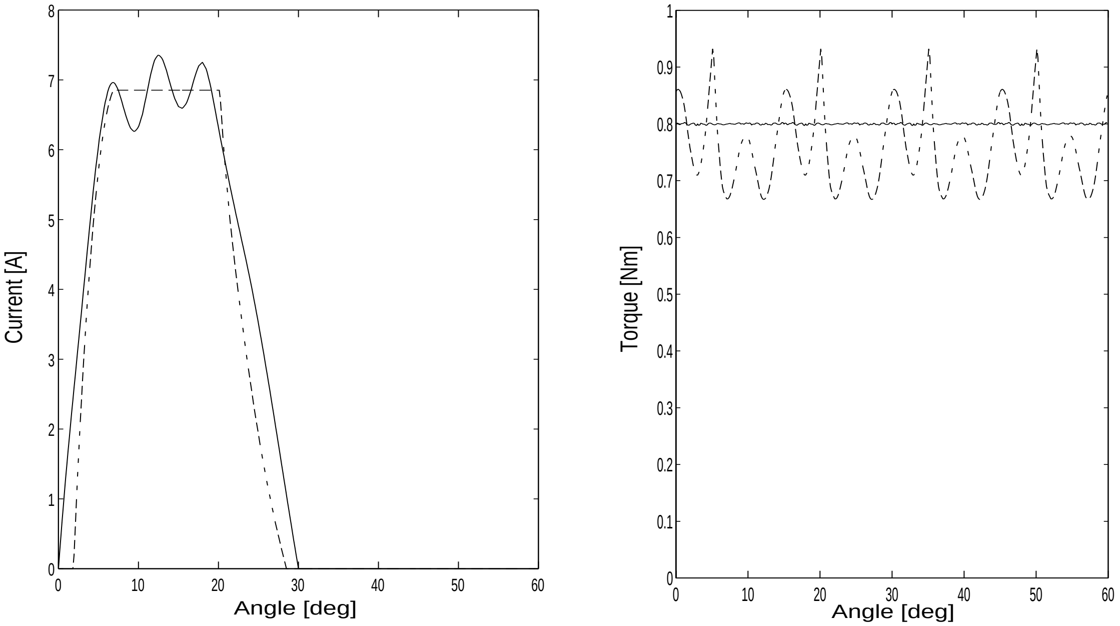

Figure 10.4: Optimal constant current waveform (dashed) and optimal current waveform (solid); left figure. Corresponding torque deviations assuming accurate model; right figure.

The speed of the SRM is approximately 300 rpm, and the torque is, with current waveforms optimized for minimal voltage requirements , $\tau^o = 0.8$ Nm (the base speed is ≈ 570 rpm with a 35 V supply voltage). The performance of the proposed controller will be compared to the “traditional” SRM controller [65]. The traditional control waveform is determined by four parameters: the turn-on angle; 1)the turn-off angle; 2)the constant chopping current level; and 4)the supply voltage. The particular traditional switching pattern considered in the experiments is optimal for its class in the sense that it minimizes torque ripple. Because of its limited number of degrees of freedom, the optimal selection of the traditional control parameters depends on both the desired nominal speed and (average) torque (and yields an increasing torque ripple away from the nominal speed). On the other hand, the optimized policy suggested here guarantees (nominal) ripple-free torque at varying speeds (but may be suboptimal in terms of minimizing the required voltage at speeds different from the nominal). Fig. 10.4 compares the optimal current waveform generated by the proposed policy and by the traditional design. Torque deviations (under the assumption of a perfect model) are also presented in Fig. 10.4 where the traditional controller is designed to produce minimal absolute deviations of torque around the nominal value τ_o. The ripple in the optimized policy is only due to finite computational accuracy, as compared to significant torque ripple (about 30 % of the average value) under the traditional switching policy. This result, while encouraging, is not very surprising, as one expects a current waveform optimized over a (much) larger family to outperform the more constrained traditional current shape.

From an implementation standpoint, a critical issue is the robustness of the proposed solution to model uncertainties and differences among phases. To simulate deviations of the model from the "actual" dependence between phase currents and fluxes, the "true" current-dependent inductance curve is perturbed in a probabilistic

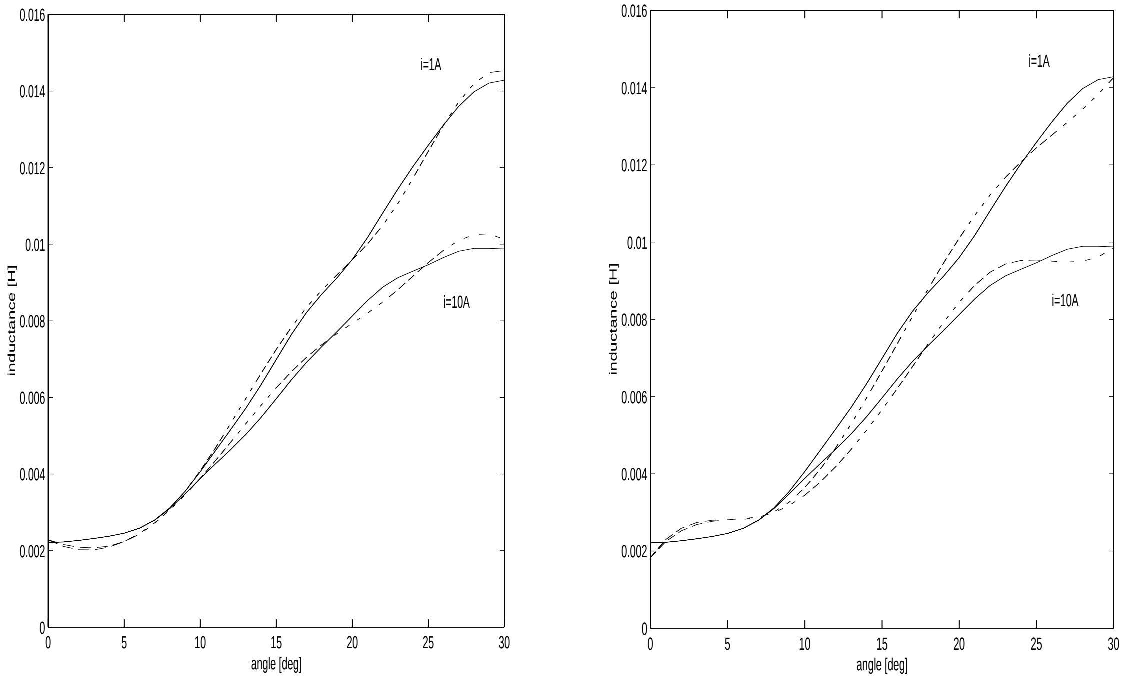

Figure 10.5: True (solid) and perturbed (dashed) inductance for two neighboring phases.

way (independently in each of the four phases). The numerically simulated variations in the *rate of inductance change* $\partial L/\partial\theta$ were significant, and reached 20 % for the phase current of 10A.

A representative current-dependent inductances and the perturbations are shown in Fig 10.5 for two neighboring phases. The resulting torque deviations are presented in Fig 10.6; the ripple is still approximately 50 % smaller with the optimized policy than in the case of traditional control. These simulations suggest that new switching policy is preferable when a reliable model is available, and that it maintains an advantage over the conventional one in cases of inaccurate models and timing in

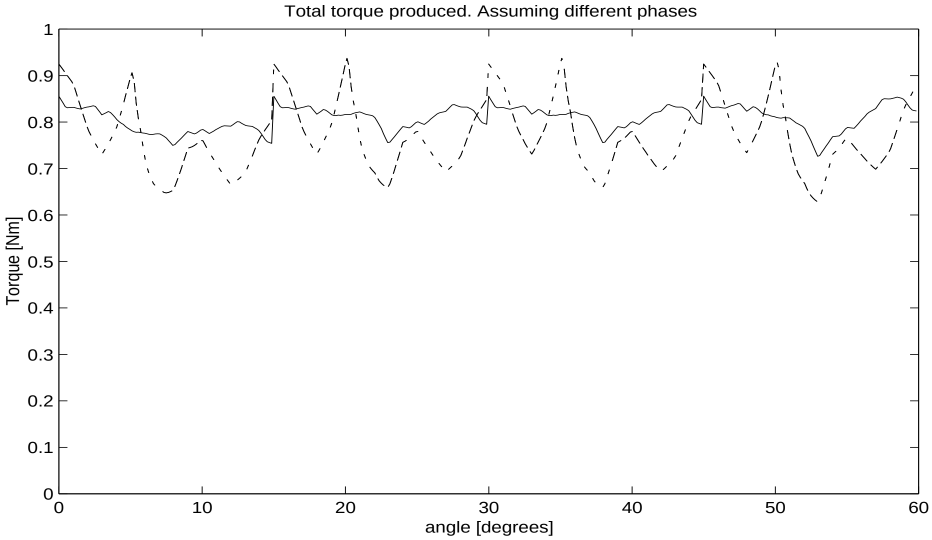

Figure 10.6: Torque deviations for the proposed controller (solid) and traditional controller (dashed), assuming inaccurate model and unequal phases.

inverter switching. The proposed policy thus retains some of the inherent robustness of the conventional design, while achieving the high accuracy characteristic of feedback-linearization type controllers.

10.4 Experimental Results

The experimental results were obtained using the "8/6" SRM whose model was the basis for the simulations above and it is equipped with an optical shaft encoder with

200 pulses per revolution. Mechanical load for the motor was provided by a dynamometer equipped with a hysteretic brake. Torque measurements were obtained with a strain gauge dynamic torquemeter (Himmelstein MCRT 4901V) with the measurement bandwidth of 300 Hz. Double-flex couplings were used to connect the motor, torquemeter and the load cell, and the test stand was placed on vibration isolation mountings. Given the limitations of the torquemeter, torsional resonant frequencies (estimated to be in the range 300-650 Hz) and the need to observe the improvement in the torque ripple, the measurements were obtained at low speeds (200 rpm corresponds to the torque ripple fundamental at 80 Hz, since each of the four phases is excited 6 times per revolution in this "8/6" SRM).

The experimental set up employs a half-bridge inverter with two transistors and two diodes per phase; it operates in a hysteretic current mode with "hard chopping [65]" (i.e., the voltage on an active phase is either positive or negative dc voltage); the hysteresis band is 0.2 A. Optimal currents are implemented rather coarsely - there are 16 quantization levels, and the target waveform for the hysteretic control is updated every 1.8 mechanical degrees. Both policies are implemented using a Motorola MC68332 micro-controller. Figs. 10.7 and 10.8 show the steady state waveforms for the two switching policies. A remarkable similarity between the simulated torque ripple (for the case of uncertain SRM model) and actual recordings can be observed. Thus a repeated (or on-line) identification of $L(\theta, i)$ is likely to lead to further improvements in ripple minimization in the proposed control policy.

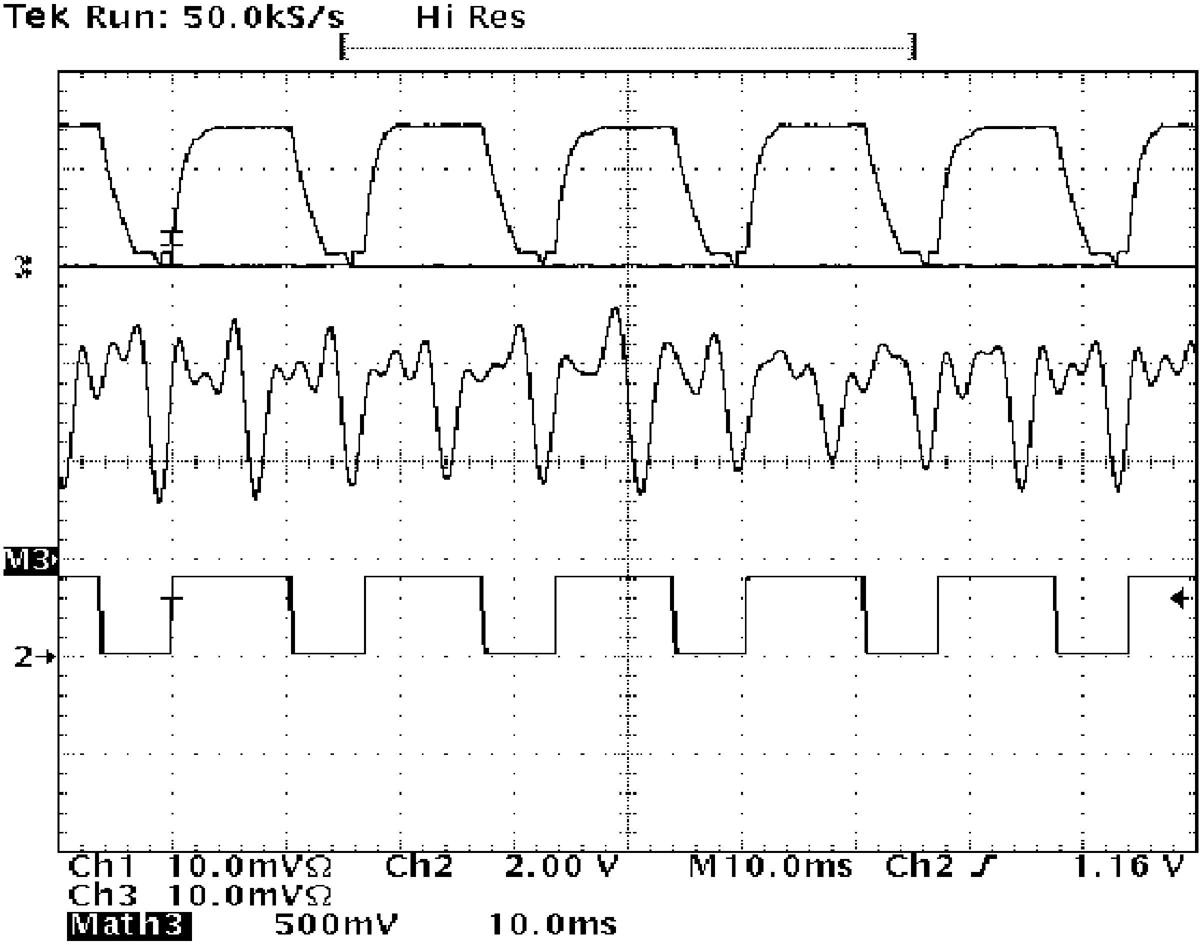

Figure 10.7: Measured steady-state waveforms for the conventional policy: top trace - actual currents for two opposite phases; middle trace - torque variations (amplitude is 32 % of the mean); bottom trace - reference current waveforms for the same two phases.

Magnitude spectra (normalized at dc) corresponding to the two control policies are shown in Figs. 10.9. Fig 10.9 also shows results obtained with “soft” chopping inverter operation for optimal control policy in which the voltage on an active phase can be zero, in addition to $\pm V_{dc}$. Under soft chopping a further 3-6dB attenuation is observed in the main and higher harmonics. This is expected, because in the case of

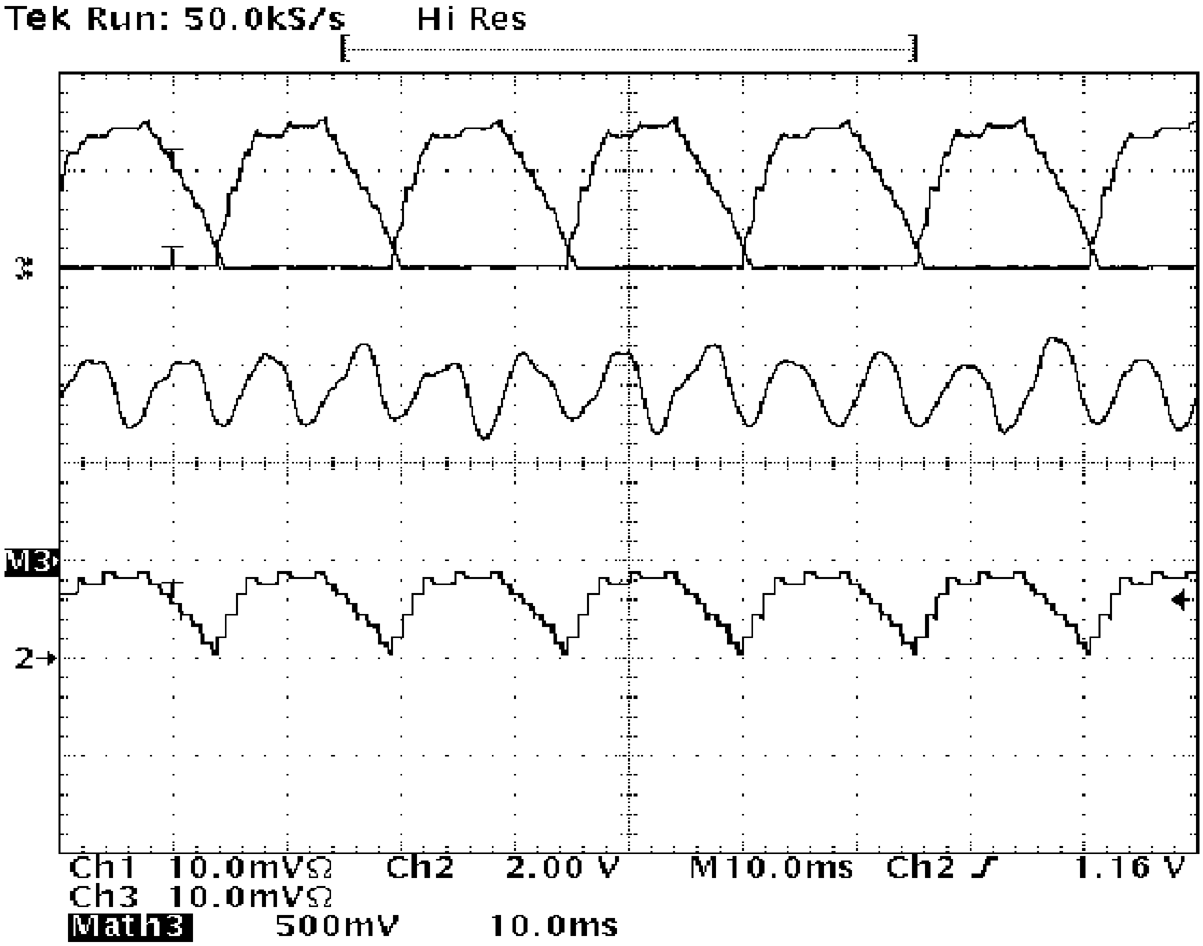

Figure 10.8: Measured steady-state waveforms for the proposed switching policy: top trace - actual currents for two opposite phases; middle trace - torque variations (amplitude is 16 % of the mean); bottom trace - reference current waveforms for the same two phases.

soft chopping the current variation and the number of switchings per period are both reduced.

These measurements have been obtained using an HP35665A spectrum analyzer and "flat–top" windowing that offers high amplitude accuracy (±0.005 dB), but somewhat lower frequency resolution. The peak at 80 Hz corresponds to the fundamental

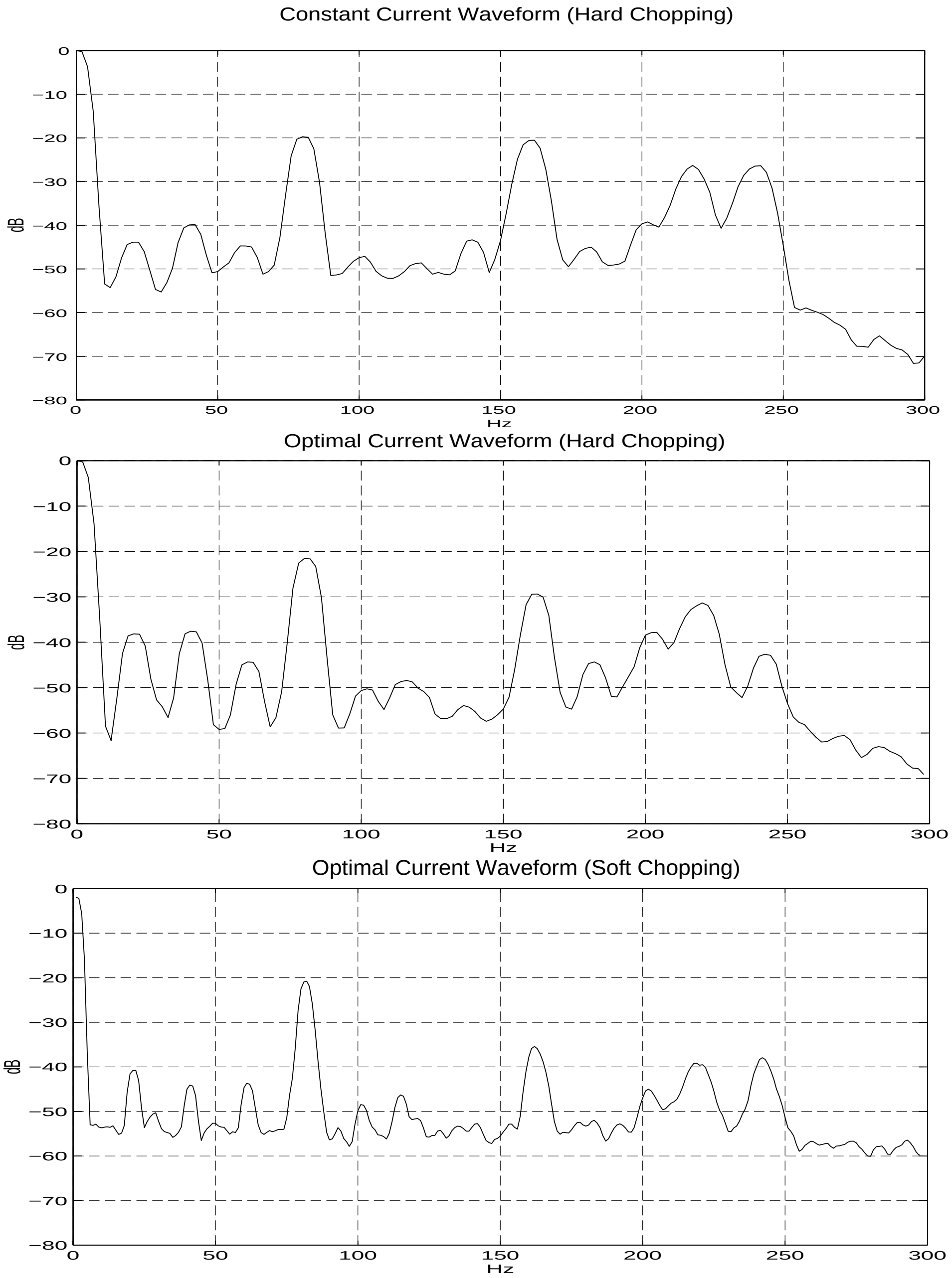

Figure 10.9: Measured normalized magnitude spectrum of the torque ripple, top figure: traditional control policy, bottom two figures: optimized control policy with both hard and soft chopping inverter operation.

of the torque ripple (rotational speed is $\approx$ 200 rpm). A marked improvement is evident in the range 150 – 250 Hz; in particular, the second harmonic is attenuated almost 8 dB (i.e., 2.5 times). The measurements at low frequencies tend to rule out shaft misalignment as a major source of torque ripple; non–symmetries of the phases are a likely cause for spectral components at 20 Hz and its multiples. Together with inevitable quantization and position errors, these findings point towards an on–line self tuning approach to torque ripple minimization as a promising research direction.

One challenge is the development of an efficient and accurate parameterization of optimized current waveforms over a wide speed and torque range. The other challenge is in further reduction of the sensitivity of these waveforms to inaccuracies in the flux model. One strategy, pursued in [32], is to compute the current waveforms using a simplified torque function $T_M(\theta, i)$, then to dynamically estimate the harmonic components of the resulting torque ripple, and finally to utilize feedback to correct the currents.

10.5 Conclusions and Research Directions

In this section, the production of ripple-free torque in SRMs has been addressed. The control goal has been to minimize torque ripple produced by an SRM using simple position and current feedback structures and standard microcontroller technology. A complete parameterization of position dependent voltage and current profiles that result in (nominal) ripple-free operation of an SRM has been developed. This parameterization serves as a computational base for optimization over candidate current waveforms. The main concern has been the minimization of the required voltage magnitude, since it is a common constraint in practice. Other useful criteria described in the chapter also rely on the same parameterization for efficient calculations. The effects of model uncertainties in SRM have been explored, and showed, via simulations, that the proposed switching strategy consistently outperforms the conventional switching policy. Experimental data presented in the section verify the analytical approach, and point out possible improvements. The proposed switching strategy is relevant for several areas of current interest in SRM drive control, as it can be naturally included in self tuning and adaptive control implementations.

As both simulations with uncertain models and experiments indicate current profiling is a major step towards torque ripple minimization. But because of practical constraints– such as unequal phases, non identical implementation of the analog hysteretic circuit (due to tolerances in resistor values and non-equal Hall current Sensors, finite quantization levels of D/A converters and finite hysteretic current band)– the improvement that can be achieved from of-line waveform optimization is limited. So in the following chapter we will explore this issue further by including adaptive controllers to compensate for these kind of nonidealities.

Chapter 11

Adaptive Closed loop Control

11.1 Introduction

In the previous chapter waveform profiling is shown to improve on torque ripple reduction. The performance of this model based control policy is limited due to the hardware implementation issues described previously. Optimal phase current waveforms are calculated for a fixed torque reference value and for a fixed motor base speed. To be able to use this control strategy in closed loop, we need to calculate such optimal current waveforms for a grid of torque reference levels. Moreover, there is need for an efficient parameterization of these optimal current waveforms for the various reference torque levels. Because of the inevitable inaccuracies and limitations described earlier, the benefits of such an optimal parameterization scheme could diminish or the scheme may turn out to be costly to implement. Therefore, we propose the use a sub-optimal (in terms of torque ripple), but easily computable torque sharing function, and include an adaptation scheme for further reduction in the torque ripple caused by the simplification.

This chapter describes the design of such an adaptive control algorithm with the dual goal of torque ripple minimization and simplicity for ease of real-time implementation. Ripple-free control strategies for SRMs have been studied extensively, and we review those that have immediate relevance to the method proposed in this chapter. In [16] spline functions are used to model the motor torque function, where the parameters are estimated using adaptive rules. With this approach the problem of inverting the torque function is alleviated considerably. Reference [85] proposes a new commutation strategy along with a PI controller to minimize torque ripple, where an easily invertible flux function is used in calculating reference phase currents. In [95] optimal reference currents are calculated based on a complete model that produces minimal supply voltage under the constraint that the produced torque is constant. Reference [66] addresses the same issue by applying adaptive fuzzy logic controller whose parameters are adjusted through LMS algorithm. Close to our approach are also [23, 78], where nonlinear adaptive torque-ripple cancellation is applied in PM drives, and harmonic coefficients of the phase inductance (due to structural nonidealities) are dynamically estimated and current harmonics are adaptively injected to cancel the torque ripple.

When an accurate machine model is used for control design, both feedback linearization techniques and the use of pre-calculated optimal torque sharing functions result in good dynamic performance. However, model inaccuracies are known to degrade performance, but are often hard to avoid: adding to inaccurate measurements, the use of an accurate model entails complex on–line computations, or the use of large lookup tables that may be impractical. In this paper we address this issue by combining the use of a simple, but easily computable, torque sharing function with adaptation. Our main goal is to reduce the torque ripple. The underlying control idea is simple: assuming a position dependent – and therefore periodic – current excitation, model inaccuracy will result in a periodic ripple in the produced torque. Harmonic components of the produced electro-magnetic torque combined with the unknown load torque are dynamically estimated from the speed signal, and corresponding correction terms are added to the commanded phase currents until speed ripple is eliminated (or considerably reduced in practice). Simulations and experiments demonstrate that our algorithm reduces the torque ripple considerably.

The organization of the chapter is as follows: Section 11.2 presents techniques for identification the SRM; Section 11.3 discuses control design, including the commutation strategy and adaptation; Section 11.4 presents and analyzes simulation and experimental results; Section 11.5 analyzes the limitations of algorithm in terms of practical implementation issues; conclusions are drawn in Section 11.6.

11.2 Identification of the SRM

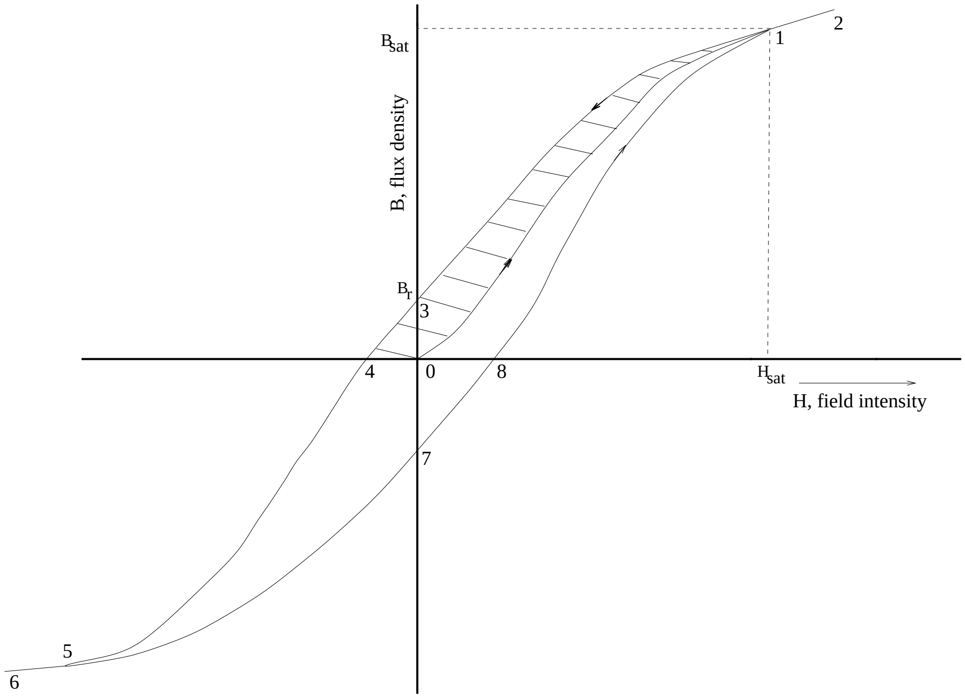

Figure 11.1: Magnetic hysteresis curve

The electrical characteristics of SRM are determined based on data obtained by off-line measurements. The procedure involves the following. First, align one of the motor phases with the closest rotor pole by applying quasi sinusoidal voltage in to the phase.

(1) Lock the rotor at the desired angular position.

(2) Apply quasi sinusoidal voltage waveform in to the associated phase and measure both phase currents and voltages with respect to time and store them.

(3) Increment the rotor position by some amount and go to step 1.

Then, the flux as a function of time can be calculated from the measurements by using the electrical equation of the motor (assuming independent phases)

$$\lambda(t) = \int_{t(0)}^{t} (v(t') - Ri(t'))dt' + \lambda(t(0)) \tag{11.1}$$

where the phase resistance R can be obtained by dc measurements. $\lambda(t(0))$ can be assumed to be zero when the current waveform crosses the zero amperes. This assumption is practically valid for soft iron (small B_r in Fig. 11.1). Note that application of a sinusoidal waveform in to motor phase is moving along the trajectory designated by points **1** through **8** on Fig. 11.1 (point **0** is the starting point when the remanent magnetization B_r is removed by some external means). If the remanent magnetization is high, it can be estimated; here we assumed that it is small. The remaining task is to find a two dimensional parameterization for the flux, $\lambda(\theta, i)$, both in terms of position, θ, and in terms of the current, i. This parameterization is achieved via two step least squares curve fitting that we describe later. The basis functions used are trigonometric functions that result in a linear fit in terms of the parameters. The torque function is calculated through co-energy using the formula

$$\tau_{M_k}(\theta, i) = \frac{\partial}{\partial \theta} \left[\int_0^i \lambda_k(\theta, i') di' \mid_{i=\texttt{const}} \right] \tag{11.2}$$

(This expression would simplify to $\tau_{M_k}(\theta, i) = \frac{1}{2} i^T \frac{dL(\theta)}{d\theta} i$ in the linear magnetics context which is not assumed here.)

The fit for the flux function, $\lambda(\theta, i)$, and the produced motor torque, $\tau_{M_k}(\theta, i)$, for the "8/6" ($N_p = 4$ phase, $N_r = 6$ rotor pole) SRM used in our simulations and

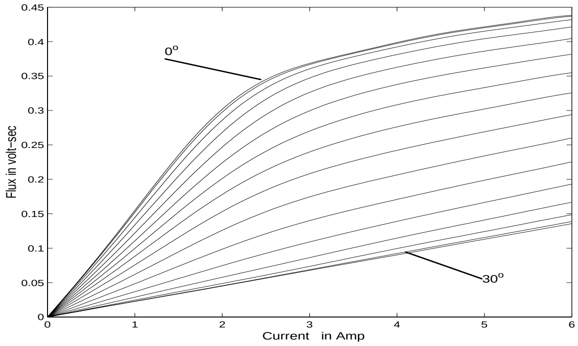

Figure 11.2: A fit for measured flux for different θ

experiments are shown in Figures 11.2 and 11.3 and are fairly general in their forms.

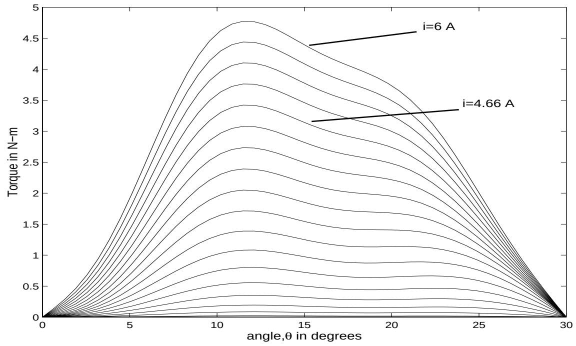

Figure 11.3: Torque function for different current levels

The mechanical parameters J and B can be calculated using spin down tests where the τ_L and τ_M is zero in (9.1). Similarly as in voltages the speed signal is measured with respect to time and an exponential function, which is the solution of the mechanical equation without forcing term, is fitted to the data.

11.2.1 Modeling the flux current ralationship

In order to adequately model the effects of saturation and the dependence on the rotor position, θ, the flux-verse-current relationship for the SRM is approximated by trigonometric functions in both λ and θ. The assumption that the current is approximated by trigonometric functions is not physical (because it results in a periodic flux function in current i which is not the actual case), but since we have measurements only for a limited range of currents, we can have use it for an accurate approximation over the available data. The resulting parameterization is not valid outside the range of data. The procedure is as follows. A model is selected first

$$\lambda_n(\theta, i_n) = \sum_{k=1}^{N_1} \alpha_k^m(\theta_n)\sin(2\pi i_n k/I_{per}) \tag{11.3}$$

where I_{per} is some artificial period of current and, is assumed to be 4-to-5 times larger than the maximum allowable phase current.

$$\alpha_k^m(\theta_n) = \sum_{l=0}^{N_2} \beta_{kl}\cos[N_r\theta_n(N_2 - l)] \tag{11.4}$$

where N_r is the number of rotor poles. N_1 and N_2 are the order of the trigonometric basis function used. The superscript m for α_k^m stands for different fixed rotor positions. For example $m = 0$ is for $\theta = 0$ and $m = k$ is for $\theta = (m-1)\Delta\theta$ where $\Delta\theta$ is the resolution in the measurement of rotor position. The expansion coefficients β_{kl} are found in the following manner. First an N_1th order trigonometric expansion of the form shown in Equation (11.3) is fit to each of the separate fixed rotor position measurements of voltage and current in a least-square sense. The yields the value for α_k^m for $k = 0, 1, ..., N_1$ at all discrete positions of θ, which can be put in a matrix form as follows

$$\begin{bmatrix} \alpha_0^0 & \alpha_1^0 & \cdots & \alpha_{N_1-1}^0 \\ \alpha_0^1 & \alpha_1^1 & \cdots & \alpha_{N_1-1}^1 \\ & & \vdots & \\ \alpha_0^{M-1} & \alpha_{M-1}^1 & \cdots & \alpha_{N_1-1}^{M-1} \end{bmatrix}$$

where M is the number of measurements in angular position θ. Next, an N_2-th order cosine series of the form shown in Equation (11.4) is fit to the M points in column once again in a least-square fashion yielding $N_2 + 1$ coefficients β_{0l}. This step is repeated for the other columns to determine the remaining β_{kl}'s, $\beta_{1l}, \beta_{2l}, ..., \beta_{N_1 l}$.

11.2.2 Estimation of the J and B of the motor

The solution of the mechanical equation in a spin–down test can be found using (9.1) ($\tau_M = 0, \tau_L = 0$) as

$$\omega(t) = Ce^{-t/(J/B)} \tag{11.5}$$

Taking the logarithm of both sides of the above results in

$$\log(\omega(t)) = \log(C) - \frac{B}{J}t \tag{11.6}$$

which puts it in to a linear form in the unknown constant $\log(C)$ and in the reciprocal of time constant $\frac{J}{B}$. The next step is to apply the least squares technique, where $\log(\omega(t))$ and t are the measured quantities. Clearly, with this step alone only the time constant can be found. To find J and B separately, the experiment should be repeated by mounting a metal disk of known inertia on the shaft (from the known mass and radius of the disk, the formula $\frac{1}{2}MR^2$ gives the moment of inertia.) Then J and B can be found by solving the two equations in two unknowns.

11.3 Control Design

The control structure involves two stages: first, a given torque reference is translated to current actuation, as discussed in the subsection Section 11.3.1; second, a closed loop compansator that provides a produced torque reference is described in Section 11.3.2.

11.3.1 The Commutation Strategy

Positive torque production by a single phase is restricted by position and available currents, and two consecutive phases are typically excited to produce a smooth torque. In an “8/6” SRM, phase–currents waveforms are periodic, with a 60° period, and currents are kept at zero during the the second half of the period to avoid generation of braking torque. To maintain the same control policy in all phases, current waveforms for the various phases (for a given produced torque reference τ_{ref}) are identical, subject to an appropriate angular shift. In particular, the currents of companion torque–producing phases, at any given motor position, are shifted by 15° [95]. The condition restricting current waveforms is thus that the sum of torques produced by the angular sections $0^o - 15^o$ and $15^o - 30^o$ should be constant. An implementation of this policy requires precise representations of the nonlinear function $i \mapsto \tau_M(\theta, i)$ (from Figure 11.3), and of its inverse. Feedback linearization controllers require on-line evaluations of these functions, typically by means of representations involving many parameters, or by very large lookup tables. This reduces the practical value of such schemes, or mandates simplifications, resulting in inaccurate torque production and ripple.

One possible solution, termed "torque sharing", is to pre-calculate and parameterize current waveforms as functions of position and τ_{ref}. For example, in [82] neural networks are used for this purpose. However such parameterizations tend to be computationally intensive when high accuracy is required. It is suggested here that a very easily computable torque–sharing current waveform be used, and that the resulting torque ripple be reduced by an adaptive controller. For the purpose of demonstrating our point, our selection in the presented experiments and simulations is a very simple two parameter model

$$i_{p,1} = \sin(6\theta)(\alpha + \beta\tau_{ref}) \tag{11.7}$$

where α and β are design variables. Comparing this parameterization (for a fixed level of τ_{ref}) with an ideal torque sharing current waveform (Figure 11.4), it is evident that (11.7) will result in torque ripple. The elimination such ripple will be done by the adaptation of τ_{ref}, as described in section 11.3.2. Indeed, Figure 11.5 compares the torques produced for one desired τ_{ref} level when the accurate and the simplified waveforms (11.7) are used($\alpha = 0, \quad \beta = 1.58$). In fact, the use of adaptation eliminates the need for precisely known constants α and β, and the pair $\alpha = 0$ and $\beta = 1$ is acceptable. Note that the torque ripple generated due to the use of simplified torque sharing current waveform is periodic with a 15° period in an 8/6 SRM.

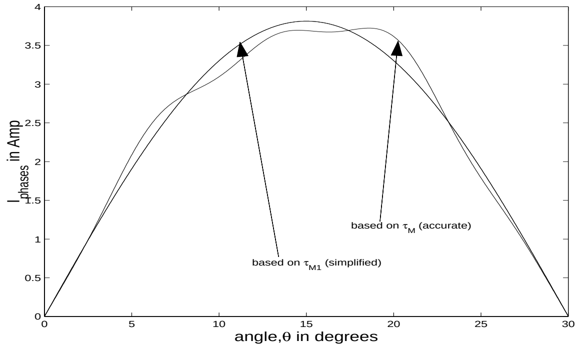

Figure 11.4: Current waveforms for different models

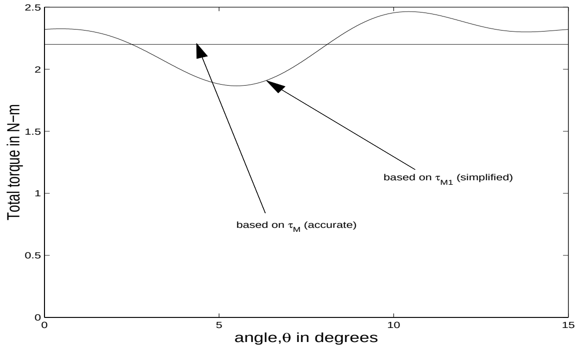

Figure 11.5: Corresponding torques for Figure 4

11.3.2 Closed loop and Adaptation law

The mechanical equation of the motor can be rewritten as follows

$$J\,\frac{d\omega}{dt} = \tau_{M1} \; - \; B\omega \; - \; (\tau_L + \tau_{M1} - \tau_M) \tag{11.8}$$

where τ_{M1} stands for the torque predicted by the simplified model; i.e. $\tau_{M1} = \tau_{ref}$ in (11.7). The term $\mathcal{T}_L := \tau_{M1} - \tau_M + \tau_L$ is referred to as the "generalized load". The closed loop speed control will be based on a dynamic estimate $\widehat{\mathcal{T}}_L$ of $\mathcal{T}_L$ that we introduce next. Assuming a constant τ_L and position–periodic current actuation, $\mathcal{T}_L$ is periodic and can be expanded in Fourier series:

$$\mathcal{T}_L = a + \sum_{k=1}^{\infty} c_k \cos(kN\theta) + s_k \sin(kN\theta) \tag{11.9}$$

where $N = 24$ in an "8/6" SRM. For simplicity (11.9) is abbreviated as $\mathcal{T}_L = F_{0,\infty}(\theta)C_{0,\infty}^T$, where $F_{0,n}(\theta) := [1, \cos(N\theta), \sin(N\theta), ..., \cos(nN\theta), \sin(nN\theta)], and\, C_{0,n} := [a, c_1, s_1, ..., c_n, s_n]$. The estimate $\widehat{\mathcal{T}}_L$ is expressed as

$$\widehat{\mathcal{T}}_L = F_{0,n}(\theta)\widehat{C}_{0,n}^T \tag{11.10}$$

where n designates the highest harmonic used (with the total of $2n + 1$ coefficients). Only a finite number of harmonics of practical significance and, the estimated vector of coefficients $\widehat{C}_{0,n}$ is obtained using a dynamic adaptation rule that utilizes speed error measurements

$$\tfrac{d}{dt}\widehat{C}_{0,n}^T \quad = \quad -J\,,\,{}^2F_{0,n}(\theta)^T e_\omega \tag{11.11}$$

where $e_\omega = \omega - \omega_d$, ω_d is the reference speed, $, \ = diag(\gamma_0, \gamma_1, \gamma_2, ...) > 0$ and the γ_i's are design parameters, determining the rate of adaptation.

To close the loop, the reference torque in (11.7) will be τ_{M1}, selected as

$$\tau_{M1} = J\frac{d\omega_d}{dt} + B\omega_d + \widehat{\mathcal{T}}_L - \alpha e_\omega \tag{11.12}$$

where the proportional negative feedback $-\alpha e_\omega$ acts as an incremental friction to accelerate convergence of the speed error; other terms in (11.12) are chosen to satisfy (11.8) at the desired speed and subject to the estimated "generalized load". In particular, the harmonic components of $\widehat{\mathcal{T}}_L$ translate, via (11.12) and (11.7), to harmonic modulation of the commanded currents. These will be used to reduce the actual torque ripple, as shown next.

Using (11.8) and (11.12), the dynamics of the speed error e_ω becomes

$$J\frac{de_\omega}{dt} = -(B+\alpha)e_\omega + F_{0,n}(\theta)\widetilde{C}_{0,n}^T - F_{n+1,\infty}(\theta)C_{n+1,\infty}^T \tag{11.13}$$

where $\widetilde{C}_{0,n} = \widehat{C}_{0,n} - C_{0,n}$. To formulate a combined error dynamics equation for speed and parameters, we introduce

$$\epsilon = \left[\begin{array}{cc} Je_\omega & \widetilde{C}_{0,n},\ ^{-1} \end{array} \right]^T \tag{11.14}$$

Then (11.13) and (11.11) yield

$$\dot{\epsilon} \ = \left[\begin{array}{cc} -(B+\alpha)/J & F_{0,n}(\theta), \\ & \\ -,\ F_{0,n}(\theta)^T & O_{2n+1\times 2n+1} \end{array} \right] \epsilon \ + \left[\begin{array}{c} -F_{n+1,\infty}(\theta)C_{n+1,\infty}^T \\ \\ -,\ ^{-1}\frac{d}{dt}C_{0,n}^T \end{array} \right] \tag{11.15}$$

The first entry of the inhomogeneous term becomes smaller as n increases, and the second entry is zero along ideal (periodic) trajectories, where the harmonic coefficients in (11.9) are time invariant.

The homogeneous part of (11.15) can be written as

$$\dot{\epsilon} \ = (\mathcal{D} + \mathcal{S}(\theta))\epsilon \tag{11.16}$$

where $\mathcal{D} = diag\{-(B+\alpha)/J,\ 0_{2n+1}\}$ and $\mathcal{S}$ is skew symmetric. A candidate quadratic Lyapunov function is selected as $V = 0.5\epsilon^T\epsilon$, and along trajectories of (11.16) it satisfies

$$\dot{V} = -J(B+\alpha)e_\omega^2 \tag{11.17}$$

Since the origin is the only invariant set of (11.16), where $e_\omega = 0$, asymptotic stability follows from LaSalle's Theorem [52]. In fact, the stronger property of uniform exponential stability of (11.16) can be established, using the fact that the periodic linearization of the pair $[\mathcal{D}+\mathcal{S}(\theta),\mathcal{D}]$, around the ideal limit trajectory, is observable [8]. This stronger property also implies BIBO stability of the inhomogeneous system (11.15).

One point we wish to stress here is that the expansion (11.9) is, in principle, operating-point dependent. The simplicity of our scheme is due to the fact that we do not seek parameterization with respect to *both* position and torque reference (or current). The penalty that we incur is the possible requirement for re-adaptation following a change in operating point.

11.4 Simulations and Experimental Results

Simulation tests of the proposed algorithm are based on data from 350W, 8/6 SRM (Magna Physics model #124 SR), whose flux and torque characteristics are shown in Figures 11.2 and 11.3. Simulations of the motor dynamics rely on a detailed and accurate nonlinear model of the motor, while control design is based on the simple family (11.7) of approximate torque sharing current waveforms, together with adaptation on the zero and the first two harmonics of $\mathcal{T}_L$.

Figure 11.6 shows the torque generated by the motor when first two harmonics of $\mathcal{T}_L$ are estimated. The estimates of the five harmonics coefficients converge to constant values, as displayed in Figure 11.7. In Figures 11.8 and 11.9 simulations are repeated for the case when only the dc term is estimated (other control parameters

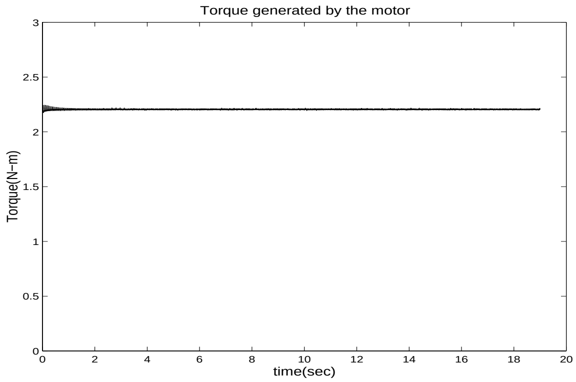

Figure 11.6: Torque produced by the motor with harmonic adaptation

are unchanged). Since the torque ripple introduced due to simplification is periodic, the estimated dc component in this case is also periodic; this fact is demonstrated in Fig. 11.8. It is worth pointing out that, due to noise, it may be impossible to implement such an aggressive controller in actual experiments. Figure 11.9 shows the corresponding torque. The signal power in the torque ripple in this case is now approximately ten times larger than that achieved when harmonic adaptation is used, demonstrating the benefit of adaptation.

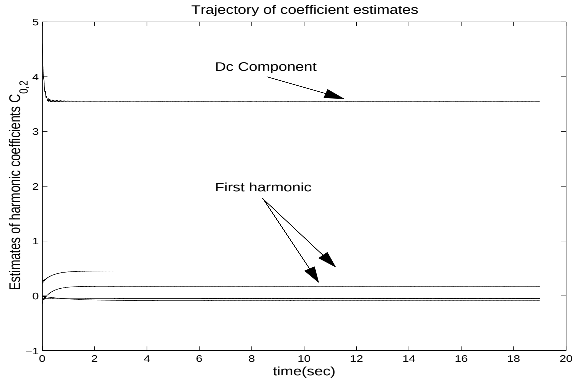

Figure 11.7: The estimated harmonic coefficients

The algorithm was tested experimentally with our 350W SRM at a constant speed

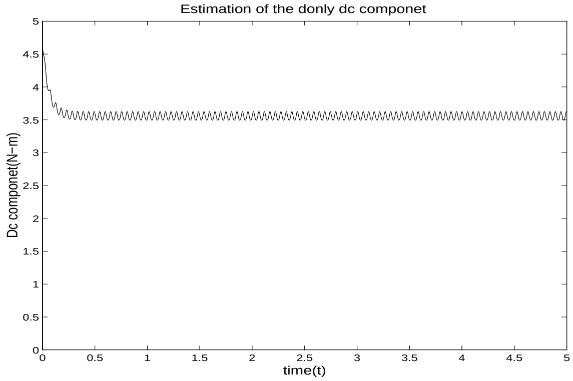

Figure 11.8: Estimate of dc component when harmonic adaptation is eliminated

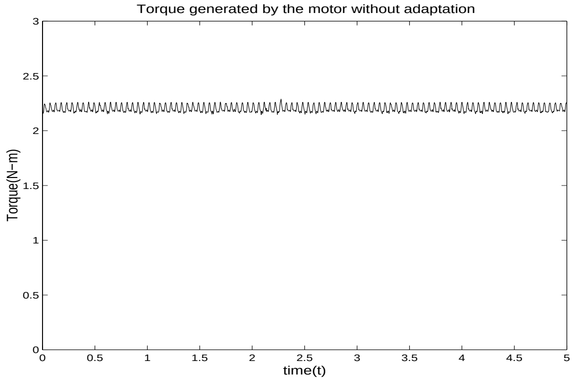

Figure 11.9: Torque generated under only dc adaptation

reference. An encoder providing 2000 incremental angular positions per revolution is mounted on the shaft. The speed estimate is obtained by counting the number of a high frequency clock pulses between two encoder lines. A hysteretic dynamo-meter, model HD-705, made by Magtrol, is used to load the SRM. The algorithm is realized on a Texas Instruments TMS320C31 DSP based dSPACE controller (DS1102). The produced torque is measured using non-contact torque meter (Himmelstein MCRT 4901V) with the measurement bandwidth of 300 Hz (this torque measurement is not used in control). Double-flex couplings were used to connect the motor, torque-meter and the load cell, and the test stand was placed on vibration isolation mountings. The spectrum of the produced torque is measured using a dynamic signal analyzer, model

Hewlett Packard 35665A, with “flat–top” windowing which offers high amplitude accuracy (±0.005 dB), but somewhat lower frequency resolution. The experimental set up employs a half-bridge inverter with two transistors and two diodes per phase; it operates in a hysteretic current mode with “hard chopping [65]” (i.e., the voltage on an active phase is either positive or negative dc voltage); the hysteresis band is 0.2 A. The reference currents are realized through 12–bit DA converters.

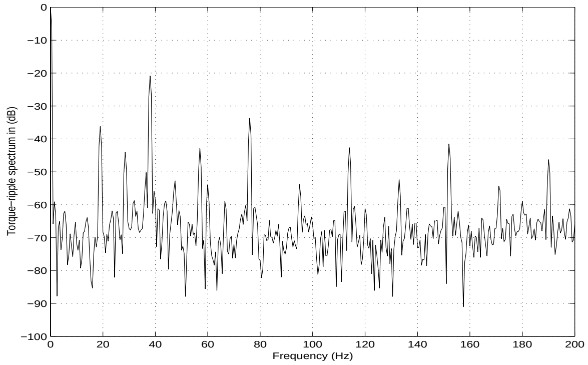

Figure 11.10: Experimental results: torque-ripple spectrum without harmonic adaptation

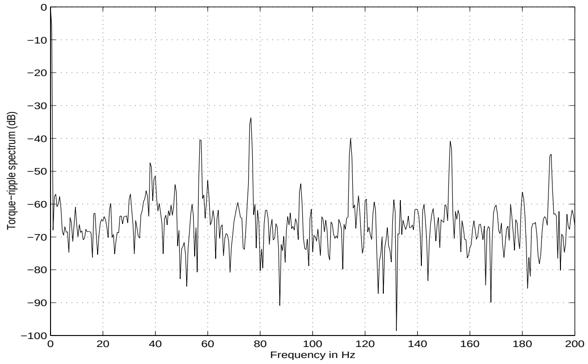

Figure 11.11: Experimental results: torque-ripple spectrum with harmonic adaptation

Figure 11.10 shows the experimental results when there is no adaptation of harmonics, while Fig. 11.11 shows experimental results including adaptation (in both cases the torque spectrum is normalized at dc and the frequency of the fundamental is 38Hz). Note that the adaptation attenuates the main torque harmonic below -40 dB (approximately -20dB attenuation when compared to the non-adapted case). Observe that in Figure 11.10 there are two harmonics at approximately 19 and 28.5Hz that are due to the fact that the phases are not identical because of the motor construction and because of non-identical implementation of the analog hysteretic control circuit in the various phases. We eliminate those sub-harmonics by including them in the adaptation mechanism. The overall torque ripple spectrum (up to the bandwidth of the torque meter) is below -33 dB. In the experiment the motor is loaded ($\approx$ 2.47 Nm), so that it is driven in to magnetic saturation. In both simulations and experiments the reference speed is low (10 rad/sec); this avoids filtering of torque harmonics by the mechanical subsystem of the motor (which acts as low pass filter). The adaptation procedure is intentionally slow to suppress the effect of noise in the speed measurements that we discuss in more detail in Section 11.5.

11.5 Limitations of the adaptive algorithm

The control algorithm is basically composed of two parts:

- The coarse tuning part is responsible for bringing the speed to the desired speed reference trajectory. This subsystem is fast, and can be manipulated according to the needs of the application as long as the hardware can provide the required actuation.

- The fine tuning part includes the adaptation of higher (non-dc) harmonic components. The harmonic estimation task needs to be slower than the estimation of the dc component, as the dc component is responsible for producing a stationary speed error spectrum (as it renders the "generalized load" periodic).

The reference current waveforms generated by the controller depend on the actual motor, the converter hardware, and the simplified torque function used. Once a simplified torque function is specified, the reference currents generated by the controller are unique. In the following subsections we quantify the main limitations of the adaptive algorithm: 1) the resolution of the inverter (as currents are realized via analog hysteretic control), 2) the useful signal content in the measured quantities, 3) the noise present in the speed measurement. Our analytical and experimental data show that we can estimate the two sub-harmonics and one main harmonic, as we explain next.

11.5.1 Limitations due to hysteretic current control

It turns out that the main limitation of the adaptive algorithm arises from the hardware implementation of the current hysteretic control. To asses the importance of this limitation, we provide simulations of the inverter and compare the spectra in cases that reference currents can be realized either fully (inverter is an ideal current source), or approximately (by a finite hysteretic current band). In ideal inverter case, reference currents generate a very low torque ripple (the spectrum of the simulated torque ripple is around -140dB for the adapted harmonics). Figure 11.12 shows a very good hysteretic approximation of reference currents; the torque ripple spectrum corresponding to the approximation is shown in Figure 11.13. Thus even with a very good hysteretic approximation (and high switching frequency of up to 10KHz) the harmonics can not be eliminated completely. In our simulations, when the switching frequency is reduced $\approx$ 10 times , the level of the torque spectrum raises $\approx 15dB$. It is thus clear that if the harmonic coefficient of the torque ripple is too small, the inverter may be unable to realize the part of the reference current that eliminates that component.

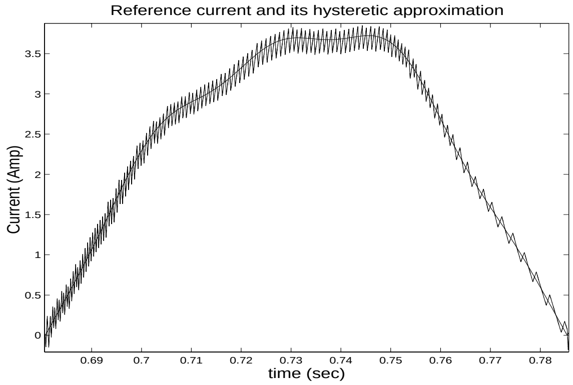

Figure 11.12: Hysteretic approximation with high supply voltage

11.5.2 Limitations due to quality of speed measurement

The controller critically depends on the quality of speed measurement. The traditional method of obtaining the speed estimate through a band-limited differentiation of the position (encoder) signal may prove suboptimal for all harmonics of interest. The differentiation amplifies noise, and adds delay to the estimate. Moreover, the quality

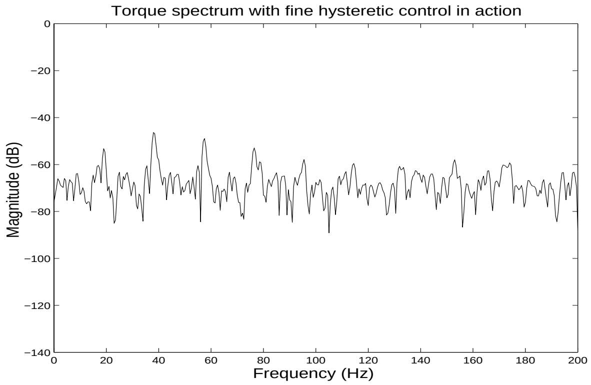

Figure 11.13: Torque ripple spectrum with better hysteretic approximation

of the speed estimate obtained through differentiation decreases at low speeds. For these reasons, we calculated a speed estimate by counting the number of pulses of a high frequency crystal clock between two encoder lines($\hat{\omega} \approx \frac{\theta_0}{nT_{clck}}$, where n is the number of clock ticks). This approach still does not resolve the issue of delays that are important for higher harmonics. As a practical rule, the delay of the filter (regardless of speed measurement technique) at the frequency of the harmonic to be estimated should be less than one quarter of the period of the harmonic being estimated to result in satisfactory closed–loop operation.

The torque harmonic to be estimated should be visible in the speed signal and the noise level due to speed measurement should not corrupt the signal. For this reason, in our experiments we kept the motor speed low, so that several torque ripple harmonics can be recovered from the speed signal. To assess the amount of noise introduced in the measured quantities, we analyze the driving term of the adaptation rule $\beta(t) = e_{\omega}(t)\sin(Nk\theta)$. While the details are presented in Appendix C, here we summarize the main result

$$E|\widehat{\beta}(t) - \beta(t)|^2 \approx sin^2(Nk\theta(t_m))((S_m - S_{m+1})^2 + \frac{T_{clck}^2 S_m^4}{6\theta_0^2}) \tag{11.18}$$

In our experimental set-up this quantity can reach numerical values around -49dB in the frequency range from DC to several times the fundamental frequency $f = 38Hz$.

Another important parameter is the number of encoder lines, which should be high enough so that the number of encoder readings per period satisfies the Nyquist rate for the estimated harmonic. Moreover, the computational cycle time should also be fast enough (above the Nyquist rate for the highest harmonic of interest) to capture the variation in the speed spectrum.

11.5.3 Limitations due to the controller structure

Next, we analyze the signal content of the measured data by assuming that the closed loop system acts as a filter on the torque ripple. The input to the filter is the torque ripple and the output is the associated speed ripple, and the filter represents the closed loop mechanical system. The speed ripple signal power at a specific harmonic is calculated from

$$\mathcal{P}_f(\omega_{ripple}) \quad = \quad |\frac{1}{Js + (\alpha + B)}|^2 \mathcal{P}_f(\tau_{ripple}) \tag{11.19}$$

where $\mathcal{P}_f$ stands for the signal power in the harmonic of frequency f, and $s = j2\pi f$. Observe that as the frequency increases, the signal power in the speed decreases because of the low–pass filtering action. Note that we have approximate knowledge of torque harmonic power, which can be used above to estimate the signal power in the speed. From the signal power level and the noise power level in the data we can derive conclusions about the highest harmonics that can be estimated. From a practical standpoint, if the noise power is 25% or more of the the signal power, then the harmonic can not be successfully estimated. Our calculations (with details given in the Appendix) show that the noise power in the speed signal is approximately -49dB in the frequency range from zero to several times the fundamental. From the measured torque ripple and (11.19), we calculate the signal power in the speed, and it turns out to be -50dB at $f = 57Hz$ and -44dB at $f = 76Hz$. These calculations are based on parameter values of our experimental setup where $J = 4e - 3\ kg\frac{m}{s^2}$ and the contribution of the term $(B + \alpha)$ can be neglected above dc. The torque ripple information is obtained from the dynamic spectrum analyzer (data are shown on Fig. 11.11). Comparing the signal power and the noise power in the speed, we note that they are comparable at $f = 57Hz$. Thus we conclude that frequency components above approximately $57Hz$ can not be estimated, as at higher frequencies the signal power decreases, while the noise power does not.

11.6 Conclusions on SRM

An adaptive SRM control algorithm for torque-ripple minimization is proposed in this chapter and verified in simulations and experiments. The algorithm alleviates on effects of modeling errors and considerably reduces the computational burden associated with the use of accurate but complex torque sharing current waveforms. It combines simple waveform parameterizations with dynamic estimation of low harmonic components of the resulting torque error to reduce the torque ripple. Comparison of the same controller with and without harmonic adaptation reveals the benefit of the proposed method. Finally, analysis on the limitations of the adaptive algorithm are provided.

Chapter 12

Introduction on Modeling of PWM Systems

12.1 Background

The common modeling approach to systems with switched power supplies [67] is to replace the pulse-width modulated (PWM) power supply unit with a fixed gain. To justify this idealization, the PWM input signal should be slowly varying in comparison with the switching frequency, and the switching frequency should be fast enough so that ripple effects on the feedback signal can be neglected. There are applications, however, in which the type of synthesized waveform, characteristics of employed semiconductor devices, or difficulties in heat removal lead to fairly low switching frequencies. This slow switching frequency causes the ripple to become considerable. This thesis deals with two major aspects associated with high ripple magnitude. First, a new equivalent PWM gain in a steady state is derived as a nonlinear function of the operating point. Second, it is shown that a system may have a non-constant duty ratio, even when input signals are constant, which may affect performance in several ways.

It is shown that delays, e.g. due to digital implementation, can substantially influence both system performance and ripple patterns. When switching is slow, the delay should not be neglected. In fact, depending on system conditions, a delay can either decrease or increase the PWM gain. The introduction of delay into the control loop also makes the system more prone to PWM switching aperiodicity. While the difference in the effective gain can be compensated in the closed-loop design, the loss of PWM periodicity, e.g. period doubling, may lead to high magnitude and lower frequency of the ripple with implication on performance such as lower power efficiency, saturation, etc.

Subharmonic oscillations in classes of closed-loop PWM power converters have been well documented, of which [87, 28, 108] are a few examples. Period doubling and bifurcations have been detected in current controlled converters and must always be avoided in practice.

This thesis attempts to analytically generalize sometimes heuristic results from power converters to arbitrary bilinear systems and to systems with delay. When the delay is set to zero and a specific circuit topology is assumed, the known stability results are recovered.

In order to analyze the complicated behavior of the time-varying PWM system, a suitable approximate model is needed. As it is well known, open-loop pulse-width modulated system can be modeled as a piecewise linear time invariant. Then an exact discrete time model can be obtained, where the time varying dynamic matrix depends on the duty cycle. If a feedback controller is used, the duty cycle will depend on the system state variables, and the closed-loop system will be non linear. The conventional averaging approach approximates such a system by linear time invariant one, and PWM block by constant gain. The main assumption which justifies this approach is that input signal of the PWM is slowly varying compared to switching frequency. Unfortunately, if the switching frequency is slow, in the closed-loop system, the high frequency harmonics produced by PWM may appear on the input of the PWM. This violates the conventional assumption that the PWM input signal is constant. It was shown in [55] that, by means of modified averaging, the PWM can be approximated as a nonlinear gain, which is always less than conventional. This model uses a periodic ripple function to improve averaging approximations. Compared to conventional averaging [63] which approximates the PWM as a constant gain and neglects ripple, this approach provides a better approximation of the system state trajectory, eliminates a DC offset error in steady state, and yields an accurate estimate of the ripple magnitude.

The analysis in this thesis is based on formal mathematical methods for periodic differential equations, and is limited only by two common assumptions:

- The system is linear in each of the switching intervals;
- The system trajectory in every switching time interval may be approximated

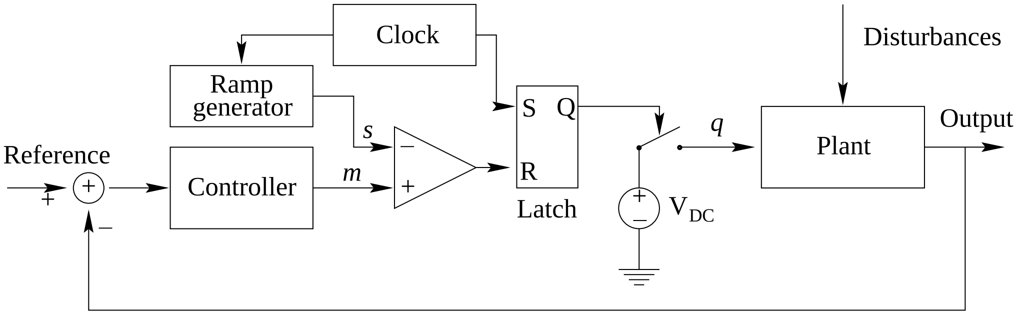

Figure 12.1: Block diagram of a PWM actuated system.

by linear segments.

Most of the available literature in the power converters subharmonic oscillations limits the discussion to some specific circuit topologies, e.g. boost or buck converter, and does not include the influence of delay. This work generalizes the averaging method of [55] to linear systems with PWM and delay, and then this new result is used to obtain a piecewise affine discrete time model, and to derive a criterion for PWM periodic operation.

The problems similar to DC PWM controlled systems arise also in AC PWM systems, where typically three phase sinusoidal voltages are produced. High-power industrial AC drives and railway traction are applications were thyristors and, increasingly, GTO's dominate as switching elements. Switching losses in such systems account for a considerable amount of the total losses [45]. Hence, the switching frequency is often kept at low values of only few hundred Hz [44]. A reduction of switching frequency generally results in increasing current distortion, and, consequently, machine torque harmonics and higher machine losses.

The effects of low switching frequency in PWM-controlled AC drives are more complicated compare to the same effects in DC systems. As a representative example of such system a permanent magnet synchronous motor drive will be considered. Control of the synchronous AC motor in the rotor reference frame ("d-q coordinates") simplifies the controller design and can be considered as a standard technique. However, the commonly used vector space implementation of the three phase PWM requires the stationary α-β representation of the voltages. The difference in the coordinate systems makes the ripple effect more difficult to study, and this effects are usually ignored by approximating the PWM as a linear gain. To analyze the effect of the current ripple a more accurate model of the PWM is needed. The d-q reference frame for such a model is the natural choice, as all quantities are constant in a steady state and analytical formulas related to averaging theory can be used.

12.2 General class of systems under consideration

This subsection discusses a general setup of DC PWM controlled systems under consideration and presents an outline of the thesis. The AC PWM controlled system can be considered, with certain assumptions, as a generalization of the DC case and will be discussed in details in Chapter 18.

Fig. 12.1 depicts a block diagram of the closed-loop system, where the plant and

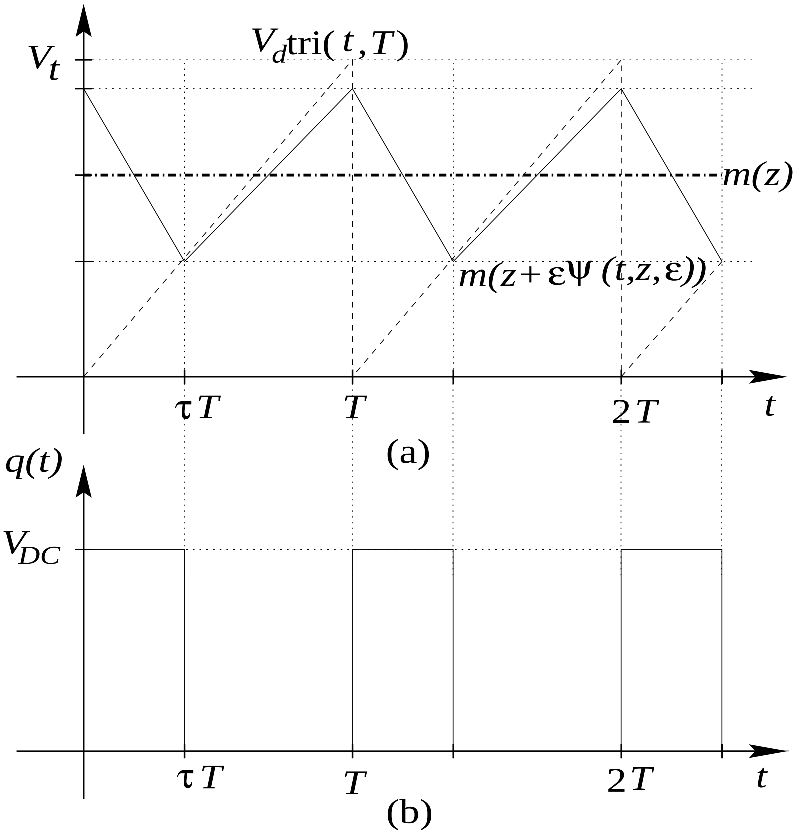

Figure 12.2: PWM input a) and output b) voltages.

the controller are linear time invariant (LTI). The output signal of the controller, m, is compared with a sawtooth function $s(t) = V_d\text{tri}(t, T)$ of period T and maximum V_d. This generates the on-off driving signal for the switch. Specifically, the switch is turned "on" at the beginning of the cycle i.e., at $t = nT$; while the switch is "on", the controller output m decreases; at $m = s$ the switch is turned "off" and remains so until the next cycle begins, as shown in Fig. 12.2. (The meaning of "**z**" and "Ψ" in Fig. 12.2 will be clarified later.) The PWM output voltage is $q(t) = V_{DC} \cdot u(m - V_d\text{tri}(t, T))$, where $u(\xi)$ is the (Heaviside) unit step function, i.e., $u(\xi) = 1$ for $\xi \geq 0$ and $u(\xi) = 0$ for $\xi < 0$. If m were a constant reference, the "classical" averaged output voltage of the PWM is $q_{av} = (V_{DC}/V_d)m$, whereby $K_{PWM} = V_{DC}/V_d$ is commonly referred to as the nominal gain of the PWM block [67]. In practice, however, PWM implementation introduces ripple (higher harmonics) into the plant state trajectory. This ripple is often fed back through the control loop, and causes ripple in the trajectory m, as illustrated by the schematic curve in Fig. 12.2(a). As a result, the classical averaging assumption that m remains constant over a period is invalid. As noted in [55] for DC-DC converters, one effect of ripple in m is a change in the equivalent effective gain when the PWM is replaced by such a gain in an averaged model, a phenomenon that becomes more pronounced at lower switching frequencies.

The starting point of this work is the analytical framework of [55]. Chapter 14 quantifies deviations from standard (idealized) models, illustrated by an example of a fractional horse power DC drive. Chapter 15 extends the averaging technique to include delay effects and presents experimental results with the DC servo motor to support analysis. The effects of low switching frequency is to reduce the effective PWM gain by up to 20% at low voltages. Delays make the gain *larger* than the idealized gain at low voltages. The relative simplicity of the gain calculation formulas makes them candidates for design toolboxes for engineers involved in control synthesis of high-performance PWM systems. In Chapter 16 a discrete-time dynamic modeling procedure is presented. A necessary and sufficient condition for existence of a T-periodic steady state equilibrium for the approximate system is developed. It is shown that obtained criterion simplifies to the well known result [98, 101], when there is no delay, or the delay is small.

Chapter 18 is devoted to study of the AC PWM systems. In Section 18.2, a general setup for AC drive is presented. The voltage space vector strategy of controlling the PWM inverter is introduced in Section 18.3. An equation for open-loop gain and estimation of the current ripple magnitude are obtained in Section 18.5. In Section 18.6 the closed-loop PWM gain is discussed. The results obtained in this chapter are illustrated in the example of the permanent magnet synchronous motor drive.

Chapter 13

Averaging Theory

The method of averaging is a very commonly used technique in the analysis of periodic differential equations. The purpose of this chapter is to review some pertinent information about averaging theory. A rigorous mathematical justification of the basic theory can be found in [12, ?]; extensions to switching systems are discussed in [54, 53].

Consider a feedback controlled pulse-width modulated system with constant input signals where the plant and the controller are linear time invariant. It easy to check that the closed-loop system can be written in the form

$$\dot{\mathbf{x}} = \mathbf{A_0}\mathbf{x} + \mathbf{B_0}U + (\mathbf{A_1}\mathbf{x} + \mathbf{B_1})u(m(\mathbf{x}) - V_d\mathrm{tri}(t, T)), \tag{13.1}$$

$$m(\mathbf{x}) = \mathbf{C}U - \mathbf{K}\mathbf{x}, \tag{13.2}$$

where m is the input to the PWM, $\mathbf{x}$ is the combined state of the plant and the controller, and U is a vector of the reference and disturbances signals. In the example of the system shown in Fig. 12.1 the matrix $\mathbf{A_1} \equiv 0$. This matrix is non-zero when switching occurs between two LTI systems, such as in PWM boost power converters.

From here to the end of this chapter assume that the reference and disturbances are constant (or vary slowly). Then (13.1) fits into the general form

$$\dot{\mathbf{x}} = \varepsilon\, f(t, \mathbf{x}), \tag{13.3}$$

where $f(t+T,\cdot) = f(t,\cdot)$ is T-periodic and, $\varepsilon = T/t_c$, where t_c is the time constant of the dominant pole of the open-loop transfer function from the output of the PWM to its input. If ε is small, the solution $\mathbf{x}$ will vary slowly relative to the period T.

It should be mentioned that, originally, averaging was justified for systems with continuous right hand side, which is not true for system (13.1). To avoid this problem two possible approaches can be taken. The first is to approximate switching by continuous commutation function with sharp, but finite slope. Since the duration of the switching transient is negligible in comparison to the switching period, the time average of the right hand side in both cases will be almost identical.

The second approach is based on the Karatheodory extension of the concept of a differential equation [36]. The essence of this extension is that instead of differential equation, we consider an equivalent integral form. In the case than $f(t, \mathbf{x})$ is piecewise continuous in t, the integral form is still well-defined, even though (13.1) may be difficult to interpret rigorously.

The aim of averaging is to approximate the solution of (13.3) by the solution of an averaged time invariant system

$$\dot{\mathbf{z}} = \varepsilon\, g(\mathbf{z}), \tag{13.4}$$

where the function g is given by the time average $g(\mathbf{z}) = \frac{1}{T}\int_0^T f(t, \mathbf{z})dt$.

It was shown by Bogolubov [12] that given a desired closeness between $\mathbf{z}(t)$ and $\mathbf{x}(t)$ and an arbitrary positive constant κ, there exists ε_0 such that when $0 < \varepsilon \leq \varepsilon_0$, solutions of averaged model are indeed as close to solutions of original system as desired on a finite interval of length κ/ε. This result was extended to the infinite time interval in [91]. The smaller the value of ε is, the closer the agreement between solutions of the original and the averaged systems. A helpful perspective for understanding the role of ε_0 is to consider the analogy between averaging and linearization. Both can be classified as perturbation methods which yield simpler approximate models. Linearization provides a linear approximation to a nonlinear system, while averaging provides a time invariant approximation to a time varying system. In both cases, the simpler approximate model is exact at some nominal point. For linearization that point is in the state space. For averaging the point is in the parameter space, $\varepsilon = 0$ (i.e., infinite switching frequency, zero ripple solution). The simpler model is a good approximation in some neighborhood of the nominal point. Linearization considers a neighborhood in the state space, and averaging considers a neighborhood in the parameter space.

Define

$$\Psi(t, \mathbf{z}) = \int_0^t [g(\mathbf{z}) - f(s, \mathbf{z})]ds - c(\mathbf{z}), \tag{13.5}$$

where $c(\mathbf{z})$ chosen so that $\Psi(t, \mathbf{z})$ is zero mean. Since $g(\mathbf{z}) - f(t, \mathbf{z})$ is zero mean and

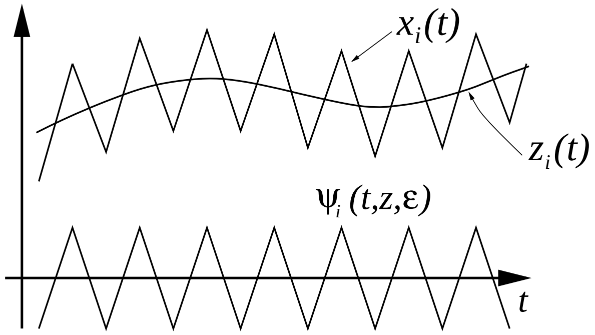

Figure 13.1: Averaged trajectory and ripple function.

T-periodic, the function Ψ is T-periodic as well. Consider the change of variables

$$\mathbf{x} = \mathbf{z} + \varepsilon\,\Psi, \tag{13.6}$$

where $\mathbf{z}$ takes the role of an averaged, slow trajectory and $\varepsilon\,\Psi$ is a ripple function (Fig.13.1). Differentiating this expression with respect to t and substituting for $\dot{\mathbf{x}}$ in (13.3) leads to the equation

$$\dot{\mathbf{z}} = \varepsilon\left[I + \varepsilon\,\frac{\partial\Psi}{\partial\mathbf{z}}\right]^{-1}\left[(f(t,\mathbf{z}) - \frac{\partial\Psi}{\partial t}) + (f(t,\mathbf{z}+\varepsilon\,\Psi) - f(t,\mathbf{z}))\right] \tag{13.7}$$

This equation is a perturbation of the averaged system (13.4). The error is introduced by approximating $\left[I + \varepsilon\,\frac{\partial\Psi}{\partial\mathbf{z}}\right]^{-1}$ by I, and by approximating $f(t,\mathbf{z}+\varepsilon\,\Psi)$ by $f(t,\mathbf{z})$. As $\varepsilon \to 0$ this error becomes small, and can be neglected. In practice $\varepsilon \neq 0$, but the error due to the approximation of $f(t,\mathbf{z}+\varepsilon\,\Psi)$ by $f(t,\mathbf{z})$ can be eliminated by a technique proposed in [55]. The idea is to redefine the functions g and Ψ so that they will simultaneously satisfy the following equations

$$g(\mathbf{z},\varepsilon) = \frac{1}{T}\int_0^T f(t,\mathbf{z}+\varepsilon\,\Psi)dt, \tag{13.8}$$

$$\frac{\partial \Psi(t, \mathbf{z}, \varepsilon)}{\partial t} = g(\mathbf{z}, \varepsilon) - f(t, \mathbf{z} + \varepsilon\,\Psi). \tag{13.9}$$

It is a difficult task to solve these equations in general, but using the special properties of (13.1) it is possible to obtain a good approximate solution. Let τT be the instant of time when the Heaviside step function switches from one to zero, or equivalently when $m(\mathbf{x}) = V_d \mathrm{tri}(t, T)$. Then $\tau \in [0, 1]$ and equals to the duty ratio. To derive a closed form solution the following properties of the components Ψ_i of the vector function Ψ will be postulated:

1. Ψ_i is zero average over both $[0, \tau T]$ and $[\tau T, T]$;
2. Ψ_i is a triangle wave (see Fig. 13.1);

Assumption 2 introduces some error due to replacing exponential curves by straight lines. The accuracy of this approximation is dependent on the decay rate of solutions of (13.1). For example, if $T/t_c < 0.1$ the calculations show that the approximation error will be less than 1%. Under the above assumptions g can be explicitly evaluated by noting the following facts:

- $\frac{1}{T}\int_0^T (\mathbf{A_0}(\mathbf{z} + \varepsilon\,\Psi) + \mathbf{B_0}U)dt = \mathbf{A_0}\mathbf{z} + \mathbf{B_0}U,$
- $\frac{1}{T}\int_0^T \mathbf{A_1}\Psi(t, \mathbf{z}, \varepsilon)u(m(\mathbf{z} + \varepsilon\,\Psi) - V_d \mathrm{tri}(t, T))dt = 0$,
- $\frac{1}{T}\int_0^T (\mathbf{A_1}\mathbf{z} + \mathbf{B_1})u(m(\mathbf{z} + \varepsilon\,\Psi) - V_d \mathrm{tri}(t, T))dt = (\mathbf{A_1}\mathbf{z} + \mathbf{B_1})\tau.$

Combining these facts the averaged model becomes

$$\dot{\mathbf{z}} = \mathbf{A_0}\mathbf{z} + \mathbf{B_0}U + \tau(\mathbf{A_1}\mathbf{z} + \mathbf{B_1}). \tag{13.10}$$

The difference between this formula and the conventional averaged model (without the modification from [55]) is only in the way τ is calculated. In the conventional method $\tau = m(\mathbf{z})/V_d$, which does not take into consideration the influence of ripple on the PWM input signal. To calculate τ using the modified method, we first find the function Ψ explicitly. Substituting explicit expressions for g and f into (13.9) and using the equality $u(m(\mathbf{z} + \varepsilon\,\Psi) - V_d\mathrm{tri}(t,T)) = u(\tau - \mathrm{tri}(t,T))$ obtain

$$\varepsilon\,\frac{\partial\Psi(t,\mathbf{z},\varepsilon)}{\partial t} = (\mathbf{A_1}\mathbf{z} + \mathbf{B_1})\tau - (\mathbf{A_1}\mathbf{z} + \mathbf{B_1})u(\tau - \mathrm{tri}(t,T)). \tag{13.11}$$

When integrating (13.11), it is assumed that $\mathbf{z}$ is a constant, which is justified when an averaged trajectory is slowly varying. This equation can then be solved explicitly. The solution defines a triangle-shaped ripple function as shown in Fig. 13.1. Because the ripple function achieves its minimum at switching instances, the ripple magnitude is

$$\varepsilon\,\Psi(\tau T,\mathbf{z},\varepsilon) = \frac{T}{2}(\mathbf{A_1}\mathbf{z} + \mathbf{B_1})(\tau - \tau^2). \tag{13.12}$$

Then, to solve for τ, note that the switching occurs when the PWM input voltage $m(\mathbf{x}) = \tau V_d$ (see Fig. 12.2). Since $m(\mathbf{x}) = \mathbf{C}U - \mathbf{K}\mathbf{x}$ and $\mathbf{x} \approx \mathbf{z} + \varepsilon\,\Psi(t,\mathbf{z},\varepsilon)$, this gives rise to the equation $m(\mathbf{z} + \varepsilon\,\Psi(\tau T,\mathbf{z},\varepsilon)) = \tau V_d$, which leads to the quadratic equation in τ

$$m(\mathbf{z}) - \frac{M(\mathbf{z},T)}{2}(\tau - \tau^2) = \tau V_d, \tag{13.13}$$

where $M(\mathbf{z},T) = M = T\mathbf{K}(\mathbf{A_1}\mathbf{z} + \mathbf{B_1})$, and the relevant solution is in $[0,1]$. The function $m(\mathbf{z})$ is interpreted as the averaged value of the PWM input. If $T \to 0$ or

$\mathbf{K} = 0$ (open-loop), then $\tau = m(\mathbf{z})/V_d$ which is the conventional solution. If $T \neq 0$ and $\mathbf{K} \neq 0$ then the effective value of the input PWM voltage is less than the averaged value by the magnitude of the ripple in m.

Chapter 14

Basic PWM Control of the DC Servo Motor

The techniques of Chapter 13 are now applied to a DC-servo motor. A model of the typical DC motor can be described as a set of the following equations [67]

$$E(t) = V_a(t) - E_a(t) = L_a \dot{I}_a(t) + R_a I_a(t), \tag{14.1}$$

$$T_{em}(t) - T_{load}(t) = J\dot{\omega}(t) + F\omega(t), \tag{14.2}$$

$$E_a(t) = K_e \omega(t), \tag{14.3}$$

$$T_{em} = K_t I_a, \tag{14.4}$$

where R_a is a winding resistance and L_a is an armature reactance, J is a rotor inertia and F is a damping coefficient friction, E_a is a back emf, which is proportional with the back emf constant K_e to the speed ω, T_{em} is the electro mechanical torque which is proportional to armature current I_a with a torque constant K_t. The parameters of the

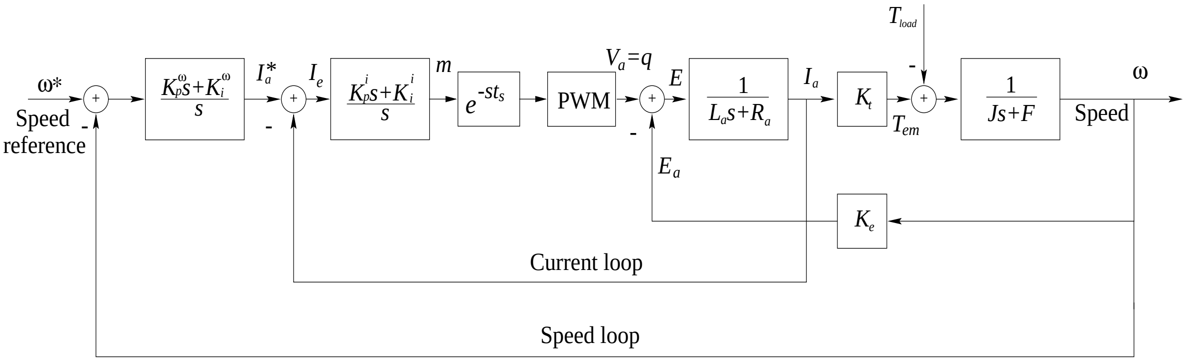
ω*
Speed reference
$\frac{K_p^\omega s+K_i^\omega}{s}$
I_a^*
I_e
$\frac{K_p^i s+K_i^i}{s}$
m
e^{-st_s}
PWM
$V_a=q$
E
$\frac{1}{L_a s+R_a}$
I_a
K_t
T_{load}
T_{em}
$\frac{1}{Js+F}$
Speed
ω
E_a
K_e
Current loop
Speed loop

Figure 14.1: DC servo motor block diagram.

motor and the constant load in the experiments, as well as the selection of controller parameters, are given in Appendix 1. In this Chapter the delay t_s is assumed to be equal to zero.

Figure 14.1 shows a block diagram of a DC servo motor with a two loop nested control structure [67]: the electrical (current) subsystem in the inner loop and the mechanical (speed) subsystem in the outer loop, with their respective PI controllers. This is a standard control structure for a DC motor in speed servo applications, and for other types of motor drives as well. A third loop can be added if positioning is required. The nested loop arrangement is widely perceived as very satisfactory, both from a control standpoint and from an apparatus protection point of view [58, 67].

14.1 Conventional Controller design

The DC motor is supplied by a pulse-width modulated voltage source in a majority of applications. A PWM power supply is intrinsically a nonlinear device due to the switching mode of operation. In the low frequency range (say a decade below the switching frequency) the PWM unit is well approximated with a gain K_{PWM}. This approximation is inaccurate at higher frequencies and may be justified only if the cut-off frequency of the current loop is much smaller then switching frequency of the PWM $f_{PWM} = 2\pi/T$.

Suppose that the motor speed ω and armature current I_a are available for measurements and the control action is exerted by changing the input voltage. Hence, the controller has two inputs and one output. The conventional design is usually done sequentially [67]. Firstly, one ignores the back emf $E_a(s) = K_e\omega(s)$, assuming that the response of the current loop is much faster (similarly ignore the effect of R_aI_a on the rate of the change of I_a). Secondly, the current loop controller is designed as a PI controller

$$T_I(s) = K_p^i + \frac{K_i^i}{s}. \tag{14.5}$$

Then the current closed-loop transfer function has

$$H_I(s) = \frac{I_a}{I_a^\star} = \frac{\frac{K_p^iK_{PWM}}{L_a}\left(s + \frac{K_i^i}{K_p^i}\right)}{s^2 + \left(\frac{K_p^iK_{PWM}}{L_a}\right)s + \left(\frac{K_i^iK_{PWM}}{L_a}\right)}. \tag{14.6}$$

a second order transfer function with coefficients depending from K_p^i and K_i^i

$$H(s) = \frac{\omega_n^2}{s^2 + 2\xi\omega_n s + \omega_n^2} \tag{14.7}$$

The natural frequency ω_n should be chosen by a factor of 10 or more smaller than the switching frequency of the PWM f_{PWM} and the damping $\xi < 1$. This will allow K_p^i and K_i^i to be calculated from the equations

$$\frac{K_i^iK_{PWM}}{L_a} = \omega_n^2, \tag{14.8}$$

$$\frac{K_p^i K_{PWM}}{L_a} = 2\xi\omega_n. \tag{14.9}$$

To design the speed controller load torque and friction $T_{load} = 0$, $F = 0$ are neglected. Next, the desired controller is at the form

$$T_\omega(s) = K_p^\omega + \frac{K_i^\omega}{s}.$$

Following a similar procedure as for the current loop one can write speed closed-loop transfer function as

$$H_\omega(s) = \frac{\omega(s)}{\omega^\star(s)} = \frac{\frac{K_p^\omega K_t}{J}\left(s + \frac{K_i^\omega}{K_p^\omega}\right)}{s^2 + \left(\frac{K_p^\omega K_t}{J}\right)s + \left(\frac{K_i^\omega K_t}{J}\right)}. \tag{14.10}$$

a second order system. To calculate K_p^ω and K_i^ω ω_n^ω in the speed loop should be chosen one-tenth of ω_n^i in the current loop and $\xi < 1$, then

$$\frac{K_i^\omega K_t}{J} = \omega_n^{\omega\,2}, \tag{14.11}$$

$$\frac{K_p^\omega K_t}{J} = 2\xi\omega_n^\omega. \tag{14.12}$$

The controller parameters in the experiments are given in Appendix 1.

14.2 State space dynamical equations for the closed-loop system

In this section the state space dynamical equations for the closed-loop system will be derived. From current equation $\dot{I}_a = -R_a/L_a I_a + 1/L_a E$ we have

$$\dot{x}_1 = -\frac{R_a}{L_a}x_1 + E = -\frac{R_a}{L_a}x_1 + V_{DC}u(m - V_t\mathrm{tri}(t,T)) - K_e\omega \tag{14.13}$$

$$I_a = \frac{1}{L_a}x_1 \tag{14.14}$$

or

$$\dot{x}_1 = -\frac{R_a}{L_a}x_1 + u(m - V_t\mathrm{tri}(t,T)) - K_e\omega \tag{14.15}$$

$$I_a = \frac{1}{L_a}x_1 \tag{14.16}$$

The equation for current PI controller is

$$\dot{x}_2 = I_e = -\frac{1}{L_a}x_1 + I_a^* \tag{14.17}$$

$$m = K_i^i x_2 + K_p^i I_e = -\frac{K_p^i}{L_a}x_1 + K_i^i x_2 + K_p^i I_a^*, \tag{14.18}$$

where $I_e = I_a^* - \frac{1}{L_a}x_1$. Similarly, the equation for the speed PI controller is

$$\dot{x}_3 = \omega^* - \omega \tag{14.19}$$

$$I_a^* = K_i^\omega x_3 + K_p^\omega(\omega^* - \omega). \tag{14.20}$$

Substitute (14.20) into (14.18) to obtain

$$m = -\frac{K_p^i}{L_a}x_1 + K_i^i x_2 + K_p^i K_i^\omega x_3 + K_p^i K_p^\omega(\omega^* - \omega). \tag{14.21}$$

From speed equation of the motor we have

$$\dot{x}_4 = \frac{F}{J}x_4 + K_t I_a - T_{load} \tag{14.22}$$

$$\omega = \frac{1}{J}x_4 \tag{14.23}$$

Substitute (14.20), (14.23) into (14.17) and (14.18) to obtain

$$\dot{x}_2 = -\frac{1}{L_a}x_1 + K_i^\omega x_3 - \frac{K_p^\omega}{J}x_4 + K_p^\omega\omega^* \tag{14.24}$$

$$m = -\frac{K_p^i}{L_a}x_1 + K_i^i x_2 + K_p^i K_i^\omega x_3 - K_p^i\frac{K_p^\omega}{J}x_4 + K_p^i K_p^\omega\omega^* \tag{14.25}$$

The output of PWM is

$$\begin{aligned} q &= V_{DC}u(K_p^i K_p^\omega \omega^* + \begin{bmatrix} -\dfrac{K_p^i}{L_a} & K_i^i & K_p^i K_i^\omega & K_p^i \dfrac{K_p^\omega}{J} \end{bmatrix} \mathbf{x} - V_t \mathrm{tri}(t,T)) = \\ & V_{DC}u(V_{ref} - \mathbf{K}\mathbf{x} - V_t \mathrm{tri}(t,T)) = V_{DC}u(m(\mathbf{x}) - V_t \mathrm{tri}(t,T)), \end{aligned} \tag{14.26}$$

where $m(\mathbf{x}) = V_{ref} - \mathbf{K}\mathbf{x}$, $\mathbf{K} = \begin{bmatrix} \frac{K_p^i}{L_a} & -K_i^i & -K_p^i K_i^\omega & K_p^i \frac{K_p^\omega}{J} \end{bmatrix}$ and $V_{ref} = K_p^i K_p^\omega \omega^*$. Finally, a state space model for the closed-loop system is

$$\begin{bmatrix} \dot{x}_1 \\ \dot{x}_2 \\ \dot{x}_3 \\ \dot{x}_4 \end{bmatrix} = \begin{bmatrix} -\frac{R_a}{L_a} & 0 & 0 & -\frac{K_e}{J} \\ -\frac{1}{L_a} & 0 & K_i^\omega & -\frac{K_p^\omega}{J} \\ 0 & 0 & 0 & -\frac{1}{J} \\ \frac{K_t}{L_a} & 0 & 0 & -\frac{F}{J} \end{bmatrix} \begin{bmatrix} x_1 \\ x_2 \\ x_3 \\ x_4 \end{bmatrix} + \begin{bmatrix} q(t) \\ K_p^\omega \omega^* \\ \omega^* \\ -T_{load} \end{bmatrix} \tag{14.27}$$

which will be written concisely in the form

$$\dot{\mathbf{x}} = \mathbf{A_0}\mathbf{x} + \mathbf{B_0} + \mathbf{B_1}u(m(\mathbf{x}) - V_t \mathrm{tri}(t,T)), \tag{14.28}$$

$$m = \mathbf{C}U - \mathbf{K}\mathbf{x}, \tag{14.29}$$

where $\mathbf{A}_0$ is the "**A**" matrix in (14.27), $\mathbf{B}_0 = \begin{bmatrix} 0 & K_p^\omega & 1 & 0 \\ 0 & 0 & 0 & -1 \end{bmatrix}^\top$, $U = [\omega^* \quad T_{load}]^\top$ and $\mathbf{B}_1 = [V_{DC} \quad 0 \quad 0 \quad 0]^\top$, $\mathbf{C} = [K_p^i K_p^\omega \quad 0]$. The averaged model (13.10) is defined accordingly.

The average duty ratio τ can be found from (13.13) with $M = TV_{DC}K_p^i/L_a$. Due to the intrinsic nonlinearity of the PWM, the average PWM gain will depend on the operating point. The magnitude of the ripple function is given by (13.12) (with $\mathbf{A}_1 = 0$). One can now compute the magnitude of the current and reference voltage ripple, as

$$\Delta I = \frac{T}{2}\frac{V_{DC}}{L_a}(\tau - \tau^2) \tag{14.30}$$

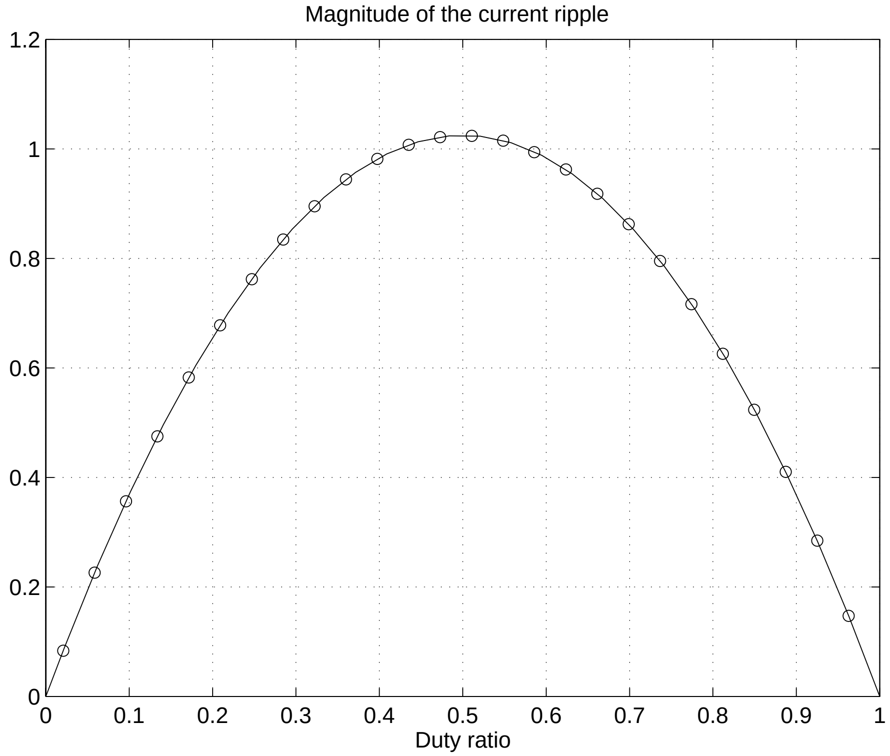

Figure 14.2: Magnitude of the current ripple, A

$$\Delta m = \frac{T}{2}\frac{K_p^i}{L_a}V_{DC}(\tau - \tau^2), \tag{14.31}$$

where the magnitude of the ripple function is defined as a difference between maximum and an average value.

Fig. 14.2 displays ripple magnitude, as a function of duty ratio. The magnitude of the current ripple obtained from a dynamical system simulation in steady state (circles) are in complete agreement with what is obtained from (14.30) (solid line). In Fig. 14.3 the ideal PWM gain (with $T = 0$) is compared with the effective gain in an averaged model. Evidently, ripple effects reduce the effective PWM gain.

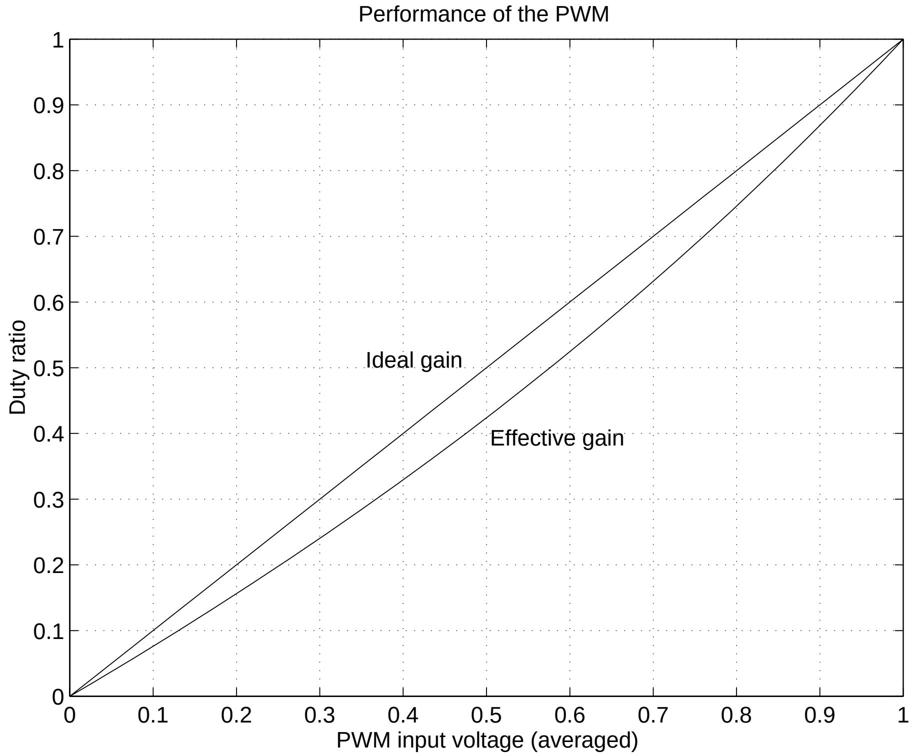

Figure 14.3: Comparison of the ideal and effective averaged PWM gain

14.3 Linearization of the PWM gain

For the purpose of controller design, a linear model of the PWM may be useful. To derive a linearized small deviation model of the PWM, assume that the system is in quasi steady state and $\lim_{t\to\infty}\mathbf{z}(t) = \mathbf{z}_{\mathrm{ss}}$. Then $m(\mathbf{z}_{\mathrm{ss}})$ is known, and

$$m(\mathbf{z}_{\mathrm{ss}}) - \frac{M}{2}(\tau_{ss} - \tau_{ss}^2) = \tau_{ss} V_d \tag{14.32}$$

can be solved for τ_{ss}. The small deviation model of the PWM is

$$\tau \approx \tau_{ss} + \frac{m - m(\mathbf{z}_{\mathrm{ss}})}{M(1/2 - \tau_{ss}) + V_d}. \tag{14.33}$$

An example of linearization around three points is shown in Fig.14.4. In this example the nonlinear gain of the PWM is approximated by three lines. Each approximation is valid, with an error of less then 2%, for one third of the input voltage range. The nonlinear characteristic of the PWM (averaged output voltage vs. averaged input voltage) was obtained by simulation of the closed-loop system with varying speed reference ω^* (from 0 to 180 rad/sec) and with load torque $T_{load} = 0.4$Nm. This corresponds to duty ratio changes from 0 to 1.

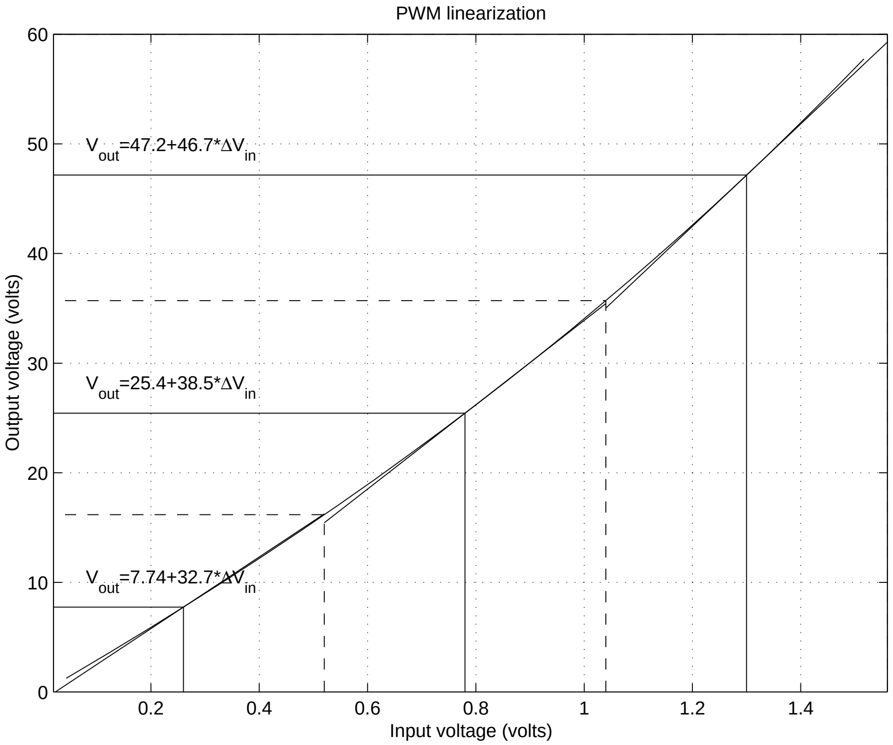

Figure 14.4: Linearization of the PWM gain around three points

Results of this section show that slow switching frequency may have pronounced effects on accuracy of PWM models. The analytical expressions (14.30), (14.33) are quite effective in quantifying the deviations from idealized (standard) models.

Chapter 15

Delay effects

In this chapter the effects of delays in the PWM input signal are studied; such delay are often caused by digital implementation of the controller. Delay effects require modifications in the computations above. Let the delay be $0 \leq t_s \leq T$. With a delay, the expression $u(m(\mathbf{x}(t)) - V_d \mathrm{tri}(t, T))$ in (13.1) is replaced by $u(m(\mathbf{x}(t - t_s)) - V_d \mathrm{tri}(t, T))$. The effect of this change on the PWM switching is depicted in Fig. 15.1. Since the basic assumption in averaging is that $\mathbf{z}(t)$ is approximately constant for $t \in [t_k, t_k + T]$, the delay in $\mathbf{z}$ can be ignored. However the ripple function Ψ represents fast zero average harmonics, where a small delay may have significant effects. That is, approximate

$$\mathbf{x}(t - t_s) \approx \mathbf{z}(t - t_s) + \varepsilon\, \Psi(t - t_s, \mathbf{z}(t - t_s), \varepsilon) \approx \mathbf{z}(t) + \varepsilon\, \Psi(t - t_s, \mathbf{z}(t), \varepsilon). \quad (15.1)$$

Justification of ignoring the delay in $\mathbf{z}$ is given in the classical averaging papers [12, 34, 35]. (Discussion on the error introduced by approximating $\mathbf{z}(t - t_s) \approx \mathbf{z}(t)$ are given in [56, 57].)

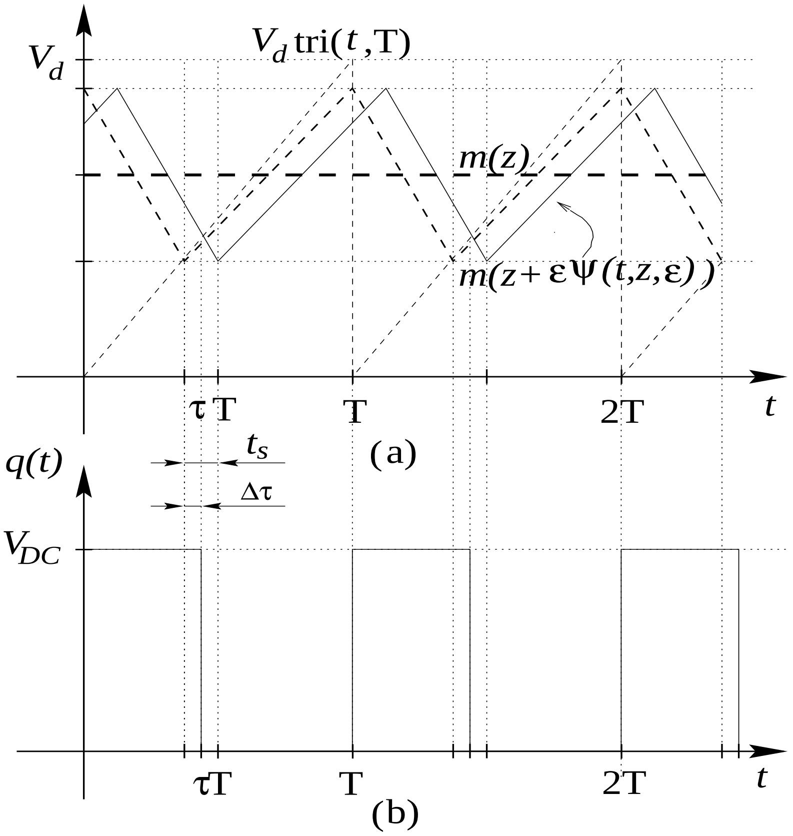
V_d
$V_d\,\mathrm{tri}(t,T)$
$m(z)$
$m(z+\varepsilon\Psi(t,z,\varepsilon))$
τT
T
2T
t
(a)
q(t)
t_s
Δτ
V_{DC}
τT
T
2T
t
(b)

Figure 15.1: PWM input a) and output b) voltages.

Now to find τ, solve

$$m(\mathbf{z} + \varepsilon\,\Psi(\tau T - t_s, \mathbf{z}, \varepsilon)) = \tau V_d. \tag{15.2}$$

Note, that the formula for the magnitude of the ripple in m as a function of τ remains the same as in (13.12)

$$\Delta m = \frac{M}{2}(\tau - \tau^2), \tag{15.3}$$

where $M = T\mathbf{K}(\mathbf{A_1}\mathbf{z} + \mathbf{B_1})$. Using piecewise linear approximations, as before, the explicit expression for $m(\mathbf{x})$ in terms of $\mathbf{z}$, Δm and τ follows from a simple geometrical observation

$$m(\mathbf{x}) \approx \begin{cases} -\frac{2\Delta m}{\tau T}(t-t_s+nT)+m(\mathbf{z})+\Delta m & \text{if } t-t_s+nT \in [0,\tau T] \\ \frac{2\Delta m}{(1-\tau)T}(t-\tau T-t_s+nT)+m(\mathbf{z})-\Delta m & \text{if } t-t_s+nT \in [\tau T, T] \end{cases} \quad, \tag{15.4}$$

where $n = \ldots -1, 0, 1, \ldots$ and $\mathbf{x} = \mathbf{z} + \varepsilon\, \Psi(t-t_s, \mathbf{z}, \varepsilon)$. Substitute (15.4) into (15.2) to obtain four equations, to be solved with ($n = 0, 1$). Then τ turns out to be the solution to one of the following two equations

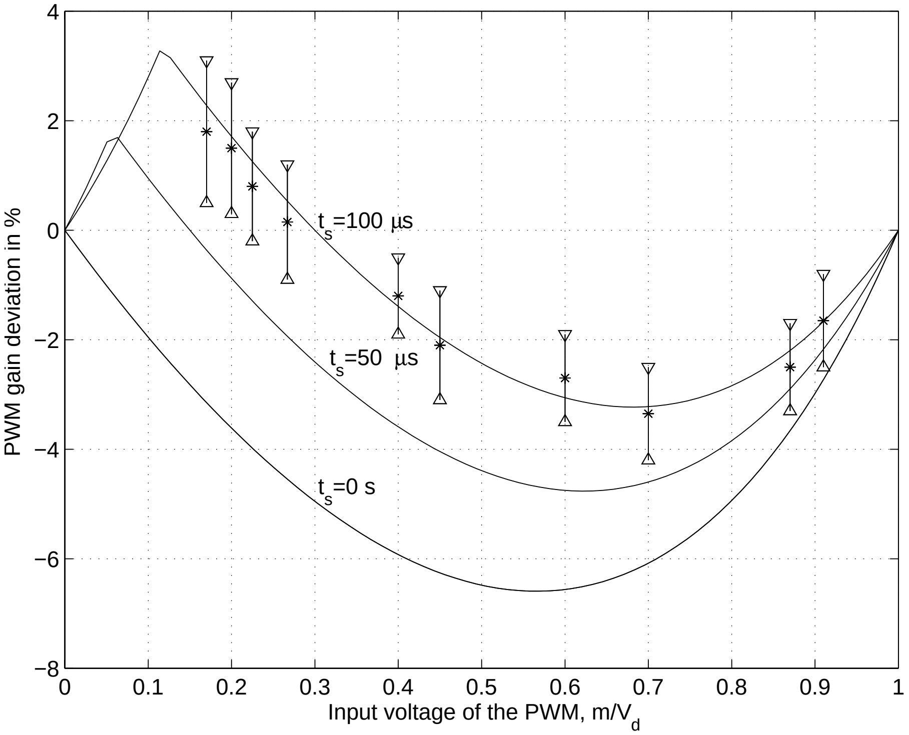

Figure 15.2: Absolute deviations ($\tau - m(\mathbf{z})/V_d$ in %) of the averaged normalized PWM gain from ideal as a function of $m(\mathbf{z})/V_d$ for different time delays.

$$m(\mathbf{z}) + \Delta m(1 - \frac{2}{\tau T}(\tau T - t_s)) = \tau V_d, \qquad \tau \geq \frac{t_s}{T} \tag{15.5}$$

$$m(\mathbf{z}) - \Delta m(1 - \frac{2}{(1-\tau)T}(-t_s + T)) = \tau V_d, \qquad \tau \leq \frac{t_s}{T} \tag{15.6}$$

or explicitly, using (15.3)

$$\frac{1}{2}\tau^2-\left[\frac{t_s}{T}+\frac{1}{2}+\frac{V_d}{M}\right]\tau+\frac{m(\mathbf{z})}{M}+\frac{t_s}{T}=0;\quad \tau\geq\frac{t_s}{T} \tag{15.7}$$

$$\frac{1}{2}\tau^2-\left[\frac{t_s}{T}-\frac{1}{2}+\frac{V_d}{M}\right]\tau+\frac{m(\mathbf{z})}{M}=0;\quad \tau\leq\frac{t_s}{T}. \tag{15.8}$$

where the smallest positive solution, τ, of each quadratic equation is selected. It is evident that equation (15.7) becomes equivalent to equation (13.13) if $t_s = 0$. These equation have the following solutions

$$\tau_{1,2}=\frac{t_s}{T}+\frac{1}{2}+\frac{V_d}{M}\pm\sqrt{\left(\frac{t_s}{T}+\frac{1}{2}+\frac{V_d}{M}\right)^2-2\left(\frac{m}{V_d}\frac{V_d}{M}+\frac{t_s}{T}\right)} \tag{15.9}$$

$$\tau_{1,2}=\frac{t_s}{T}-\frac{1}{2}+\frac{V_d}{M}\pm\sqrt{\left(\frac{t_s}{T}-\frac{1}{2}+\frac{V_d}{M}\right)^2-2\left(\frac{m}{V_d}\frac{V_d}{M}\right)} \tag{15.10}$$

Fig. 15.2 depicts the absolute deviation of the averaged normalized PWM gain from the idealized model (defined as $\tau - m(\mathbf{z})/V_d$), for different time delays in the example of the DC motor. (Maximum relative deviation $\approx 30\%$ for $t_s = 100\mu$s at input voltage $m/V_d = 0.1$.) With no delay, the average PWM gain is always less than ideal. The presence of delay may increase the average gain to a level higher than the ideal, as verified in the experiments Fig. 15.2 presents the theoretical predictions of $\tau - m/V_d$ for different delays by the solid curves. Experimental measurements are also plotted. Since there is noise present, approximately 15 experiments were performed to obtain data. Average of the data points are represented by '*' and the upper and lower bounds of the experiments are given by $\bigtriangledown$ and $\bigtriangleup$ respectively in the figure.

Fig. 15.3 depicts the PWM sawtooth and the averaged (over 100 cycles) PWM input voltage for the experimental servo motor. Notice that the minimum of m is

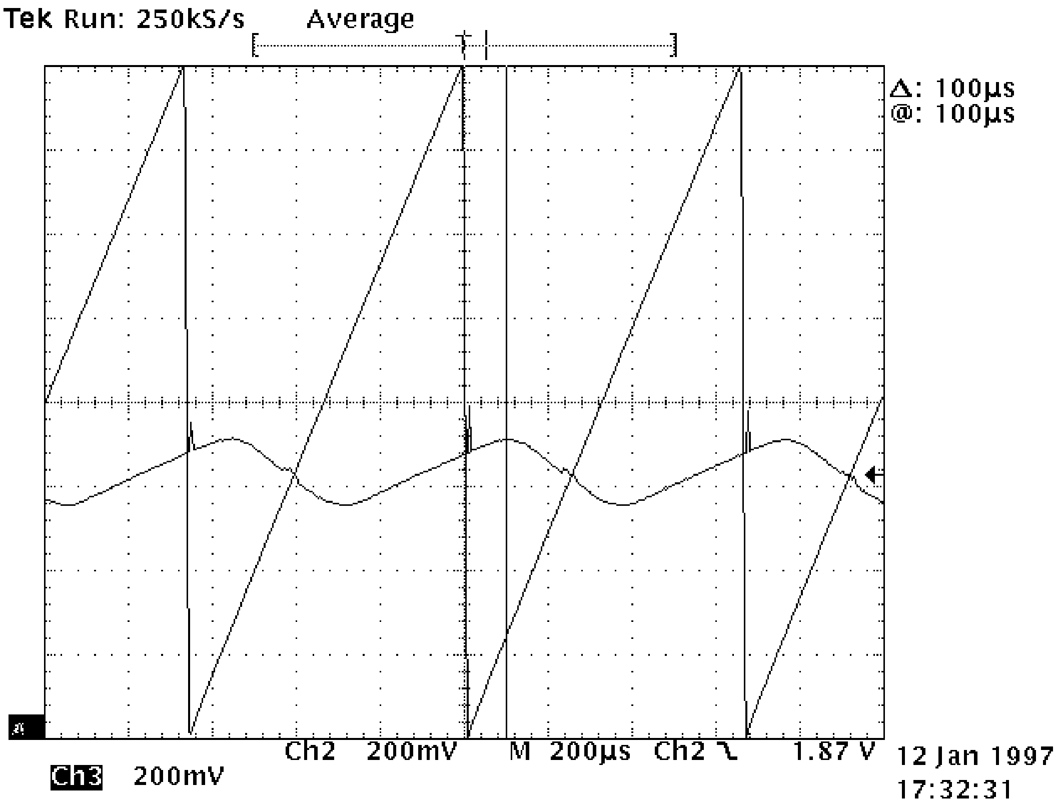

Figure 15.3: The PWM sawtooth (triangles) and PWM input (200μs per division horizontally)

shifted by $t_s \approx 100\mu$s.

In this section tools for analysis of combined effects of finite switching frequency and delay have been developed. Resulting expressions (15.7),(15.8) are of modest complexity, while their predictive power is considerable, as evidenced by our experiments.

Chapter 16

Discrete-time simulation

In this chapter a nonlinear discrete-time state-space model for a PWM controlled system is derived. Discrete-time state-space models most commonly come from regular state sampling of a continuous-time model. However, a model that involves one sample per PWM cycle ignores the ripple. To obtain a better model, note that the system under consideration is piecewise LTI [51]. Using this property, it is possible to successively solve for state variables in each of the two systems' successive configuration and invoke the continuity of the state at switching points. This procedure naturally leads to a discrete-time state-space model with two samples per PWM cycle.

Computations are further simplified using a linear approximation of the state trajectory between samplings. First, analyze a system without delay using the model introduced in Chapter 13

$$\dot{\mathbf{x}} = \mathbf{A_0}\mathbf{x} + \mathbf{B_0}U + (\mathbf{A_1}\mathbf{x} + \mathbf{B_1})u(m(\mathbf{x}) - V_d\mathrm{tri}(t,T)), \tag{16.1}$$

$$m(\mathbf{x}) = \mathbf{C}U - \mathbf{K}\mathbf{x}, \tag{16.2}$$

with a constant U. (The analysis can be easily extended for the case where U is a low-frequency signal, which can be approximated as a constant $U(t) \approx U_k$ on the each time interval $t \in (kT, kT + T]$.) The system operates cyclically taking a succession of two configuration in each cycle. The state vector is governed by the LTI equations

$$\begin{aligned} \dot{\mathbf{x}} &= (\mathbf{A}_0 + \mathbf{A}_1)\mathbf{x} + \mathbf{B}_0 U + \mathbf{B}_1, & t &\in (kT, kT + \tau_k T] & (16.3) \\ \dot{\mathbf{x}} &= \mathbf{A}_0 \mathbf{x} + \mathbf{B}_0 U, & t &\in (kT + \tau_k T, kT + T] & (16.4) \end{aligned}$$

and has the following time-domain trajectory

$$\begin{aligned} \mathbf{x}(t_k + \theta T) &= e^{\mathbf{A}T\theta}\mathbf{x}_k + \int_0^\theta e^{\mathbf{A}T(\theta - s)}\left(\mathbf{B}_0 U + \mathbf{B}_1\right) ds & \theta &\in [0, \tau_k], & (16.5) \\ \mathbf{x}(t_k + \tau_k T + \theta T) &= e^{\mathbf{A}_0 T\theta}\mathbf{x}(t_k + \tau_k T) + \int_0^\theta e^{\mathbf{A}_0 T(\theta - s)}\mathbf{B}_0 U ds & \theta &\in [0, 1 - \tau_k], & (16.6) \end{aligned}$$

where $\mathbf{A} = \mathbf{A}_0 + \mathbf{A}_1$, $t_k = kT$, $\mathbf{x}_k = \mathbf{x}(kT)$ and $\tau_k T$ is the switching time. Denoting $\mathbf{x}_k^\tau = \mathbf{x}(t_k + \tau_k T)$, leads to

$$\begin{aligned} \mathbf{x}_k^\tau &= \mathbf{A}^d(\tau_k)\mathbf{x}_k + \mathbf{B}^d(\tau_k) & (16.7) \\ \mathbf{x}_{k+1} &= \mathbf{A}_0^d(1 - \tau_k)\mathbf{x}_k^\tau + \mathbf{B}_0^d(1 - \tau_k) & (16.8) \end{aligned}$$

where $\mathbf{B}^d(s) = \int_0^s e^{\mathbf{A}T(s-t)}, (\mathbf{B}_0 U + \mathbf{B}_1)dt$, $\mathbf{B}_0^d(s) = \int_0^s e^{\mathbf{A}_0 T(s-t)}\mathbf{B}_0 U dt$, $\mathbf{A}_0^d(s) = e^{\mathbf{A}_0 Ts}$, and $\mathbf{A}^d(s) = e^{\mathbf{A}Ts}$. In these formulas τ_k should be determined as the first intersection point of m and $V_d \mathrm{tri}(t, T)$ on the time interval $[t_k, t_{k+1}]$. To compute τ_k, suppose that pulse of the length T instead of τ_k applied to the system at the time t_k, then the time response $\tilde{\mathbf{x}}(t)$ is completely defined, and

$$m(\tilde{\mathbf{x}}(t)) = m(\mathbf{x}(t)) \tag{16.9}$$

for all $t \in [t_k, t_k + \tau_k]$. At this point τ_k can be found with approximating the state trajectory along $[t_k, t_k + T]$ with a straight line, denoted by $\hat{\mathbf{x}}(t)$. From

$$m(\hat{\mathbf{x}}(\tau_k T)) = V_d \mathrm{tri}(\tau_k T, T) \tag{16.10}$$

we obtain

$$\tau_k = \frac{m_k}{m_k - \hat{m}_{k+1} + V_d}, \tag{16.11}$$

where $m_k = m(\mathbf{x}_k)$, $\hat{m}_{k+1} = m(\hat{\mathbf{x}}_{k+1})$, and $\hat{\mathbf{x}}_{k+1}$ is

$$\hat{\mathbf{x}}_{k+1} = \mathbf{A}^d(1)\mathbf{x}_k + \mathbf{B}^d(1). \tag{16.12}$$

When τ_k is determined it can be substituted into (16.7)-(16.8) to obtain $\mathbf{x}_k^\tau$ and $\mathbf{x}_{k+1}$. This completes one cycle of calculations.

In the presence of a delay in the control loop, the behavior of the system is still governed by the equations (16.5)- (16.6), but τ_k now should be found from

$$m(\mathbf{x}(\tau_k T - t_s)) = V_d \mathrm{tri}(\tau_k T, T). \tag{16.13}$$

With the delay $t_s \in [0, T]$ the function $V_d \mathrm{tri}(t, T)$ may possibly intersect three different slopes of the function m. The different types of intersections are shown schematically on Fig. 16.1. The slopes 1 and 2 are completely defined by the time $t = t_k$, while the slope 3 depends on τ_k. This implies that $m(\mathbf{x}(t)) = m(\hat{\mathbf{x}}(t))$, when $t \in [t_k, t_k + \tau_k]$.

To solve (16.13) for τ_k, an explicit equation for m as a function of time should be derived. From simple geometrical observations and using that for the slope 1

$$\Delta m = (m_{k-1} - m_{k-1}^\tau)/2, \qquad m = (m_{k-1} + m_{k-1}^\tau)/2$$

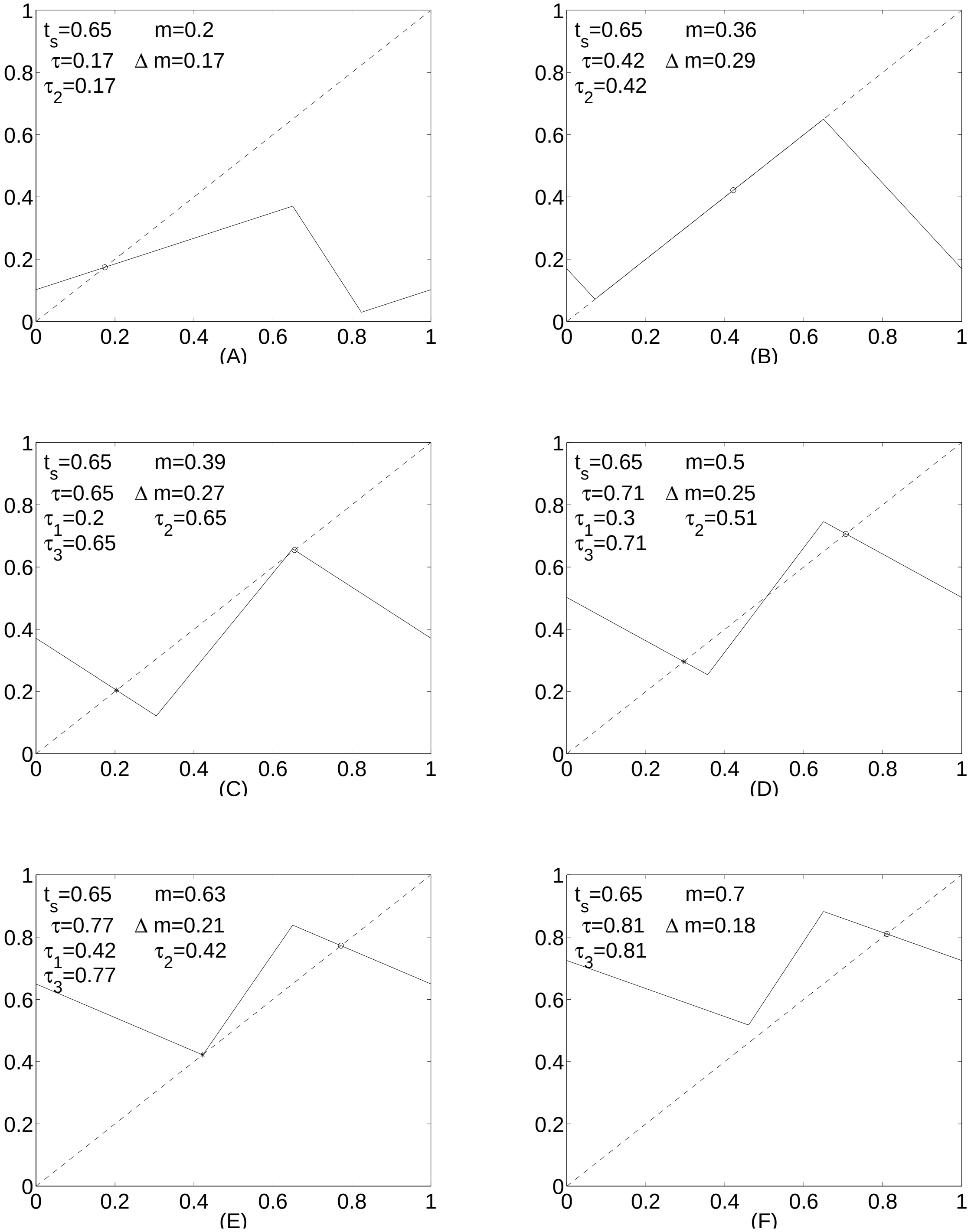

Figure 16.1: Different types of intersection $\frac{m(\mathbf{x}(t/T))}{V_d}$ (solid line) and tri$(t, 1)$ (dashed line) for DC motor, $\frac{V_d}{M} = 0.421$.

and for the slope 2

$$\Delta m = (m_k - m^{\tau}_{k-1})/2, \qquad m = (m_k + m^{\tau}_{k-1})/2$$

follows (see Fig. 16.2)

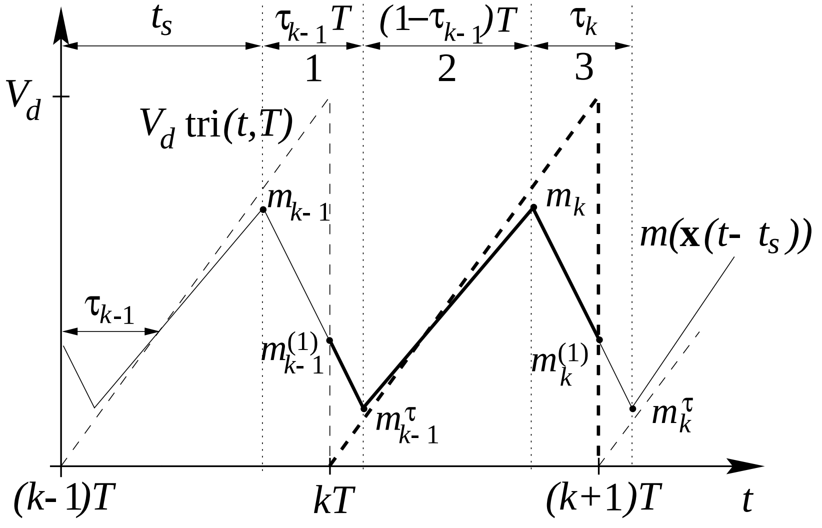
t_s
$\tau_{k-1}T$
$(1-\tau_{k-1})T$
τ_k
1
2
3
V_d
V_d tri(t,T)
m_{k-1}
m_k
$m(\mathbf{x}(t-t_s))$
τ_{k-1}
$m^{(1)}_{k-1}$
$m^{(1)}_k$
m^{τ}_{k-1}
m^{τ}_k
$(k-1)T$
kT
$(k+1)T$
t

Figure 16.2: PWM input voltage and a sawtooth in the presence of a delay.

$$m(\mathbf{x}((k-1)T+\theta T)) = \frac{m^{\tau}_{k-1} - m_{k-1}}{\tau_{k-1}}\theta + m_{k-1} \qquad \theta \in [0, \tau_{k-1}], \tag{16.14}$$

$$m(\mathbf{x}((k-1)T+\tau_{k-1}T+\theta T))) = \frac{m_k - m^{\tau}_{k-1}}{1-\tau_{k-1}}\theta + m^{\tau}_{k-1} \qquad \theta \in [0, 1-\tau_{k-1}], \tag{16.15}$$

$$m(\hat{\mathbf{x}}(kT+\theta T) = (\hat{m}^{\tau}_{k+1} - m_k)\theta + m_k \qquad \theta \in [0,1], \tag{16.16}$$

where $m^{\tau}_k = m(\mathbf{x}^{\tau}_k)$.

Now the duty ratio τ_k on the next time interval $t \in [t_k, t_k+T]$ can be obtained, as the smallest solution of (16.13), meaning that one of the following three equations holds

$$\tau_k^{(1)} = \frac{(t_s/T-1)(m_{k-1}-m_{k-1}^{\tau})+m_{k-1}\tau_{k-1}}{m_{k-1}-m_{k-1}^{\tau}+V_d\tau_{k-1}} \qquad \tau_k^{(1)} \in [0, t_s/T-(1-\tau_{k-1})], \tag{16.17}$$

$$\tau_k^{(2)} = \frac{(t_s/T)(m_k-m_{k-1}^{\tau})+m_k(\tau_{k-1}-1)}{m_k-m_{k-1}^{\tau}+V_d(\tau_{k-1}-1)} \qquad \tau_k^{(2)} \in [t_s/T-(1-\tau_{k-1}), t_s/T], \tag{16.18}$$

$$\tau_k^{(3)} = \frac{(t_s/T)(m_k-\hat{m}_{k+1})+m_k}{m_k-\hat{m}_{k+1}+V_d} \qquad \tau_k^{(3)} \in [t_s/T, 1], \tag{16.19}$$

It is possible that none of equations (16.17-16.19) has solution. This means that no intersection of sawtooth function $V_d\mathrm{tri}(t,T)$ with m occurs during the time interval $[t_k, t_k+T]$. To complete calculation of τ_k two more conditions should therefore be added. If $m > V_d\mathrm{tri}(t,T)$ on $t \in [t_k, t_k+T]$, then $\tau_k = 1$; if $m < V_d\mathrm{tri}(t,T)$ on $t \in [t_k, t_k+T]$, then $\tau_k = 0$. Substituting τ_k back into (16.7-16.8) yields $\mathbf{x}_k^{\tau}$ and $\mathbf{x}_{k+1}$. This completes one cycle of calculations. Since to calculate the next value of the state vector only simple linear equations are used, the required computational load is greatly reduced compare to straightforward simulation of the PWM controlled system. The proposed simulation method can be used to evaluate performance and ripple magnitude in a steady state for a given system.

Chapter 17

Existence of a T-Periodic Steady State

Equations (15.7-15.8) were obtained under the assumption of existence of a T-periodic steady state and using a piecewise linear approximation of the steady state averaged current trajectory. They thus form a necessary, but not a sufficient condition for the existence of a T-periodic equilibrium with the duty ratio τ for the approximate system. In this chapter necessary and sufficient conditions for the existence of a T-periodic solution of the approximate system are further explored.

This search is important, because deviation from a T-periodic regime may result in an increase of ripple magnitude and in the creation of low frequency harmonics. To illustrate this point, note that, from (13.12) the maximum ripple magnitude is achieved if $\tau = 0.5$. If the system is in a $2T$-periodic regime the maximum ripple magnitude will exist if the switch is "on" during one cycle and "off", during the next one. In this case, the magnitude of the ripple function will be twice larger, and its frequency will be twice lower than initially assumed. Higher magnitude and lower frequency components may have adverse influence on the performance of the system, because low frequency components are less attenuated by the plant and input and output filters.

In this chapter, conditions are presented for the existence of a T-periodic steady state of a PWM system. All conditions are based on the analysis of the averaged system, and therefore are approximate. The conditions derived are very simple to apply; however, the derivations and proofs to verify the conditions are, at times, complicated. Therefore, it is beneficial to give a summary of the results obtained in this section.

In Section 17.1 a necessary condition will be derived for existence of a T-periodic steady state that involves only basic system parameters and does not depend on the system operating point, (i.e., on the input signals). A meaning of the obtained condition is that, if normalized delay t_s/T is larger than V_d/M, then for the given system parameters an operating point exists for which system will not have a T-periodic steady state. The converse statement is not necessary true.

In Section 17.2, stronger conditions are given for the existence of a T-periodic steady state. These conditions are given in the terms of normalized (by the slope of the sawtooth T/V_d) rising β and falling α slopes of the PWM input signal $m(\mathbf{x})$. These slopes depend not only on system parameters, but also on the operating point of the system. Specifically, suppose that $\mathbf{z}_{css}$ is stable operating of averaged equation

(13.10), then

$$\alpha = -T\mathbf{K}\left[(\mathbf{A}_0+\mathbf{A}_1)\mathbf{z}_{css}+\mathbf{B}_0U+\mathbf{B}_1\right]/V_d, \tag{17.1}$$

$$\beta = -T\mathbf{K}\left[\mathbf{A}_0\mathbf{z}_{css}+\mathbf{B}_0U\right]/V_d. \tag{17.2}$$

(Note, that this will lead to $\alpha \leq 0$ and $\beta \geq 0$.) Then a T-periodic steady state exists if and only if:

(a) if $\beta/(\beta-\alpha) < t_s/T$ then

$$\beta < 2/3 \quad \text{and} \quad \alpha > 3\beta - 2 \tag{17.3}$$

(b) if $\beta/(\beta-\alpha) > t_s/T$ then

$$\beta < 2 \quad \text{or} \quad \alpha < 2-\beta, \tag{17.4}$$

Furthermore, the average duty ratio, given by $\tau_{ss} = \beta/(\beta-\alpha)$, does not depend on the particular slope within which the intersection occurs.

Fig. 17.1(a) and (b) show these regions graphically. From these plots it is clear that the “rule of thumb” used in practice ($\beta < 1$) does not guarantee the existence of a T-periodic steady state if the delay is sufficiently large.

Section 17.2 also gives conditions for the existence of a T-periodic steady state of a PWM system subject to uniform sampling. The stability region for this case, presented on Fig. 17.1(c), does not depend on sampling instance.

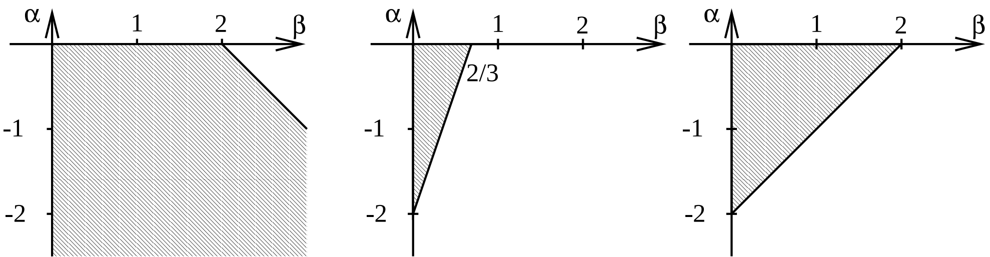

(a) (b) (c)

Figure 17.1: Stability regions on (α,β) plane: (a) $t_s/T < \beta/(\beta-\alpha) < 1$, (b) $1 > t_s/T > \beta/(\beta-\alpha)$, (c) uniform sampling.

17.1 A Necessary Condition for Existence of a T-Periodic Steady State of the Approximate System

Assume existence of a T-periodic steady states with duty ratio τ and use a piecewise linear approximation of the steady state trajectory. Then the input of the PWM is given by (15.4), where the trajectory $m(\mathbf{x}(t))$ is a function of time alone, as τ is fixed now. Solving $m(\mathbf{x}(\sigma T)) = \sigma V_d$ for σ, may give rise to up to three possible solutions $\sigma = \tau^{(i)}$, $i = 1,2,3$ within one PWM period. Those points are given by

$$\tau^{(1)} = \frac{(2(t_s/T-1)+\tau)\Delta m + m\tau}{2\Delta m + V_d\tau} \qquad \tau^{(1)} - t_s/T \in [-1, \tau-1] \tag{17.5}$$

$$\tau^{(2)} = \frac{(2(t_s/T-1)+\tau+1)\Delta m + m(\tau-1)}{2\Delta m + V_d(\tau-1)} \qquad \tau^{(2)} - t_s/T \in [\tau-1, 0] \tag{17.6}$$

$$\tau^{(3)} = \frac{(2t_s/T+\tau)\Delta m + m\tau}{2\Delta m + V_d\tau} \qquad \tau^{(3)} - t_s/T \in [0, \tau] \tag{17.7}$$

where $\tau^{(1)}$, $\tau^{(2)}$ and $\tau^{(3)}$ corresponds to the intersections with the slopes 1, 2 and 3, as marked on Fig.17.2. Following from the PWM switching rule, in a T-periodic

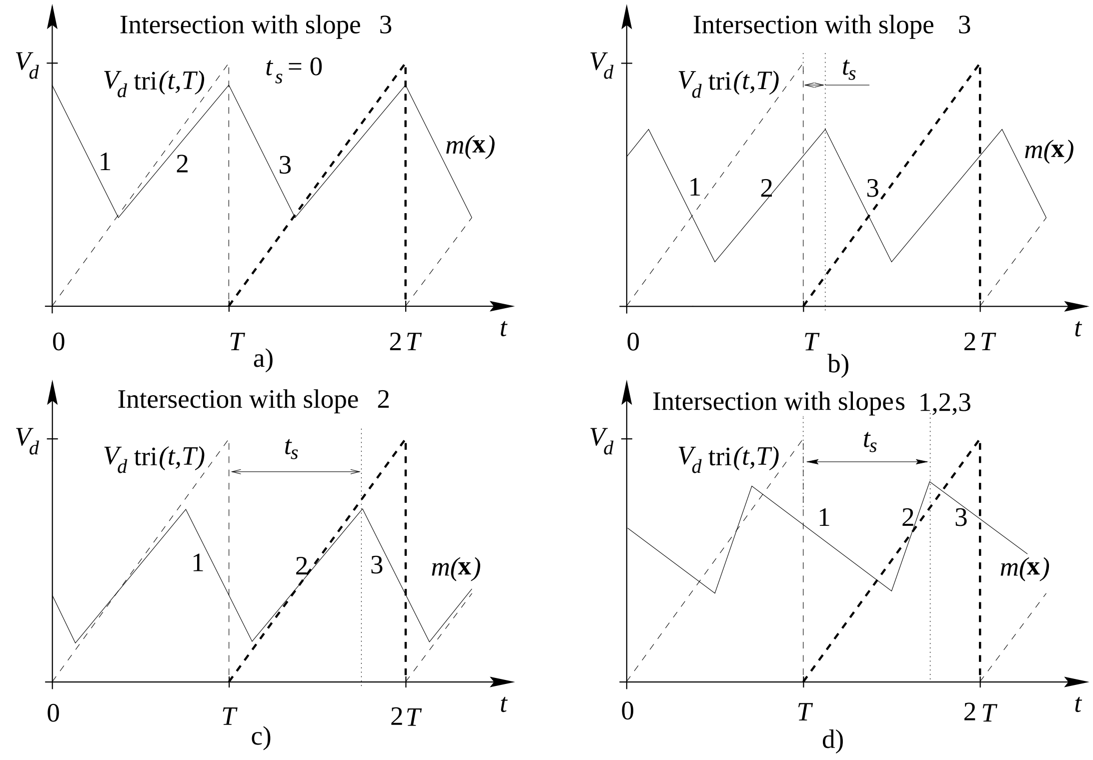

Figure 17.2: Different types of intersections for the time interval $T < t \leq 2T$

steady state, τ must coincide with the smallest of these solutions; also (when existing) $\tau^{(1)} \leq \tau^{(2)} \leq \tau^{(3)}$.

The existence of an intersection at $\tau^{(1)}T$ creates a contradiction that precludes the assumed existence of a T-periodic trajectory. Indeed, since $\tau^{(1)}$ is the smallest possible solution, its existence requires $\tau = \tau^{(1)}$, but the situation $\tau = \tau^{(1)}$ is impossible because $t_s/T < 1$ contradicts (17.5). Therefore in order to derive a necessary condition of a T-periodic steady state, an algebraic condition will be derived for equation (17.5) to have no solution.

If $\tau^{(1)}$ exists it requires that $t_s/T - 1 \leq \tau^{(1)} \leq t_s/T + \tau - 1$. Substituting into this inequality the right hand side of (17.5) for $\tau^{(1)}$, denoting

$$\bar{m}_{min} = \frac{m - \Delta m}{V_d}; \qquad \bar{m}_{max} = \frac{m + \Delta m}{V_d} \tag{17.8}$$

and after a few simple algebraic manipulations, it can be concluded that $\tau^{(1)}$ does not exist if

$$\bar{m}_{min} > t_s/T + \tau - 1 \tag{17.9}$$

(the condition $\bar{m}_{max} < t_s/T - 1$ is dropped, as it is always false). To make the condition (17.9) practically useful, an expression for $\bar{m}_{min}$ in terms of system parameters is now derived. Invoking (15.3) and (15.7-15.8)

$$\bar{m}_{min} = \frac{M}{V_d}\frac{t_s}{T}\tau + \tau - \frac{M}{V_d}\tau \qquad \tau \in [0, t_s/T] \tag{17.10}$$

$$\bar{m}_{min} = \frac{M}{V_d}\frac{t_s}{T}\tau + \tau - \frac{M}{V_d}\frac{t_s}{T} \qquad \tau \in [t_s/T, 1] \tag{17.11}$$

Substituting this into (17.9) the following equations are obtained:

$$\frac{M}{V_d}\frac{t_s}{T}\tau - \frac{M}{V_d}\tau - \frac{t_s}{T} + 1 > 0 \qquad \tau \in [0, t_s/T] \tag{17.12}$$

$$\frac{M}{V_d}\frac{t_s}{T}\tau - \frac{M}{V_d}\frac{t_s}{T} - \frac{t_s}{T} + 1 > 0 \qquad \tau \in [t_s/T, 1] \tag{17.13}$$

The left hand side of both inequalities achieves its minimum at $\tau = t_s/T$ (as $t_s/T - 1 < 0$). It means that if the inequality

$$\frac{M}{V_d}\left(\frac{t_s}{T}\right)^2 - \left(\frac{M}{V_d} + 1\right)\frac{t_s}{T} + 1 > 0. \tag{17.14}$$

is satisfied then (17.9) will be true for any τ. This quadratic equation in t_s/T has roots at $\frac{V_d}{M}$ and 1. Since, t_s/T is always smaller then 1, a necessary condition for the existence of an equilibrium point is

$$\frac{t_s}{T} < \frac{V_d}{M}, \tag{17.15}$$

where $M = T\mathbf{K}(\mathbf{A_1 z} + \mathbf{B_1})$. This condition is the strongest condition that can obtained from this analysis. Indeed, the possibility of $\tau = \tau^{(3)}$ requires that $\tau^{(2)}$ does not exist. It is easy to see that if $\tau = \tau^{(3)}$, then the existence of $\tau^{(2)}$ implies also the existence of $\tau^{(1)}$.

The condition (17.15) is conservative, but has the advantage that it involves only basic system parameters. It is noted that while condition (17.15) guarantees the existence of a candidate equilibrium duty ratio, and is necessary for the actual existence of a T-periodic equilibrium, it does not guarantee that such an equilibrium will exist as a stable steady state.

Simulations show that, for an operational point, it is possible that a solution shifts from being T-periodic to a stable $2T$-periodic, nT-periodic or chaotic regime.

Example (DC servo motor) For the DC servo motor a standard design procedure leads to the selection of $K_p^i = 0.1$, then the inequality (17.15) is true for any $t_s/T < 1$, but if $K_p^i = 0.45$ is selected to make the controller more aggressive, then $\frac{L_a V_d}{T K_p^i V_{DC}} = 0.421$ and a necessary condition for the existence of a T-periodic equilibrium is that $t_s/T < 0.421$.

17.2 Further Necessary and Sufficient Conditions for Existence of a T-Periodic Stable Equilibrium (Based on the Approximate System)

In this section necessary and sufficient conditions for existence of a T-periodic equilibrium point are derived, and uniqueness and local stability of such a point is established. Although I do not provide a rigorous proof for global stability, extensive simulations suggest that, under the local stability condition, the equilibrium point is indeed globally stable. The main tool used in this section is a discrete piecewise affine map, which describes the evolution of the closed-loop system duty ratio from one time interval to the next. The conditions for existence and stability of the equilibrium point will be derived from an analysis of this map.

As was shown on the Chapter 16 the trajectory of the system state space vector and switching instant in the time interval $[t_k, t_k + T]$ are completely determined by $\mathbf{x}(t_k)$ and τ_{k-1}. Equations (16.7-16.8) and (16.17-16.19) may be used to obtain an iterative map for τ, but this map will be nonlinear. In this chapter an approximate affine map is derived.

First, an explicit equation for m as a function of time will be derived. As before, assume that the reference and disturbance signals are constant, but that the system is not necessarily in a T-periodic steady state and assume a piecewise linear approximation for m. To define m as a piecewise linear function it is sufficient to find the derivative of m in every switching interval. By definition $\dot{m}(\mathbf{x}(t)) = -\mathbf{K}\dot{\mathbf{x}}$ and therefore the derivative of m depends on the state vector as in

$$\dot{\mathbf{x}} = (\mathbf{A}_0 + \mathbf{A}_1)\mathbf{x} + \mathbf{B}_0 U + \mathbf{B}_1, \qquad t \in (kT, kT + \tau_k T] \tag{17.16}$$

$$\dot{\mathbf{x}} = \mathbf{A}_0\mathbf{x} + \mathbf{B}_0 U, \qquad t \in (kT + \tau_k T, kT + T] \tag{17.17}$$

The assumption that m is piecewise linear within every time interval $[t_k, t_k{+}T]$ implies that $\mathbf{x}(t)$ in the right hand side of (17.16-17.17) is approximated by a constant $\mathbf{z}_k$, equal to the time averaged value of $\mathbf{x}(t)$ over that interval. Equivalently, the term $\varepsilon\,\Psi$ in $\mathbf{x}(t)$ is neglected. In a T-periodic steady state regime, $\mathbf{z}_k$ remains constant from one time interval to another. When the system is not in a T-periodic steady state, $\mathbf{z}_k$ may vary. To determine $\dot{m}(\mathbf{x}(t))$ a crude approximation of $\mathbf{z}_k$ by a constant $\mathbf{z}_{css}$ will be used. The validity of this approximation is justified if the error $\mathbf{K}\mathbf{A}_i(\mathbf{z}_k - \mathbf{z}_{css})$ has the same order as $\mathbf{K}\mathbf{A}_i(\mathbf{z}_k - \mathbf{x})$ for $i = 0, 1$.

The approximate value of the state space vector, for the case $\mathbf{A}_1 = 0$, will be found as a steady state solution of the conventional averaged model

$$\dot{\mathbf{z}} = (\mathbf{A}_0 + \mathbf{A}_1\tau)\mathbf{z} + \mathbf{B}_0 U + \mathbf{B}_1\tau, \tag{17.18}$$

$$m(\mathbf{z}) = \mathbf{C}U - \mathbf{K}\mathbf{z}, \tag{17.19}$$

where $\tau = m(\mathbf{z})/V_d$. Using the modified method described in Chapter 13, it is possible to get a better approximation, but due to the nonlinearity of the equation for τ it is difficult to derive a simple close form expression for $\mathbf{z}_{css}$.

Substituting $m(\mathbf{z})/V_d$ for τ and letting $\dot{\mathbf{z}} = 0$, from (17.18-17.19) the steady state averaged closed-loop vector is obtained

$$\dot{\mathbf{z}} \;=\; (\mathbf{A}_0 - \mathbf{B}_1\mathbf{K}/V_d)\mathbf{z} + (\mathbf{B}_0 + \mathbf{B}_1\mathbf{D}/V_d)U. \tag{17.20}$$

By letting $\dot{\mathbf{z}} = 0$, the averaged steady state vector is

$$\mathbf{z}_{css} \;=\; -(\mathbf{A}_0 - \mathbf{B}_1\mathbf{K}/V_d)^{-1}(\mathbf{B}_0 + \mathbf{B}_1\mathbf{C}/V_d)U. \tag{17.21}$$

Now equations for the straight line segments of the function $m(\mathbf{x}(t))$ will be derived. From (16.3-16.4) it follows that in steady state, if $\mathbf{K}\mathbf{A}_i\mathbf{x}$ is approximated by $\mathbf{K}\mathbf{A}_i\mathbf{z}_{css}$ $(i = 0, 1)$, then $\frac{d}{dt}m((\mathbf{x}(t))$ is

$$\dot{m} \;=\; -\mathbf{K}\left[(\mathbf{A}_0 + \mathbf{A}_1)\mathbf{z}_{css} + \mathbf{B}_0U + \mathbf{B}_1\right], \qquad t \in (t_k, t_k + \tau_kT] \tag{17.22}$$

$$\dot{m} \;=\; -\mathbf{K}\left[\mathbf{A}_0\mathbf{z}_{css} + \mathbf{B}_0U\right] \qquad t \in (t_k + \tau_kT, t_{k+1}] \tag{17.23}$$

With the notations $\dot{m}T/V_d = \alpha$ for $t \in (t_k, t_k + \tau_kT]$, and $\dot{m}T/V_d = \beta$ for $t \in (t_k + \tau_kT, t_k]$ the function m/V_d over $[t_k, t_k + T]$ is

$$m(\mathbf{x}(t_k + \theta T))/V_d \;=\; \begin{cases} \bar{m}_k + \alpha\theta & \text{if } \theta \in [0, \tau_k] \\ \bar{m}_k^{\tau} + \beta(\theta - \tau_k) & \text{if } \theta \in [\tau_k, 1] \end{cases}, \tag{17.24}$$

where $\bar{m}_k = m(\mathbf{x}(t_k))/V_d$, and $\bar{m}_k^{\tau} = m(\mathbf{x}(t_k + \tau_kT))/V_d$. (Explicit formulas for α and β in terms of the system parameters in the DC servo motor example, are given in Appendix 2.)

Next, an affine iterative map for τ_k is derived. In Chapter 16 we distinguished between three cases where the sawtooth function $V_d\text{tri}(t, T)$ intersects with the function

m at different slopes of m (enumerated from 1 to 3). To completely determine the behavior of the system, two more cases must be considered. There are two possibilities that an absence of an intersection occurs due to saturation: one when $m < V_d \mathrm{tri}(T,t)$ and $\tau_k = 0$ and the other when $m > V_d \mathrm{tri}(T,t)$ and $\tau_k = 1$ for all $t \in [t_k, t_k + T]$ (enumerated by 4 and 5). In general, one more state, e.g. $\bar{m}_k$, should be added to make the discrete evolution of τ_k well posed, which is not necessary if only cases 2 and 3 are considered.

In Appendix 3 the transition from the state $(\tau_{k-1}, \bar{m}_{k-1})$ to $(\tau_k, \bar{m}_k)$ is derived to be a continuous, piecewise affine map of the form

$$\begin{bmatrix} \tau_k \\ \bar{m}_k \end{bmatrix} = \mathbf{A}^{(\mathbf{i})} \begin{bmatrix} \tau_{k-1} \\ \bar{m}_{k-1} \end{bmatrix} + \mathbf{B}^{(\mathbf{i})}, \tag{17.25}$$

where $i = 1, ..., 5$ is determined by the validity of one of five inequalities

$$\mathbf{C}^{(\mathbf{i})} \begin{bmatrix} \tau_{k-1} \\ \bar{m}_{k-1} \end{bmatrix} + \mathbf{D}^{(\mathbf{i})} > 0, \tag{17.26}$$

which divide the region of all possible pairs $(\tau_l, \bar{m}_l)$ into five non intersecting subregions (excluding boundary intervals). The matrices $\mathbf{A}^{(\mathbf{i})}$ and $\mathbf{C}^{(\mathbf{i})}$ depend only on α and β; $\mathbf{B}^{(\mathbf{i})}$ and $\mathbf{D}^{(\mathbf{i})}$ depend also on t_s/T.

The following conditions can be derived from (17.25-17.26).

A necessary and sufficient condition for existence of a T-periodic steady state. By (17.25) a T-periodic steady state exists within the region ℓ if and only if

$$\begin{bmatrix} \tau_{ss} \\ m_{ss} \end{bmatrix} = \left(\mathbf{I}_{\mathbf{2}\times\mathbf{2}} - \mathbf{A}^{(\ell)}\right)^{-1} \mathbf{B}^{(\ell)} \tag{17.27}$$

and if the inequality (17.26) is satisfied, meaning

$$\mathbf{C}^{(\ell)}\left(\mathbf{I_{2\times 2}}-\mathbf{A}^{(\ell)}\right)^{-1}\mathbf{B}^{(\ell)}+\mathbf{D}^{(\ell)}>0. \tag{17.28}$$

A sufficient condition for local stability of a T-periodic steady state. If and only if the matrix $\mathbf{A}^{(\ell)}$ is stable, i.e., all its eigenvalues are inside the unit circle in the complex plane, then the equilibrium point given by (17.27) is locally stable.

Now explicit expressions for the necessary and sufficient conditions for existence of a stable T-periodic equilibrium within different regions ℓ will be obtained from (17.27-17.28). It easy to see that a T-periodic equilibrium within the saturation region $\ell = 4$ may exist if and only if $\tau_{ss} = 0$ and $\beta = 0$; and within saturation region $\ell = 5$ if and only if $\tau_{ss} = 1$ and $\alpha = 0$. These two simple cases will be excluded from the remaining discussion. In Section 17.1 it was shown that a T-periodic steady state equilibrium may not exist if $i = 1$. Thus it is two cases left.

Intersection within slope 2

Using the explicit formulas from Appendix 3 condition (17.28) becomes

$$\begin{array}{rcl} |(1-\beta)|\,\beta/(\beta-\alpha) & > & 0 \\ |(1-\beta)|\,(1-t_s/T) & > & 0 \\ |(1-\beta)|\,(-\beta(1-t_s/T)-\alpha t_s/T)/(\beta-\alpha) & > & 0 \end{array} \tag{17.29}$$

The first two inequalities are trivially satisfied, as $\alpha < 0$ and $\beta > 0$. The third one can be simplified to $\tau_{ss} = \beta/(\beta-\alpha) < t_s/T$. As the matrix $\mathbf{A}^{(2)}$ has only one non zero eigenvalue, stability of the solution is equivalent to

$$\left|1-\frac{\alpha-\beta}{\beta-1}\right| < 1 \tag{17.30}$$

which is further equivalent to $\beta < 2/3$ and $\alpha > 3\beta - 2$.

The coordinates of the equilibrium point are given by (17.27)

$$\left[\begin{array}{c} \tau_{ss} \\ m_{ss} \end{array}\right] = \left[\begin{array}{c} \beta/(\beta-\alpha) \\ t_s/T\beta + (1-\beta)\beta/(\beta-\alpha) \end{array}\right]. \tag{17.31}$$

Intersection within slope 3

A similar analysis, applied to the slope 3, yields the intersection condition

$$\begin{array}{rcl} -(1-\alpha)t_s/T + (1-\alpha)\beta/(\beta-\alpha) & > & 0 \\ -\alpha(1-\alpha)/(\beta-\alpha) & > & 0 \end{array} \tag{17.32}$$

which is true if $\tau_{ss} = \beta/(\beta-\alpha) > t_s/T$ (the second inequality always holds). As the matrix $\mathbf{A}^{(3)}$ has only one non zero eigenvalue, stability of the solution is equivalent to

$$\left|\frac{1-\beta}{1-\alpha}\right| < 1 \tag{17.33}$$

which is true when $\beta < 2$ or $\alpha < 2 - \beta$. The coordinates of the equilibrium point are given by (17.27)

$$\left[\begin{array}{c} \tau_{ss} \\ m_{ss} \end{array}\right] = \left[\begin{array}{c} \beta/(\beta-\alpha) \\ (1-\alpha)\beta/(\beta-\alpha) + \alpha t_s/T \end{array}\right]. \tag{17.34}$$

Uniqueness of a T-periodic stable equilibrium. The conditions (17.30) and (17.33) for existence of an equilibrium point for $\ell = 2$ and $\ell = 3$ (and the conditions for cases 4 and 5) are mutually exclusive. Therefore a T-periodic equilibrium, should it exist, is unique.

In order to demonstrate the broad applications of the results in this section a few examples will be considered next.

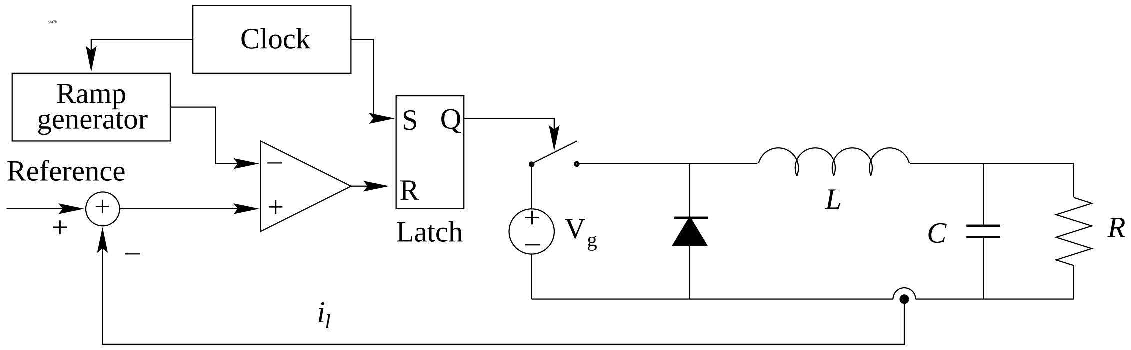

Figure 17.3: A current -programmed buck converter.

17.3 Examples

17.3.1 Current programmed DC-DC converter.

In this section a brief introduction to the basics of current programming in DC-DC converters is first presented. Then standard results in modeling of such converters are discussed and compared with results developed in this thesis.

Current programming has become widely adopted as a useful technique for improving performance of switched-mode DC-DC converters, because of its advantages in better line-noise rejection, automatic overload protection, easy paralleling of multiple converters, and design flexibility in improving small-signal dynamics.

Figure 17.3 shows an illustrative diagram for a current programmed buck converter, where inductor current is sensed. The converter switch is turned on every T_s

seconds and turned off whenever i_l equals the sum of control signal i_c and a compensating ramp of the fixed slope $-m_c$ that restarts at 0 every cycle. Thus, the duty ratio depends not only on the value of control current, but also on how long it takes the inductor current to reach the reference value. Also, this time duration is determined by the starting value and the up-slope of inductor current. Use of inductor current to determine duty ratio introduces feedback into the converter and makes it prone to instability. To add a compensation ramp m_c (sawtooth signal in our terminology) is a common practice to alleviate this problem. It is easy to see that the current programmed converters fall into the class of closed-loop linear system with PWM and zero delay considered in the Introduction.

The usual switched converter approximation is to represent the inductor current waveform as piecewise linear, with slopes m_1 and $-m_2$ during charging and discharging operations. It is also usually assumed that these slopes, as well as control signal i_c, change only slowly from cycle to cycle and they are constant in steady state.

The following notation conventions are commonly adopted. Capital letters are used to indicate quantities associated with steady-state, letters with tilde are quantities associated with small-signal perturbations, and small letters represent perturbed signals, i.e., quantities which are the sum of capital and letters with tilde. Since usually the stabilizing ramp is constant $M_c = m_c$. The average inductor current over an interval of length T_s is denoted by $\bar{i}_l$.

Figure 17.4 shows inductor current waveform in steady state, where $-m_c$ is the

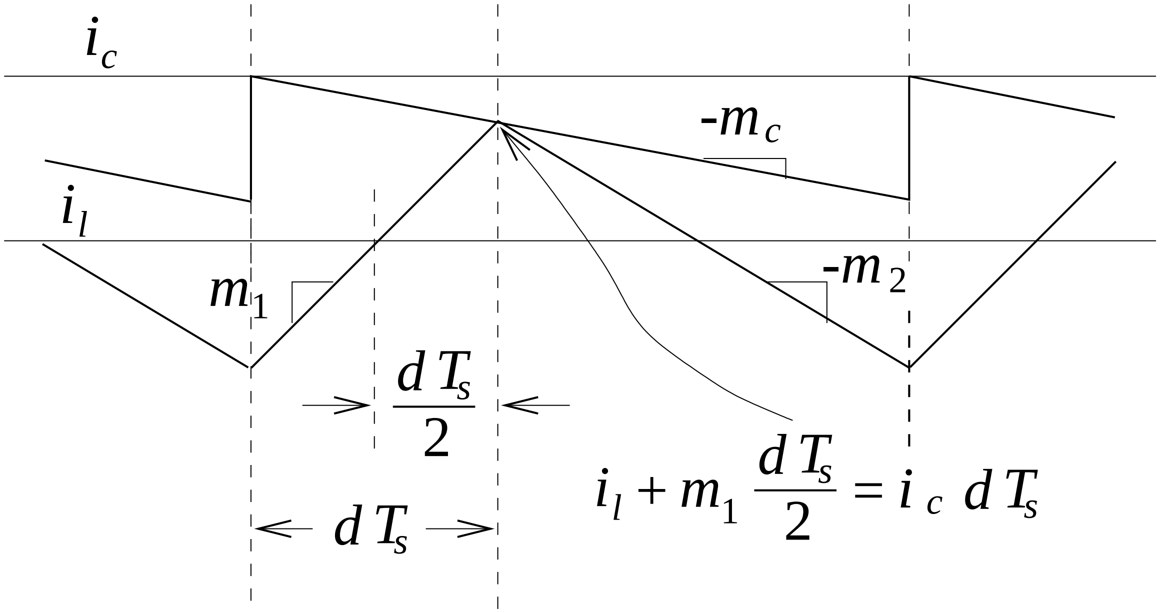

Figure 17.4: Geometries of inductor current in steady state.

slope of the compensating ramp, m_1 is the up-slope and $-m_2$ is the down-slope of the inductor current. The geometries of the waveforms is used to provide information for derivation of a converter model. From the geometry of the inductor current waveform in steady state and with slopes m_1, m_2, and m_c constant, one can write two equations:

$$\begin{aligned} \bar{i}_l &= i_c - m_c dT_s - \tfrac{1}{2} m_1 dT_s, \\ \bar{i}_l &= i_c - m_c dT_s - \tfrac{1}{2} m_2 (1-d) T_s. \end{aligned} \tag{17.35}$$

To unify these two equations into a single expression, one can use the following general expressions, originated in [62], for m_1 and m_2:

$$\begin{aligned} m_1 &= (1-d) V_g / L, \\ m_2 &= d V_g / L. \end{aligned} \tag{17.36}$$

These equations can be derived from the following observation. During the switch "on" time the inductor is connected between line input and output voltage V_g and v, so

$$m_1 = \frac{V_g - v}{L} \tag{17.37}$$

the dc conversion ratio is $V = DV_g$, hence

$$M_1 = \frac{(1-D)V_g}{L}. \tag{17.38}$$

Substitution of (17.36) into either expression in (17.35) leads to the same expression:

$$\bar{i}_l = i_c - m_c T_s d - \frac{d(1-d)T_s}{2L} V_g, \tag{17.39}$$

satisfaction of which is equivalent to both equations in (17.35), simultaneously. Equation (17.39) is a unified large-signal expression which describes how a duty ratio d is determined. This formula can be obtained from results developed in Chapter 13. In our notation an averaged PWM input $m(\mathbf{z})$ is $i_c - \bar{i}_l$, the magnitude of compensating ramp (sawtooth signal) V_d is $m_c T_s$, and coefficient $M(\mathbf{z}, T) = M = T\mathbf{K}(\mathbf{A_1 z} + \mathbf{B_1})$ is equal to $\frac{V_g T}{L}$. Substituting this into (17.39) equation (13.13) can be recovered

$$m(\mathbf{z}) - \frac{M(\mathbf{z}, T)}{2}(\tau - \tau^2) = \tau V_d. \tag{17.40}$$

Note that in this special case purely geometric considerations yield the same result as the averaging theory we used previously.

Small-signal information can be derived by its perturbation, which yields

$$\tilde{i}_l = \tilde{i}_c - \left(M_c + \frac{1-2D}{2L} V_g\right) T_s \tilde{d}. \tag{17.41}$$

Then, the unified modulator model is obtained as

$$\tilde{d} = \frac{1}{\left(m_c + (1-2D)V_g/(2L)\right)T_s}\left(\tilde{i}_c - \tilde{i}_l\right). \tag{17.42}$$

The small deviation model of the PWM was obtained in Chapter 14, equation (14.33)

$$\tau = \tau_{ss} + \frac{m(\mathbf{x}) - m(\mathbf{z_{ss}})}{M(\mathbf{z},T)(1/2-\tau_{ss}) + V_d}, \tag{17.43}$$

where $\tau - \tau_{ss} = \tilde{d}$, $\tau_{ss} = D$ and $\tilde{i}_c - \tilde{i}_l = m(\mathbf{x}) - m(\mathbf{z_{ss}})$.

Two independent approaches are used to stability analysis. The first approach is based on geometric construction of the perturbed programmed current [101]. The second approach is to find a rational function approximation of sampled representation of the closed-loop transfer function $\tilde{i}_l/\tilde{i}_c$ [98]. These approaches yield the same result, which is presented bellow.

From the geometry of the currents in Fig. 17.5, one can write two discrete-time equations:

$$\begin{aligned} \tilde{i}_c(k) &= \tilde{i}_l(k) + M_1\tilde{t}(k+1) + m_c\tilde{t}(k+1) & (17.44)\\ \tilde{i}_l(k+1) &= \tilde{i}_c(k+1) - m_c\tilde{t}(k+1) + M_2\tilde{t}(k+1). & (17.45)\end{aligned}$$

Information about the duty ratio can be obtained by solving for $\tilde{t}(k+1)$. Subtraction of the first expression from the second and then rearranging yields

$$\tilde{d}(k+1) = \frac{\tilde{t}(k+1)}{T_s} = \frac{\tilde{i}_c(k+1) - (\tilde{i}_l(k+1) + \tilde{i}_l(k))/2}{\left(m_c + (M_1 - M_2)/2\right)T_s}. \tag{17.46}$$

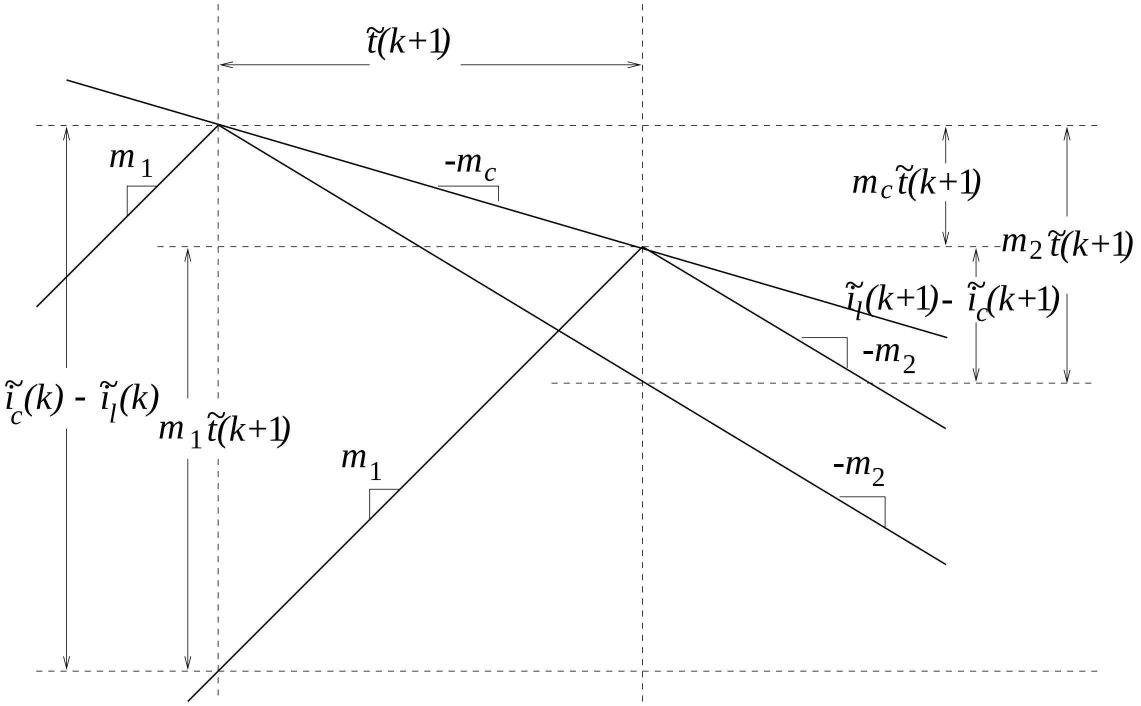

Figure 17.5: Geometries of inductor current in steady state.

With the restriction of low-frequency perturbation, one has $\tilde{i}_l(k+1) \approx \tilde{i}_l(k)$, which in turn gives

$$\tilde{d} = \frac{\tilde{i}_c - \tilde{i}_l}{(m_c + (M_1 - M_2)/2)\,T_s}, \tag{17.47}$$

which shows the same coefficient as in (17.42). The discrete transfer function from control Δi_c to inductor current Δi_l is derived by introduction of the z-transform into the two equations in (17.44), which leads to

$$\frac{\Delta i_l(z)}{\Delta i_c(z)} = (a+1)\frac{z}{z+a}, \tag{17.48}$$

where

$$a = \frac{M_2 - M_c}{M_1 + M_c}. \tag{17.49}$$

This discrete transfer function is stable if $|a| < 1$. This is the same condition as the condition for existence of a T- periodic steady state (17.33)

$$\left|\frac{1-\beta}{1-\alpha}\right| < 1, \tag{17.50}$$

developed in this chapter. Equation (17.33) becomes identical to (17.49) and to stability criterion available in the literature (e.g. equation (17) in [101]) after the following substitution $\beta = M_2/M_c$ and $\alpha = -M_1/M_c$.

Conclusions. It was shown in this section that applying the theory developed in the thesis to the DC-DC current programmed converters the well known results [62] can be recovered. Equation (13.13) to calculate duty ratio in steady state derived in Chapter 13 is exactly the same as (17.39). The same results are also obtained for small deviation model of the PWM (equations (17.42) and (14.33)), and for existence of a T-periodic steady state (equations (17.33) and (17.49)). Explanation of this result follows from the fact that the same assumptions are made in both approaches about the shape and piecewise linear nature of the ripple function. After these results are written in terms of the slopes of the ripple function, both methods arrive to the same equations.

The differences between these two approaches are the following:

1. The averaging theory provides justification for using certain approximation of the ripple function, while the geometric method assumes the ripple as piecewise linear based on practical observations.

2. The results obtained in the thesis are general and can be applied not only to a first order system, but to any linear system with a PWM block.

3. Our approach allows to study more complicated ripple patterns such as in the case of delays, or nT-periodic steady state.

17.3.2 DC servo motor.

For the benchmark PWM DC servo motor previously discussed, $\mathbf{A}_1 = 0$ and formulas for α and β are given in Appendix 2. Using the motors values from Appendix 1,

$$\alpha = K_p^i(2.626 \cdot 10^{-2}\omega^* + 0.274T_{load} - 5.256) \tag{17.51}$$

and

$$\beta = K_p^i(2.626 \cdot 10^{-2}\omega^* + 0.274T_{load}). \tag{17.52}$$

This leads to the existence of a stable T-periodic orbit of the system if $\tau_{ss} < t_s/T$ and (17.3) is satisfied or $\tau_{ss} > t_s/T$ and (17.4) is satisfied, where

$$\tau_{ss} = 4.996 \cdot 10^{-3}\omega^* + 5.218 \cdot 10^{-2}T_{load}. \tag{17.53}$$

Finally, note that in absence of a stable steady state T-periodic equilibrium, the system may have nT-periodic equilibrium or may even display an aperiodic (chaotic) behavior. This can be illustrated by the following the examples.

If $K_p^i = 0.2$, $t_s/T = 0.8$ and $\omega^* = 120.6$, then $\alpha = -0.394$ and $\beta = 0.658$. In this case inequality (17.28) is satisfied only for $i = 2$, but the matrix $\mathbf{A}^{(2)}$ is unstable.

It was observed in the simulations (see Fig. 17.6) that the system has $3T$-periodic equilibrium.

If $K_p^i = 0.3$, $t_s/T = 0.75$ and $\omega^* = 63.3$, then $\alpha = -1.042$ and $\beta = 0.535$. In this case again inequality (17.28) is satisfied only for $i = 2$, but the matrix $\mathbf{A}^{(2)}$ is unstable. The system exhibit an aperiodic behavior shown in Fig. 17.7.

While it may be feasible to obtain an analytical condition for the existence of nT-periodic solution, this formula will likely be far more complicated than the expression for the T-periodic case.

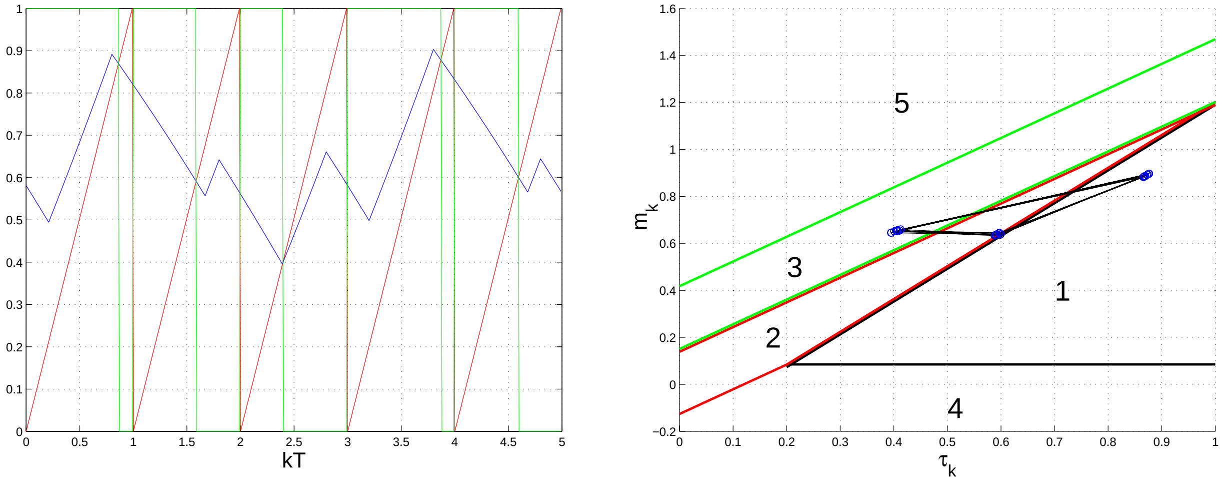

Figure 17.6: $3T$-periodic stable equilibrium. The PWM input voltage and sawtooth - (a). The evolution of the state vector (τ_k, m_k) - (b).

17.3.3 PWM with uniform sampling.

The PWM technique discussed in the Introduction for the generation of switching instants is simple to implement using analog comparators. It is challenging, however,

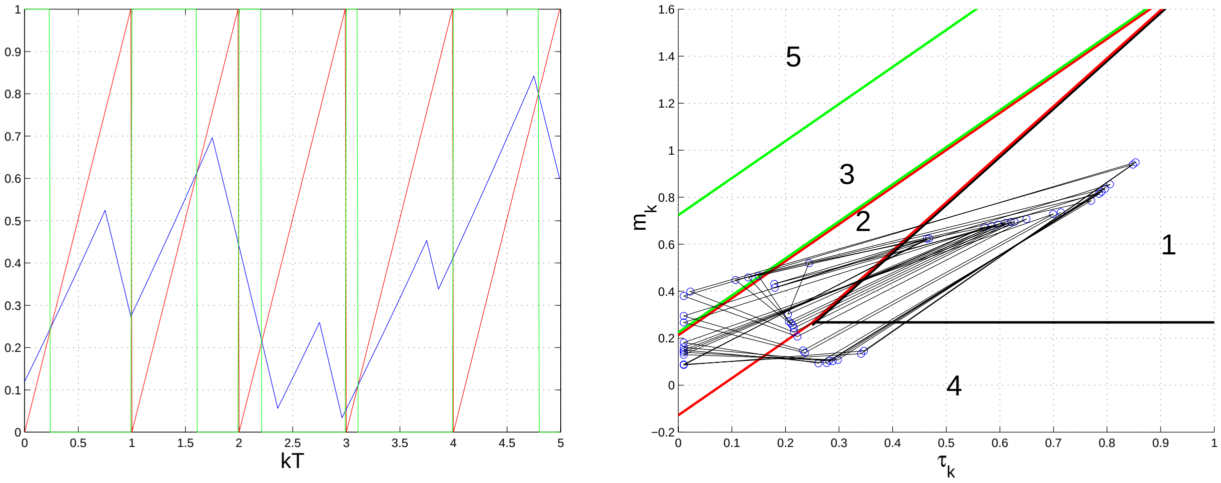

Figure 17.7: Aperiodic behavior. The PWM input voltage and sawtooth - (a). The evolution of the state vector (τ_k, m_k) - (b).

to detect the crossing instant of two time-variable signals when a microprocessor is used. This difficulty is often bypassed with the help of sampling and hold techniques. The PWM input signal is sampled only once within the switching period T. The switching instants are computed on-line as the respective points where the triangular slope reaches the sampled value.

Now, the technique developed in this chapter will be used to obtain condition for existence of a T-periodic stable equilibrium. Assume that sampling instants are $t_s/T + kT$, where $0 \leq t_s < T$ and $t_s/T < \tau_k$. Then $\tau_k = \bar{m}_{k-1} + \alpha t_s/T$, and iterative map $\bar{m}_k = \bar{m}_{k-1} + (\alpha - \beta)\tau_k + \beta$ can be rewritten as

$$\bar{m}_k = (1 + \alpha - \beta)\bar{m}_{k-1} + (\alpha - \beta)\alpha t_s/T + \beta. \tag{17.54}$$

Stability of the solution is equivalent to

$$|1+\alpha-\beta|<1 \tag{17.55}$$

which is further equivalent to $\alpha > \beta - 2$ (see Fig. 17.1(c)).

17.3.4 PWM with two sided sawtooth function

In this section the results developed in the thesis will be applied to show that two sided PWM technique eliminates the influence of the current ripple on the averaged PWM output or, equivalently, that the closed-loop PWM gain is equal to the nominal PWM gain. The difference between conventional single-slope PWM and the two sided PWM is that, instead of single-slope sawtooth function the two sided function is used. One period of T periodic two sided sawtooth function is defined as

$$\mathrm{tri}_2(t,T) = \begin{cases} 2t/T & \text{if } t \in [0, T/2] \\ 2(1-t/T) & \text{if } t \in [T/2, T] \end{cases} . \tag{17.56}$$

The switching rule remains the same as for single-slope PWM. Namely, the switch is "on" while the PWM input voltage $m(\mathbf{x})$ exceed the sawtooth voltage $V_d\mathrm{tri}_2(t,T)$. The PWM output voltage can be formalized as $q(t) = V_{DC} \cdot u(m(\mathbf{x}) - V_d\mathrm{tri}_2(t,T))$, where u is the unit step function. If the same assumption about piecewise linear nature of the current ripple as in Chapter 13 is made, then from Fig. 17.8

$$\bar{m}_k = \beta(1-\tau_k) + \bar{m}_k^{\tau} \tag{17.57}$$

$$\bar{m}_k^{\tau} = \tau_{k-1}\alpha + \bar{m}_{k-1}. \tag{17.58}$$

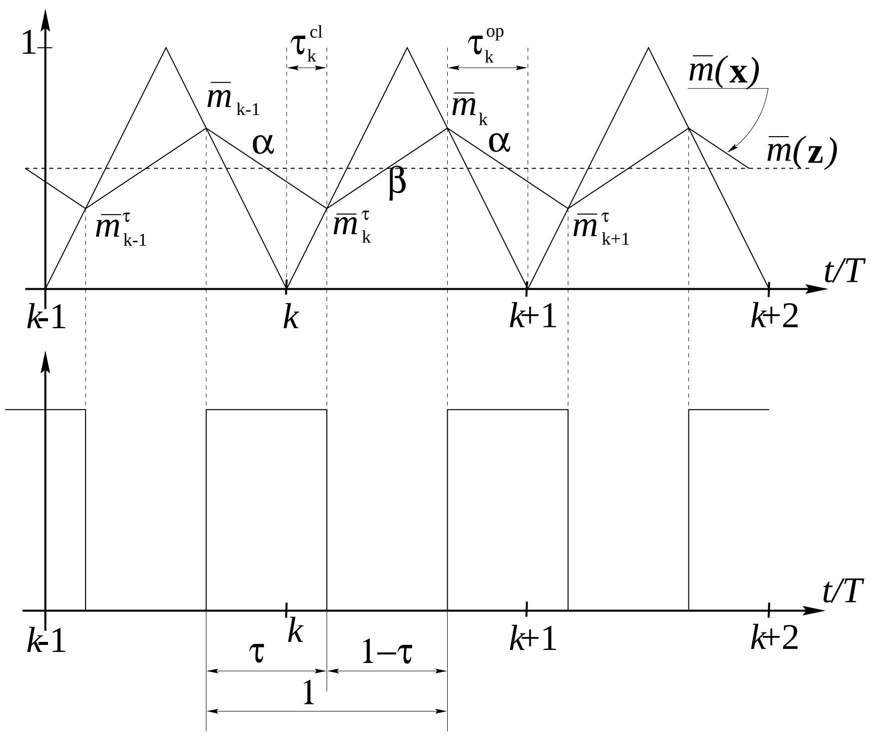
1
τ_k^{cl}
τ_k^{op}
$\bar{m}(\mathbf{x})$
$\bar{m}_{k-1}$
$\bar{m}_k$
α
α
$\bar{m}(\mathbf{z})$
β
$\bar{m}_{k-1}^{\tau}$
$\bar{m}_k^{\tau}$
$\bar{m}_{k+1}^{\tau}$
t/T
k-1
k
k+1
k+2
t/T
k-1
k
k+1
k+2
τ
$1-\tau$
1

Figure 17.8: Two sided PWM input and output voltages.

In steady state $\bar{m}_k = \bar{m}_{k-1}$, $\bar{m}_k^{\tau} = \bar{m}_{k-1}^{\tau}$, and $\tau_k = \tau_{k-1} = \tau_{ss}$, then

$$\tau_{ss} = \frac{\beta}{\beta - \alpha}. \tag{17.59}$$

The duty ratio depends only on slopes of the ripple function α, β. This is the fundamental property: duty ratio is the same for single- and two sided PWM.

Now, the relation between averaged PWM input and averaged PWM output voltages in steady state will be found. Let consider time interval $[kT, (k+1)T]$. At the time $kT + \tau_k^{cl}$ switch turns "off" and at the time $(k+1)T - \tau_k^{op}$ switch turns "on". From equation $\bar{m}(\mathbf{x}) = \mathrm{tri}_2(t,1))$ follows, that $\tau_k^{ol} = 2\bar{m}_k^{\tau}$ and $\tau_k^{op} = 2\bar{m}_k^{\tau}$. The average

PWM input voltage is

$$\bar{m}(\mathbf{z}) = \frac{\bar{m}_k + \bar{m}_k^\tau}{2}, \tag{17.60}$$

which is equal to $\tau_k^{cl} + \tau_k^{op} = \tau_k$. Finally, $\bar{m}(\mathbf{z}) = \tau_{ss}$ and closed-loop PWM gain defined as ratio of averaged output and averaged input PWM voltages is V_{DC}/V_d and equal to nominal PWM gain K_{PWM}.

17.4 Conclusions

In this chapter analytical and experimental study of effects of finite switching frequency and delays on linear systems with pulse-width modulated power supplies has been presented. In the first part of the paper deviations from standard (idealized) fixed-gain models have been quantified and experimentally verified. In the second part the discrete-time piecewise affine map, which describes the behavior of the closed-loop system, has been derived, and conditions for existence of a T-periodic stable equilibrium have been presented.

Chapter 18

Effects of Low Switching Frequency on AC Drives

In this chapter analytical results and numerical simulations that quantify effects of low switching frequency in AC drives are presented. These results build on related developments for DC converters. Specifically, the models of pulse-width modulated (PWM) inverters that are used in high efficiency AC drives are examined. The standard modeling procedure assumes that the switching frequency of the PWM block is high enough, so that the resulting supply waveform can be replaced by its first harmonic in control-oriented models. Our aim is to re-examine this assumption and quantify the introduced errors.

Any PWM strategy for a power converter involves a trade-off between the quality of the output current and the amount of switching losses incurred in the converter. In low and medium power three-phase voltage-controlled inverters, existing PWM techniques allow on-line realization of ultrasonic switching patterns resulting in practically pure sinusoidal output currents. Unfortunately, high switching frequency may cause a significant reduction of efficiency. This limits the switching frequency mandating a re-evaluation of standard models.

In active filter applications the control goal is to regulate as many harmonics of the fundamental as possible. This often results in operation in which highest harmonic waveform is composed of a fairly small number of switching cycles (assuming a fixed switching frequency). In this chapter averaging theoretical tools will be used to model the PWM policy known as space vector modulation, which is commonly used in high performance drives, and derive results that are relevant for a number of AC drives.

18.1 Introduction

PWM inverter-fed induction motors are increasingly used in industrial and traction applications. The developments in this field have been greatly influenced by introduction of digital signal processing methods for pulse-width modulation and drive control, and their implementation in integrated electronic hardware.

Advances in power electronics have also made significant contributions to establishing variable-speed AC machine drives as a preferred technology in motion control applications. Fast switching devices like MOSFET's and IGBT's have accelerated the application of reliable, low-harmonic waveform inverters in the lower and medium power range. These systems are widely used in machine tools, robotics, and various other applications.

High-power industrial AC drives and railway traction are applications were thyristors and, increasingly, GTO's dominate as switching elements. Switching losses in such systems account for a considerable amount of the total losses [45]. Hence, the switching frequency must be kept at low values of only few hundred Hertz [44]. A reduction of switching frequency generally results in increasing current distortion, and, consequently, machine torque harmonics and higher machine losses.

The common modeling approach to linear systems with power switches [67] is to replace the pulse-width modulated block with a fixed gain. However, this approach does not provide adequate representation when the switching frequency is not much higher then the fundamental of the waveform being synthesised. Slow switching frequency causes ripple to become considerable. Harmonic distortion of current waveforms and different optimal modulation strategies in AC drive applications have been well studied during the past decade, of which [42, 46, 43] are few examples. However, the influence of the current ripple on PWM gain in the closed-loop system has not been studied yet. In this chapter analytical formulas which quantify the effects of low switching frequency in PWM-controlled AC drives are derived. A permanent magnet synchronous motor drive will be considered as a representative example of such system. Control of the synchronous AC motor in the rotor reference frame ("d-q coordinates") simplifies controller design, such a model commonly ignores the effects of the PWM ripple. On the other hand, the space vector inverter switching policy is defined in a stationary ("α-β") reference frame.

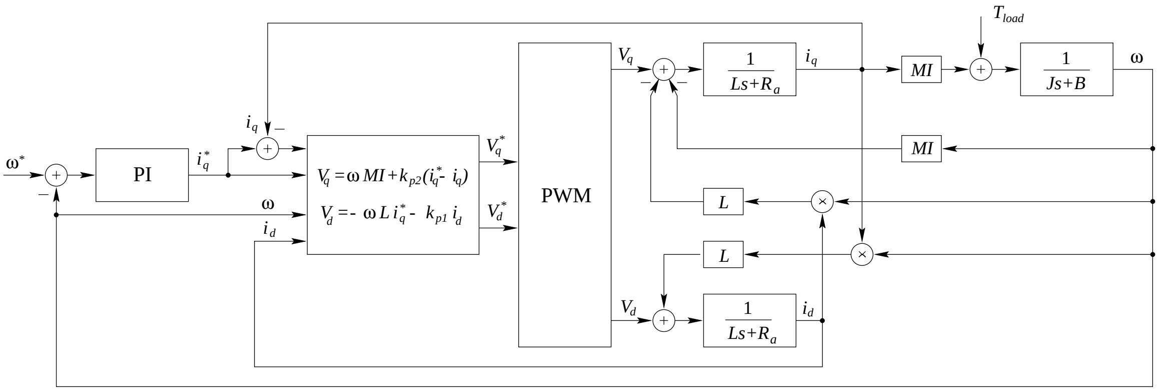

Figure 18.1: AC servo motor block diagram.

The space vector approach to pulse-width modulation owes its popularity mainly to its simplicity and elegance. Previously, the analysis and design of PWM techniques have been performed in the domain of switching signals of each individual phase of the inverter. The concept of space vector representation of a PWM is based on a reduction of a balanced three-phase system to an equivalent two-phase one. A significant advantage of PWM techniques based on voltage space vectors is the simplicity of implementation of inverter control. Instead of coupled timing of three independent switching signals, only the duration of the current state of the inverter is controlled. From analytical point of view, however, the representation of the PWM in the α-β coordinates makes the ripple effect more difficult to study when compared to the d-q coordinates. The d-q reference frame is the natural choice, because all periodic quantities are constant in a steady state, and analytical formulas from previous chapters of this thesis and [55], [88] related to averaging theory and near-identity transformation can be used.

18.2 Model of an AC Drive

A synchronous permanent magnet motor (with a non-salient rotor) is described in the rotor reference frame ("d-q coordinates") by the following equations [13]

$$\begin{aligned} L\frac{di_d}{dt} &= -R_a i_d + \omega L i_q + V_d && (18.1)\\ L\frac{di_q}{dt} &= -R_a i_q - \omega L i_d - \omega\, MI + V_q && (18.2)\\ J\frac{d\omega}{dt} &= MI\, i_q - B\omega - T_{load}. && (18.3) \end{aligned}$$

The d-q reference frame is the natural choice for our analysis, because all periodic quantities are constant in steady state, and model is linear at constant speed. In this model, J is the motor and load inertia, B is friction coefficient, T_{load} is load torque, MI is the back-emf constant, and i_d, i_q and V_d, V_q are the currents and voltages in d-q frame. The resistance and inductance of the d and q windings are $R_d = R_q = R_a$ and $L_d = L_q = L$ (as a non-salient machine is assumed). The standard controller structure for a drive involves two loops (inner current loop, and outer speed loop), each with a PI-type controller. This setup is shown in Fig.18.1, together with a feed-forward term commonly used to calculate V_q^*.

When the switching frequency of the PWM is fairly low, a pronounced ripple may appear in the currents. This ripple is ignored when a constant gain model of PWM is used. An accurate model of the PWM is needed to analyze the effects of the current ripple. Since the control of the synchronous AC motor is performed in the rotor reference frame, a model of PWM should be derived in the same coordinate system. The space vector PWM switching strategy, however, is based on reduction of a balanced three-phase system to an equivalent two-phase system, and defined in a stationary (α-β) reference frame.

To obtain the desired model of the PWM, first, the PWM **reference voltages** V_d^*, V_q^* in the d-q coordinates are transformed to V_α^*, V_β^* in the stationary reference frame

$$\begin{aligned} V_\alpha^* &= \cos(\theta)V_d^* - \sin(\theta)V_q^* \\ V_\beta^* &= \sin(\theta)V_d^* + \cos(\theta)V_q^*, \end{aligned} \tag{18.4}$$

where $\theta(t)$ is the rotor angle (in "electrical degrees"), and ω is the corresponding speed of the rotor in radians per second. When the system is close to a steady state $\omega = 2\pi/T$ is approximately constant, where T is the time required for one revolution.

The computed voltages V_α^*, V_β^* are used as reference for the space vector inverter, which produces the **actual** 3-phase PWM output line voltages V_1, V_2, V_3 waveforms, where voltages V_ℓ, $\ell = 1, 2, 3$ equal to $\pm V_{DC}$ at any particular time instant. The balanced line voltages are converted into α-β coordinates

$$\begin{aligned} V_\alpha &= V_1 + \cos(2/3\pi)V_2 + \cos(2/3\pi)V_3 \\ V_\beta &= \quad - \sin(2/3\pi)V_2 + \sin(2/3\pi)V_3. \end{aligned} \tag{18.5}$$

Finally, by means of the inverse transformation

$$\begin{aligned} V_d &= \cos(\theta)V_\alpha + \sin(\theta)V_\beta \\ V_q &= -\sin(\theta)V_\alpha + \cos(\theta)V_\beta \end{aligned} \tag{18.6}$$

the **actual** PWM output voltage V_d and V_q converted in d-q coordinates:

$$V_d = \cos(\theta)V_1 + \cos(\theta + 2/3\pi)V_2 + \cos(\theta - 2/3\pi)V_3$$

$$V_q = -\sin(\theta)V_1 - \sin(\theta + 2/3\pi)V_2 - \sin(\theta - 2/3\pi)V_3,$$

or in complex notation:

$$V_d + jV_q \quad = \quad e^{-j\theta}V_1 + e^{-j(\theta+2/3\pi)}V_2 + e^{-j(\theta-2/3\pi)}V_3. \tag{18.7}$$

If it is assumed that the switching frequency of the PWM is fairly low and the mechanical time constant of the motor is relatively large, then an approximate solution for the currents i_d, i_q can be found as follows: the voltage output V_d and V_q will be approximated by *piecewise constant* functions, and the currents i_d and i_q by *piecewise linear* functions. Approximations of V_d^* and V_q^* can be obtained from an analytical solution for currents, and with the assumption that the system is close to steady state. This analysis will allow us to estimate the magnitude of the current ripple, and to quantify deviations of the actual PWM gain from the idealized one.

18.3 Voltage space vector PWM

Pulse-width modulation has been one of the most intensively studied areas of power electronics for over three decades now. For variable frequency voltage-source inverters, two widely applied PWM methods are the space vector modulation and the suboscilation method. Both methods have moderate requirements on realization hardware and feature good transient responses.

PWM strategies based on the concept of voltage space vectors have established numerous advantages in practice. They are capable of producing the highest available fundamental output voltage with low harmonic distortion of the output current, and are well suited for microprocessor implementation [100].

Space vector PWM strategies have gained widespread recognition after the simultaneous appearance of the articles [49] by Holtz, Lammert, and Lotzkat, and [33] by Van der Broeck, Skudelny, and Stanke, in 1986. In 1988, Fukuda, Hasegawa and Iwaiji published their version of a PWM technique based on the space vectors of inverter voltage [86]. Their method is based on the same principle, along with certain modifications that were introduced to improve inverter performance.

Besides the space vector PWM method, probably most common alternative is the class of the microprocessor-implemented, regular-sampling strategies [18] based on the concept of modulating function (suboscilation method), which has replaced the classical, natural-sampling, triangular-carrier analog technique. In the regular-sampling method, pulse patterns are generated by comparing reference voltages (also called modulation waves) with a triangular wave. For practical implementation using digital technologies, it is advantageous first to sample the modulation wave once (or twice) every cycle of the triangular wave at regularly spaced intervals to produce a sampled-held modulation wave, and then to compare it (digitally) with the triangular wave to define the switching instants. By adding triplen harmonics (of order 3,6, ...) [70] to the modulation waves, the performance of regular-sampled PWM can be improved in terms of maximized output voltage range, minimized harmonic distortions, or reduced switching losses [96]. The comparison between regular-sampled PWM and space vector modulation has been the subject of many papers, e.g. [33, 96, 102].

Our analysis will address only the space vector PWM technique [104]. Space vector

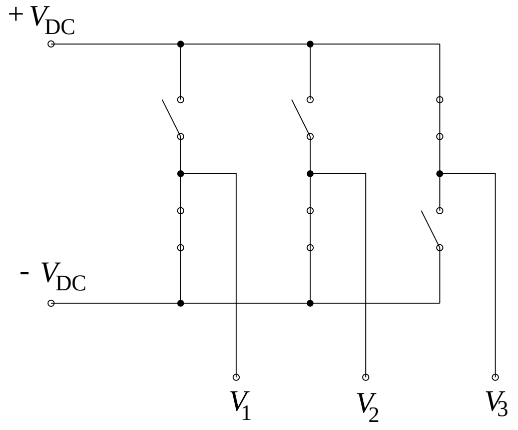

Figure 18.2: Inverter for three-phase AC motor.

modulation is based on transforming three-phase quantities into the α-β plane. (The desired three-phase sinusoidal output voltages correspond to a circular path in the α-β plane.) Assume that the waveform produced by the inverter consists of basic switching cycles with frequency $\omega_0 = 2\pi/T_0$, which is a multiple to the (slower) fundamental stator frequency $\omega = 2\pi/T$, where multiplication factor is denoted as $N = \omega_0/\omega = T/T_0$. The PWM inverter shown in Fig.18.2 attempts to reproduce (in a given basic switching cycle $(k-\frac{1}{2})T_0 < t \leq (k+\frac{1}{2})T_0$) a voltage vector $V^*(t) = V^*_\alpha + jV^*_\beta$ demanded by the current controllers. Here V^* is assumed to be given in the α-β reference frame. The best approximation would be achieved if the reference voltage $V^*(t)$ is sampled at $\tilde{t}_k = kT_0 + t_s$ $(|t_s| \leq T_0/2)$ such that the sampled value $V^*(\tilde{t}_k)$ would be equal to the average voltage within the present subinterval $[t_k - T_0/2, t_k + T_0/2]$. This is not possible, however, because the switching sequence has to be determined by the time $(k - \frac{1}{2})T_0$. For this reason $V^*(\tilde{t}_k)$ is approximated by a phase-shifted quantity $V^*(\tilde{t}_{k-1})e^{j2\pi T_0/T} = V_{DC}R^*(k)e^{j\theta^*(k)}$ (see Fig. 18.3), where V_{DC} is the inverter DC link voltage, and

$$\begin{aligned} R^*(k) &= \left(\sqrt{(V_d^*(\tilde{t}_{k-1}))^2 + (V_q^*(\tilde{t}_{k-1}))^2}\right) / V_{DC}, \\ \theta^*(k) &= \angle V^*(\tilde{t}_{k-1}) + 2\pi \frac{T_0}{T}. \end{aligned} \tag{18.8}$$

There are important practical constraints on switching patterns that are implemented by the inverter - none of the three inverter phases ("legs") is allowed to short-circuit the DC link voltage V_{DC}, and contours must exist so that all motor phase currents are continuous. Hence one switch in each leg must be off, while the other is conducting. The switching state of each leg is indicated by a binary variable 0 (top switch off) or 1 (top switch on).

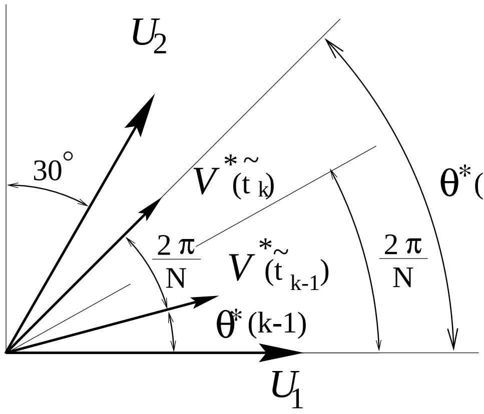

Figure 18.3: Explanation of the definition of reference input voltage vectors. In this example $N = \frac{T}{T_0} = 12$ and $t_s = 0$.

The switching state of the inverter may thus be described by three numbers characterizing 8 permissible states. States 000 and 111 correspond to the situation when all motor terminals are connected to the upper or lower bus of the DC link circuit,

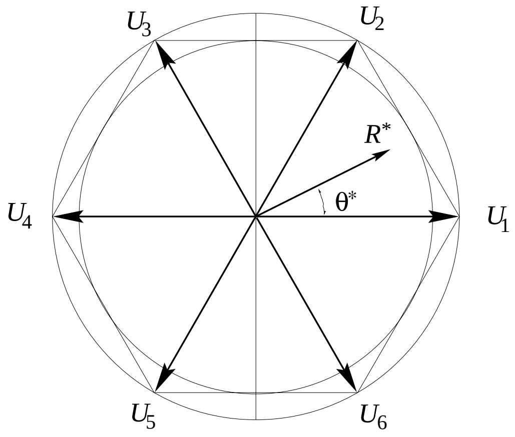

Figure 18.4: Voltage vectors created by the switching states of the inverter.

thus being shorted. All possible output states of the converter corresponds to eight voltage vectors: six active vectors that form a hexagon shown in Fig.18.4 [75] and two null (zero) vectors located at the origin. The states are shown in the following table:

U_0^u	U_1	U_2	U_3	U_4	U_5	U_6	U_0^l
1	0	0	1	1	1	0	0
1	1	1	1	0	0	0	0
1	1	0	0	0	1	1	0

(18.9)

For example, switching state U_6 is depicted in Fig.18.2. The three phase voltages V_1, V_2, V_3 applied to the motor terminals and produced by the inverter should approximate the desired three phase sinusoidal voltages. Since the commanded reference voltage vector $V^*(t)$ is typically not coinciding with one of the available 8 voltage vectors in each switching period, the required (sampled) reference voltage vector is realized by a switching sequence comprising the directly adjacent active vectors U_{ld}

and $U_{lg} = U_{ld}e^{-j\pi/3}$. The durations t_{ld} and t_{lg} of the two adjacent vectors are determined in such a way that the actual output voltage vector, when averaged over one switching cycle, coincides with the reference vector $V^*(t)$. These durations are computed using the following "projection" equations, directly derived from Fig.18.4

$$\frac{t_{ld}(k)}{T_0} = \frac{2R^*(k)}{\sqrt{3}}\sin(\theta^*(k)), \tag{18.10}$$

$$\frac{t_{lg}(k)}{T_0} = R^*(k)\cos(\theta^*(k)) - \frac{R^*(k)}{\sqrt{3}}\sin(\theta^*(k)), \tag{18.11}$$

where $\theta^*(k)$ is the angle of the reference voltage within the first sector $\theta^*(k) \in [0, \pi/3]$, for angles θ^* within other five sectors the same equations can be obtained by substitution $\theta^*\mathrm{mod}(\pi/3)$ into (18.10), (18.11) instead of θ^*. The sum $t_{ld}+t_{lg}$ is smaller than T_0 as long as the reference vector $V^*(t)$ lies inside the inner circle shown in Fig.18.4, implying that the two active vectors occupy only part of a switching cycle; the rest has to be filled out by using null vectors and is called null-vector time

$$\frac{t_z(k)}{T_0} = 1 - \frac{t_{ld} + t_{lg}}{T_0}. \tag{18.12}$$

The magnitude $|V_d^* + jV_q^*|$ of the reference voltage in the range up to $(\sqrt{3}/2)V_{DC}$ can be reproduced by this method. Further increase of the reference voltage leads to saturation of the PWM; the saturation phenomenon is discussed in the next section. The following normalized notation $\tau_1(k) = \frac{t_{ld}(k)}{T_0}$, $\tau_2(k) = \frac{t_{lg}(k)}{T_0}$ and $\tau_z = \frac{t_z(k)}{T_0}$ will be used, where τ_1, τ_2 and τ_z are duty ratios of leading U_{ld}, lagging U_{lg} and null vectors

$$\tau_1(k) = \frac{2R^*(k)}{\sqrt{3}}\sin(\theta^*(k)), \tag{18.13}$$

$$\tau_2(k) = \frac{2R^*(k)}{\sqrt{3}} \cos\left(\theta^*(k) + \frac{\pi}{6}\right), \quad (18.14)$$

$$\tau_z(k) = 1 - \tau_1(k) - \tau_2(k), \quad (18.15)$$

where $\theta^*(k) \in [0, \pi/3]$. The ability to apportion the null-vector time around two active vectors represents a degree of freedom that is used to improve the performance of space vector modulation.

18.3.1 Saturation issues

It is apparent from the space vector modulation technique, that the zero vector duration t_z decreases as the length of the input voltage vector R^* increases. The duration $t_z = 0$ is reached at $R^* = \sqrt{3}/2$, which means that the circular path of the reference vector V^*/V_{DC}, normalized by the constant DC link voltage V_{DC}, touches the inner hexagon shown in Fig.18.4. The modulation range of conventional modulation methods terminates at this point and the PWM reaches saturation. In this case, equations (18.10) and (18.11) could not be used any more to compute the durations of the two adjacent vectors, in general, because $t_{ld} + t_{lg}$, given by these formulas, may be larger than T_0.

Control in the range $R^* > \sqrt{3}/2$ can be achieved by overmodulation. It is convenient to consider $\bar{V}/V_{DC}$ the output voltage vector normalized by V_{DC}, averaged over a subcycle as the characteristic variable. The overmodulation technique subdivides into two different modes. In mode 1, the trajectory of the average voltage vector follows a circle with radius $\sqrt{3}/2 < R^* < 1$ as long as the circle arc is located within the hexagon; it tracks the hexagon sides in the remaining portion. Equations (18.13) and (18.14) can still be used to compute the switching durations while $\bar{V}/V_{DC}$ is on the arc. On the hexagon side, when $\theta^{*}\mathrm{mod}(\pi/3) \in (\theta_1, \theta_2)$, where

$$\theta_{1,2} = \arg\tan \frac{\sqrt{3}\left(1 \mp \sqrt{4R^{*2} - 3}\right)}{3 \pm \sqrt{4R^{*2} - 3}} \tag{18.16}$$

the duty ratios are governed by $t_z = 0$ and by

$$\begin{aligned} \tau_1 &= \frac{\tau_2^r - \tau_1^r}{\theta_2 - \theta_1}(\theta^* - \theta_1) + \tau_1^r, && (18.17) \\ \tau_2 &= \frac{\tau_1^r - \tau_2^r}{\theta_2 - \theta_1}(\theta^* - \theta_1) + \tau_2^r, && (18.18) \end{aligned}$$

where

$$\tau_{1,2}^r = \frac{1}{2}(1 \pm \sqrt{4R^{*2} - 3}). \tag{18.19}$$

Note, that $0 \le \theta_1 \le \theta_2 \le \pi/3$ and $\theta_1 \to 0$, $\theta_2 \to \pi/3$, then $R^* \to 1$. Overmodulation mode 2 is reached at $R^* = 1$ when the length of the arcs reduces to zero and the trajectory of $\bar{V}/V_{DC}$ becomes purely hexagonal. In this mode, the velocity of the average voltage vector is controlled along its linear trajectory by varying the duty cycle of the two adjacent switching state vectors. The velocity becomes gradually higher on the center portion of the hexagon side, and lower near the corners, as R^* increases. Overmodulation mode 2 converges smoothly to six-step operation when the instantaneous velocity on the edges becomes infinite and, the instantaneous velocity at the corners zero [42].

18.3.2 Switching pattern

The freedom of choice of either one of the two zero vectors per switching cycle allows various combinations of the sequence of states. In the most commonly employed regular sampling mode, the time interval length of T, which corresponds to one revolution of the reference vector V^*, is divided into six wide sectors and each sector into $N/6$ segments representing individual switching intervals, where N is a ratio of inverter basic switching cycle frequency ω_0 and fundamental stator frequency ω ($N = \omega_0/\omega = T/T_0$).

Several ways are used in practice to order the active and zero vectors within a basic switching cycle. We concentrate on one of the frequently used patterns that is denoted as symmetric or centered PWM switching sequence [59]. In this vector PWM strategy, the inverter state is changed four times within each segment. The state sequence within a given sector is

Voltage vector	Zero	U_{lg}	U_{ld}	U_{lg}	Zero
Duration	$t_z/2$	$t_{lg}/2$	t_{ld}	$t_{lg}/2$	$t_z/2$

(18.20)

where U_{ld} and U_{lg} are the leading and lagging adjacent to the reference V^* vectors. For example, if V^* is in the first sector i.e., $0 < \theta^* < \pi/3$, then $U_{ld} = U_2$ and $U_{lg} = U_1$. For this switching pattern there are four switching instances

$$t_k - d_1(k)T_0,\ t_k - d_2(k)T_0,\ t_k + d_2(k)T_0,\ t_k + d_1(k)T_0$$

within every time interval $[t_k - T_0/2, t_k + T_0/2]$, where t_k is the middle point of the given time interval and $d_1(k) = (\tau_1 + \tau_2)/2$, $d_2(k) = \tau_1/2$ can be computed from (18.10),(18.11) as

$$\begin{aligned} d_1(k) &= \frac{R^*(k)}{\sqrt{3}} \cos\left(\theta^*(k) - \frac{\pi}{6}\right), \\ d_2(k) &= \frac{R^*(k)}{\sqrt{3}} \sin(\theta^*(k)). \end{aligned} \tag{18.21}$$

where $\theta^* \in [0, \pi/3]$. For angles θ^* within other five sectors the same equations can be obtained by substitution $\theta^*\mathrm{mod}(\pi/3)$ into (18.10), (18.11) instead of θ^*, so that d_1, d_2 are $\pi/3$ periodic as functions of θ^*.

18.3.3 An analytical expression for d-q voltages

Assume for now that the system is in steady state, so that reference voltages in d-q coordinates V_d^* and V_q^* are constant. Then the actual 3-phase PWM output line voltages $V_1(t)$, $V_2(t)$ and $V_3(t)$ are T-periodic functions; moreover it can be concluded that there is a constant phase delay among these waveforms

$$V_2(t) = V_1(t + T/3), \qquad V_3(t) = V_1(t - T/3), \tag{18.22}$$

where T is the period of the fundamental stator frequency. To show this, first, note that τ_1 and τ_2 as functions of time are $T/6$ periodic. It means, firstly, that all 6 time intervals duration of $T/6$ are differ only by vectors U_{ld} and U_{lg} used to produce $V_1(t)$, $V_2(t)$ and $V_3(t)$. Secondly, vectors U_{ld} and U_{lg} take values from U_ℓ, $\ell = 1, ...6$, such that $U_{ld} = U_1$, $U_{lg} = U_2$ for the first sector, $U_{ld} = U_2$, $U_{lg} = U_3$ for the second sector, etc. Then analyses of the table (18.9) leads to (18.22). Now equation (18.7) for PWM output voltages in d-q coordinates V_d and V_q simplifies to

$$V_d(t) + jV_q(t) = F(t - T/3) + F(t) + F(t + T/3),$$

where $F(t) = e^{-j(2\pi/T)t}V_1(t)$. From the last equation it follows that $V_d(t) + jV_q(t)$ is a $T/6$ periodic function, i.e., it is enough to consider a time interval length of $T/6$. Without a loss of generality, suppose that this interval corresponds to $[0, \pi/3]$ in angular coordinates, so that vector $U_1 = U_{lg} = [011]'$ and $U_2 = U_{ld} = [010]'$ are used to produce the switching sequence. Such a time interval is shown on Fig. 18.5. The interval $[0, T/6]$ consists of $N/6$ subintervals, each of length T_0, where T_0 is the inverter basic switching cycle. These subintervals have similar structure, as the same vectors U_{ld}, U_{lg} are used, but different duration t_{ld}, t_{lg} given by (18.10), (18.11). Each subinterval can be divided into five smaller intervals within which the line voltages are constant (zero, lag, lead, lag, zero). Using this observation it can be concluded that $(V_d(t) + jV_q(t))/V_{DC}$ equals 0 within zero intervals, $e^{-j(2t/T+2/3)\pi}$ within lead interval and $e^{-j(2t/T+2/3)\pi} + e^{-j(2t/T-2/3)\pi}$ within lag intervals. Note that

$$e^{-j(2t/T+2/3)\pi} + e^{-j(2t/T-2/3)\pi} = -e^{-j(2t/T)\pi}. \tag{18.23}$$

Finally, V_d and V_q are the piecewise sinusoidal functions

$$\frac{V_d(t_k + \gamma T_0) + jV_q(t_k + \gamma T_0)}{V_{DC}} =$$

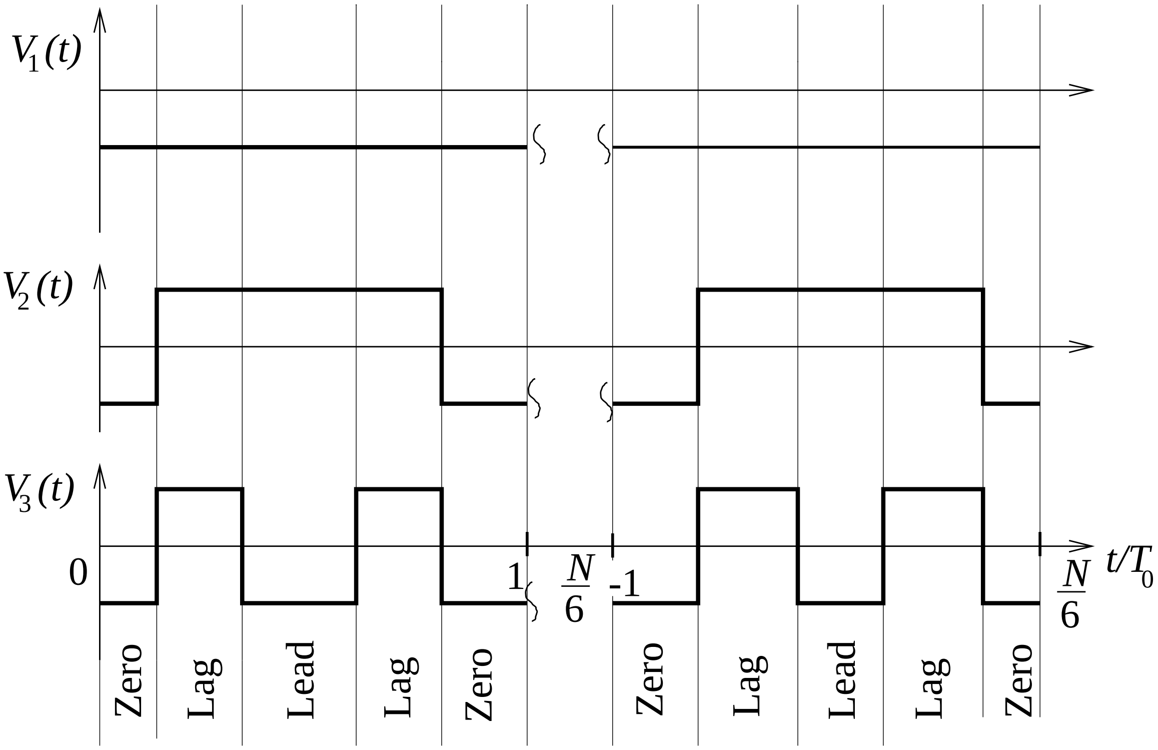

Figure 18.5: 3-Phase output voltage of the PWM, $t \in [0, T/6]$, $N = T/T_0$.

$$\begin{cases} 0 & \text{if } \gamma \in \left[-\frac{1}{2}, -d_1(n)\right) & \text{Zero Vector} \\ -e^{-j(\frac{2\pi}{N}(\frac{2n+1}{2}+\gamma)-\theta_0)} & \text{if } \gamma \in [-d_1(n), -d_2(n)) & \text{Lag Vector} \\ e^{-j(\frac{2\pi}{N}(\frac{2n+1}{2}+\gamma)+\frac{2}{3}\pi-\theta_0)} & \text{if } \gamma \in [-d_2(n), d_2(n)) & \text{Lead Vector} \\ -e^{-j(\frac{2\pi}{N}(\frac{2n+1}{2}+\gamma)-\theta_0)} & \text{if } \gamma \in [d_2(n), d_1(n)) & \text{Lag Vector} \\ 0 & \text{if } \gamma \in \left[d_1(n), \frac{1}{2}\right) & \text{Zero Vector} \end{cases}$$

where, as before, $N = T/T_0$, $n = k \mod(N/6)$, and θ_0 is an angle between reference voltage in d-q coordinate and real axis, which can be determine as a difference between rotor angle θ and reference voltage angle $V_\alpha^* + jV_\beta^*$ (in the α-β coordinate) $\theta_0 = \angle(V_d^* + jV_q^*) = \theta^* - \theta$ (see equation (18.4)). In steady state both θ^* and θ are changing with constant speed ω, so that θ_0 is constant.

18.4 Open-loop PWM gain

An averaged open-loop PWM gain is defined as a ratio of averaged output PWM voltage $\bar{V}_d + j\bar{V}_q$ to the constant input

$$K^{o.l.}_{PWM} = \frac{\bar{V}_d + j\bar{V}_q}{V^*_d + jV^*_q}, \tag{18.24}$$

where $V^*_d + jV^*_q$ is the constant reference. Ideally the open-loop gain is equal to 1, but this may not be the case due to the vector space PWM implementation. The deviation of open-loop gain from ideal is studied in this section.

Since the output voltage of the PWM periodic with period $T/6$, it is sufficient to consider one such period. It was shown in Section 18.3.2 that an interval of the length $T/6$ consists of $N/6$ subintervals length of T_0 with a similar structure defined by the switching pattern, where $N = T/T_0$ is the total number of basic inverter cycles per fundamental stator frequency period T. Then the averaged PWM output voltage can be obtained as following

$$\bar{V}_d + j\bar{V}_q = \frac{6}{N} \sum_{n=0}^{N/6-1} \left(S_d(n) + jS_q(n)\right), \tag{18.25}$$

where

$$S_d(n) + jS_q(n) = \frac{1}{T_0} \int_{-T_0/2+t_k}^{T_0/2+t_k} \left(V_d(t) + jV_q(t)\right) dt, \tag{18.26}$$

and $n = k \bmod(N/6)$ is the index of current switching cycle within $\pi/3$ interval. To evaluate the integral, the interval $[t_k - T_0/2, t_k + T_0/2]$ is divided into 5 subintervals according to the switching pattern

$$t_k - T_0/2,\ t_k - d_1(n)T_0,\ t_k - d_2(n)T_0,\ t_k + d_2(n)T_0,\ t_k + d_1(n)T_0, t_k + T_0/2,$$

where

$$\begin{aligned} d_1(n) &= \frac{R^*}{\sqrt{3}}\cos\left(\frac{2n+1}{N}\pi - \frac{\pi}{6}\right) \\ d_2(n) &= \frac{R^*}{\sqrt{3}}\sin\left(\frac{2n+1}{N}\pi\right). \end{aligned} \tag{18.27}$$

The integral (18.26) is equal to a sum of five integrals $S_d^\ell(n) + jS_q^\ell(n)$, $\ell = 0, ..., 4$, where $S^0 = 0$ and $S^4 = 0$ and

$$S_d^1(n) + jS_q^1(n) = V_{DC}\int_{-d_1(n)}^{-d_2(n)} -e^{-j(\frac{2\pi}{N}(\frac{2n+1}{2}+s)-\theta_0)}ds, \tag{18.28}$$

$$S_d^2(n) + jS_q^2(n) = V_{DC}\int_{-d_2(n)}^{d_2(n)} e^{-j(\frac{2\pi}{N}(\frac{2n+1}{2}+s)+\frac{2}{3}\pi-\theta_0)}ds, \tag{18.29}$$

$$S_d^3(n) + jS_q^3(n) = V_{DC}\int_{d_2(n)}^{d_1(n)} -e^{-j(\frac{2\pi}{N}(\frac{2n+1}{2}+s)-\theta_0)}ds. \tag{18.30}$$

After some algebra, the following expressions are obtained

$$\begin{aligned} \bar{V}_d(n) = V_{DC}\frac{N}{\pi} \Bigg[& \cos\left(\frac{2n+1}{N}\pi - \theta_0\right)\left\{\sin\left(\frac{2}{\sqrt{3}}\frac{\pi}{N}R^*\sin\left(\frac{2n+1}{N}\pi + \frac{\pi}{3}\right)\right) - \right. \\ & \left. \sin\left(\frac{2}{\sqrt{3}}\frac{\pi}{N}R^*\sin\left(\frac{2n+1}{N}\pi\right)\right)\right\} + \\ & \sin\left(\frac{2n+1}{N}\pi - \theta_0 + \frac{\pi}{6}\right)\sin\left(\frac{2}{\sqrt{3}}\frac{\pi}{N}R^*\sin\left(\frac{2n+1}{N}\pi\right)\right)\Bigg] \end{aligned} \tag{18.31}$$

$$\begin{aligned} \bar{V}_q(n) = V_{DC}\frac{N}{\pi} \Bigg[& \sin\left(\frac{2n+1}{N}\pi - \theta_0\right)\left\{\sin\left(\frac{2}{\sqrt{3}}\frac{\pi}{N}R^*\sin\left(\frac{2n+1}{N}\pi\right)\right) - \right. \\ & \left. \sin\left(\frac{2}{\sqrt{3}}\frac{\pi}{N}R^*\sin\left(\frac{2n+1}{N}\pi + \frac{\pi}{3}\right)\right)\right\} + \\ & \cos\left(\frac{2n+1}{N}\pi - \theta_0 + \frac{\pi}{6}\right)\sin\left(\frac{2}{\sqrt{3}}\frac{\pi}{N}R^*\sin\left(\frac{2n+1}{N}\pi\right)\right)\Bigg] \end{aligned} \tag{18.32}$$

These equation are nonlinear in R^*, which makes them difficult to analyze. To obtain an approximate solution, a Taylor series expansion can be used

$$\bar{V}_d(n) = V_{DC}\sum_{m=0}^{\infty}\left(R^*\frac{2}{\sqrt{3}}\right)^{2m+1}\left(\frac{\pi}{N}\right)^{2m}\frac{(-1)^m}{(2m+1)!}\Bigg[\cos\left(\frac{2n+1}{N}\pi - \theta_0\right) \times$$

$$\begin{aligned}
&\left(-\sin\left(\frac{2n+1}{N}\pi\right)^{2m+1}+\sin\left(\frac{2n+1}{N}\pi+\frac{\pi}{3}\right)^{2m+1}\right)+\\
&\sin\left(\frac{2n+1}{N}\pi-\theta_0+\frac{\pi}{6}\right)\sin\left(\frac{2n+1}{N}\pi\right)^{2m+1}\Bigg],
\end{aligned}\tag{18.33}$$

$$\begin{aligned}
\bar{V}_q(n) \;=\;& V_{DC}\sum_{m=0}^{\infty}\left(R^*\frac{2}{\sqrt{3}}\right)^{2m+1}\left(\frac{\pi}{N}\right)^{2m}\frac{(-1)^m}{(2m+1)!}\Bigg[\sin\left(\frac{2n+1}{N}\pi-\theta_0\right)\times\\
&\left(\sin\left(\frac{2n+1}{N}\pi\right)^{2m+1}-\sin\left(\frac{2n+1}{N}\pi+\frac{\pi}{3}\right)^{2m+1}\right)+\\
&\cos\left(\frac{2n+1}{N}\pi-\theta_0+\frac{\pi}{6}\right)\sin\left(\frac{2n+1}{N}\pi\right)^{2m+1}\Bigg].
\end{aligned}\tag{18.34}$$

From the following equalities

$$\sin(\theta_0) \;=\; +\sin(a-\theta_0)\left(\sin(a)-\sin(a+\frac{\pi}{3})\right)+\cos(a-\theta_0+\frac{\pi}{6})\sin(a)\tag{18.35}$$

$$\cos(\theta_0) \;=\; -\cos(a-\theta_0)\left(\sin(a)-\sin(a+\frac{\pi}{3})\right)+\sin(a-\theta_0+\frac{\pi}{6})\sin(a)\tag{18.36}$$

the first two terms of the expansion (18.33), (18.34) can be simplified to

$$\begin{aligned}
\frac{\bar{V}_d(n)}{V_{DC}} = R^*\;\cos(\theta_0)\;-&\\
&\left(R^*\frac{2}{\sqrt{3}}\right)^3\left(\frac{\pi}{N}\right)^2\frac{1}{6}\Bigg[\cos\left(\frac{2n+1}{N}\pi-\theta_0\right)\times\\
&\left(-\sin\left(\frac{2n+1}{N}\pi\right)^3+\sin\left(\frac{2n+1}{N}\pi+\frac{\pi}{3}\right)^3\right)+\\
&\sin\left(\frac{2n+1}{N}\pi-\theta_0+\frac{\pi}{6}\right)\sin\left(\frac{2n+1}{N}\pi\right)^3\Bigg]+O((R^*)^5)
\end{aligned}\tag{18.37}$$

$$\begin{aligned}
\frac{\bar{V}_q(n)}{V_{DC}} = R^*\;\sin(\theta_0)\;-&\\
&\left(R^*\frac{2}{\sqrt{3}}\right)^3\left(\frac{\pi}{N}\right)^2\frac{1}{6}\Bigg[\sin\left(\frac{2n+1}{N}\pi-\theta_0\right)\times\\
&\left(\sin\left(\frac{2n+1}{N}\pi\right)^3-\sin\left(\frac{2n+1}{N}\pi+\frac{\pi}{3}\right)^3\right)+\\
&\cos\left(\frac{2n+1}{N}\pi-\theta_0+\frac{\pi}{6}\right)\sin\left(\frac{2n+1}{N}\pi\right)^3\Bigg]+O((R^*)^5)
\end{aligned}\tag{18.38}$$

the first term is linear on R^* and represents ideal output of the PWM. Note, that $\left(R^* \frac{2}{\sqrt{3}}\right)$ is always less then 1. The m-th term is less then $\left(\frac{\pi}{N}\right)^{2m} \frac{1}{(2m+1)!}$ and, decreases rapidly with m.

Finally we conclude that the open-loop gain of the PWM

$$K_{PWM}^{o.l.} = \frac{\bar{V}_d + j\bar{V}_q}{V_d^* + jV_q^*} = \frac{\bar{V}_d + j\bar{V}_q}{V_{DC} R^* e^{j\theta_0}} \approx 1. \tag{18.39}$$

The error in the gain of the PWM is in order of $\frac{1}{6}\left(\frac{2}{\sqrt{3}}\right)^3 \left(\frac{\pi}{N}\right)^2$ and does not depend on the absolute switching frequency $\omega_0 = 2\pi/T_0$, but depends on the relative switching frequency N, i.e., the number of basic switching cycles per period of the fundamental stator frequency.

Example

In this subsection a numerical example is presented. Let $N = 12$ and $V_{DC} = 1$, then within every $T/6$ time interval there are two subintervals $n = 0, 1$ with

$$d_1(0) = R^* \frac{\sqrt{3}+1}{2\sqrt{6}} = 0.5577R^* \tag{18.40}$$

$$d_2(0) = R^* \frac{\sqrt{3}-1}{2\sqrt{6}} = 0.1494R^* \tag{18.41}$$

for the first one, and

$$d_1(1) = R^* \frac{\sqrt{3}+1}{2\sqrt{6}} = 0.5577R^* \tag{18.42}$$

$$d_2(1) = R^* \frac{1}{\sqrt{6}} = 0.4082R^* \tag{18.43}$$

for the second one. Integrating (18.28)-(18.30), obtain

$$\bar{V}_d = 3.1952\cos(\theta_0)\sin(0.2920R^*) +$$

$$1.8447\sin(\theta_0)\left(\sin(0.2920R^*)-\sin(0.2138R^*)-\sin(0.0782R^*)\right)+$$
$$0.4943\cos(\theta_0)\left(\sin(0.2138R^*)-\sin(0.0782R^*)\right); \qquad (18.44)$$

$$\begin{aligned}\bar{V}_q &= 3.1952\sin(\theta_0)\sin(0.2920R^*)+\\ &\quad 1.8447\cos(\theta_0)\left(-\sin(0.2920R^*)+\sin(0.2138R^*)+\sin(0.0782R^*)\right)+\\ &\quad 0.4943\sin(\theta_0)\left(\sin(0.2138R^*)-\sin(0.0782R^*)\right); \qquad (18.45)\end{aligned}$$

The fifth order Taylor polynomial approximation to $\bar{V}_d$ and $\bar{V}_q$ is:

$$\bar{V}_d \approx R^*\cos(\theta_0)-1.4730\cdot 10^{-2}R^{*3}\cos(\theta_0-0.3108) \qquad (18.46)$$

$$\bar{V}_q \approx R^*\sin(\theta_0)-1.4730\cdot 10^{-2}R^{*3}\sin(\theta_0-0.3108) \qquad (18.47)$$

The complex gain

$$K_{PWM}^{o.l.} \approx 1.0-1.4730\cdot 10^{-2}R^{*2}e^{-j0.3108}\approx 1. \qquad (18.48)$$

For this particular example the averaged PWM output voltage differ from the ideal by less then 1.5%.

18.4.1 Estimation of the current ripple magnitude

In this section the formula for the magnitude of the current ripple will be obtained a piecewise linear approximation for the current. To find the currents i_d and i_q, the voltage waveforms $V_d^f = V_d + Li_q\omega$ and $V_q^f = V_q - MI\,\omega - Li_d\omega$ are applied to the motor phases represented by first order system $1/(Ls+R_a)$. While evaluating V_d^f

and V_q^f, we will neglect ripple in i_d, i_q, and ω. This can be justified by the low-pass filtering provided by the plant, and by the relatively small magnitude of corresponding terms when compared with V_d, V_q (PWM output voltage). With this assumption, the currents waveforms will depend only on V_d and V_q. Other terms in V_d^f and V_q^f will contribute to the constant DC value of the currents. Thus, for the purpose of ripple evaluation, voltages V_d, V_q can be used instead of V_d^f and V_q^f. As it was shown in Section 18.3.3 voltages V_d, V_q are piecewise sinusoidal functions. To find simplified solutions for currents, voltages V_d, V_q will be approximated by piecewise constant functions such that the averaged values in every time interval between switchings are preserved.

The following discussion equally applies to d and q phases. To facilitate notations the subindexes d and q are omitted if the same equations applies to both axes; for example, V stands for V_d or V_q.

Let the current at the time t_0 be $i(t_0)$ and let the constant voltage V is applied to the motor phase represented by first order system $1/(Ls + R_a)$; then current at $t_0 + \Delta t$ is approximately

$$i(t_0 + \Delta t) = \frac{V - R_a i(t_0)}{L}\Delta t + i(t_0). \tag{18.49}$$

Assume that $|R_a(i(t_0+\Delta t)-i(t_0))| \ll |V|$, then further simplification can be obtained

$$i(t_0 + \Delta t) = \frac{V - R_a \bar{i}}{L}\Delta t + i(t_0), \tag{18.50}$$

where $\bar{i}$ is an averaged current. Typical voltage and corresponding current waveforms for switching pattern (18.20) are shown on Fig. 18.6.

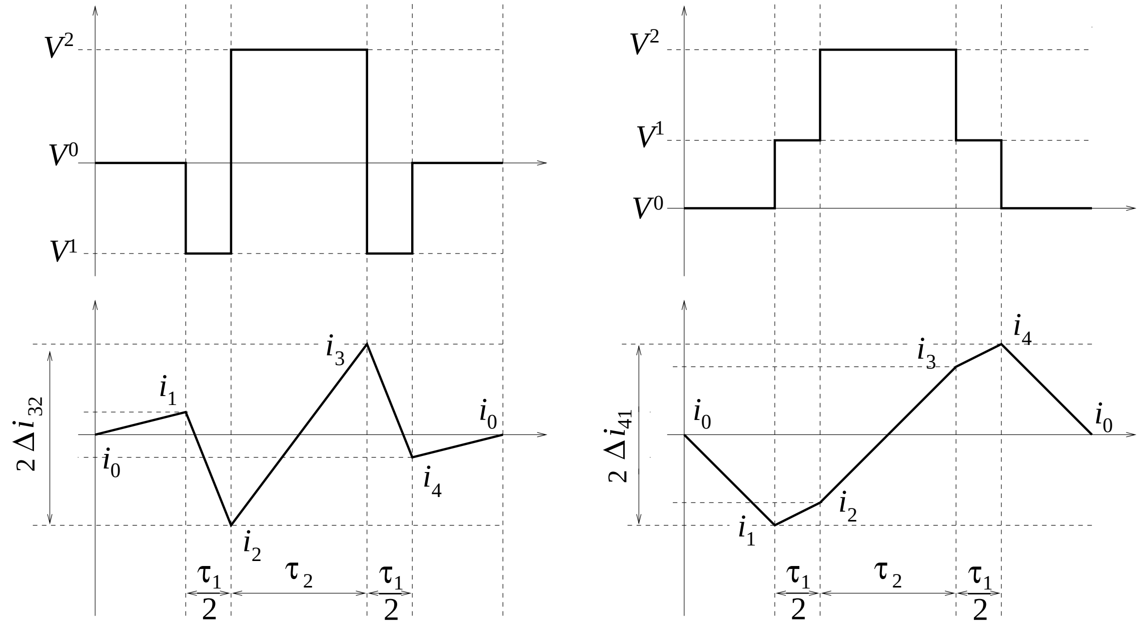

Figure 18.6: Typical voltages and corresponding currents waveform patterns for one basic inverter cycle T_0. Magnitude of the current ripple is defined differently for each pattern $\Delta i_{3,2} = (i_3 - i_2)/2$ and $\Delta i_{4,1} = (i_4 - i_1)/2$.

To find the piecewise constant approximation of the voltage V, each subinterval length of T/N is divided into five smaller intervals within which the voltage will be approximated by constants $V^\ell(n)$, $\ell = 0, ..., 4$, each equal to the averaged voltage within the corresponding interval. It will be assumed that each two consecutive subintervals of length of $T_0 = T/N$ within $T/6$ are identical. Then using piecewise constant approximation (18.50), the peak current values are

$$i_1 = \frac{V^0 - R_a \bar{i}}{L} \frac{\tau_z T_0}{2} + i_0, \tag{18.51}$$

$$i_2 = \frac{V^1 - R_a \bar{i}}{L} \frac{\tau_1 T_0}{2} + i_1, \tag{18.52}$$

$$i_3 = \frac{V^2 - R_a \bar{i}}{L} \tau_2 T_0 + i_2, \tag{18.53}$$

$$\begin{aligned} i_4 &= \frac{V^3 - R_a\bar{i}}{L}\,\frac{\tau_1 T_0}{2} + i_3, && (18.54)\\ i_5 &= \frac{V^0 - R_a\bar{i}}{L}\,\frac{\tau_z T_0}{2} + i_4. && (18.55) \end{aligned}$$

Since for the considered setup $V^0 = 0$, $V^1 = 2S^1/\tau_1$, $V^2 = S^2/\tau_2$, $V^3 = 2S^3/\tau_1$ and $V^4 = 0$, where S^ℓ are given by (18.28)-(18.30), then

$$\bar{i} = \frac{S^1 + S^2 + S^3}{R_a} \qquad (18.56)$$

$$\begin{aligned} i_1 - i_0 &= -\frac{S^1 + S^2 + S^3}{L}\,\frac{\tau_z T_0}{2}, && (18.57)\\ i_2 - i_1 &= -\frac{S^1 + S^2 + S^3 - V^1}{L}\,\frac{\tau_1 T_0}{2}, && (18.58)\\ i_3 - i_2 &= -\frac{S^1 + S^2 + S^3 - V^2}{L}\,\tau_2 T_0, && (18.59)\\ i_4 - i_3 &= -\frac{S^1 + S^2 + S^3 - V^3}{L}\,\frac{\tau_1 T_0}{2}, && (18.60)\\ i_0 - i_4 &= -\frac{S^1 + S^2 + S^3}{L}\,\frac{\tau_z T_0}{2}. && (18.61) \end{aligned}$$

Define $\Delta i_{\ell,k} = (i_\ell - i_k)/2$ to obtain

$$\begin{aligned} \Delta i_{1,0} &= -\frac{1}{2}\frac{S(n)}{L}\,\frac{\tau_z T_0}{2}, && (18.62)\\ \Delta i_{2,1} &= -\frac{1}{2}\left[\frac{S(n)}{L}\,\frac{\tau_1 T_0}{2} - \frac{S^1(n)}{L}\,T_0\right], && (18.63)\\ \Delta i_{3,2} &= -\frac{1}{2}\left[\frac{S(n)}{L}\,\tau_2 T_0 - \frac{S^2(n)}{L}\,T_0\right], && (18.64)\\ \Delta i_{4,3} &= -\frac{1}{2}\left[\frac{S(n)}{L}\,\frac{\tau_1 T_0}{2} - \frac{S^3(n)}{L}\,T_0\right], && (18.65)\\ \Delta i_{0,4} &= -\frac{1}{2}\frac{S(n)}{L}\,\frac{\tau_z T_0}{2}. && (18.66) \end{aligned}$$

The ripple magnitude is the larger of ($|\Delta i_{4,1}|$) and ($|\Delta i_{3,2}|$)

$$\Delta i_{4,1} = -\frac{1}{2}\frac{S(n)}{L}\,\tau_z T_0, \qquad (18.67)$$

$$\Delta i_{3,2} = -\frac{1}{2}\left[\frac{S(n)}{L}\,\tau_2 T_0 - \frac{S^2(n)}{L}\,T_0\right]. \tag{18.68}$$

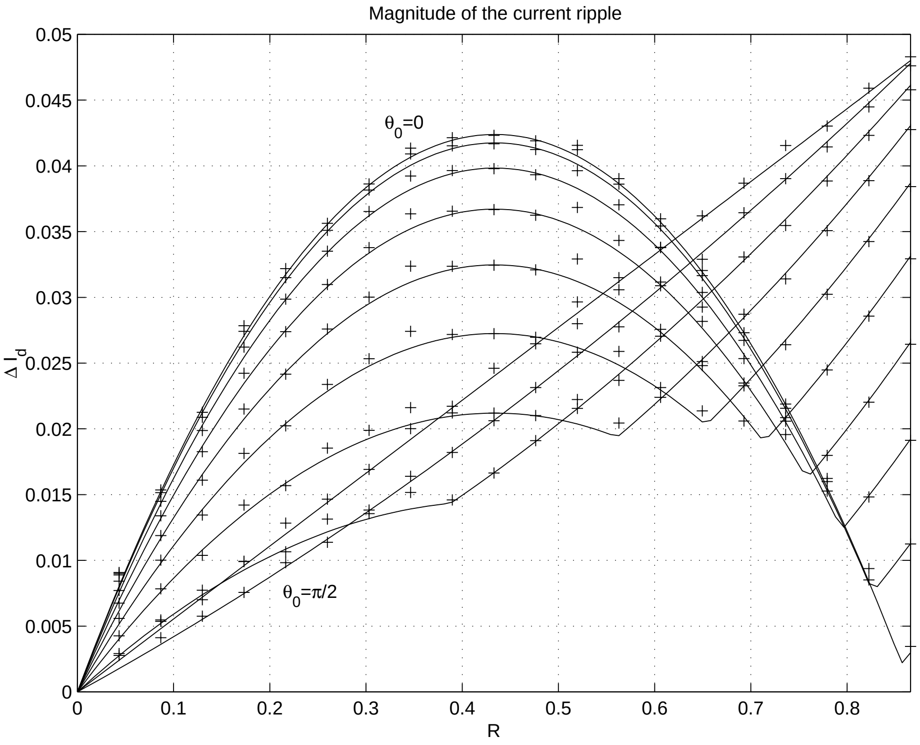

Figure 18.7: Magnitude of d-current ripple normalized by V_{DC} as a function of R^* and θ_0 ($N = 24$, $n = 1$, $M/V_{DC} = 0.195$), theoretical (-) obtained by formula $\max[|\Delta i^d_{4,1}|, |\Delta i^d_{3,2}|]$ and experimental obtained by simulation of the nonlinear closed-loop system (+).

Using Taylor series expansion the following approximate solution can be obtained

$$\Delta i^d_{4,1} = MR^*\cos(\theta_0)\left(1-\frac{2}{\sqrt{3}}R^*\cos\left(\frac{2n+1}{N}\pi-\frac{\pi}{6}\right)\right), \tag{18.69}$$

$$\Delta i^q_{4,1} = MR^*\sin(\theta_0)\left(1-\frac{2}{\sqrt{3}}R^*\cos\left(\frac{2n+1}{N}\pi-\frac{\pi}{6}\right)\right), \tag{18.70}$$

$$\Delta i^d_{3,2} = M\frac{2}{\sqrt{3}}R^*\sin\left(\frac{2n+1}{N}\pi\right)\left(\sin\left(\frac{2n+1}{N}\pi-\theta_0+\frac{\pi}{6}\right)-R^*\cos(\theta_0)\right) \tag{18.71}$$

$$\Delta i^q_{3,2} = M\frac{2}{\sqrt{3}}R^*\sin\left(\frac{2n+1}{N}\pi\right)\left(\cos\left(\frac{2n+1}{N}\pi-\theta_0+\frac{\pi}{6}\right)-R^*\sin(\theta_0)\right) \tag{18.72}$$

where

$$M = \frac{\pi}{N\omega}\frac{V_{DC}}{L} = \frac{T_0}{2}\frac{V_{DC}}{L}. \qquad (18.73)$$

Note, that $\Delta i_{4,1} = M\frac{V_d^* + jV_q^*}{V_{DC}}(1 - \tau_1 - \tau_2)$. The largest ripple occurs then the reference voltage vector $V_d^* + jV_q^* = R^* e^{j\theta_0}$ aligned with d or q axis, i.e., $\theta_0 = \frac{\pi}{2}\ell$, $\ell = 0, \pm 1, \pm 2$. Let $\theta_0 = 0$ or $\theta_0 = \pi$, then $\Delta i_{4,1}^q = 0$ and $\Delta i_{4,1}^d$ is a second degree polynomial in R^*, whose maximum can be found by differentiating $\Delta i_{4,1}^d$ by R^*

$$\frac{d\Delta i_{4,1}^d}{dR^*} = M\left(1 - \frac{4}{\sqrt{3}}R^* \cos\left(\frac{2n+1}{N}\pi - \frac{\pi}{6}\right)\right). \qquad (18.74)$$

The maximum value $\Delta i_{41,max}^d$ can be obtained by solving equation $\frac{d\Delta i_{4,1}^d}{dR^*} = 0$

$$\Delta i_{41,max}^d = \frac{M}{\frac{8}{\sqrt{3}}\cos\left(\frac{2n+1}{N}\pi - \frac{\pi}{6}\right)}. \qquad (18.75)$$

The maximum is achieved when

$$R^* = \left(\frac{4}{\sqrt{3}}\cos\left(\frac{2n+1}{N}\pi - \frac{\pi}{6}\right)\right)^{-1}. \qquad (18.76)$$

From equations (18.69),(18.70) it follows that when $V_d^* + jV_q^*$ is aligned with either the d or the q axis, the ripple magnitude $\Delta i_{4,1}^d$ or $\Delta i_{4,1}^q$ becomes a second degree polynomial of R^* with the maximum near the middle point of the range of R^*, i.e., $\sqrt{3}/4$. This result is very similar to the one obtained for DC PWM (14.30). For the natural-sampled DC PWM the ripple magnitude is equal to $M \cdot \tau \cdot \tau_z$, where $\tau_z = 1 - \tau$ and $M = (T/2)(V_{DC}/L_a)$. In this case the normalized effective value of the PWM input voltage, which is the value of the PWM input voltage (normalized by magnitude of the sawtooth function) at the switching time $Tk + \tau$, is equal to the duty ratio τ. In DC/DC converters, the "sampling" instants $Tk+\tau$ occur, when the input voltage is equal to sawtooth carrier signal.

For the AC PWM case, the $\Delta i_{4,1}$ ripple magnitude is $M\frac{V_d^*+jV_q^*}{V_{DC}}\tau_z$, where $\tau_z = 1-\tau_1-\tau_2$, $M=(T_0/2)(V_{DC}/L)$ and $V_d^*+jV_q^*$ is the effective value of the AC PWM reference voltage, which is the value of the PWM input voltage at the sampling instants T_0k+t_s. Comparing with the natural-sampled DC PWM, the voltage space AC PWM is digitally implemented, and the sampling instants T_0k+t_s can be chosen as t_s is a design parameter. While there is a difference in implementation of these two PWM strategies, the magnitude of the current ripple obeys a similar relationship (compare also Fig. 18.7 and 18.8 with Fig. 14.2).

For different subintervals the absolute maximum $\max_n[\Delta i^d_{41,max}(n)] = M/4$ is achieved in the first $n=0$ and the last $n=N/6-1$ subintervals. The minimum corresponds to the middle subinterval $n=\frac{N/6-1}{2}$, so

$$\frac{\sqrt{3}}{8}M \le \Delta i^d_{41,max}(n) \le \frac{1}{4}M. \tag{18.77}$$

Next we turn our attention to $\Delta i^d_{3,2}$ and $\Delta i^q_{3,2}$ will be analyzed. As $\theta_0=0$ or $\theta_0=\pi/2$, then

$$\Delta i^d_{3,2} = M\frac{2}{\sqrt{3}}R^*\sin\left(\frac{2n+1}{N}\pi\right)\left(\sin\left(\frac{2n+1}{N}\pi+\frac{\pi}{6}\right)-R^*\right), \tag{18.78}$$

$$\Delta i^q_{3,2} = M\frac{2}{\sqrt{3}}R^*\sin\left(\frac{2n+1}{N}\pi\right)\cos\left(\frac{2n+1}{N}\pi+\frac{\pi}{6}\right). \tag{18.79}$$

The first equation is a second degree polynomial in R^*, whose maximum can be find by differentiating $\Delta i^d_{32,max}$ by R^*. The maximum value

$$\Delta i^d_{32,max} = \frac{M}{2\sqrt{3}} \sin\left(\frac{2n+1}{N}\pi\right) \sin\left(\frac{2n+1}{N}\pi + \frac{\pi}{6}\right)^2 \tag{18.80}$$

is achieved for

$$R^* = \frac{\sin\left(\frac{2n+1}{N}\pi\right)}{2}. \tag{18.81}$$

The absolute maximum $\max_n[\Delta i^d_{32,max}(n)] = \frac{M}{2\sqrt{3}} \sin\left(\frac{\pi}{3} - \frac{\pi}{N}\right) \cos\left(\frac{\pi}{N}\right)^2$ is reached at the last subinterval $n = N/6 - 1$

$$\frac{M}{2\sqrt{3}} \sin\left(\frac{\pi}{N}\right) \sin\left(\frac{\pi}{N} + \frac{\pi}{6}\right)^2 \leq \Delta i^d_{32,max}(n) < \frac{M}{4}. \tag{18.82}$$

The second equation is a linear function of R^*, with the maximum at $R^* = \sqrt{3}/2$ equal to

$$\Delta i^q_{32,max} \quad = \quad M \sin\left(\frac{2n+1}{N}\pi\right) \cos\left(\frac{2n+1}{N}\pi + \frac{\pi}{6}\right). \tag{18.83}$$

For different subintervals the absolute maximum $\max_n[\Delta i^q_{32,max}(n)] = M/4$ is achieved in the middle subinterval $n = \frac{N/6-1}{2}$, and the minimum in the first $(n = 0)$ and the last $(n = N/6 - 1)$ subinterval

$$M \sin\left(\frac{\pi}{N}\right) \cos\left(\frac{\pi}{N} + \frac{\pi}{6}\right) \leq \Delta i^q_{32,max}(n) \leq \frac{1}{4}M. \tag{18.84}$$

The same analysis can be performed for $\theta_0 = \pm\frac{\pi}{2}$, then $\Delta i^d_{4,1} = 0$, $\max_n[\Delta i^q_{41,max}(n)] = M/4$, $\max_n[\Delta i^d_{32,max}(n)] = M/4$ and $\max_n[\Delta i^q_{32,max}(n)] < M/4$.

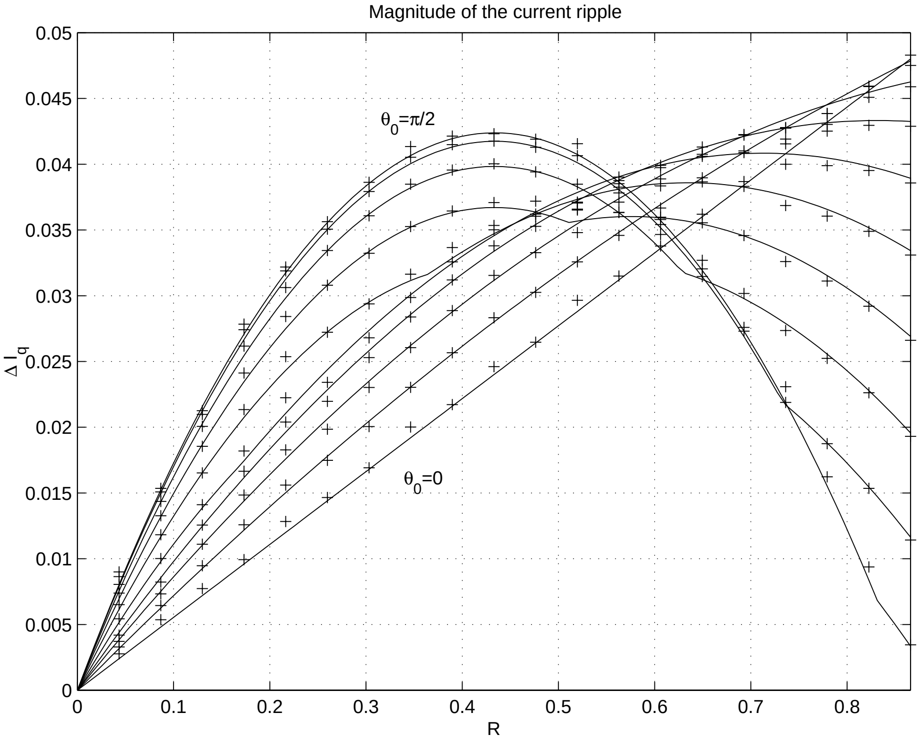

Figure 18.8: Magnitude of q-current ripple normalized by V_{DC} as a function of R^* and θ_0 ($N = 24$, $n = 1$, $M/V_{DC} = 0.195$), theoretical (-) obtained by formula $\max[|\Delta i^q_{4,1}|, |\Delta i^q_{3,2}|]$ and experimental obtained by simulation of the nonlinear closed-loop system (+).

18.5 Closed-loop PWM gain

Closed-loop PWM gain is defined as a ratio of averaged PWM output and averaged PWM input voltages in the closed feedback loop setup. The averaged values are considered over the period T_0, and with the system is in a steady state. If the PWM input (reference) voltage is constant, the closed-loop PWM gain is equal to the open-loop gain. However, in the closed-loop system, current ripple may appear in the input of PWM. Let us consider voltages and currents presented in d-q frame. If a T_0-periodic input of PWM V_d^* is sampled with period T_0 (the analysis that follows applies equally to q axis voltage and current), then this is equivalent to a constant PWM input reference voltage $V_d^* = V_d^*(kT_0 + t_s)$, where t_s is the sampling instance. The output d voltage of the PWM, will be proportional to $V_d^*(kT_0 + t_s)$, but not necessary to the average of the $V_d(t)^*$. If t_s is chosen such that $V_d^*(kT_0 + t_s)$ is equal to the averaged value of the $V_d(t)^*$, then the closed-loop PWM gain is equal to the open-loop gain. To determine the closed-loop gain, $V_d^*(kT_0 + t_s)$ and $V_q^*(kT_0 + t_s)$ are needed first. For a closed-loop system

$$\begin{aligned} V_d^*(t) &= -\omega L i_q^* - k_{p1} i_d(t), && (18.85)\\ V_q^*(t) &= \omega\, MI\, + k_{p2} i_q^* - k_{p2} i_q(t). && (18.86) \end{aligned}$$

Assuming that ω, i_q and i_q^* vary slowly over a switching period

$$\begin{aligned} V_d^*(t) &= \bar{V}_d^* + \tilde{V}_d^*(t) = (-\omega L i_q^* - k_{p1}\bar{i}_d) - k_{p1}\tilde{i}_d(t), && (18.87)\\ V_q^*(t) &= \bar{V}_q^* + \tilde{V}_q^*(t) = (\omega\, MI\, + k_{p2} i_q^* - k_{p2}\bar{i}_q) - k_{p2}\tilde{i}_q(t), && (18.88) \end{aligned}$$

where voltages and currents are represented as a sum of averaged value (symbol with bar) and ripple (symbol with tilde). The closed-loop gain then is

$$\begin{aligned} K_{PWM,d}^{c.l.} &= \frac{\bar{V}_d}{\bar{V}_d^*} = \frac{V_d^*(kT_0 + t_s)}{\bar{V}_d^*} = \\ & 1 + \frac{\tilde{V}_d^*(kT_0 + t_s)}{\bar{V}_d^*} = 1 + G_d \frac{\tilde{i}_d(kT_0 + t_s)}{\bar{V}_d^*}, && (18.89) \end{aligned}$$

where $G_d = k_{p1}$ (in terms of Fig. 18.1). The same equation applies to the $K_{PWM,q}^{c.l.}$, where $G_q = k_{p2}$. In the above equation the open-loop gain is assumed to be equal to 1, as it was shown in the previous section the error introduced by this approximation is very small. Now, our aim is to find $\tilde{i}(kT_0 + t_s)$. It was shown previously that the shape of the current ripple is quite complicated. Thus only two sampling strategies will be examined in detail: **1)** $t_s/T_0 = -1/2$ and **2)** $t_s/T_0 = 0$.

First, an explicit equation for i_ℓ, $\ell = 0, 1, ..., 4$ is needed; since (18.57)-(18.61) are not linearly independent, one more equation should be added to solve for i_ℓ

$$\bar{i} = \int_{kT_0}^{kT_0+T_0} i(t)dt. \tag{18.90}$$

After integrating we obtain

$$\bar{i} = \frac{i_1 + i_0}{4}\tau_z + \frac{i_2 + i_1}{4}\tau_1 + \frac{i_3 + i_2}{2}\tau_2 + \frac{i_3 + i_4}{4}\tau_1 + \frac{i_4 + i_0}{4}\tau_z \tag{18.91}$$

and rearranging

$$\bar{i} = i_0\frac{\tau_z}{2} + i_1\frac{\tau_z + \tau_1}{4} + i_2\frac{\tau_1/2 + \tau_2}{2} + i_3\frac{\tau_1/2 + \tau_2}{2} + i_4\frac{\tau_1 + \tau_2}{4}. \tag{18.92}$$

Then i_ℓ can be found from the following equation

$$\begin{bmatrix} \Delta i_{1,0} \\ \Delta i_{2,1} \\ \Delta i_{3,2} \\ \Delta i_{4,3} \\ \Delta i_{0,4} \\ \bar{i} \end{bmatrix} = \begin{bmatrix} -1/2 & 1/2 & 0 & 0 & 0 \\ 0 & -1/2 & 1/2 & 0 & 0 \\ 0 & 0 & -1/2 & 1/2 & 0 \\ 0 & 0 & 0 & -1/2 & 1/2 \\ 1/2 & 0 & 0 & 0 & -1/2 \\ a_0 & a_1 & a_2 & a_3 & a_4 \end{bmatrix} \begin{bmatrix} i_0 \\ i_1 \\ i_2 \\ i_3 \\ i_4 \end{bmatrix}, \tag{18.93}$$

where

$$a_0 = \frac{\tau_z}{2}, \qquad a_1 = \frac{\tau_z + \tau_1}{4}, \qquad a_2 = \frac{\tau_1/2 + \tau_2}{2}, \qquad a_3 = a_2, \qquad a_4 = a_1. \tag{18.94}$$

1) If current is sampled at $kT_0 - T_0/2$, then $i(kT_0 - T_0/2) = i_0$. Solving for i_0

$$i_0 = \frac{\bar{i} - a_1(2\Delta i_{1,0} + \Delta i_{2,1} + \Delta i_{3,2} + \Delta i_{4,3}) - a_2(2\Delta i_{1,0} + 2\Delta i_{2,1} + \Delta i_{3,2})}{a_0 + 2a_1 + 2a_2}. \tag{18.95}$$

Note, that $2\Delta i_{1,0} + \Delta i_{2,1} + \Delta i_{3,2} + \Delta i_{4,3} = 0$ and $a_0 + 2a_1 + 2a_2 = 1$, then

$$i_0 = \bar{i} - a_2(2\Delta i_{1,0} + 2\Delta i_{2,1} + \Delta i_{3,2}) \tag{18.96}$$

and $\tilde{i}(kT_0 - T_0/2) = i_0 - \bar{i}$

$$\tilde{i}(kT_0 - T_0/2) = -(\tau_1/2 + \tau_2)\frac{S^1 - S^3}{2}\frac{T_0}{L}. \tag{18.97}$$

2) If current is sampled at kT_0, then $i(kT_0) = (i_2 + i_3)/2$

$$i(kT_0) = \Delta i_{1,0} + \Delta i_{2,1} + \Delta i_{3,2}/2 + i_0 \tag{18.98}$$

and $\tilde{i}(kT_0 - T_0/2) = (i_2 + i_3)/2 - \bar{i}$

$$\tilde{i}(kT_0) = (1 - \tau_1/2 - \tau_2)\frac{S^1 - S^3}{2}\frac{T_0}{L}. \tag{18.99}$$

Integration of (18.28),(18.30) leads to

$$\begin{aligned}
\frac{S_d^1 - S_d^3}{2} &= V_{DC}\sin\left(\frac{2n+1}{N}\pi - \theta_0\right)\left(\cos\left(\tau_1\frac{\pi}{N}\right) - \cos\left(\tau_2\frac{\pi}{N}\right)\right), && (18.100)\\
\frac{S_q^1 - S_q^3}{2} &= V_{DC}\cos\left(\frac{2n+1}{N}\pi - \theta_0\right)\left(\cos\left(\tau_1\frac{\pi}{N}\right) - \cos\left(\tau_2\frac{\pi}{N}\right)\right). && (18.101)
\end{aligned}$$

After substituting this into (18.97),(18.98), and taking first two elements of the Taylor series expansion, the following approximation is obtained

$$\begin{aligned}
\tilde{i}(kT_0 - T_0/2) &\approx V_{DC}(\tau_2^2 - \tau_1^2)\left(\frac{\pi}{N}\right)^2\frac{T_0}{L}\sin\left(\frac{2n+1}{N}\pi - \theta_0\right)(\tau_1/2 + \tau_2) && (18.102)\\
\tilde{i}(kT_0) &\approx V_{DC}(\tau_2^2 - \tau_1^2)\left(\frac{\pi}{N}\right)^2\frac{T_0}{L}\sin\left(\frac{2n+1}{N}\pi - \theta_0\right)(\tau_1/2 + \tau_z) && (18.103)
\end{aligned}$$

From these equations, it follows that the error associated with choice of the sampling instance $t_s/T_0 = -1/2$ is larger then the error associated with choice of the sampling instance $t_s/T_0 = 0$ if $\tau_2 > \tau_z$, or equivalently if

$$R^* > \frac{\sqrt{3}}{2}\frac{1}{2\sin\left(\frac{2n+1}{N}\pi\right) + \sqrt{3}\cos\left(\frac{2n+1}{N}\pi\right)}, \tag{18.104}$$

where

$$1.732 < 2\sin\left(\frac{2n+1}{N}\pi\right) + \sqrt{3}\cos\left(\frac{2n+1}{N}\pi\right) < 2.646. \tag{18.105}$$

The emerging rule is: if $R^* < \sqrt{3}/4$, then it is better to sample at $kT_0 - T_0/2$; if $R^* > \sqrt{3}/4$ then sampling at kT_0 provides smaller error. In either case, the error in current measurements associated with sampling at $t_s = T_0/2$ or $t_s = 0$ is less then $V_{DC}\left(\frac{\pi}{N}\right)^2\frac{T_0}{L}$. This error is inverse proportional to PWM basic cycle frequency $\omega_0 = 2\pi/T_0$ and to the square of the number of PWM cycles per fundamental stator period $N = T/T_0$. In other words, the error in current due to sampling at the middle (kT_0) or beginning ($kT_0 - T_0/2$) of the PWM basic cycle is proportional to the maximum ripple magnitude $V_{DC}\frac{T_0}{8L}$, and to the voltage pulse asymmetry $S^1 - S^3$ (which is proportional to $(\pi/N)^2$). The voltage pulse asymmetry does not depend on absolute switching frequency ω_0.

In the worst case of sampling, when current $i(t)$ achieves its maximum or minimum at $kT_0 + t_s$, the deviation of the PWM gain will be maximum. In this case the error in current due to sampling (difference between averaged current and sampled one) can be equal to $\Delta i_{32,max}$ or $\Delta i_{41,max}$, with the maximum equal to the current ripple magnitude $V_{DC}\frac{T_0}{8L}$.

18.6 Example

The effectiveness of the approximations derived in this chapter is illustrated on a fractional horse power PM synchronous motor. The parameters of the motor the controller in this numerical experiment are: $R_a = 1.25\Omega$; $L = 6.7\text{mH}$; $J = 2.0 \cdot 10^{-2}\text{kg-m}^2$; $B = 1.0 \cdot 10^{-3}\text{Nms}$; $T_{load} = 0.8\text{Nm}$; $MI = 0.4\text{Nm/A}$; $V_{DC} = \pm 60\text{V}$; $k_{p1} = 1$; $k_{p2} = 1$. The system was simulated in SIMULINK using a full nonlinear model, i.e., without any simplifications. The switching frequency is such that there are 12 basic cycles within each period of fundamental frequency (i.e., $T = 12T_0$ or $N = 12$). The normalized line voltages are shown in Fig. 18.9, while Fig. 18.10 shows voltages V_d and V_q and currents i_d and i_q both for complete model, and for approximate model, derived in this chapter.

The approximating error for currents is quite small. This confirms that our technique can be used to estimate magnitude and ripple behavior. The currents are feed back to the controller, causing ripple in V_d^* and V_q^*. Because of this effect, the average value of the PWM input voltages $\bar{V}_d^*$, $\bar{V}_q^*$ and actual measured voltages $V_d^*(kT_0 + t_s)$ and $V_q^*(kT_0 + t_s)$ can be different. Thus the average PWM gain can deviate from ideal. In our example, the average $\bar{V}_q^* \approx 42.4\text{V}$. The maximum possible magnitude of the ripple $\Delta V_{q,max} = k_{p2}\Delta i^q_{max}$ is 5.86 V, and the gain of PWM along q axis $K^{c.l.}_{PWM,q} = 1 + k_{p2}\Delta i^q_{max}/\bar{V}_q^* = 1.14$ which corresponds approximately to 14% deviation from nominal. For the d axis, $\bar{V}_d^* \approx -2.4\text{V}$, and the maximum possible magnitude of the ripple $\Delta V_{d,max} = k_{p1}\Delta i^q_{max}$ has the same value of 5.86 V. Thus the

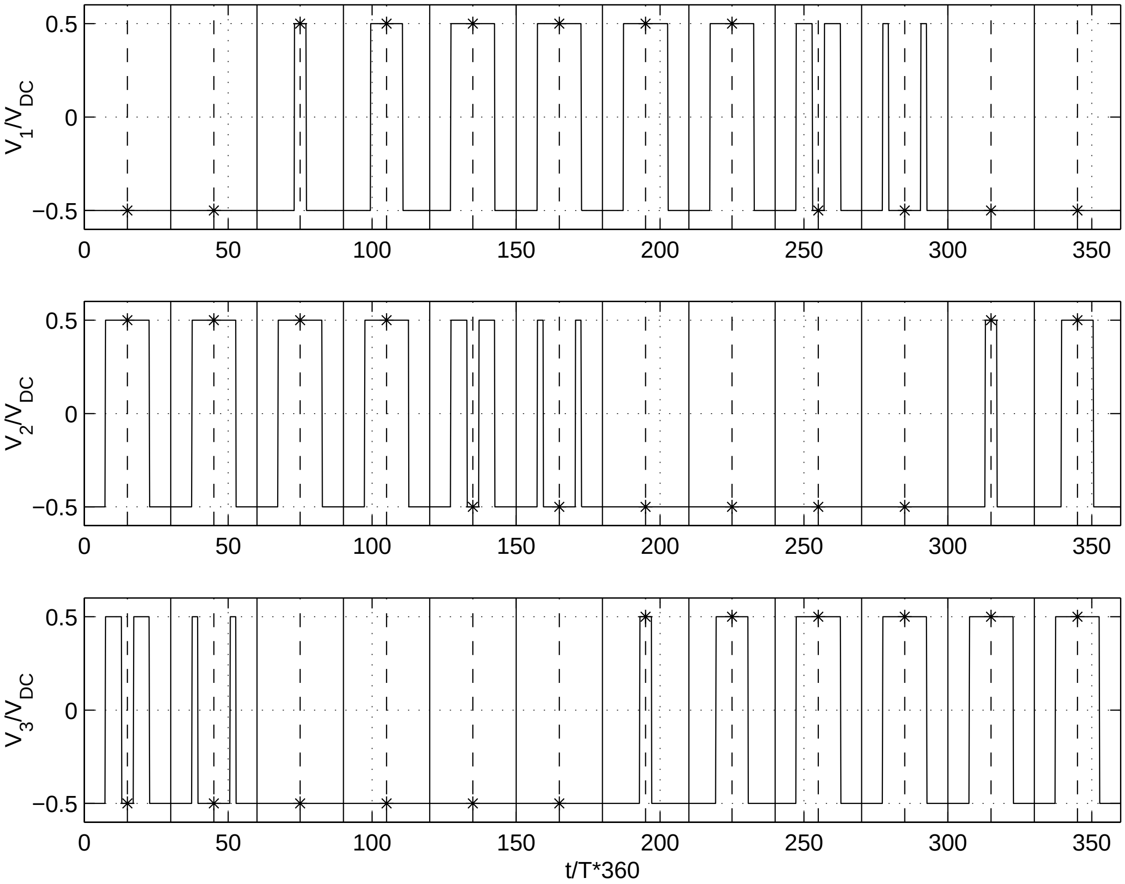

Figure 18.9: PWM 3-phase line voltages.

gain of PWM along d axis may achieve $K^{c.l.}_{PWM,d} = 1 + k_{p1}\Delta i^{d}_{max}/\bar{V}^{*}_{d} = 3.44$, which corresponds approximately to 244% deviation from nominal. If the input voltage is aligned with q axis, then V^{*}_{d} is equal to zero, and any $\widetilde{V}^{*}_{d}(kT_0 + t_s) \neq 0$ will produce infinite error in the PWM gain along the axis d. This example illustrates the fact that the deviation of the PWM gain may become large then the input voltage $V^{*}_{d} + jV^{*}_{q}$ is close to one of the axis (in this example $\theta^{*} = 93.2^{o}$).

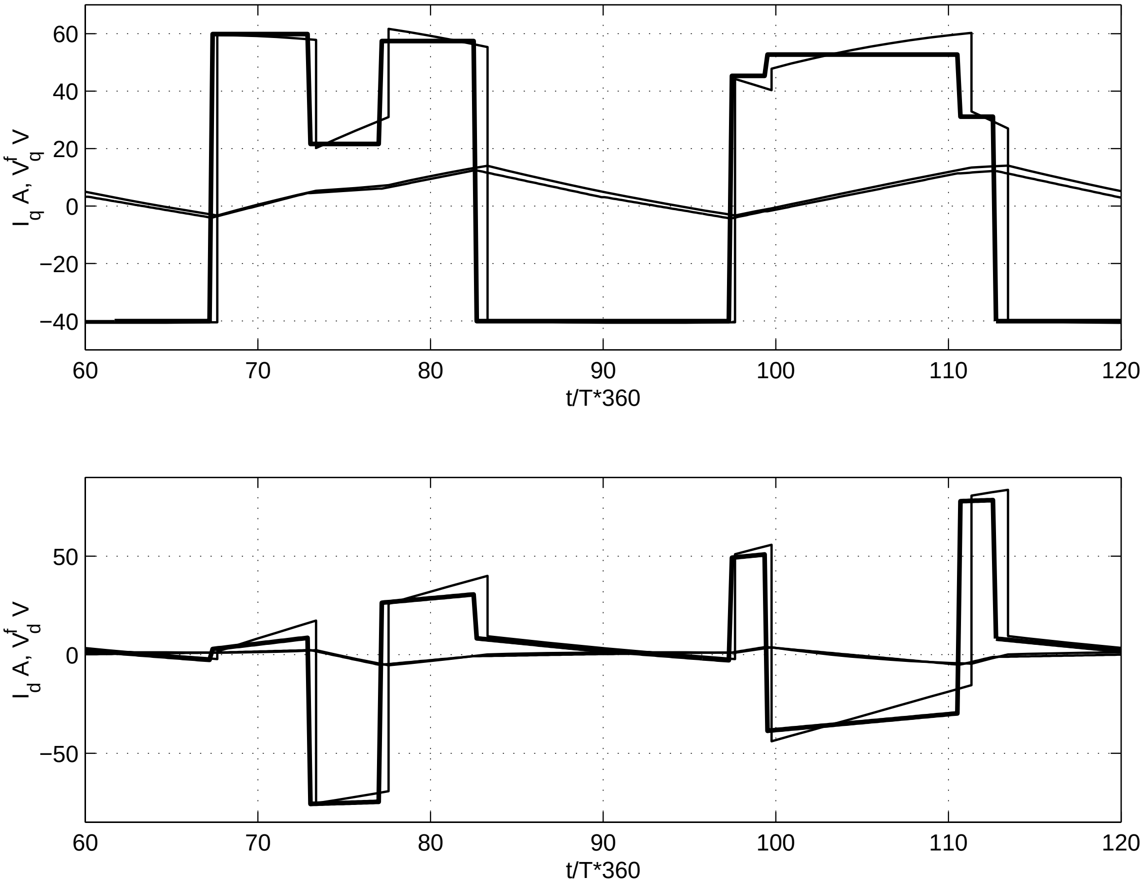

Figure 18.10: Output of the PWM in d-q coordinates, actual (thin lines) and approximated (bold lines).

18.7 Conclusions

Analytical and simulation results which quantify the effects of finite switching frequency on synchronous AC electric drives are presented in this chapter. The ripple pattern in AC PWM system is analyzed, open- and closed-loop PWM gain is evaluated, and the magnitude of the current ripple in the closed-loop system is estimated. These results are useful for control design, and for evaluation of current and torque ripple in a number of examples such as very high power drives and active filters.

Chapter 19

Conclusions on PWM Modeling

19.1 Summary

The thesis examines the effects of (low) switching frequency and delays on systems with PWM power supplies. Open- and closed-loop modeling procedures were described together with analytical formulas. Deviations from standard (idealized) models which replace a PWM block with a fixed gain were quantified.

Results of Chapter 14 show that slow switching frequency may have pronounced effects on accuracy of PWM models. The analytical expressions of the magnitude of the current and reference voltage ripple

$$\Delta I = \frac{T}{2}\frac{V_{DC}}{L_a}\tau(1-\tau) \tag{19.1}$$

$$\Delta m = \frac{T}{2}\frac{K_p^i}{L_a}V_{DC}\tau(1-\tau), \tag{19.2}$$

and the small deviation model of the PWM

$$\tau \approx \tau_{ss} + \frac{m - m(\mathbf{z}_{\mathrm{ss}})}{M(1/2-\tau_{ss}) + V_d} \tag{19.3}$$

are quite effective in quantifying the deviations from idealized (standard) models. Here τ_{ss} is a solution of the following quadratic equation, with $\mathbf{z} = \mathbf{z_{ss}}$

$$\frac{1}{2}\tau^2 - (\frac{1}{2} + \frac{V_d}{M})\tau + \frac{m(\mathbf{z})}{M} = 0 \tag{19.4}$$

and M is equal to $TV_{DC}/(2L_a)$.

In Chapter 15 the effects of delays in the PWM input signal were studied. Such delays are often caused by digital implementation of the controller. Delay effects require modifications in the computations made for system without delay. The tools for analysis of combined effects of finite switching frequency and delay have been developed. Resulting expressions for duty ratio τ

$$\frac{1}{2}\tau^2 - \left[\frac{t_s}{T} + \frac{1}{2} + \frac{V_d}{M}\right]\tau + \frac{m(\mathbf{z})}{M} + \frac{t_s}{T} = 0; \quad \tau \geq \frac{t_s}{T} \tag{19.5}$$

$$\frac{1}{2}\tau^2 - \left[\frac{t_s}{T} - \frac{1}{2} + \frac{V_d}{M}\right]\tau + \frac{m(\mathbf{z})}{M} = 0; \quad \tau \leq \frac{t_s}{T}, \tag{19.6}$$

where the smallest positive solution of each quadratic equation is selected, are of modest complexity, while their predictive power is considerable, as evidenced by the experiments. It has been shown that in DC drives low switching frequency reduces the effective PWM gain, and delays make the gain larger than the idealized one at low voltages.

A nonlinear discrete-time state-space model for a PWM controlled system was derived in Chapter 16. Discrete-time state-space models are most commonly derived via a regular sampling of a continuous-time model. However, a model that involves one sample per PWM cycle ignores ripple. To obtain a better model, the property that the system under consideration is piecewise LTI was used. It was thus possible to successively solve for the state variable in each of the two successive systems' configurations, and to invoke the continuity of the state at switching points. This procedure naturally leads to a discrete-time state-space model with two samples per PWM cycle. Computations were further simplified by a linear approximation of the state trajectory between samplings. The proposed simulation method can be used to evaluate performance and ripple magnitude at steady state for a system with PWM elements, and requires less computation then a straightforward conventional simulation of a general switching system.

In Chapter 17, the discrete-time piecewise affine map, which describes the behavior of the closed-loop system, was derived and conditions for existence of a T-periodic stable equilibrium were presented.

The necessary and sufficient condition for existence of a T-periodic stable equilibrium in the closed-loop linear system with a DC PWM was obtained. This result was based on analysis of a piecewise affine discrete-time map obtained for the averaged system under assumed linear-ripple approximation. The conditions derived are very simple to apply. In Section 17.1 a necessary condition was derived for existence of a T-periodic steady state that involves only basic system parameters, and does not depend on the system operating point (i.e., on the input signals). A meaning of the obtained condition is that, if normalized delay t_s/T is larger than V_d/M, then for the given system parameters an operating point exists for which system will not have a

T-periodic steady state. The converse statement is not necessary true. In Section 17.2, stronger conditions were given for the existence of a T-periodic steady state. These conditions were given in the terms of rising β and falling α slopes of the PWM input signal (normalized by the slope of the sawtooth T/V_d). These slopes depend not only on system parameters, but also on the operating point of the system. Note that always $\alpha \leq 0$ and $\beta \geq 0$. A T-periodic steady state exists if and only if:

(a) if $\beta/(\beta-\alpha) < t_s/T$, then

$$\beta < 2/3 \quad \text{and} \quad \alpha > 3\beta - 2 \tag{19.7}$$

(b) if $\beta/(\beta-\alpha) > t_s/T$, then

$$\beta < 2 \quad \text{or} \quad \alpha < 2 - \beta, \tag{19.8}$$

Furthermore, the average duty ratio, given by $\tau_{ss} = \beta/(\beta-\alpha)$, does not depend on the particular slope within which the intersection occurs. From these results it is clear that the "rule of thumb" $\beta < 1$ which is used in practice that does not always guarantee the existence of a T-periodic steady state if the delay is sufficiently large. In Section 17.2 the condition for the existence of a T-periodic steady state of a PWM system subject to uniform sampling

$$\alpha > \beta - 2 \tag{19.9}$$

was obtained. Stability regions for these cases are presented on Fig. 17.1.

Experimental results are provided for a PWM controlled DC servo motor, while analytical results are presented for some standard DC/DC examples from the power electronics literature.

The standard results in modeling of current programming in DC-DC converters were discussed and compared with results developed in the thesis. The conventional result obtained by geometrical observation shows that the small deviation discrete transfer function from control current to inductor current is stable if and only if

$$\left|\frac{M_2 - M_c}{M_1 + M_c}\right| < 1, \tag{19.10}$$

where M_c is the constant stabilizing ramp, M_1 is the up-slope and $-M_2$ is the down-slope of the inductor current in steady-state. This is the same condition as the condition for existence of a T- periodic steady state

$$\left|\frac{1-\beta}{1-\alpha}\right| < 1, \tag{19.11}$$

developed in Section 17.2. Equation (19.11) becomes identical to (19.10) and to stability criterion available in the literature (e.g. equation (17) in [101]) after the substitution $\beta = M_2/M_c$ and $\alpha = -M_1/M_c$.

It was also shown that the same results are obtained for small deviation model of the PWM (equations (17.42) and (14.33)), and for duty ratio in steady state (equations (17.39) and (13.13)). An explanation stems from the fact that the same assumption is made in both approaches about the shape and piecewise linear nature of the ripple function. As soon as these assumptions are written in terms of the slopes of the ripple function, both methods result in the same equations.

The differences between these two approaches include the following:

1. The averaging theory provides a justification for using the particular approximation of the ripple function, while the geometric method assumes the ripple piecewise linear because of practical observations.
2. The results obtained in the thesis are general, and can be applied not only to a first order system, but to any linear system with a PWM block.
3. Our approach allows to study more complicated ripple patterns, such as in the case of delay or in nT-periodic steady state.

In Chapter 18 analytical and simulation results which quantify the effects of finite switching frequency on AC electric drives were presented. In this chapter analytical formulas which quantify the effects of low switching frequency in PWM-controlled AC drives were derived. A permanent magnet synchronous motor drive is considered as a representative example. These results are useful for control design, and for evaluation of current and torque ripple in a number of examples such as very high power drives and active filters.

The ripple pattern in AC PWM system was analyzed. The magnitude of the current ripple in the closed-loop system was estimated, and open- and closed-loop PWM gain was evaluated. It has been shown that the first term of the series expansion of the averaged PWM output voltage is

$$\bar{V}_d + j\bar{V}_q \approx V_{DC} R^* e^{j\theta_0}$$

which is linear on R^* and represents ideal output of the PWM. The m-th term is less then $\left(\frac{\pi}{N}\right)^{2\ell}\frac{1}{(2\ell+1)!}$ and, decreases rapidly with ℓ. Thus the error in the gain of the PWM is in order of $\frac{1}{6}\left(\frac{2}{\sqrt{3}}\right)^3\left(\frac{\pi}{N}\right)^2$, and does not depend on the absolute switching frequency $\omega_0 = 2\pi/T_0$. It depends on the relative switching frequency N, i.e., the number of basic switching cycles per period of the fundamental stator frequency.

Using the Taylor series expansion, it was shown that the magnitude of the current ripple is the maximum value of $\Delta i_{3,2}$ and $\Delta i_{4,1}$

$$\begin{aligned}\Delta i_{3,2} &= \frac{T_0}{2}\frac{V_{DC}}{L}\,\tau_1\left(e^{-j\left(\frac{2n+1}{N}\pi-\theta_0-\frac{\pi}{3}\right)} - R^* e^{j\theta_0}\right), &(19.12)\\ \Delta i_{4,1} &= \frac{T_0}{2}\frac{V_{DC}}{L}\,R^* e^{j\theta_0}(1-\tau_1-\tau_2), &(19.13)\end{aligned}$$

where τ_1 and τ_2 are generalized duty ratios, and $R^* e^{j\theta_0}$ is an effective value of the PWM reference input voltage. From above equations, it can be seen that when $R^* e^{j\theta_0}$ is aligned with either the d or the q axis, the ripple magnitude $\Delta i^d_{4,1}$ or $\Delta i^q_{4,1}$ becomes a second degree polynomial of R^* with the maximum near the middle point of the range of R^*, i.e., $\sqrt{3}/4$. This result is very similar to the one obtained for DC PWM (19.1). It was proved that maximum current ripple magnitude is always less then $T_0 V_{DC}/(8L)$.

In Section 18.6, the closed-loop PWM gain was studied. The currents are feed back to the controller, causing ripple in V_d^* and V_q^*. Because of this effect, the average value of the PWM input voltages $\bar{V}_d^*$, $\bar{V}_q^*$ and actual measured voltages $V_d^*(kT_0+t_s)$ and $V_q^*(kT_0+t_s)$ can be different. Thus the average PWM gain can deviate from ideal. As in the DC PWM case, the normalized closed-loop gain is given by the general formula

$$K^{c.l.}_{PWM,d} = 1 + G_d \frac{\widetilde{i}_d(kT_0 + t_s)}{\bar{V}^*_d}, \tag{19.14}$$

$$K^{c.l.}_{PWM,q} = 1 + G_q \frac{\widetilde{i}_q(kT_0 + t_s)}{\bar{V}^*_q}, \tag{19.15}$$

where $G_d = k_{p1}$, $G_q = k_{p2}$ (in terms of Fig. 18.1), t_s is the sampling instance, and $\widetilde{i}_d(t)$, $\widetilde{i}_q(t)$ are the ripple component of the $i_d(t)$ and $i_q(t)$ currents. If the input voltage is aligned with one axis, then the input voltage along the other one is equal to zero and even a very small error in its measurement will produce an infinite relative error in the PWM gain along that axis.

The effective value of the PWM input voltage $V^*_d(kT_0+t_s)+jV^*_q(kT_0+t_s)$ depends on the sampling instance t_s, which is a design parameter and ideally should be chosen such that $V^*_d(kT_0+t_s)+jV^*_q(kT_0+t_s) = \bar{V}^*_d + j\bar{V}^*_q$. Two different sampling strategies $t_s/T_0 = -1/2$ and $t_s/T_0 = 0$ were compared. It was shown that the error associated with choice of the sampling instance $t_s/T_0 = -1/2$ is larger then the error associated with choice of the sampling instance $t_s/T_0 = 0$ if $\tau_2 > \tau_z$. The emerging rule is: if $R^* < \sqrt{3}/4$, then it is better to sample at $kT_0 - T_0/2$; if $R^* > \sqrt{3}/4$ then sampling at kT_0 provides smaller error. In either case, the error in current measurements associated with sampling at $t_s = T_0/2$ or $t_s = 0$ is less then $V_{DC}\left(\frac{\pi}{N}\right)^2 \frac{T_0}{L}$. This error is inverse proportional to the PWM basic cycle frequency $\omega_0 = 2\pi/T_0$, and to square of the number number of PWM cycles per fundamental stator period $N = T/T_0$. In other words, the error in current due to sampling at the middle (kT_0) or beginning ($kT_0 - T_0/2$) of the PWM basic cycle is proportional to the maximal ripple magnitude

$V_{DC}\frac{T_0}{8L}$, and to the voltage pulse asymmetry $S^1 - S^3$ (which is proportional to $(\pi/N)^2$). The voltage pulse asymmetry does not depend on absolute switching frequency ω_0.

In the worst case of sampling, when current $i(t)$ achieves its maximal or minimum at $kT_0 + t_s$, the deviation of the PWM gain will be maximal. In this case the error in current due to sampling (difference between averaged current and sampled one) can equal $\Delta i_{32,max}$ or $\Delta i_{41,max}$, with the maximum equal to the current ripple magnitude $V_{DC}\frac{T_0}{8L}$.

The actual magnitude of the current ripple (obtained by simulation) is in good agreement with approximate one calculated by formulas derived in the thesis. This confirms that the proposed technique can be used to estimate magnitude and ripple behavior.

To summarize, main contributions of the thesis include:

- Tools for analysis of combined effects of finite switching frequency and delay for DC PWM controlled systems.
- A discrete-time piecewise affine map, which describes the behavior of the closed-loop system with DC PWM.
- A necessary and sufficient condition for existence of a T-periodic stable equilibrium in the closed-loop linear system with a DC PWM.
- An analytical and simulation results which quantify the effects of low switching frequency in PWM-controlled AC electric drives.

- An estimate of the open- and closed-loop PWM gain.
- An estimate of the magnitude of the current ripple in a closed-loop AC PWM controlled system.
- A comparative evaluation of two different sampling strategies $t_s = -T_0/2$ and $t_s = 0$.

19.2 Suggestions for future work

The necessary and sufficient condition for existence of a T-periodic stable equilibrium point in the closed-loop linear system with a DC PWM has been derived in this thesis. Uniqueness and local stability of such a point has been established. Although extensive simulations suggest that, under the local stability condition, the equilibrium point is actually globally stable, a rigorous proof for this has not been provided. This may be a topic of a future theoretical research.

Another open problem, which is of both theoretical and practical interest, is to obtain analytical conditions for the existence of nT-periodic regime of operation, and to estimate magnitude of the current ripple. A basis for this exploration is developed in the thesis, but the actual computation may require extensive symbolic manipulations, as the final formula is likely to be far more complicated than the one for the T-periodic case.

Analytical and simulation results which quantify the effects of low switching frequency on PWM-controlled synchronous AC electric drives, which are provided in the thesis assume for a particular symmetrical switching pattern. Alternative switching patterns can be analyzed and compared in the same way, although general formulas for arbitrary switching pattern are probably too complicated. Similarly, the approach could be applied to other AC drives, such as induction motor drives.

A significant area of research that is not covered in the thesis is design of controllers which utilize the new models. These controllers may, for example, use non-uniform sampling technique. The sampling instances should be adjusted so that the sampling error due to the current ripple is minimized.

Bibliography

[1] *ADSP-2100 Family User's Manual.* Prentice Hall, 1994.

[2] *ADSP-2100 Family Assembler Tools and Simulator Manual.* Analog Devices, 1995.

[3] *ADSP-2100 Family EZ Tools Manual.* Analog Devices, 1995.

[4] *Motion Coprocessor ADMC201.* Analog Devices, 1995.

[5] M. T. Alrifai, J. H. Chow, and D. A. Torrey. A backstepping nonlinear control approach to switched reluctance motors. In *Proceedings of IEEE Conference on Decision and Control*, pages 4652–4657, 1998.

[6] L. Ben Amor, L.A. Dessaint, O. Akhrif, and G. Olivier. Adaptive feedback linearization for position control of a switched reluctance motor: Analysis and simulation. In *Int. Jour. of Adaptive Control and Signal Processing*, volume 7, pages 117–136, Mar-Apr1993.

[7] A.A. Arkadan and B.W. Kielgas. Coupled problem in SRM drive systems during fault conditions. *IEEE Transactions on Magnetics Proceedings*, 30:3256 – 3259, 1994.

[8] Z. Artstein. Stability, observability and invariance. *J. Differential Eqs.*, 44:224 – 248, 1982.

[9] A. Barnett, V. Davidkovich, A. M. Stanković, and G. Tadmor. A versatile test-bed for evaluation of controllers for permanent magnet AC drives. In *Naval Symposium on Electric Machines, Newport, RI*, 1997.

[10] J.T. Bass, T.J.M. Miller, and R.L. Steigerwald. Development of a unipolar converter for variable reluctance motor drives. *IEEE Transactions on Industrial Applications*, 23:545 – 553, 1987.

[11] A. Blondel. *Synchronous Motors and Converters, Part III.* McGraw-Hill, 1913.

[12] N. N. Bogoliubov and Y. A. Mitropolsky. *Asymptotic Methods in the theory of Non-linear Oscillators.* Gordon and Breach, New York, 1961.

[13] I. Boldea. *Electric Machine Dynamics.* MacMillan, 1986.

[14] I. Boldea. *Reluctance Synchronous Machines and Drives.* Oxford Press, New York, 1996.

[15] I. Boldea and S.A. Nasar. *Electric Machine Dynamics.* Macmillan, New York, 1986.

[16] S. A. Bortoff, R. R. Kohan, and R. Milman. Adatptive control of variable reluctance motors: a spline function approach. *IEEE Transactions on Industrial Electronics*, 45:433 – 444, June 1998.

[17] B.K. Bose, T.J.M. Miller, P.M. Szczesny, and B.K. Bicknell. A microcomputer control of switched reluctance motor. *IEEE Transactions on Industrial Applications*, 22:708 – 715, 1986.

[18] S. R. Bowes and A. Midoum. Suboptimal switching strategies for microprocessor- controlled PWM inverter drives. In *IEE Proceedings*, volume 132, pages 133 – 148, 1985.

[19] G.S. Buja and M.I. Valla. Control Characteristics of the SRM Drives — Part I: Operation in the Linear Region. *IEEE Transactions on Industrial Electronics*, 38(8):313–321, 1991.

[20] H. Cailleux, B. LePioufle, B. Multon, and C. Sol. Effects of the sampling and of the phase commutation in nonlinear position control of a switched reluctance motor - analysis and compensation. In *Proc. 32-nd CDC*, pages 3403–3404, 1993.

[21] D.E. Cameron. Origin and reduction of acoustic noise on variable-reluctance motors. Master's thesis, MIT, Dept. EECS, 1990.

[22] J.J. Carroll, D.M. Dawson, and P. Vedagarbha. Experimental verification of adaptive and robust trajectory tracking controllers for switched reluctance motors. In *Proceedings of IEEE Conference on Decision and Control*, pages 1856–1861, 1994.

[23] D. Chen and B. Paden. Nonlinear adaptive torque–ripple cancellation for step motor. In *Proceedings of IEEE Conference on Decision and Control*, pages 3319 – 3324, 1990.

[24] J.Y. Le Chenadec, B. Multon, and S. Hassine. Current feeding of switched reluctance motor: Optimization of the current wave form to minimize the torque ripple. In *IMACS-TC1 Fourth International Conference*, pages 267 – 272, July 1993.

[25] R. A. Comstock. Trends in brushless PM drive and motor technology overview. In *Proc. Ninth International MOTOR-CON Conference, Boston, MA*, 1986.

[26] Z. Coric. *Low Torque Ripple control of Current-fed Switched Reluctance Motors.* M.S. Thesis, Norteastern Univ, 1995.

[27] R.M. Crowder. *Electric Drives and Their Controls.* Oxford Press, New York, 1995.

[28] J.H.B. Deane and D.C. Hamill. Instability, subharmonics, and chaos in power electronics systems. *IEEE Transactions on Power Electronics*, 5:260 – 268, 1990.

[29] Yasuhiko Dote. *Servo Motor and Motion Control Using Digital Signal Processors.* Prentice-Hall, New Jersey, 1990.

[30] G. Dunlop. A switched reluctance motor drive with zero torque ripple and a constant inverter bus current. In *Proc. of the Inst. of Mechanical Engineers*, volume 208, pages 61 – 68, 1994.

[31] F. Filicori, C.G. Lo Bianco, and A. Tonielle. Modeling and control strategies for variable reluctance direct-drive motor. *IEEE Transactions on Industrial Electronics*, 40:105 – 115, 1993.

[32] İ. Ağırman, A. M. Stanković, and G. Tadmor. Adaptive torque-ripple minimization in switched reluctance motors. In *Proceedings of IEEE Conference on Decision and Control*, pages 983 – 988, 1998.

[33] H. C. Skudelny H. W. Van der Broeck and G. Stanke. Analysis and realization of a pulse width modulator based on voltage space vectors. In *Proc. IEEE Industry Appl. Society Annual Meeting*, pages 244 – 251, 1986.

[34] A. Halanay. Averaging methods for differential equations with retarded arguments with a small parameter. *Journal of Differential Equations*, 2:57 – 73, 1966.

[35] A. Hale. On the method of averaging for differential equations with retarded arguments. *Journal on Mathematical Analysis and Applications*, 14:70 – 76, 1966.

[36] J.K. Hale. *Ordinary Differential Equations.* Robert E. Krieger, New York, 1980.

[37] N.N. Hancock. *Matrix analysis of electric machinery.* Pergamon Press, 1974.

[38] D.C. Hanselman. Resolver signal requirements for high accuracy resolver-to-digital conversion. *IEEE Transactions on Industrial Electronics*, 37:556–561, 1990.

[39] D.C. Hanselman. *Brushless Permanent-Magnet Motor Design.* McGraw-Hill, New York, 1994.

[40] J.R. Hendershot and T.J.E. Miller. *Design of Brushless Permanent-Magnet Motors.* Magna Physics, 1990.

[41] D.J. Hill and P.J. Moylan. Dissipative dynamical systems: Basic input-output and state properties. *Jour. of the Franklin Institute*, 309(5):327–357, 1980.

[42] J. Holtz. Pulsewidth modulation - a survey. *IEEE Transactions on Power Electronics*, 39:410 – 420, 1992.

[43] J. Holtz and B. Beyer. Optimal pulsewidth modulation for AC servos and low-cost industrial drives. *IEEE Transactions on Power Electronics*, 30:1039 – 1047, 1994.

[44] J. Holtz and E. Bube. Field oriented asynchronous pulse-width modulation for high performance AC machine drives operating at low switching frequency. In *Proc. IEEE Industry Appl. Society Annual Meeting*, pages 412 – 417, 1988.

[45] J. Holtz and A. Khambadkone. Low switching frequency and high dynamic pulsewidth modulation based on field-orientation for high-power inverter drive. *IEEE Transactions on Power Electronics*, 7:627 – 632, 1992.

[46] J. Holtz, W. Lotzkat, and A.M. Khambadkone. On continuous control of PWM inverters in the overmodulation range including the six-step mode. *IEEE Transactions on Power Electronics*, 8:546 – 553, 1993.

[47] I. Husain and M. Ehsani. Torque ripple minimization in switched reluctance motor drives by PWM current control. *IEEE Transactions on Power Electronics*, 11:83 – 88, 1996.

[48] M. Ilic-Spong, R. Marino, S. M. Peresada, and D. G. Taylor. Feedback linearization control of switched reluctance motors. *IEEE Transactions on Automatic Control*, AC – 32(5):371–279, 1987.

[49] P. Lammert J. Holtz and W.Lotzkat. High-speed drive system with ultrasonic MOSFET PWM inverter and single-chip microprocessor control. In *Proc. IEEE Industry Appl. Society Annual Meeting*, pages 12 – 17, 1986.

[50] C. A. Jacobson, A. M. Stanković, G. Tadmor, and Z. Ćorić. A family of robust control strategies for switched reluctance motors. In *Proceedings of the Intl. Conf. on Power Electronics and Drive Systems (PEDS)*, pages 192–197, 1995.

[51] J. G. Kassakian, M. F. Schlecht, and G. C. Verghese. *Principles of Power Electronics.* Addison-Wesley, 1991.

[52] H. K. Khalil. *Nonlinear Systems.* Prentice Hall, 2-nd edition, 1996.

[53] P. T. Krein, J. Bentsman, R. M. Bass, and B. C. Lesieutre. On the use of averaging for the analysis of power electronic systems. *IEEE Transactions on Power Electronics*, 5:182 – 190, 1990.

[54] B. Lehman and R.M. Bass. Extensions of averaging theory for power electronic systems. *IEEE Transactions on Power Electronics*, 11:542 – 553, 1996.

[55] B. Lehman and R.M. Bass. Switching frequency dependent averaged models for PWM DC-DC converters. *IEEE Transactions on Power Electronics*, 11:89 – 98, 1996.

[56] B. Lehman and V.M. Kolmanovskii. Extensions of classical averaging techniques to delay differential equations. *Proceedings of IEEE Conference on Decision and Control*, pages 411 – 416, 1994.

[57] B. Lehman and S. Weibel. Fundamental averaging theorems for functional differential equations. *Proceedings of the American Control Conference*, 5:3215 – 3219, 1997.

[58] W. Leonard. High performance microcomputer control of electrical drives. In C.T. Leondes, editor, *Control and Dynamic Systems - Analysis and Control System Techniques for Electric Power Systems*, volume 43. Academic Press, New York, 1991.

[59] W. Leonhard. *Control of Electric Drives.* Springer-Verlag, New York, 1985.

[60] X.Z. Liu, G.C. Verghese, J.H. Lang, and M.K. Onder. Generalizing the Blondel-Park transformations of electrical machines: Necessary and sufficient conditions. *IEEE Transactions on Circuits and Systems*, 36:1058–1067, 1989.

[61] S. R. MacMinn and J.W. Sember. Control of switched reluctance aircraft engine starter-generator over a very wide speed range. In *Proc. of the Intersociety Energy Conversion Engineering Conference (IECEC), August 6-11*, 1989.

[62] D. Maksimović and S. Ćuk. A unified analysis of PWM converters in discontinuous modes. *in Int. PCIM Conf. Rec.*, June 1989.

[63] R.D. Middlebrook and S. Ćuk. A general unified approach to modeling switching converter power stages. *IEEE Power Electron. Spec. Conf. Rec.*, pages 18 – 34, 1976.

[64] T.J.E. Miller. *Brushless Permanent-Magnet and Reluctant Motor Drives.* Oxford Press, New York, 1989.

[65] T.J.E. Miller. *Switched Reluctance Motors and Their Control.* Oxford Press, New York, 1993.

[66] S. Mir, M. Elbuluk, and I. Husain. Torque ripple minimization in switched reluctance motors using adaptive fuzzy control. In *IEEE-IAS Annual Meeting*, volume 1, pages 571 – 578, 1997.

[67] N. Mohan, T. M. Undeland, and W. P. Robbins. *Power Electronics.* Wiley, 2-nd edition, 1995.

[68] J.F. Moynihan, M.G. Egan, and J.M.D. Murphy. The appliction of state observers in current regulated PM synchronous drives. *IEEE IECON*, pages 20 – 25, 1994.

[69] S. Mulukutla. *Electric Machines Steady-State Theory and Dynamic Performance.* West Publishing Company, St. Paul, MN, 1985.

[70] J. M. D. Murphy and F. G. Turnbull. *Power Electronic Control of AC motors.* Pergamon Press, 1988.

[71] A. Murray and P. Kettle. AC motor control experiments using the ADMC-200-EVAL board. *Analog Devices Application Note #407*, 1995.

[72] S.A. Nasar and I. Boldea. *Electric Machines: Steady-State Operation.* Hemisphere Publishing Corp., New York, 1990.

[73] S.A. Nasar and I. Boldea. *Electric Machines: Dynamics and Control.* CRC Press, 1993.

[74] S.A. Nasar, I. Boldea, and L.E. Unnewehr. *Permanent Magnet, Reluctance and Self-Synchronous Motors.* CRC Press, 1993.

[75] D.W. Novotny and T.A. Lipo. *Vector Control And Dynamics Of AC Drives.* Oxford University Press, 1996.

[76] R. Ortega and G. Espinosa. Torque regulation in induction motors. *Automatica*, 29(3):621–633, 1993.

[77] R.H. Park. Two reaction theory of synchronous machines: Part I. *AIEE Transactions*, 48:716–730, 1929.

[78] V. Petrović, A.M. Stanković, and G. Tadmor. An adaptive controller for minimization of torque ripple in permanent magnet synchronous motors. In *Power Electronics Specialists Conference*, pages 113–118, 1998.

[79] C. L. Phillips and R. D. Harbor. *Feedback Control Systems.* Prentice-Hall, New Jersey, 1988.

[80] R. Ortega P.J. Nicklasson and G. Espinosa. Passivity-based control of the general rotating electrical machine. In *Proceedings of IEEE Conference on Decision and Control*, pages 4018 – 4023, 1994.

[81] R. Ortega P.J. Nicklasson and G. Espinosa. Passivity-based control of a class of blondel-park transformable electrical machines. *IEEE Transactions on Automatic Control*, TAC – 42:629 – 647, 1997.

[82] K. M. Rahman, A. V. Rajarathnam, and M. Ehsani. Optimized instantaneous torque control of switched reluctance motor by neural network. In *IEEE-IAS Annual Meeting*, volume 1, pages 556 – 563, 1997.

[83] K. Rajashekara, A. Kawamura, and K. Matsuse. Position sensorless control of permanent magnet ac motors. In *Sensorless Control of AC Motor Drives*, pages 259 – 268. IEEE Press, 1996.

[84] C. Rossi and A. Tonielli. Feedback linearizing and sliding mode control of a variable reluctance motor. *Int. J. Control*, 60:543 – 568, 1994.

[85] K. Russa, I. Husain, and M. Elbuluk. Torque ripple minimization in switched reluctance machines over a wide speed range. *IEEE Transactions on Industrial Applications*, 34:1105 – 1112, 1998.

[86] H. Hasagawa S. Fukuda and Y. Iwaiji. PWM technique for inverter with sinusoidal current. In *IEEE PESC Rec.*, pages 35 – 41, 1988.

[87] L. Resnik S. Hsu, A.R. Brown and R.D. Middlebrook. Modeling and analysis of switch dc-to-dc converters in constant-frequency current-programmed mode. *IEEE PESC Rec.*, pages 284 – 301, 1979.

[88] T. A. Sakharuk, B. Lehman, A. M. Stanković, and G. Tadmor. Effects of finite switching frequency and computational delay on PWM controlled servo DC drives. In *Proc. 32 IEEE Industry Appl. Society Annual Meeting*, pages 699 – 707, 1997.

[89] D. J. Schramm, B.W. Williams, and T.C. Green. Optimum commutation–current profile on torque linearization of switched reluctance motors. In *Proc. Intl. Conf. on Electric Machines*, pages 484 – 488, September 1992.

[90] M. Schroedl. Sensorless control of permanent magnet synchronous motor. *Electric Machines and Power Systems*, 22:173 – 185, 1994.

[91] P. R. Sethna and T. J. Morgan. Some nonlocal results for weakly nonlinear dynamical systems. *Quarterly of Applied Mathematics*, 26(2):175 – 185, 1968.

[92] G.R. Slemon. Electrical machines for variable-frequency drives. *Proceedings of the IEEE*, 82(8):1123–1139, 1994.

[93] R. Slemon. Electrical machines for variable frequency drives. *Proceedings of the IEEE*, 82:1123 – 1139, 1994.

[94] T.J. Sokira and W. Jaffe. *Brushless DC Motors: Electronics Commutation and Controls*. Tab Books, 1990.

[95] A. M. Stanković, G. Tadmor, Z. Ćorić, and İ. Ağırman. Low torque ripple control of current fed switched reluctance motors. *IEEE Transactions on Industrial Electronics*, 46:171 – 183, 1999.

[96] J. Sun and H. Grotstollen. Optimized space vector modulation and regular-sampled PWM: A Reexamination. In *Proc. IEEE Industry Appl. Society Annual Meeting*, volume 2, pages 956 – 963, 1996.

[97] N. Ohba T. Mizutani, K.Okamoto and Y.W. Zhang. Fundamental study on effects of sampling period to digital servo system. *Intl. Jour. Japan Soc. Precision Eng.*, 25:309–314, 1991.

[98] F.D. Tan and R.D. Middlebrook. A unified model for current-programmed converters. *IEEE Transactions on Power Electronics*, 10:397 – 408, 1995.

[99] D.G. Taylor. Nonlinear control of electric machines: An overview. *IEEE Control Systems*, 14:41–51, 1994.

[100] A. M. Trzynadlowski and S. Legowski. Minimum-loss vector PWM strategy for three-phase inverters. *IEEE Transactions on Power Electronics*, 9:26 – 34, 1994.

[101] R. Tymerski and D. Li. State-space models for current programmed pulsewidth-modulated converters. *IEEE Transactions on Power Electronics*, 8:271 – 278, 1993.

[102] H. van der Broeck. Analysis of the harmonics in voltage fed inverter drives caused by PWM schemes with discontinuous switching operation. In *Proc. of EPE'91*, volume 3, pages 261 – 266, 1991.

[103] A. van der Schaft. *L2-Gain and Passivity Techniques in Nonlinear Control*, volume LNCIS 218. Springer, 1996.

[104] P. Vas. *Electrical Machines and Drives. A space-vector theory approach.* Oxford University Press, New York, 1992.

[105] S. Vukosavić and M. Stojić. SRM inverter topologies: A comperative evaluation. *IEEE Transactions on Industrial Applications*, 27:1034 – 1047, 1991.

[106] R.S. Wallace and D.G. Taylor. A balanced commutator for switched reluctance motors to reduce torque ripple. *IEEE Int. Conf. on Systems Engineering*, pages 597 – 600, 1990.

[107] R. Wu and G.R. Slemon. A permanent magnet motor drive without a shaft sensor. *IEEE Transactions on Industrial Applications*, 27:1005 – 1011, 1991.

[108] I. Zafrany and S. Ben-Yaakov. A chaos model of subharmonic oscillations in current mode pwm boost converters. *IEEE PESC Rec.*, pages 1111 – 1117, 1995.

Appendix A

Selection of controller parameters

Case I: $\lambda = 0$

When $\lambda = 0$ is selected, the closed loop dynamics of the combined incremental state $e = [e_1, \ldots, e_5]^T$ is governed by the following differential equation

$$\frac{d}{dt}e = \begin{bmatrix} A_{1,1} & 0_{2\times 3} \\ & \\ A_{2,1} & A_{2,2} \end{bmatrix} e + \begin{bmatrix} 0_{2\times 1} \\ B_2 \end{bmatrix} \frac{d}{dt}T_L \tag{A.1}$$

where

$$A_{1,1} = \begin{bmatrix} -\rho & \gamma \\ -\gamma & -\rho \end{bmatrix}$$

The form of $A_{1,1}$ shows that the selection of ρ does provide for the desired decay rate in the homogeneous component of the incremental currents dynamics. The selection of $\gamma = 0$ is one obvious option. The selection of $\gamma \neq 0$ adds a lossless exchange between the two incremental currents, allowing faster and easier balancing of their respective magnitudes. Formally, this adds an imaginary component to the two eigenvalues of $A_{1,1}$, which is known to shorten response time in second order systems.

The following lemma concerns the corresponding stability of the interconnection of the mechanical and the electrical components of the incremental system.

Lemma A.0.1 *Let the selection of* $\lambda = 0$ *be made and let the other control and design parameters be as in (4.11), (4.15), (4.21) and (4.22). Then there exist constants* α_0, α_1 *and* α_2 *such that*

$$\|e(t)\|_E \leq \left((\alpha_0 + \alpha_1 \cdot t) \cdot exp(-\rho t) \|e(0)\|_E + \alpha_2 \int_0^t exp(\rho(s-t)) \left| \frac{d}{ds} T_L(s) \right| ds \right) \tag{A.2}$$

Note: Lemma A.0.1 guarantees the decay of initial error effects to zero, at the prescribed exponential rate, as well as a related bounded input bounded output stability of the mapping $\frac{d}{dt} T_L \mapsto e$.

Proof: Since the system (A.1) is lower block triangular, and since the constant matrix $A_{1,1}$ is stable with the exponential decay rate $-\rho$, the component of the result that pertains to e_1 and e_2 is obvious. Furthermore, these variables are not affected by the load torque derivative, whereby the norm of the state subvector $[e_1(t), e_2(t)]^T$ decays to zero at a rate that is proportional to $\|[e_1(0), e_2(0)]^T\|_E \, exp(-\rho t)$.

Looking at the dynamics of $[e_1, e_2, e_3]^T$ one considers the system (4.12). Applying the variation of parameters formula, we obtain

$$\begin{bmatrix} e_3 \\ e_4 \\ e_5 \end{bmatrix} (t) = exp(A_{2,2} t) \begin{bmatrix} e_3 \\ e_4 \\ e_5 \end{bmatrix} (0) + \int_0^t exp(A_{2,2}(t-s)) \left(A_{2,1}(s) \begin{bmatrix} e_1 \\ e_2 \end{bmatrix} (s) + B_2 \frac{d}{ds} T_L(s) \right) ds \tag{A.3}$$

By the designed stability of $A_{2,2}$, there is a fixed $a > 0$ so that

$$\|exp(A_{2,2}t)\| \leq a \cdot exp(-\rho t) \tag{A.4}$$

(where, as mentioned in Section 4.2, the norm of a matrix is its maximal singular value.) The established decay rates of $[e_1(t), e_2(t)]^T$ and of $exp(A_{2,2}t)$ imply that

$$\left\| exp(A_{2,2}(t-s))A_{2,1}(s) \begin{bmatrix} e_1 \\ e_2 \end{bmatrix} (s) \right\|_E \leq b \cdot exp(-\rho t)\|A_{2,1}(s)\| \tag{A.5}$$

where b is proportional to $a\|[e_1(0), e_2(0)]^T\|_E$. Similarly, with $c = a\|B_2\|$, one has

$$\left\| \int_0^t exp(A_{2,2}(t-s))B_2 \frac{d}{ds}T_L(s)ds \right\|_E \leq c \int_0^t exp(\rho(s-t)) \left| \frac{d}{ds}T_L(s) \right| ds \tag{A.6}$$

Let us focus now on the term involving the matrix $A_{2,1}$. The non-zero component of $A_{2,1}$ is the row η^T, as defined in (4.13). We can write

$$\eta = \Delta L \begin{bmatrix} i_{q,d} \\ i_{d,d} \end{bmatrix} + \begin{bmatrix} \frac{\Delta L}{L_q} e_2 \\ MI \end{bmatrix} \tag{A.7}$$

The established decay of e_2 implies that the norm of the second term on the right hand side of (A.7) is uniformly bounded in terms of $\|e(0)\|_E$. The other term is proportional to the vector of desired currents $[i_{d,d}, i_{q,d}]^T$. Given that this vector solves the optimization problem (4.6), its Euclidean norm is smaller than any other current vector that would produce the desired motor torque. Since one possible selection is $i_d = 0$ and $i_q = \frac{T_{M,d}}{MI}$, this implies, in particular

$$\left\| \begin{bmatrix} i_{d,d} \\ i_{q,d} \end{bmatrix} \right\|_E \leq \frac{|T_{M,d}|}{MI} \tag{A.8}$$

Invoking (4.4) and the equality $\widehat{T}_L = T_L + \tau e_4$, we can further obtain a bound of the form

$$\left\| \begin{bmatrix} i_{d,d} \\ i_{q,d} \end{bmatrix} \right\|_E \leq d + f \left\| \begin{bmatrix} e_3 \\ e_4 \\ e_5 \end{bmatrix} \right\|_E \tag{A.9}$$

where d is determined by the assumed a priori bounds over ω_d, $\dot{\omega}_d$, $\ddot{\omega}_d$ and T_L. By (A.7) and an appropriate modification in d and f, we thus have

$$b\|A_{2,1}\| \leq d + f \left\| \begin{bmatrix} e_3 \\ e_4 \\ e_5 \end{bmatrix} \right\|_E \tag{A.10}$$

Note that, since the left hand side of (A.10) is multiplied by "b", which is proportional to $\|[e_1(0), e_2(0)]^T\|_E$, the modified "d" and "f" are both proportional to $\|[e_1(0), e_2(0)]^T\|_E$.

Denote $\epsilon(t) = \|[e_1, e_2, e_3]^T(t)\|_E$. A summary of (A.3), (A.4), (A.5), (A.6) and (A.10) is an inequality of the following form

$$\epsilon(t) \leq exp(-\rho t)\left(a\epsilon(0) + d \cdot t + f\int_0^t \epsilon(s)ds\right) + c\int_0^t exp(\rho(s-t))\left|\frac{d}{ds}T_L(s)\right| ds \tag{A.11}$$

Clearly, $\epsilon(t)$ is dominated by the solution of (A.11) with an equality substituting the inequality; that is, $\epsilon(t) \leq \delta(t)$ where

$$\delta(t) = exp(-\rho t)\left(a\epsilon(0) + d \cdot t + f\int_0^t \delta(s)ds\right) + c\int_0^t exp(\rho(s-t))\left|\frac{d}{ds}T_L(s)\right| ds \tag{A.12}$$

Equivalently, $\delta(t)$ satisfies the differential equation

$$\frac{d}{dt}\delta(t) = -\left(\rho - f \cdot exp(-\rho t)\right)\delta(t) + d \cdot exp(-\rho t) + c\left|\frac{d}{dt}T_L(t)\right| \tag{A.13}$$

with $\delta(0) = a\epsilon(0)$.

Consider the transition function $\Phi(t,s)$ that is generated by $m(t) = -\left(\rho - f \cdot exp(-\rho t)\right)$; that is

$$\frac{d}{dt}\Phi(t,s) = -\left(\rho - f \cdot exp(-\rho t)\right)\Phi(t,s), \qquad \Phi(s,s) = 1, \quad t,s \geq 0 \tag{A.14}$$

Since $m(t) + \rho \to 0$ as $t \to \infty$, it is clear that $0 \leq \Phi(t,s) \leq \mu \cdot exp((\rho - \nu)(s-t))$ for a fixed, arbitrarily small ν, a corresponding, fixed μ and all $t \geq s \geq 0$. Applying this bound, along with the variations of parameters formula, one thus has

$$\begin{aligned} \Phi(t,s) &= exp(\rho(s-t)) + \textstyle\int_s^t \exp(\rho(r-t)) \cdot f \cdot exp(-\rho r)\Phi(r,s)dr \\ &\leq exp(\rho(s-t)) + \textstyle\int_s^t \exp(\rho(r-t)) \cdot f \cdot exp(-\rho r) \cdot \mu \cdot exp((\rho-\nu)(s-r))dr \\ &\leq \left(1 + \tfrac{\mu f}{\rho - \nu}\right) exp(\rho(s-t)) \end{aligned} \tag{A.15}$$

Now, the solution of (A.13) is also determined by an associated variations of parameters formula. Using the bound (A.15), it immediately follows that $\delta(t)$ is bounded by an expression of the form of the right hand side of (A.2). This completes the proof of Lemma A.0.1. □

Case II: $\lambda \neq 0$

We consider the scaled incremental states $\tilde{e}_i = \lambda e_i$, $i = 3,4,5$ and set $\tilde{e}_i = e_i$, $i = 1,2$. The scaled state dynamics are governed, in closed loop, by the following differential equation.

$$\frac{d}{dt}\tilde{e} = \begin{bmatrix} A_{1,1} & -\lambda A_{2,1}^T \\ \\ \lambda A_{2,1} & A_{2,2} \end{bmatrix} \tilde{e} + \lambda \begin{bmatrix} 0_{2\times 1} \\ B_2 \end{bmatrix} \frac{d}{dt}T_L \tag{A.16}$$

This system is driven by a matrix that is the sum of a fixed negative definite component and a skew symmetric state dependent matrix.

As explained in the Appendix B, this form guarantees stable dynamics, where the skew symmetric matrix governs the lossless component, relative to the incremental energy storage $0.5\|\tilde{e}\|_E^2$. This applies, in particular, to the two blocks involving $\pm\lambda A_{2,1}$. Together these blocks form a skew-symmetric matrix that governs lossless exchanges between the electric and the mechanical incremental states. The selection of λ determines the rate of such lossless dynamics, which facilitate balancing the decay of the various incremental states. The selection of λ can be guided by eigenvalue analysis of (A.16) in an expected steady state. In a "non-salient rotor" case, when $\Delta L = 0$, the matrix $A_{2,1}$ is constant and (A.16) is linear time-invariant, making the effects of eigenvalue selections global.

Having thus motivated the selection of a non-zero λ, we observe that we do not have a counterpart of Lemma A.0.1 in that case. Specifically, the fact that $A_{1,1}$ and $A_{2,2}$ separately govern homogeneous dynamics with the exponential decay rate $-\rho$ does not imply that the overall dynamics of (A.16) enjoys such a decay rate. The example below illustrates this fact and sheds more light on the potential effects of selecting $\lambda \neq 0$. These effects are also demonstrated in our experimental results.

Example: The purpose of this example is to illustrate the fact that a skew-symmetric perturbation of a block diagonal "negative semidefinite + skew symmetric" matrix can affect and slow its associated decay rate. For simplicity, we focus on the smallest size matrices where this phenomenon can be observed, which is 3×3. Consider the matrices

$$M = \begin{bmatrix} -1 & 0 & 0 \\ 0 & 0 & -1 \\ 0 & 1 & -2 \end{bmatrix}, \quad S = \begin{bmatrix} 0 & -1 & 0 \\ 1 & 0 & 0 \\ 0 & 0 & 0 \end{bmatrix}, \quad A = M + aS$$

Clearly, all three eigenvalues of M are located at -1. A simple root-locus analysis would demonstrate that as the constant "a" increases, one eigenvalue of $A = M + aS$ approaches -2 while the other two asymptotically approach $-0.5 \pm \jmath a$.

An intuitive explanation of the example can be obtained from the "dissipativity" analysis perspective. In the equation $\dot{z} = Mz$, the first state is self–dissipated at the rate of -1, and the last, at the rate of -2. Dissipation of the second state is obtained, indirectly, via a lossless channel between the second and the third states, as governed by the skew symmetric component of M. The added skew symmetric component aS creates a second lossless channel, between the first and the second states, with faster dynamics as the constant "a" increases. This second channel takes some of the energy stored in the second state to the slower dissipating first state, instead of to the faster dissipating third state, hence the slower overall decay.

Despite its lower dimensionality, the example is directly related to the situation in (A.16), where the lossless channels that are created by the blocks $\lambda A_{2,1}$ and $-\lambda A_{2,1}^T$ between $\tilde{e}_3$ and $(\tilde{e}_1, \tilde{e}_2)$ compete with the two channels between $\tilde{e}_3$ and $\tilde{e}_4$ and between $\tilde{e}_3$ and $\tilde{e}_5$. Unless the design parameters of the block $A_{2,2}$ are modified, we should thus expect that higher levels of λ entail slower convergence of the load torque estimate. Relating to eigenvalue placement, a simple root locus analysis reveals that higher values of λ – with the rest of the design parameters being fixed – moves two of the "mechanical eigenvalues" to the left, while one is moved to the right, approaching the origin as $\lambda \to \infty$. This phenomenon was observed in experiments (not shown) which featured a shorter initial speed response time ("rise time"), but a longer time constant for eventual convergence. The lengthening of the resulting settling time can be offset, as was done in the experiments shown in Chapter 6, by a more aggressive load torque adaptation (meaning using higher values of τ) and a coordinated eigenvalue assignment for the entire 5×5 incremental system matrix.

Appendix B

Stability of dissipative systems

This section summarizes some results concerning stability properties in a class of dissipative systems that is relevant to our analysis. While these observations are specific variants of well known Lyapunov stability results, it is helpful to provide them here.

We consider systems of the form

$$\dot{x}(t) = -(D + S(t, x(t)))x(t) + f(t) \tag{B.1}$$

where D is a positive semidefinite constant matrix and where $S(t, x)$ is a skew symmetric, matrix valued function (meaning that $S(t, x) + S(t, x)^T = 0$ for all t and x). Such systems are naturally associated with the "energy" storage (or, Lyapunov) function $V(x) = 0.5\|x\|_E^2$. Indeed, many systems whose models are derived from energy conversion lows are of the form (B.1), where $V(x)$ is the actual energy of the system state at any given moment. The PMSM is one such example, and it can be easily brought to the form (B.1) with the state $[\sqrt{L_d} i_d, \sqrt{L_q} i_q, \sqrt{H}\omega]^T$.

Given the ingredients, as described right above, differentiation of the storage function $V(x)$ along trajectories of (B.1) provides for

$$\frac{d}{dt}V(x) = x^T(f - Dx) \tag{B.2}$$

One initial implications of (B.2) concerns some basic stability properties.

Lemma B.0.2 *(i) If $f(t) = 0$ then trajectories of (B.1) are trapped in a ball whose radius is determined the Euclidean norm of the initial state. Furthermore, then components of the state that are proportional to eigenvectors of D with strictly negative eigenvalues, tend to zero as $t \to \infty$. (ii) If $f = Dg$ with a uniformly bounded input g then the trajectory Dx is asymptotically trapped in the ball $\|D^{\frac{1}{2}}(x(t) - 0.5g(t))\|_E \leq 0.5\|g(t)\|_E$. (iii) If D is positive definite then solutions (B.1) satisfy a positive exponential* decay *bound of the form*

$$\|x(t)\|_E \leq \mu \left(exp(\nu(s - t))\|x(s)\|_E + \int_s^t exp(\nu(r - t))\|f(r)\|_E dr \right) \tag{B.3}$$

for some fixed, positive μ and ν, for all $t > s$ and all initial states $x(s)$ and inputs f. (iv) Solutions of (B.1) always satisfy a uniform growth *bound of the form (B.3), with $\nu = 0$.*

Proof: Part (i) of the lemma is an obvious consequence of the fact that D is positive semidefinite, hence that the derivative of $V(x)$ is non-positive along trajectories of (B.1) in the homogeneous case. Part (ii) follows similarly, noting that when $f = Dg$ one can re-write (B.2) in the form

$$\frac{d}{dt}V(x) = 0.25\|f\|_E^2 - \|D^{\frac{1}{2}}(x - 0.5g)\|_E^2 \tag{B.4}$$

Along any trajectory $x(t)$, the nonlinear system (B.1) is equivalent to a linear time varying (LTV) system where the "A" matrix is $A(t) = D + S(t, x(t))$. Part (iii) follows by analyzing first, for each trajectory $x(t)$ of (B.1), the allied homogeneous LTV equation $\dot{z}(t) = A(t)z(t)$. It easily follows that solutions of this LTV system satisfy the following variant of (B.2)

$$\frac{d}{dt}0.5\|z(t)\|_E^2 = -z(t)^T Dz(t) \leq -\nu\|z(t)\|_E^2 \tag{B.5}$$

where $\nu = \lambda_{min}(D)$ is the minimal eigenvalue of D, which, by assumption, is positive. It is a standard fact that the inequality (B.5) implies a uniform exponential decay of $\|z(t)\|_E^2$, at the exponential rate of -2ν. Consequently, the transition matrices $\Phi(t, s)$ that are generated by the various "$A(t)$" decay at the exponential rate $-\nu$, regardless of the underlying trajectory "$x(t)$". Now, each trajectory $x(t)$ of (B.1) can be represented by the variation of parameters formula, as a trajectory of the allied LTV system $\dot{x}(t) = A(t)x(t) + f(t)$. The bound (B.3) – with $\mu = 1$ – readily follows from that formula and the just established exponential decay of the associated $\Phi(t, s)$.

In establishing Part (iv) it is noted that, with any positive semidefinite D, the inequality in (B.5) is valid with $\nu = 0$. From here the proof continues as in Part (iii). □

The following discussion concerns exponential stability properties in the case of a non-positive definite D. To that end we recall the definition that the pair $[A, D^{\frac{1}{2}}]$ is *uniformly observable* if there exist positive constants ϵ and δ with the property that for any solution of the homogeneous LTV system $\dot{z}(t) = A(t)z(t)$ and any $t \geq 0$ there holds $\|z\|_{L_2[t,t+\epsilon]} \geq \delta\|x(t)\|_E$. The following lemma presents – without proof – two basic facts from LTV system theory.

Lemma B.0.3 *Consider a LTV system* $\dot{z}(t) = F(t)z(t) + f(t)$, $y(t) = G(t)z(t)$, *where* $G(t)$ *is a uniformly bounded coefficient and the transition matrix generated by* $F(t)$ *enjoys a uniform exponential growth bound. Then the following hold: (i) If the pair* $[F, G]$ *is uniformly observable, then there exists* $\kappa > 0$ *such that* $\|z\|_{L_2[a,t]} \leq \kappa(\|f\|_{L_2[s,t]} + \|y\|_{L_2[s,t]} + \|z(s)\|_E)$ *for all* $t > s$, *input* $f \in L_2[s,t]$ *and initial state* $z(s)$. *Furthermore, the constant* κ *is a function of the uniform bound over* $\|G(t)\|$, *the exponential growth bound over the transition matrix generated by* $F(t)$ *and the constants* ϵ *and* δ *that characterize the observability property, as above.* $\gamma\|z(t)\|_E)$ *when* $f = 0$, *for all* t *and all initial states* $z(t)$, *then the transition matrix* $\Phi(t,s)$ *that is generated by* $F(t)$ *is uniformly exponentially stable, meaning that there are positive* μ *and* ν *such that* $\|\Phi(t,s)\| \leq \mu \cdot exp(\nu(s-t)$, $t > s$. *Furthermore, an upper bound over* μ *and a lower bound over* ν *can be determined in terms of the constant* γ *and the a priori assumed exponential growth bound on* $\Phi(t,s)$.

A corollary of Lemma B.0.3 relates to a stability of (B.1) in a subclass of systems that is relevant to our derivation.

Corollary B.0.1 *Let the notation of the allied matrix functions* $A(t)$ *remain as above. Assume that the corresponding pairs* $[A, D^{\frac{1}{2}}]$ *are each uniformly observable, with the same "*ϵ*" and "*δ*" (as above) applying to all of them. Then there exist constants* $\mu > 0$ *and* $\nu > 0$ *such that each of the said trajectories satisfies (B.3).*

Outline of the proof. By part (iv) of Lemma B.0.2, the transition matrices generated by the allied matrix valued functions "$A(t)$" are uniformly bounded. One can thus appeal to the results in Lemma B.0.3. By Part (i) of that lemma, solutions of the family of the LTV homogeneous differential equations $\dot{z}(t) = A(t)z(t)$ satisfy

$$\|z\|_{L_2[s,t]} \leq \kappa \left(\|D^{\frac{1}{2}} z\|_{L_2[s,t]} + \|z(s)\|_E \right) \tag{B.6}$$

for all $t > s$, all initial states $z(s)$, and with the same κ applying to all these systems. Integrating (B.5) along an interval one obtains

$$\|D^{\frac{1}{2}} z\|^2_{L_2[s,t]} \leq \|D^{\frac{1}{2}} z\|^2_{L_2[s,t]} + 0.5\|z(t)\|^2_E = 0.5\|z(s)\|^2_E \tag{B.7}$$

This translates (B.6) into a bound that depends only on the initial state

$$\|z\|_{L_2[s,t]} \leq 1.5\kappa \|z(s)\|_E \tag{B.8}$$

Appealing to part (ii) of Lemma B.0.3, the family of transition matrices that are generated by the various $A(t)$ are guaranteed a uniform exponential stability. That is, the transition matrices $\Phi(t,s)$ that are generated by the various A's, adhere to a uniform exponential decay rate $\|\Phi(t,s)\| \leq \mu \cdot exp(\nu(s-t))$, $t > s$. As noted earlier, the bound (B.3) is an immediate consequence. $\Box$

Appendix C

Calculation of Speed Error Power

Figure C.1 schematically describes the encoder signal. S_m is the slope (hence the average speed) between time instances t_{m-1} and t_m. Note that t_m is the time at which a new encoder line is received, it is measured with some random error, and does not necessarily coincide with time samples of computational cycle that are T_s apart. The speed measured as an average in $[t_{m-1}, t_m]$ is used as the speed estimate in $[t_m, t_{m+1}]$.

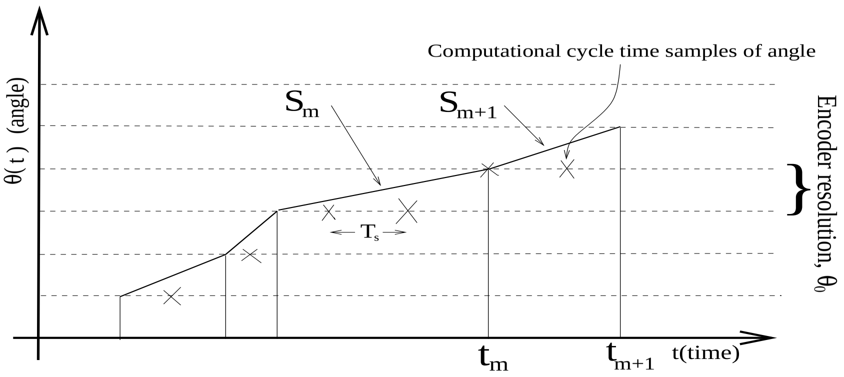
Computational cycle time samples of angle
θ(t) (angle)
S_m
S_{m+1}
Encoder resolution, θ_0
T_s
t_m
t_{m+1}
t(time)

Figure C.1: The actual dependence of angle on computational cycle time

We calculate the speed estimate from

$$\hat{\omega}_m = \frac{\theta_0}{t_m - t_{m-1} + \Delta t_m - \Delta t_{m-1}} \tag{C.1}$$

where Δt_i 's are random variables (uniform on $[-T_{clck}/2, T_{clck}/2]$) modeling the inaccuracy in the measurement of time due to finite resolution of the speed measuring clock. Assuming the frequency of the clock is high, we can approximate (C.1) by the following (we retain the first two terms in the Taylor series):

$$\hat{\omega}_m \approx \frac{\theta_0}{t_m - t_{m-1}}(1 - \xi_m + \xi_m^2 - \xi_m^3 + \ldots) \tag{C.2}$$

where $\xi_m = \frac{\Delta t_m - \Delta t_{m-1}}{t_m - t_{m-1}}$. Now we define $\beta(t) = e_\omega(t) sin(Nk\theta(t))$ to be the actual driving term in the adaptation rule (without noise) and $\hat{\beta}(t)$ as its estimate. Here our task is to characterize the quantity $E|\widehat{\beta}(t) - \beta(t)|^2$ as the noise power, where E is the mathematical expectation operator. Using the properties of expectation operator($E|Z|^2 = var(Z) + |E(Z)|^2$) we obtain:

$$E|\widehat{\beta}(t) - \beta(t)|^2 = E|\widehat{\beta}(t) - E\widehat{\beta}(t)|^2 + |E\widehat{\beta}(t) - \beta(t)|^2 \tag{C.3}$$

Now we calculate both terms on the right side of the above equation. First we evaluate $E\hat{\beta}(t)$

$$E\hat{\beta}(t) = E\{(\hat{\omega}_m - \omega_d) sin(Nk\theta(t_m))\} \approx (S_m - \omega_d) sin(Nk\theta(t_m)) \tag{C.4}$$

where $S_m = \theta_0/(t_m - t_{m-1})$. To assess the noise in the measurement, we still need to have a knowledge of $\beta(t)$. If we assume that the actual speed is constant between two encoder lines, then the additional inaccuracies enter because of delay effects and because of the evaluation of the trigonometric quantity. The delay effect is because the speed estimate used is the one calculated in the previous encoder slot. The inaccuracy in the calculation of the trigonometric quantity comes from the fact that the angle is assumed constant in the time interval preceding the arrival of a new encoder pulse. Thus,

$$\beta(t) = (\frac{\theta_0}{t_{m+1} - t_m} - \omega_d) sin[Nk(\theta(t_m) + (t - t_m)\frac{\theta_0}{t_{m+1} - t_m})] \tag{C.5}$$

After some algebra we can find a conservative upper bound for $|E\hat{\beta}(t) - \beta(t)|^2$ as:

$$|E\hat{\beta}(t) - \beta(t)|^2 \leq sin^2(Nk\theta(t_k))S_{m+1}^2 \tag{C.6}$$

The above expression simplifies if the error in the calculation of the trigonometric quantity is ignored (which is valid for low order harmonics). In that case the expression simplifies to

$$|E\hat{\beta}(t) - \beta(t)|^2 \approx sin^2(Nk\theta(t_m))(S_m - S_{m+1})^2 \tag{C.7}$$

Observe that for higher harmonics this approximation is not valid, and the inaccuracy in the calculation of the trigonometric quantity becomes important. To calculate the variance $E|\hat{\beta}(t) - E\beta(t)|^2$ we write

$$\begin{aligned} E|\hat{\beta}(t) - E\hat{\beta}(t)|^2 &= |S_m(1 - \xi_m)sin(Nk\theta(t_m)) - S_m sin(Nk\theta(t_m))|^2 \qquad (C.8) \\ &= var(\xi_m)S_m^2 sin^2(Nk\theta(t_m)) \leq var(\xi_m)S_m^2 = \frac{T_{clck}^2 S_m^4}{6\theta_0^2} \end{aligned}$$

The final result (averaged squared error term driving the adaptation) will be the sum of expressions (C.7) and (C.8), showing that the quality of the speed estimate that uses (C.1) decreases at higher speeds. Note that when the speed gets higher, we can include more terms in the Taylor expansion (which adds more noise to the estimate in addition to the fourth power dependence on speed, proportional to S_M^4), or use a different speed estimation algorithm. Using the parameter values as in our experimental test bed, the quantity contributing to the error sum coming from equation (C.8) is small due to the high frequency(6.25 MHz) clock. Equation (C.7) thus provides the dominant contribution and experimental speed data show that this can reach levels around -49dB.

Appendix D

Parameters of the DC servo motor setup

The motor and load parameters are: $R_a = 0.92\Omega$, $L_a = 4.9\text{mH}$, $J = 3.9 \cdot 10^{-3}\text{kg-m}^2$, $F = 1.2 \cdot 10^{-3}\text{Nms}$, $K_e = 0.296\text{V}/(\text{rad/sec})$, $K_t = 0.294\text{Nm/A}$ and $T_{load} = 0.44\text{Nm}$.

Following the standard procedure [67], the PI control parameters were selected as $K_p^i = 0.1$, $K_i^i = 47.283$, $K_p^\omega = 2.513$ and $K_i^\omega = 118.416$. These selections provides for a damping of "$\zeta = 1$" in both loops, with the respective desired natural frequencies of $\approx 10^3$rad/sec (current loop) and $\approx 10^2$rad/sec (speed loop), when the PWM block is replaced by a nominal gain. The switching frequency of the PWM is 1.5kHz, $V_d = 1.56$ V and $V_{DC} = 60$ V. The compensator sampling frequency in our experiments is 10kHz.

Appendix E

The ripple function coefficients

The coefficients of the ripple function slopes in terms of system parameters

$$\alpha = K_p^i T \; \frac{\omega^*(FR_a + K_t K_e) + R_a T_{load} - V_{DC} K_t}{L_a K_t V_d} \tag{E.1}$$

$$\beta = K_p^i T \; \frac{\omega^*(FR_a + K_t K_e) + R_a T_{load}}{L_a K_t V_d} \tag{E.2}$$

$$\beta - \alpha = \frac{1}{2M} = \frac{K_p^i T V_{DC}}{L_a V_d} \tag{E.3}$$

$$\tau_{ss} = \frac{\beta}{\beta - \alpha} = \omega^* \; \frac{FR_a + K_t K_e}{K_t V_{DC}} + T_{load} \; \frac{R_a}{K_t V_{DC}} \tag{E.4}$$

Appendix F

Derivation of the piecewise affine map

In this section, with the help of simple geometrical observations (see Fig. 16.2), explicit expressions used in (17.25-17.26) for matricses $\mathbf{A}^{(\ell)}$, $\mathbf{B}^{(\ell)}$, $\mathbf{C}^{(\ell)}$, $\mathbf{D}^{(\ell)}$ will be derived. First, equations for the straight line segments which correspond to slopes 1, 2 and 3 for the time interval $t \in [t_k, t_k + T]$ will be obtained. Then conditions for existence of the intersection of the specific slope of $m(\mathbf{x})$ with the sawtooth function will yield inequalities (17.26). An equation for τ_k will be obtained as a solution of (16.13) or, for the given slope, from the equivalent linear equation

$$m(\mathbf{x}(t_k + \theta T - t_s))/V_d = \theta. \tag{F.1}$$

An equation for $\bar{m}_k$ as a function of $\bar{m}_{k-1}$ and τ_{k-1} is straightforward and does not depend on the intersected slope

$$\bar{m}_k = \bar{m}_{k-1} + \alpha\tau_{k-1} + \beta(1 - \tau_{k-1}). \tag{F.2}$$

Both these equations yield (17.25).

Equations for $m(\mathbf{x}(t_k + \theta T - t_s))/V_d$ along the slopes 1, 2, 3 for the interval $[t_k, t_k + T]$ are

$$\bar{m}_{k-1} + \alpha(\theta - t_s/T + 1) \qquad \theta \in [t_s/T - 1, t_s/T - 1 + \tau_{k-1}] \tag{F.3}$$

$$\bar{m}^{\tau}_{k-1} + \beta(\theta - t_s/T + 1 - \tau_{k-1}) \qquad \theta \in [t_s/T - 1 + \tau_{k-1}, t_s/T] \tag{F.4}$$

$$\bar{m}_k + \alpha(\theta - t_s/T) \qquad \theta \in [t_s/T, t_s/T + \tau_k] \tag{F.5}$$

where

$$\bar{m}^{\tau}_{k-1} = \bar{m}_{k-1} + \alpha\tau_{k-1}. \tag{F.6}$$

To simplify derivations some more notations are introduced (see Fig. 16.2)

$$\bar{m}^{(1)}_{k-1} = \bar{m}_{k-1} + \alpha(1 - t_s/T) \tag{F.7}$$

$$\bar{m}^{(2)}_{k-1} = \bar{m}^{\tau}_{k-1} + \beta(1 - t_s/T - \tau_{k-1}) \tag{F.8}$$

$$\tag{F.9}$$

Case 1 - Intersection within slope 1

Intersection of the slope 1 with the sawtooth function may occur if and only if the inequalities

$$\bar{m}^{(1)}_{k-1} > 0 \quad \text{and} \quad \bar{m}^{\tau}_{k-1} < t_s/T + \tau_{k-1} - 1 \tag{F.10}$$

are true, or equivalently, if

$$\bar{m}_{k-1} + \alpha(1 - t_s/T) > 0 \tag{F.11}$$

$$(\alpha-1)\tau_{k-1}+\bar{m}_{k-1}+1-t_s/T<0 \tag{F.12}$$

If an intersection occurs, then the next τ_k can be found from (F.1)

$$\tau_k=\frac{\bar{m}_{k-1}}{1-\alpha}+\frac{\alpha(1-t_s/T)}{1-\alpha} \tag{F.13}$$

and the next ripple peak magnitude $\bar{m}_k$ is computed from (F.2)

$$\bar{m}_k=(\alpha-\beta)\tau_{k-1}+\bar{m}_{k-1}+\beta. \tag{F.14}$$

Finally we obtain

$$\mathbf{A}^{(1)}=\begin{bmatrix}0 & 1/(1-\alpha)\\ \alpha-\beta & 1\end{bmatrix}; \qquad \mathbf{B}^{(1)}=\begin{bmatrix}\alpha(1-t_s/T)/(1-\alpha)\\ \beta\end{bmatrix}; \tag{F.15}$$

$$\mathbf{C}^{(1)}=\begin{bmatrix}0 & 1\\ 1-\alpha & -1\end{bmatrix}; \qquad \mathbf{D}^{(1)}=\begin{bmatrix}\alpha(1-t_s/T)\\ t_s/T-1\end{bmatrix}. \tag{F.16}$$

Case 2 - Intersection within slope 2

Consider two cases $\beta>1$ and $\beta<1$. For $\beta>1$ then intersection of the slope 2 with the sawtooth function may occur if and only if inequalities

$$\bar{m}^{\tau}_{k-1}>t_s/T+\tau_{k-1}-1, \quad \bar{m}^{(2)}_{k-1}>0 \quad \text{and} \quad \bar{m}_k<t_s/T \tag{F.17}$$

are true, or equivalently, if

$$(\alpha-1)\tau_{k-1}+\bar{m}_{k-1}+1-t_s/T>0 \tag{F.18}$$

$$(\alpha-\beta)\tau_{k-1}-\bar{m}_{k-1}+\beta(1-t_s/T)>0 \tag{F.19}$$

$$(\alpha-\beta)\tau_{k-1}+\bar{m}_{k-1}+\beta-t_s/T<0 \tag{F.20}$$

For $\beta < 1$ inequalities (F.18- F.20) change sign. If an intersection occurs, then the next τ_k can be found from (F.1)

$$\tau_k = \frac{\alpha-\beta}{1-\beta}\tau_{k-1} + \frac{\bar{m}_{k-1}}{1-\beta} + \frac{\beta(1-t_s/T)}{1-\beta} \tag{F.21}$$

and the $\bar{m}_k$ is given by (F.14).

Thus

$$\mathbf{A^{(2)}} = \begin{bmatrix} (\alpha-\beta)/(1-\beta) & 1/(1-\beta) \\ \alpha-\beta & 1 \end{bmatrix}; \qquad \mathbf{B^{(2)}} = \begin{bmatrix} \beta(1-t_s/T)/(1-\beta) \\ \beta \end{bmatrix}; \tag{F.22}$$

$$\mathbf{C^{(2)}} = \begin{bmatrix} \alpha-1 & 1 \\ \alpha-\beta & 1 \\ \beta-\alpha & -1 \end{bmatrix} \mathrm{sig}(1-\beta); \qquad \mathbf{D^{(2)}} = \begin{bmatrix} 1-t_s/T \\ \beta(1-t_s/T) \\ -\beta+t_s/T \end{bmatrix} \mathrm{sig}(1-\beta). \tag{F.23}$$

Case 3 - Intersection within slope 3

An intersection of the slope 3 with the sawtooth function may occur if and only if the inequalities

$$\bar{m}_k > t_s/T, \qquad \text{and} \quad \bar{m}_k^{(1)} < 1 \tag{F.24}$$

are true, or equivalently, if

$$(\alpha-\beta)\tau_{k-1} + \bar{m}_{k-1} + \beta - t_s/T > 0 \tag{F.25}$$

$$(\alpha-\beta)\tau_{k-1} + \bar{m}_{k-1} + \beta + \alpha(1-t_s/T) - 1 < 0 \tag{F.26}$$

If an intersection occurs, then the next τ_k can be found from (F.1)

$$\tau_k = \frac{\alpha-\beta}{1-\alpha}\tau_{k-1} + \frac{\bar{m}_{k-1}}{1-\alpha} + \frac{\beta-\alpha t_s/T}{1-\alpha} \tag{F.27}$$

and the $\bar{m}_k$ is given by (F.14).

Thus

$$\mathbf{A^{(3)}} = \begin{bmatrix} (\alpha-\beta)/(1-\alpha) & 1/(1-\alpha) \\ \alpha-\beta & 1 \end{bmatrix}; \quad \mathbf{B^{(3)}} = \begin{bmatrix} (\beta-\alpha t_s/T)/(1-\alpha) \\ \beta \end{bmatrix}; \tag{F.28}$$

$$\mathbf{C^{(3)}} = \begin{bmatrix} \alpha-\beta & 1 \\ \beta-\alpha & -1 \end{bmatrix}; \qquad \mathbf{D^{(3)}} = \begin{bmatrix} \beta - t_s/T \\ 1-\beta-\alpha(1-t_s/T) \end{bmatrix}. \tag{F.29}$$

Case 4 - No intersection ($m < V_d\mathrm{tri}(T,t)$)

This may occur if and only if inequalities

$$\bar{m}^{(1)}_{k-1} < 0, \quad \bar{m}^{\tau}_{k-1} < t_s/T + \tau_{k-1} - 1, \quad \bar{m}_k < t_s/T \quad \text{and} \quad \bar{m}^{(1)}_k < 1 \tag{F.30}$$

are true, or equivalently, if

$$\bar{m}_{k-1} + \alpha(1-t_s/T) < 0 \tag{F.31}$$

$$(\alpha-1)\tau_{k-1} + \bar{m}_{k-1} + 1 - t_s/T < 0 \tag{F.32}$$

$$(\alpha-\beta)\tau_{k-1} + \bar{m}_{k-1} + \beta - t_s/T < 0 \tag{F.33}$$

$$(\alpha-\beta)\tau_{k-1} + \bar{m}_{k-1} + \beta + \alpha(1-t_s/T) - 1 < 0 \tag{F.34}$$

It is easy to see that if $\beta < 1$, then (F.32) implies (F.33); if $\beta > 1$ then (F.33) implies (F.32). Inequality (F.33) always implies (F.34). Thus a minimal set of conditions is

$$\bar{m}_{k-1} + \alpha(1-t_s/T) < 0 \tag{F.35}$$

$$(\alpha - \max(\beta,1))\tau_{k-1} + \bar{m}_{k-1} + \max(\beta,1) - t_s/T < 0. \tag{F.36}$$

If the above conditions hold, then $\tau_k = 0$ and the $\bar{m}_k$ is given by (F.14).

Thus

$$\mathbf{A^{(4)}} = \begin{bmatrix} 0 & 0 \\ \alpha - \beta & 1 \end{bmatrix}, \qquad \mathbf{B^{(4)}} = \begin{bmatrix} 0 \\ \beta \end{bmatrix}, \tag{F.37}$$

$$\mathbf{C^{(4)}} = \begin{bmatrix} 0 & -1 \\ \max(\beta,1) - \alpha & -1 \end{bmatrix}, \qquad \mathbf{D^{(4)}} = \begin{bmatrix} \alpha(t_s/T - 1) \\ t_s/T - \max(\beta,1) \end{bmatrix}. \tag{F.38}$$

Case 5 - No intersection ($m > V_d\mathrm{tri}(T,t)$)

This may occur if and only if the inequalities

$$\bar{m}^{(1)}_{k-1} > 0, \quad \bar{m}^{\tau}_{k-1} > t_s/T + \tau_{k-1} - 1, \quad \bar{m}_k > t_s/T \quad \text{and} \quad \bar{m}^{(1)}_k > 1 \tag{F.39}$$

are true, or equivalently, if

$$\bar{m}_{k-1} + \alpha(1 - t_s/T) > 0 \tag{F.40}$$

$$(\alpha - 1)\tau_{k-1} + \bar{m}_{k-1} + 1 - t_s/T > 0 \tag{F.41}$$

$$(\alpha - \beta)\tau_{k-1} + \bar{m}_{k-1} + \beta - t_s/T > 0 \tag{F.42}$$

$$(\alpha - \beta)\tau_{k-1} + \bar{m}_{k-1} + \beta + \alpha(1 - t_s/T) - 1 > 0 \tag{F.43}$$

It is easy to see that if $\beta > 1$, then (F.41) implies (F.42); if $\beta < 1$ then (F.42) implies (F.41). Inequality (F.43) always implies (F.42). Then, for $\beta < 1$

$$\bar{m}_{k-1} + \alpha(1 - t_s/T) > 0 \tag{F.44}$$

$$(\alpha - \beta)\tau_{k-1} + \bar{m}_{k-1} + \beta + \alpha(1 - t_s/T) - 1 > 0 \tag{F.45}$$

For $\beta > 1$ one more inequality should be added

$$(\alpha - 1)\tau_{k-1} + \bar{m}_{k-1} + 1 - t_s/T > 0. \tag{F.46}$$

If the above conditions hold, then $\tau_k = 1$, and the $\bar{m}_k$ is given by (F.14). Thus

$$\mathbf{A}^{(5)} = \begin{bmatrix} 0 & 0 \\ \alpha - \beta & 1 \end{bmatrix}, \qquad \mathbf{B}^{(5)} = \begin{bmatrix} 1 \\ \beta \end{bmatrix}, \tag{F.47}$$

$$\mathbf{C}^{(5)} = \begin{bmatrix} 0 & 1 \\ \alpha - \beta & 1 \\ \alpha - 1 & 1 \end{bmatrix}, \qquad \mathbf{D}^{(5)} = \begin{bmatrix} \alpha(1 - t_s/T) \\ \beta - 1 + \alpha(1 - t_s/T) \\ 1 - t_s/T \end{bmatrix}. \tag{F.48}$$